A UNITED STATES DEPARTMENT OF COMMERCE PUBLICATION

SECTION A

JOURNAL OF RESEARCH

of the NATIONAL BUREAU OF STANDARDS

Volume 75A, Number 3 May-June 1971

Physics and Chemistry

U.S. DEPARTMENT OF COMMERCE
National Bureau of Standards

Journal of Research

of the

National Bureau of Standards

A. Physics and Chemistry

May–June • 1971

VOLUME • 75A

NUMBER • 3

Editor: C. W. Beckett

Associate Editor: D. D. Wagman

Publication dates:
Feb. 1, Apr. 1, June 1, Aug. 1, Oct. 1, Dec. 1, 1971

J. Res. Nat. Bur. Stand. (U.S.), A
CODEN: JNBAA 75A (3) 141–245 (1971)

JOURNAL OF RESEARCH

The National Bureau of Standards Journal of Research reports research and development in the fields of activity shown at right. Also included from time to time are survey articles on topics closely related to the Bureau's scientific and technical program.

The Journal is published in three separate sections as follows:

A. Physics and Chemistry

Contains papers of interest primarily to scientists working in these fields. Issued six times a year. Annual subscription: domestic, $9.50; foreign, $11.75. Single copy, varies.

B. Mathematical Sciences

Presents studies and compilations designed mainly for the mathematician and the theoretical physicist. Issued quarterly. Annual subscription: domestic, $5.00; foreign, $6.25. Single copy, $1.25.

C. Engineering and Instrumentation

Reports research and development results of interest chiefly to the engineer and the applied scientist. Issued quarterly. Annual subscription: domestic, $5.00; foreign, $6.25. Single copy, $1.25.

The National Bureau of Standards[1] was established by an act of Congress March 3, 1901. The Bureau's overall goal is to strengthen and advance the Nation's science and technology and facilitate their effective application for public benefit. To this end, the Bureau conducts research and provides: (1) a basis for the Nation's physical measurement system, (2) scientific and technological services for industry and government, (3) a technical basis for equity in trade, and (4) technical services to promote public safety. The Bureau consists of the Institute for Basic Standards, the Institute for Materials Research, the Institute for Applied Technology, the Center for Computer Sciences and Technology, and the Office for Information Programs.

THE INSTITUTE FOR BASIC STANDARDS provides the central basis within the United States of a complete and consistent system of physical measurement; coordinates that system with measurement systems of other nations; and furnishes essential services leading to accurate and uniform physical measurements throughout the Nation's scientific community, industry, and commerce. The Institute consists of a Center for Radiation Research, an Office of Measurement Services and the following divisions:

Applied Mathematics—Electricity—Heat—Mechanics—Optical Physics—Linac Radiation[2]—Nuclear Radiation[2]—Applied Radiation[2]—Quantum Electronics[3]—Electromagnetics[3]—Time and Frequency[3]—Laboratory Astrophysics[3]—Cryogenics[3].

THE INSTITUTE FOR MATERIALS RESEARCH conducts materials research leading to improved methods of measurement, standards, and data on the properties of well-characterized materials needed by industry, commerce, educational institutions, and Government; provides advisory and research services to other Government agencies; and develops, produces, and distributes standard reference materials. The Institute consists of the Office of Standard Reference Materials and the following divisions:

Analytical Chemistry—Polymers—Metallurgy—Inorganic Materials—Reactor Radiation—Physical Chemistry.

THE INSTITUTE FOR APPLIED TECHNOLOGY provides technical services to promote the use of available technology and to facilitate technological innovation in industry and Government; cooperates with public and private organizations leading to the development of technological standards (including mandatory safety standards), codes and methods of test; and provides technical advice and services to Government agencies upon request. The Institute also monitors NBS engineering standards activities and provides liaison between NBS and national and international engineering standards bodies. The Institute consists of the following technical divisions and offices:

Engineering Standards Services—Weights and Measures—Flammable Fabrics—Invention and Innovation—Vehicle Systems Research—Product Evaluation Technology—Building Research—Electronic Technology—Technical Analysis—Measurement Engineering.

THE CENTER FOR COMPUTER SCIENCES AND TECHNOLOGY conducts research and provides technical services designed to aid Government agencies in improving cost effectiveness in the conduct of their programs through the selection, acquisition, and effective utilization of automatic data processing equipment; and serves as the principal focus within the executive branch for the development of Federal standards for automatic data processing equipment, techniques, and computer languages. The Center consists of the following offices and divisions:

Information Processing Standards—Computer Information—Computer Services—Systems Development—Information Processing Technology.

THE OFFICE FOR INFORMATION PROGRAMS promotes optimum dissemination and accessibility of scientific information generated within NBS and other agencies of the Federal Government; promotes the development of the National Standard Reference Data System and a system of information analysis centers dealing with the broader aspects of the National Measurement System; provides appropriate services to ensure that the NBS staff has optimum accessibility to the scientific information of the world, and directs the public information activities of the Bureau. The Office consists of the following organizational units:

Office of Standard Reference Data—Office of Technical Information and Publications—Library—Office of Public Information—Office of International Relations.

[1] Headquarters and Laboratories at Gaithersburg, Maryland, unless otherwise noted; mailing address Washington, D.C. 20234.
[2] Part of the Center for Radiation Research.
[3] Located at Boulder, Colorado 80302.

U.S. DEPARTMENT OF COMMERCE
Maurice H. Stans, Secretary
NATIONAL BUREAU OF STANDARDS
Lewis M. Branscomb, Director

Order all publications from the Superintendent of Documents
U.S. Government Printing Office, Washington, D.C. 20402

Use of funds for printing this publication approved by the Director of the Bureau of the Budget (June 22, 1966).

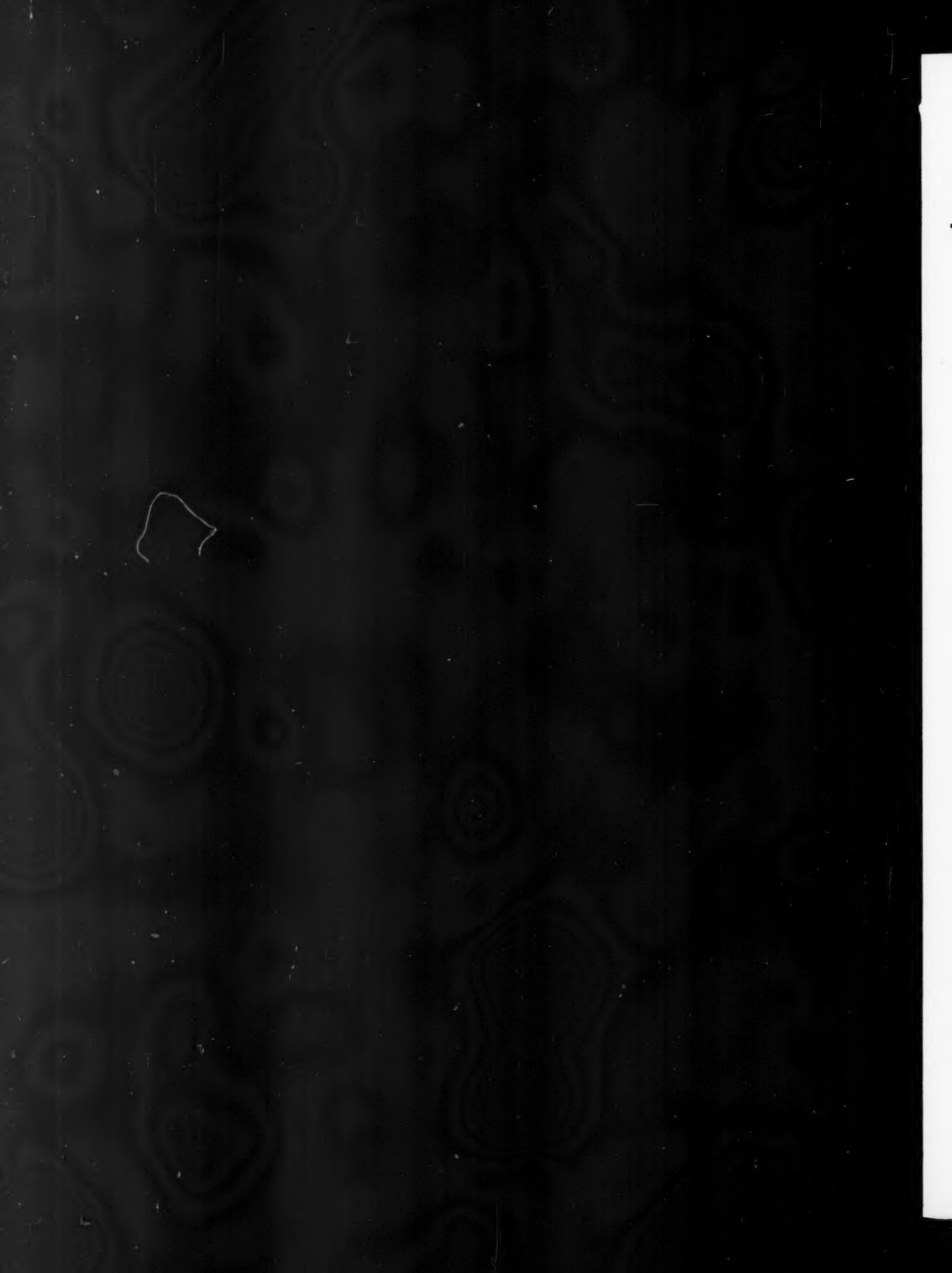

JOURNAL OF RESEARCH of the National Bureau of Standards—A. Physics and Chemistry
Vol. 75A, No. 3, May–June 1971

The Solid Phase Photolysis and Radiolysis of Ethylene at 20 to 77 K*

R. Gorden, Jr., and P. Ausloos

Institute for Materials Research, National Bureau of Standards, Washington, D.C. 20234

(January 11, 1971)

Films of ethylene condensed onto a cold finger maintained at 20 K were irradiated with photons whose energy ranged from 8.4 to 21.2 eV. At the higher photon energies the relative yields of products compare well with those seen in the radiolysis of solid ethylene. Experiments on CH_2CD_2 demonstrate that in the photolysis hydrogen is mainly formed by the elimination processes $CH_2CD_2^* \rightarrow H_2(D_2) + C_2D_2(C_2H_2)$ and $CH_2CD_2^* \rightarrow HD + C_2HD$. The relative probabilities of these three processes are independent of the energy of the incident photons from 8.4 to 11.6 eV and are within experimental error identical to those observed in earlier gas phase photolysis experiments. Relative to acetylene, cyclobutane is a minor product at 8.4 eV but increases by an order of magnitude at higher energies where ions play a role. Cyclobutane, 1-butene and methylcyclopropane formed upon irradiation of frozen $C_2H_4-C_2D_4$ mixtures consisted mainly of C_4D_8, $C_4D_4H_4$, and C_4H_8. Plausible mechanisms which may account for the formation of the latter products are examined. In the solid phase as in the gas phase the relative importance of H-atom production is seen to increase with increasing photon energy. Cyclopropane, apparently formed by insertion of CH_2 into C_2H_4, is observed as a product at all wavelengths in the photolysis, and in the radiolysis.

Key words: Ethylene; free radical reactions; ion-molecule reactions; photolysis; polymerization; radiolysis.

1. Introduction

The condensed phase photolysis of simple olefins has not as yet been investigated in detail. Only one experiment dealing with ethylene (8.4 eV photons, 36 K) has been discussed [1][1] in the literature. It was suggested that the products (1-C_4H_8 and methylcyclopropane) observed in the latter experiment were formed by the addition of ethylidene radicals to ethylene. The condensed phase radiolysis of olefins, on the other hand, has been investigated extensively [2, 3]. In the radiolysis studies on ethylene, 1-butene was noted as a major product and was thought to be produced by addition of an ethylene ion to ethylene. Hexenes, octenes, and decenes which were also observed were suggested to be formed by subsequent additions of product ions to ethylene. Isotopic analysis of the C_4, C_6, and C_8 products formed in the radiolysis of $C_2H_4-C_2D_4$ did reveal [3c] that these products are indeed mainly formed by consecutive additions to form polymer molecules containing deuterium in multiples of four.

The purpose of the study reported here is to explore the processes occurring in the solid phase irradiation of ethylene more fully. The photolysis has been investigated at four different energies. At the lowest of these energies (8.4 eV) ionic processes can be assumed to be relatively unimportant. At the highest energy (21.2 eV) it is likely that a large fraction of photons absorbed lead to the formation of ethylene parent ions. Therefore, this series of experiments may allow us to contrast the product formation which follows ionization with that associated with neutral excited molecule formation. In addition, certain aspects of the solid phase radiolysis have been reinvestigated.

Finally deuterium labeling has been utilized in several experiments in order to examine in more detail the modes of formation of certain products.

2. Experimental Procedure

The apparatus and procedure for the solid phase photolysis and radiolysis experiments have been described previously [4, 5]. A detailed description of the rare gas resonance light sources has also been given in an earlier report [6]. The NBS 20,000 Curie cobalt-60 source was used for the gamma radiolysis experiments. One radiation experiment with 21.2 eV photons was carried out with a helium resonance lamp provided with an aluminum window [6]. Isotopic analyses of hydrocarbon products were carried out on a high resolution mass spectrometer using a low energy (12–15 eV) electron beam.

*This research was supported by the Atomic Energy Commission.

[1] Figures in brackets indicate the literature references at the end of this paper.

3. Results

The relative yields of the major products which were measured are given in table 1. Only the sum of the hexene yields is given in the last column. At least eight different C_6H_{12} isomers are formed in the radiolysis as well as in the photolysis at all wavelengths. No attempt was made to analyze for products with molecular weights higher than those of the C_6 products. In the photolysis of C_2H_4—C_2D_4 mixtures at 11.6–11.8 eV, 70 percent of the hexene mixture consisted of C_6D_{12}, $C_6D_8H_4$, $C_6D_4H_8$, and C_6H_{12}.

Two products, cyclopropene and methylcyclopropene which were previously reported to be formed in the 8.4 eV photolysis of C_2H_4 at 36 K were not observed in our study. In accord with the observation made in the previous investigation, there was a compound which eluted from a squalane column between *i*-C_4H_{10} and 1-C_4H_8. However, mass spectrometric analysis indicated it to be a C_4H_4 isomer rather than methylcyclopropene (C_4H_6) as suggested previously. The yield of the C_4H_4 product was seen to increase relative to that of the other products when the irradiation time was increased. It may, therefore, be ascribed to secondary photolysis of a product, probably acetylene. Two other products, cyclobutene and an unknown C_4H_6 product were also seen to increase with the percent conversion of ethylene. At the lowest percent decomposition (0.02%), the yields of C_4H_4 and cyclobutene were less than 1 percent of that of acetylene. It is of interest that the cyclobutene product formed in the irradiation of a C_2H_4—C_2D_4 mixture with 8.4 eV photons consisted mainly (~ 90%) of C_4D_6, $C_4D_4H_2$, $C_4D_2H_4$, and C_4H_6. Such a distribution is consistent with a mechanism involving the addition of an acetylene molecule to ethylene.

In pure ethylene, the relative yields of all products listed in table 1 showed only minor (~ 10%) variations when the percent conversion was varied over a 10-fold range (from 0.02 to 0.2%). The precision with which the relative yields are measured is approximately 10 percent for products whose yields are 1 percent or more of that of acetylene. For the other products the precision is estimated at 10 to 20 percent.

Quantum yields were not determined in any of the photolysis experiments. However, at any particular wavelength the yield of acetylene per unit time was seen to change by not more than 20 percent from one experiment to the next.

Besides the isotopic analyses referred to above and in tables 2, 3, and 4, several other products have been analyzed isotopically. Cyclopropane in the 11.6–11.8 eV photolysis of $C_2H_4-C_2D_4$ (1:1) at 20 K: C_3H_6-100; C_3DH_5-25, $C_3D_2H_4-98$; $C_3D_3H_3-16$; $C_3D_4H_2-97$; C_3D_5H-11 and C_3D_6-89. Cyclobutane in the 10.0 eV photolysis of $C_2H_4-C_2D_4$ (1:1) at 20 K: C_4H_8-120; C_4DH_9-6; $C_4D_3H_5-15$; $C_4D_4H_4-140$; $C_4D_5H_3-10$; $C_4D_6H_2-16$; C_4D_7H-11, and C_4D_8-110.

4. Discussion

Table 1 shows the relative yields of products formed in the photolysis of ethylene at 20 K with 8.4, 10.0, 11.6–11.8, and 21.2 eV photons, as well as in the gamma-radiolysis at 77 K. In the gas phase, the ionization energy of ethylene is 10.5 eV; [7] the ionization energy in the solid phase is unknown, and may be 1–2

TABLE 1. *Products in the solid phase photolysis and radiolysis of* C_2H_4

Radiation	Additive	C_2H_2	H_2	CH_3CHCH_2	*c*-C_3H_6	*c*-C_4H_8	1-C_4H_8	2-C_4H_8	CH_3-*c*-C_3H_5	*n*-C_4H_{10}	C_6H_{12}
		Relative yields									
Photolysis[b]											
8.4 eV	None	100	106	0.35	0.40	0.39	14.1	0.40	0.31	1.10	3.1
	Ar[a]	100	n.d.	0.22	0.12	0.47	13.5	0.25	0.20	0.82	n.d.
	O_2(5%)	100	110	0.42	0.40	0.50	11.0	n.d.	n.d.	0.38	n.d.
	CCl_4(6.3%)	100	n.d.	n.d.	0.13	0.39	10.1	0.25	n.d.	1.08	8.4
10.0 eV	None	100	90	1.4	1.1	3.05	16.0	1.15	0.63	1.90	16.9
	Ar[a]	100	n.d.	1.5	1.05	n.d.	20.7	1.20	0.60	2.07	n.d.
	CCl_4(6.3%)	100	n.d.	n.d.	0.49	3.40	20.0	0.40	n.d.	2.10	47.0
11.6–11.8 eV	None	100	n.d.	1.7	2.2	7.2	23.0	1.50	0.73	3.20	37.0
	CCl_4(6.3%)	100	n.d.	n.d.	0.55	7.3	29.0	1.40	n.d.	3.70	140.0
21.2 eV	None	100	n.d.	n.d.	n.d.	5.1	30.0	n.d.	n.d.	13.0	n.d.
Radiolysis[c]											
γ	None	100 [d](1.4)	n.d.	0.30	0.7	5.45	29.2	0.8	0.8	9.2	3.0
	CCl_4(6.3%)	100 (1.5)	n.d.	n.d.	0.65	6.0	32.4	n.d.	1.1	9.9	6.0
	CCl_4(14.7%)	100 (1.5)	n.d.	n.d.	0.75	5.7	29.6	0.60	2.23	8.3	9.0

[a] $Ar/C_2H_4 = 50$.
[b] $T = 20'$ K.
[c] $T = 77'$ K.
[d] Values in parenthesis are *G*-values (molecules of acetylene formed per 100 eV).

TABLE 2. *Hydrogen and acetylene from* $C_2H_4-C_2D_4$ *(1:1) at 20 K*

	Percent distributions					
	C_2H_2	C_2HD	C_2D_2	H_2	HD	D_2
8.4 eV	59.0	7.0	34.0	61.0	3.0	36.0
11.6–11.8 eV	60.5	5.0	34.5	62.0	3.5	34.5
γ-ray	57.0	6.0	37.0	52.6	6.6	40.8

TABLE 3. *Acetylene and hydrogen in the photolysis and radiolysis of* CH_2CD_2

		C_2H_2	C_2HD	C_2D_2	D_2	HD	H_2
		Percent distribution					
Photolysis							
8.4 eV	Gas	11.0	63.9	25.1	16.9	41.1	42.0
	Solid	23.1	37.3	39.6	23.9	38.0	40.1
10.0 eV	Gas	10.5	63.5	26.0	17.6	40.6	41.8
	Solid	21.7	41.7	36.6	20.6	39.1	39.6
11.6–11.8 eV	Gas	11.1	62.2	26.7	16.7	41.5	41.8
	Solid	14.1	53.4	32.5	16.8	41.0	42.2
Radiolysis							
γ	Gas	12.7	65.1	22.2	15.1	46.4	38.5
	Solid	17.7	52.7	29.6	26.5	31.0	42.5

Pressure in gas phase experiments: 10 torr.
Temperature in solid phase experiments: 20 K.

TABLE 4. *1-Butene yields from* $C_2H_4-C_2D_4$ *(1:1)*

	γ-Rays 77 K	10 eV Photons 20 K	8.4 eV Photons 20 K
C_4H_8	100	100	100
C_4H_7D	11	12	14
$C_4H_6D_2$	5	7	11
$C_4H_5D_3$	17	22	18
$C_4H_4D_4$	122	125	110
$C_4H_3D_5$	8	9	11
$C_4H_2D_6$	3	4	5
C_4HD_7	8	8	10
C_4D_8	39	39	35

eV lower than the gas phase value [8]. Most likely, ionization is unimportant in the solid phase photolysis at 8.4 eV, which is more than 2 eV below the gas phase ionization energy, but in all other experiments shown in table 1, ionic processes undoubtedly play a major role. In the gas phase the photoionization quantum yield of C_2H_4 at pressures around 20 torr is approximately 0.2 and 0.9 at 11.6 and 16.8 eV respectively [6, 9]. The photoionization quantum yield of C_2H_4 in the solid phase is not known and may be expected to differ from the gas phase values. Keeping in mind the lack of knowledge concerning the ionization processes in the solid phase, the modes of formation of some of the major products will now be discussed by considering both neutral and ionic mechanisms.

4.1. The Formation of Acetylene and Hydrogen

In the solid phase radiolysis and photolysis of ethylene, the major products formed at all energies are acetylene and hydrogen. It is seen, first of all, from the results obtained with $C_2D_4 : C_2H_4$ (1 : 1) mixtures (table 2) that in the solid phase essentially all the hydrogen and acetylene are produced in molecular elimination processes or by geminate disproportionation reactions (which in such a mixture lead to the formation of C_2H_2 and C_2D_2, D_2, and H_2, exclusively). Although in the gas phase radiolysis C_2H_2 may be formed by charge transfer [10] from $C_2H_2^+$ to C_2H_4 such a mechanism can be discounted in the condensed phase because of the reduced fragmentation of parent ions with increase in density [11]. Therefore, in the condensed phase photolysis and radiolysis, acetylene is tentatively assumed to be formed via decomposition of neutral excited ethylene molecules formed by direct excitation and by neutralization of the parent ion.

In the gas phase, the excited ethylene formed by absorption of 8.4 to 11.8 eV photons, dissociates as follows [9, 12]:

$$(1)\quad C_2H_4^* \rightarrow CHCH + H_2$$
$$(2)\quad \rightarrow CH_2C + H_2$$
$$(3)\quad \rightarrow C_2H_2 + 2H$$

At atmospheric pressure the excited vinyl radicals formed as intermediates in process 3 dissociate at wavelengths below 147 nm (8.4 eV). Only at wavelengths above 155 nm, have stable CH_2CH radicals been noted [13]. In the condensed phase photolysis and radiolysis all, or at least a considerable fraction, of the vinyl radicals may be expected to be stabilized. Actually vinyl radicals have been observed by ESR in the liquid phase radiolysis of ethylene [3f].

The occurrence of process 2 has been established from the isotopic distributions of the hydrogen products [12] formed in the photolysis of CD_2CH_2. The relative importance of processes 4 through 6 (i.e., 1 and 2) are approximately 0.41:0.42:0.17 in the gas phase, invariant with energy:

$$(4)\quad CD_2CH_2^* \rightarrow CDCH + HD$$
$$(5)\quad \rightarrow CD_2C + H_2$$
$$(6)\quad \rightarrow CH_2C + D_2$$

The gas phase results are compared with the analogous results obtained in the solid phase experiments in table 3. It is seen that the isotopic composition of the hydrogen fractions in the solid phase photolysis experiments closely resemble those observed in the gas phase.

Furthermore, in the solid phase photolysis experiments at 8.4 and 10.0 eV, there is a near equality between the yields of hydrogen and acetylene (table 1);

in fact, in the photolysis of CD_2CH_2 the yields of the various complementary isotopically labeled hydrogen and acetylene species match roughly ($C_2H_2 \approx D_2$, $C_2HD \approx HD$, $C_2D_2 \approx H_2$). This indicates that in these experiments, decomposition of vinyl radicals is indeed not important and that reaction 7, which in the gas phase accounts for a considerable fraction of the CHCD yield [12], occurs via an excited vinyl radical intermediate.

$$(7) \qquad CH_2CD_2^* \rightarrow CHCD + H + D$$

Assuming that in the solid phase experiments the disproportionation reaction

$$(8) \qquad [CH_2CD \text{ (or } CD_2CH) + D \text{ (or H)}] \rightarrow CHCD + HD$$

occurs with a low probability, it may be concluded that molecular hydrogen elimination processes occur via the same excited state in the gas as in the solid phase independent of the energy of the photon. In gas phase photolysis experiments the yield of acetylene is always considerably higher than that of "molecular" hydrogen ($C_2H_2/H_2 = 2.8$ at 10 eV). The occurrence of process 3 (process 7 in the case of CH_2CD_2) accounts for this, as is clearly illustrated by the fact that in all gas phase CH_2CD_2 experiments the abundance of CHCD in the acetylene fraction is considerably higher than that of HD in the hydrogen fraction. In the solid phase photolysis at 11.6–11.8 eV and in the radiolysis the abundance of C_2HD in the acetylene fraction is somewhat higher than that of HD in the hydrogen fraction indicating that at these energies reaction 7 may occur. Disproportionation reactions involving CH_2CD or CD_2CH and any other radical are however a more likely source of the excess C_2HD in the solid phase.

The absence of HD in the photolysis and radiolysis of C_2D_4:C_2H_4 (1:1) mixtures demonstrates that if H(D) atoms are indeed eliminated in the primary process they do not combine with other H atoms to form hydrogen in these experiments. The most probable fate of these H atoms especially if they are formed with excess kinetic energy, is addition to ethylene to form ethyl radicals:

$$(9) \qquad H + C_2H_4 \rightarrow C_2H_5$$

The C_2H_5 radicals thus formed will combine or disproportionate with other radicals in situ or during warm-up. *n*-Butane is one of the products which may originate from such a free radical combination reaction. The fact that the yield of *n*-butane relative to that of acetylene is quenched by oxygen at 8.4 eV (table 1) supports this view. The relative yield of *n*-butane is seen to increase with the energy of the photon, indicating that the H-atom production becomes relatively more important at high energies. The highest yield of *n*-butane is observed in the 21.2 eV photon irradiation and in the radiolysis. Increasing H-atom production with increasing energy has also been noted in the gas phase photolysis of ethylene [9, 12], and is a general trend seen in the photolysis of other hydrocarbons [14].

4.2. The Formation of C_4H_8 Products

In the gas phase radiolysis of ethylene and in the photolysis at energies above the ionization energy, the ethylene parent ion reacts with ethylene to form $C_4H_8^+$ ions [15]:

$$(10) \qquad C_2H_4^+ + C_2H_4 \rightarrow C_4H_8^+ \quad k_{13} = 8.3 \times 10^{-10} \text{cm}^3/\text{molecule-s}.$$

In the presence of a charge acceptor (CA) such as $(CH_3)_2NH$ or NO, the $C_4H_8^+$ ions have been shown to react to form C_4H_8 products [16]

$$(11) \qquad C_4H_8^+ + CA \rightarrow C_4H_8 + CA^+$$

whose structures are assumed to correspond to the structures of the precursor $C_4H_8^+$ ions. In the gas phase at pressures of 100 torr or less, reaction sequence 10–11 leads to the formation of 2-butene and isobutene; the relative amounts of these isomeric C_4H_8 products depend on the energy in the $C_4H_8^+$ ion [17]. As the pressure is raised, for example, the formation of *iso*-C_4H_8 (i.e., *iso*-$C_4H_8^+$) is quenched. If reaction 10 can compete with neutralization of the $C_2H_4^+$ ions in the solid phase, it is possible that the resulting $C_4H_8^+$ ions might lead to the formation of C_4H_8 products, through neutralization of the ion:

$$(12) \qquad C_4H_8^+ + e \rightarrow C_4H_8$$

It has actually been suggested before [3c] that in the solid phase radiolysis reaction 10 followed by 12 might account for the formation of 1-butene.

The results given in table 1 show that 1-butene is the most important C_4H_8 product in all the solid phase experiments. More than 80 percent of the 1-butene formed in the photolysis and radiolysis of C_2D_4—C_2H_4 (1 : 1) mixtures (table 4) consists of C_4H_8, $C_4H_4D_4$, and C_4D_8. That is, 1-butene seems to be formed mainly by the combination of two $C_2H_4(C_2D_4)$ units.

As mentioned above, in the gas phase very little 1-butene is formed in reaction sequence 10–11; isomerization of the $C_4H_8^+$ ions formed in reaction 10 to the 1-$C_4H_8^+$ structure is evidently an improbable process under those conditions. The fact that the yield of 1-butene is relatively large in the 8.4 eV photolysis where ionization is presumably unimportant, and furthermore undergoes a relatively small increase with increasing energy, seems to indicate that the 1-butene is at least in part formed through a nonionic mechanism. A plausible mechanism which would lead to the observed isotopic distribution in the C_2H_4—C_2D_4 (1 : 1) experiment would be H atom elimination from ethylene and addition of the hot H-atom to a neighboring ethylene molecule (reaction 9), followed by a recombination in the cage of the two radicals (reaction 13).

$$(13) \qquad [CH_2CH + CH_2CH_3] \rightarrow CH_2{=}CHCH_2CH_3.$$

It is of interest that the increase in the yield of 1-butene with photon energy parallels the increase in the yield of *n*-butane, which as we have shown above, is formed in a reaction sequence involving H atom addition to ethylene. The presence of deuterium labeled butenes other than C_4D_8 and $C_4D_4H_4$ in the photolysis and radiolysis of $C_2H_4-C_2D_4$ mixtures might be explained by the participation of diffusive recombination of vinyl and ethyl radicals in the overall 1-butene production. Increased diffusion would explain the observation that butenes such as C_4H_7D, C_4D_7H, CH_3D_5, and $C_3H_5D_3$ are formed at relatively higher yields in the liquid phase [3d] than in the solid phase radiolysis and that in the liquid phase they increase relative to the yields of C_4H_8, $C_4H_4D_4$ and C_4D_8, with an increase in temperature [3d].

It is understood that proposed mechanism is a tentative one and that other mechanisms such as those proposed in previous studies cannot be ruled out.

Of the C_4H_8 products formed in the solid phase irradiations of ethylene (table 1) there is one product, cyclobutane, which seems to be formed via a $C_2H_4^+$ intermediate. This statement is based on the fact that the relative yield of cyclobutane is very small in the photolysis with 8.4 eV photons where presumably few ions are formed (cyclobutane was not even detected in the earlier study [1] at this energy), and increases by nearly an order of magnitude when the photon energy is raised to 10.0 eV and again increases when the energy is raised to 11.6–11.8 eV. This large increase in yield with energy can be contrasted with the yields of the butene products, which increase by less than a factor of two when the energy is augmented from 8.4 eV to 11.6–11.8 eV. Furthermore, the fact that approximately 90 percent of the cyclobutane formed in the photolysis and radiolysis of $C_2D_4-C_2H_4$ mixtures consists of C_4H_8, $C_4H_4D_4$, and C_4D_8 (see Results) indicates that this product is formed mainly in a reaction of C_2H_4 (C_2D_4) entities as has been shown before [3d] in the liquid phase radiolysis of ethylene.

Cyclobutane is also formed in the mercury photosensitized photolysis [18] of ethylene at a pressure of 700 torr, with a quantum yield of 3.8×10^{-6}. In those experiments, the cyclobutane product was suggested to be formed as a result of a reaction between triplet state ethylene and ground state ethylene:

$$(14) \qquad C_2H_4^T + C_2H_4 \rightarrow (c-C_4H_8)^*$$

$$(15) \qquad (c-C_4H_8)^* + M \rightarrow c-C_4H_8$$

If, in the solid phase photolysis experiments, cyclobutane originates in reaction 14 we must conclude that the formation of triplet state ethylene is important only at photon energies higher than 8.4 eV. This could be explained if triplet state ethylene were formed in a neutralization reaction such as:

$$(16) \qquad C_2H_4^+ + e \rightarrow C_2H_4^T.$$

In radiolysis, triplet ethylene may also be formed by direct excitation:

$$(17) \qquad C_2H_4 + e \rightarrow C_2H_4^T + e.$$

Cyclobutane has been reported [19] as a product ($G \sim 0.1$) in the gas phase radiolysis of C_2H_4 (pressure: 100 torr) and ascribed to the participation of triplet ethylene. Reaction 17 cannot be operative in the 10 and 11.6 eV photolysis experiments, since the ejected electrons will have insufficient energy to bring about the optically forbidden transition to the lowest triplet state at 3.6 eV [20].

The 2-butenes are formed as minor products in all the solid phase irradiations given in table 1. Their yield shows little or no variation with increasing energy; hence, their formation is probably not associated with an ionic process. This is of interest, since, as indicated above, in the gas phase at pressures of 100 torr or less, it has been shown that reaction 10 of the ethylene ion with ethylene leads mainly to the formation of 2-$C_4H_8^+$ ions. Thus, at any rate, the absence of 2-butene as an important product in any of the solid phase experiments demonstrates that $C_4H_8^+$ ions formed in reaction 10 do not undergo neutralization to form 2-C_4H_8, under these conditions.

Methylcyclopropane is also formed in small yields in all the solid phase photolysis and radiolysis experiments reported in table 1. In experiments carried out with C_2H_4:C_2D_4(1:1) mixtures, about 75–80 percent of this product consists of C_4H_8, $C_4H_4D_4$, or C_4D_8. In an earlier study [1] of the solid phase photolysis of ethylene at 8.4 eV, the formation of methylcyclopropane was attributed to a reaction of an ethylidene with ethylene:

$$(18) \qquad CH_3CH + C_2H_4 \rightarrow c\text{-}C_3H_5(CH_3).$$

Although this mechanism which requires a rearrangement of a long-lived excited ethylene molecule would indeed account for the isotopic distribution of methylcyclopropane products formed in the C_2H_4:C_2D_4 mixture, a free radical mechanism occurring in the cage may also explain the experimental observation. Addition of CH_2CH to C_2H_4 occurs with a low activation energy (0.14 eV) for thermal CH_2CH radicals and may involve a neighboring molecule, especially if, as in the gas phase, the CH_2CH retains some internal energy after its formation. Such an addition process would lead to the formation of the 3-butenyl radical [3f] and conceivably also of the methylene cyclopropyl radical. These two radicals may capture a neighboring hydrogen atom to form dimeric 1-butene and methylcyclopropane respectively.

4.3 The Formation of Cyclopropane

The results given in table 1 show that cyclopropane is a product in all experiments. Since the addition of methylene to ethylene to form cyclopropane:

$$(19) \qquad CH_2 + C_2H_4 \rightarrow c\text{-}C_3H_6$$

is a well-known reaction [21], the presence of this product suggests that methylene is formed in the solid

phase photolysis and radiolysis of ethylene. Indeed, the isotopic composition of the cyclopropane produced in the photolysis and radiolysis of a $C_2H_4 : C_2D_4$ (1 : 1) mixture (see Results) indicates that more than 80 percent of the cyclopropane consists of c-C_3H_6, c-$C_3H_4D_2$, c-$C_3D_4H_2$, and c-C_3D_6. This distribution is consistent with the formation of cyclopropane through addition of $CH_2(CD_2)$ to $C_2H_4(C_2D_4)$. Insertion of a CH_2 species into a C−H bond of ethylene would also lead to the formation of propylene

$$(20) \qquad CH_2 + C_2H_4 \rightarrow CH_3CHCH_2.$$

Propylene is formed as a product in these experiments (table 1), but has not been analyzed isotopically.

If indeed the cyclopropane and propylene products can be assumed to result from reactions 19 and 20, we can infer the occurrence of the primary process:

$$(21) \qquad C_2H_4^* \rightarrow 2CH_2.$$

This process requires less than 8.3 eV [7a] so there is enough energy available even in the 8.4 eV photolysis for its occurrence. It is seen that in the photolysis the relative importance of cyclopropane formation increases with increasing energy.

4.4. The Formation of Hexenes

Several C_6H_{12} products are formed in the solid phase irradiations. The total yields of these products are listed in table 1.

The yields of the hexene products are relatively small in the 8.4 eV photolysis, but undergo a large increase when the energy is raised to 10.0 eV, and more than double again when the energy is further raised to 11.6–11.8 eV. These observations are very similar to those made above concerning the yields of the cyclobutane product. As in that case, we can infer that the large increase in yield when the energy is raised to a point where ionization is certainly of importance (10.0 eV) may be related to participation of ions in the formation of the products in question. It has been reported before [3c] that the 2-hexene product formed in the radiolysis of a $C_2D_4 - C_2H_4$ (1 : 1) mixture at 77 K consisted of more than 75 percent C_6H_{12}, $C_6H_4D_8$, $C_6H_8D_4$, and C_6D_{12}. In the present study (see Results) it is seen that the 2-hexenes, as well as the 1-hexene product have a similar isotopic composition when an equimolar ethylene mixture is irradiated with 11.6–11.8 eV photons. That is, most of the hexene products are evidently made up of $C_2H_4(C_2D_4)$ units.

In the earlier radiolysis study [3c] it was suggested that hexene is formed in a process initiated by reaction of the $C_2H_4^+$ ion with ethylene and terminated by electron recombination with a $C_6H_{12}^+$ species. The present photolysis experiments seem to substantiate this interpretation. Especially if one considers that an electron scavenger such as CCl_4 has a profound effect on the yields of the hexene (table 1). The actual role of CCl_4 in the enhancement is uncertain. It is however of interest to note that the yields of the C_4 products are not seriously affected by CCl_4.

5. References

[1] Tschuikow-Roux, E., McNesby, J. R., Jackson, W. M., and Faris, J. L., J. Phys. Chem., **71**, 1531 (1967).
[2] For a review see Holroyd, R., in Fundamental Processes in Radiation Chemistry, Ausloos, P., Ed. (1968).
[3] (a) Chang, P. C., Yang, N. C., and Wagner, C. D., J. Am. Chem. Soc. **81**, 2060 (1959); (b) Collinson, E., Dainton, F. S., and Walker, D. C., Trans. Faraday Soc. **57**, 1732 (1961); (c) Wagner, C. D., J. Phys. Chem. **66**, 1158 (1962); (d) Holroyd, R. A., and Fessenden, R. W., J. Phys. Chem. **67**, 2743 (1963); (e) Wagner, C. D., Trans. Faraday Soc. **64**, 163 (1968); (f) Fessenden, R. W., and Schuler, R. H., J. Chem. Phys. **39**, 2147 (1963); (g) Brash, J. L., and Golub, M. A., Can. J. Chem. **46**, 593 (1968); (h) Klassen, N. V., J. Phys. Chem. **71**, 2409 (1967); (i) Wagner, C. D., J. Phys. Chem. **71**, 3445 (1967).
[4] Rebbert, R. E., and Ausloos, P., J. Chem. Phys. **46**, 4333 (1967).
[5] Scala, A. A., and Ausloos, P., J. Chem. Phys. **47**, 5129 (1967).
[6] Gorden, R., Jr., Rebbert, R. E., and Ausloos, P., Natl. Bur. Std. Technical Note **496** (1969).
[7] (a) Chupka, W. A., Berkowitz, J., and Refaey, K. M. A., J. Chem. Phys. **50**, 1938 (1969); (b) Botter, R., Dibeler, V. H., Walker, J. A., and Rosenstock, H. M., J. Chem. Phys. **45**, 1298 (1966); (c) Brehm, B., Z. Naturforschg. **21a**, 196 (1966); (d) Al-Joboury, M. I., and Turner, D. W., J. Chem. Soc., 4434 (1964).
[8] Vermeil, C., Matheson, M., Leach, S., and Muller, F., J. Chim. Phys. **34**, 596 (1964).
[9] Gorden, R., Jr., and Ausloos, P., J. Chem. Phys. **47**, 1799 (1967).
[10] Tiernan, T. O., and Futrell, J. H., J. Phys. Chem. **72**, 3080 (1968).
[11] (a) Stevenson, P., Rad. Res. **10**, 610 (1959); (b) Ausloos, P., and Lias, S. G., Actions Chimiques et Biologiques des Radiation, **11**, 1 (1967).
[12] (a) Sauer, M. C., and Dorfman, L. M., J. Chem. Phys. **35**, 497 (1961); (b) Okabe, H., and McNesby, J. R., J. Chem. Phys. **36**, 601 (1962); (c) Ausloos, P., and Gorden, R., Jr., J. Chem. Phys. **36**, 5 (1962).
[13] Back, R. A., and Griffiths, D. W. L., J. Chem. Phys. **46**, 4839 (1967); and Borrell, P., Cashmore, P., Cervenka, A., and James, F. C., J. Chim. Phys. 229 (1970).
[14] Sieck, L. W., in Fundamental Processes in Radiation Chemistry Ausloos, P., Ed. (1968).
[15] Ausloos, P., Rebbert, R. E., and Sieck, L. W., J. Chem. Phys. in press and references cited therein.
[16] Meisels, G. G., J. Chem. Phys. **42**, 3237 (1965).
[17] Ausloos, P., Structure and Reactivity of Hydrocarbon Ions in Ion-Molecule Reaction, J. L. Franklin, Ed. (Plenum Press, 1971).
[18] Chesick, J. P., J. Am. Chem. Soc. **85**, 3718 (1963).
[19] Meisels, G. G., J. Am. Chem. Soc. **87**, 950 (1965).
[20] Evans, D. F., J. Chem. Soc. 1351 (1957); 1735 (1960).
[21] Frey, H. M., Progr. Reaction Kin. **2**, 131 (1964).

(Paper 75A3–657)

JOURNAL OF RESEARCH of the National Bureau of Standards—A. Physics and Chemistry
Vol. 75A, No. 3, May–June 1971

Kinetic Mass Spectrometric Investigation of the Ion-Molecule Reactions Occurring in C_4 and C_5 Alkanes Following Photoionization at 106.7 and 104.8 nm *

L. Wayne Sieck, S. K. Searles, ** and P. Ausloos**

Institute for Materials Research, National Bureau of Standards, Washington, D.C. 20234

(January 11, 1971)

The photoionization of C_4 and C_5 alkanes has been investigated at 106.7 and 104.8 nm in a mass spectrometer specifically designed for the investigation of ion-molecule reactions occurring at thermal kinetic energies. Absolute rate constants are reported for the reactions of various fragment ions with the corresponding parent molecule.

The rate constants found for reactions of *sec*-$C_3H_7^+$ ions with *i*-C_4H_{10}, *n*-C_4H_{10}, *i*-C_5H_{12}, and *n*-C_5H_{12} were found to be 3.3, 4.4, 4.7, and 5.2×10^{-10} cm^3/molecule-second respectively. The $C_4H_9^+$ ions were also found to be highly reactive, exhibiting rate constants of 3.6 and 3.8×10^{-10} cm^3/molecule-second in reactions with *i*-C_5H_{12} and *n*-C_5H_{12}. The rate constants for reaction of $C_3H_6^+$ with *i*-C_4H_{10}, *n*-C_4H_{10}, *i*-C_5H_{12}, and *n*-C_5H_{12} were found to be 4.9, 4.9, 7.6, and 7.9×10^{-10} cm^3/molecule-second, respectively. Butene ions are less reactive by an order of magnitude. The results are compared with complementary data derived from electron impact experiments, and the relationship between the structure and reactivity of the various ions is discussed.

Key words: gas phase; hydrocarbons; ion-molecule reactions; mass spectrometry; photoionization; rate constants.

1. Introduction

Recent publications from this laboratory [1] have illustrated that a photoionization mass spectrometer is advantageous for studying the reactions of parent hydrocarbon ions. In some cases selective ionization of hydrocarbons in the presence of organic or inorganic additives may be achieved by proper utilization of the line emission (123.6, 116.4, or 106.7 nm) of rare gas resonance lamps. Furthermore, when ionization is induced by photoabsorption at energies only slightly above the ionization threshold, it is possible to investigate the reactions of parent ions with parent molecules in the absence of those complicating reactions associated with those fragment ions which would be produced at higher energies. The fact that parent ion-parent molecule reactions could be investigated at thermal kinetic energies in such an instrument at room temperature over a considerable pressure range was instrumental in the elucidation of the kinetics of formation and reaction of alkane dimer ions $(C_nH_{2n+2})_2^+$[1e, 1f].

The present photoionization study differs from those mentioned above in that C_4-C_5 alkanes were irradiated with photons of sufficient energy to induce unimolecular fragmentation of the parent ion. The reactivities of the resultant fragment ions towards the alkanes were derived from the variation of the composite mass spectrum of a particular system as a function of pressure. The ion-molecule chemistry occurring in some of these alkanes (*n*-C_4H_{10}, *i*-C_4H_{10}, and *neo*-C_5H_{12}) has been investigated previously by kinetic mass spectrometry using high energy electrons [2]. In those studies, however, the temperature of the ion source was approximately 500 K and the electron energy was well above that of the photons used in this investigation. Consequently, a considerable variety of fragment ions were produced and it was difficult in some instances to determine which of the many fragment ions were responsible for the formation of ionic products.

It was also considered of interest to compare rate data obtained from this study with that derived from analysis of the neutral products of ion-molecule reactions occurring in alkane systems [3]. Such a comparison is of particular importance since end product analysis has recently revealed the formation of alkyl and olefinic ions with more than one structure in the unimolecular decomposition of *n*-alkane and cycloalkane parent ions [4]. Since isomeric ions are known to exhibit different reactivities, one might expect to de-

*This research was supported by the Atomic Energy Commission.
**NBS Postdoctoral Research Associate 1968–70.

rive additional information from the contour of the ion decay plots obtained from the mass spectrometer.

2. Experimental and Results

The high-pressure photoionization mass spectrometer used in the present study has been described elsewhere in detail [1a, b]. In all experiments the reaction chamber (ion source) was operated at 300 ± 2 K in the absence of any internal electric or magnetic fields.

All materials were purified by gas chromatography and subsequently distilled at low temperatures in order to remove traces of water. The techniques used for the evaluation of absolute rate constants for bimolecular reactions have been described in detail elsewhere [1a, b]. Experimentally, the method involves a determination of the composite mass spectrum, including all reactant and product ions, as a function of sample pressure in the photoionization chamber. The logarithm of the percentage composition of the mass spectrum is then plotted versus pressure in the manner displayed in figures 1–6. The thermal bimolecular rate constant is then determined from the slope of the resultant decay curves found for primary ions, which are straight lines for a single reactive species, and the calculated ionic residence time in the photoionization chamber. Rate constants are always derived from initial slopes since the ionic residence time may increase at higher pressures due to nonreactive scattering of ions exhibiting low overall reactivities. This latter condition will yield decay curves which exhibit an increased slope at higher pressures and are concave downward. Alternatively, a decay curve which is concave upwards at low pressures indicates that two or more empirically equivalent ions are present at this particular mass-to-charge ratio, each of which exhibits a different overall reactivity.

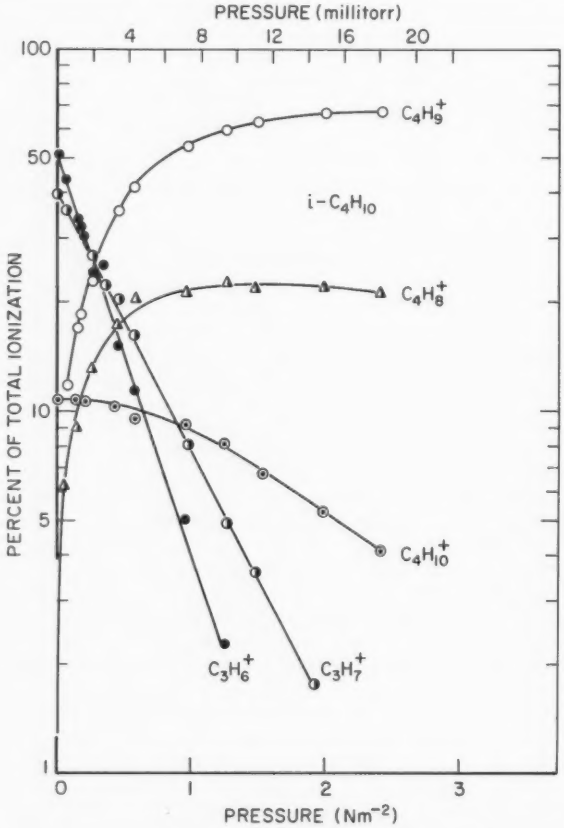

FIGURE 1. *Composite mass spectrum obtained from the photoionization (106.7–104.8 nm) of* i-C_4H_{10} *versus pressure of* i-C_4H_{10}.

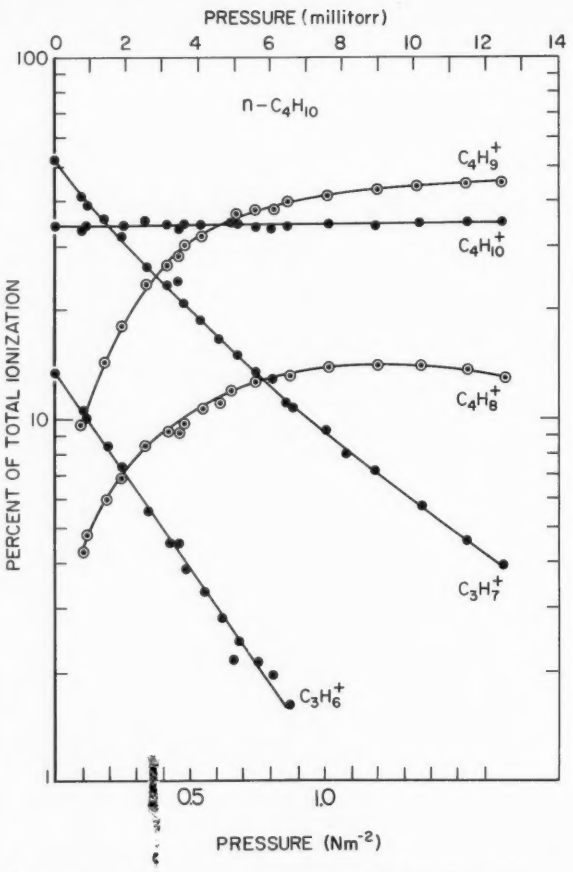

FIGURE 2. *Composite mass spectrum obtained from the photoionization (106.7–104.8 nm) of* n-C_4H_{10} *versus pressure of* n-C_4H_{10}.

3. Discussion

3.1. Unimolecular Fragmentation

The primary mass spectrum resulting from photoionization of the C_4–C_5 alkanes by 11.6–11.8 eV photons may be obtained by extrapolating the parent and fragment ion curves given in figures 1 through 6 to

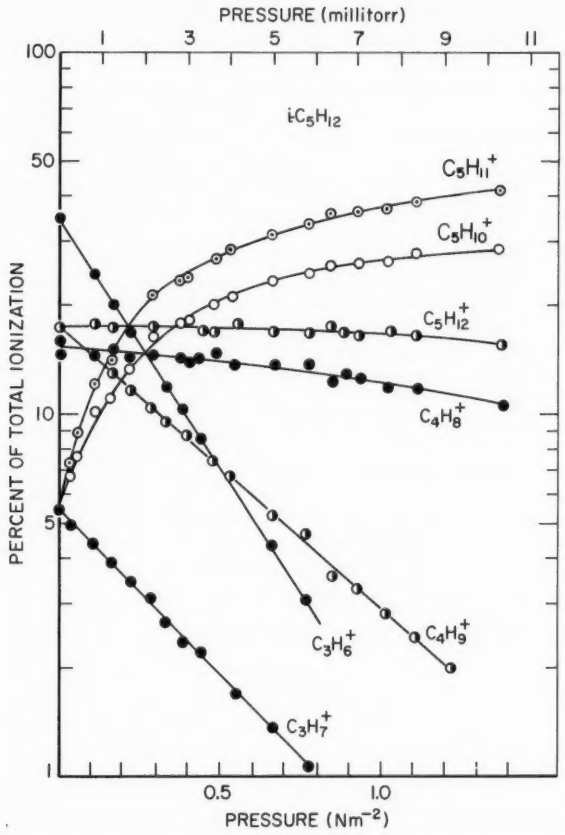

FIGURE 3. *Composite mass spectrum obtained from the photoionization (106.7–104.8 nm) of* i-C_5H_{12} *versus pressure of* i-C_5H_{12}.

"zero" pressure. Because the "parent minus one" and "parent minus two" ions in each system are also the products of fast ion-molecule reactions, it was not possible to obtain an accurate estimate of their abundance in the primary mass spectrum. However, it is apparent (figs. 1 to 15) that the primary yields of these ions approach low values at low pressure. For *n*-C_5H_{12} and *i*-C_5H_{12}, the $\Sigma(C_5H_{10}^+ + C_5H_{11}^+)$ comprise approximately 2 and 10 percent of the primary mass spectra, respectively. As indicated by the summary in table 1, all of the major fragment ions have appearance potentials less than 11.2 eV at 300 K [5].Ions such as $C_2H_4^+$, $C_3H_5^+$, $C_2H_3^+$, etc., were not observed since the threshold energy requirements for formation of these species from C_4–C_5 alkanes are either very close to or in excess of [6, 7] the energies of the photons used in this study. The ions listed in table 1 are also the major species observed in a previous study of the photoionization of alkanes at energies approaching 11.5 eV [5]. For comparison, the relative abundances measured in the latter study at 11.25 eV are also included in table 1. As expected, for all compounds listed, the relative abundance of the parent ion is reduced at 11.6–11.8 eV. The other major difference between the mass spectral patterns is reflected in the greater probability for C–C scissions over four center olefin ion elimination processes when the energy is increased from 11.25 to 11.6–11.7 eV. In view of the slight differences in energy requirements for these two processes, this observation can largely be ascribed to the lower frequency factor associated with rearrangement reactions [8]. In the discussion which follows, the structures of the reacting ions will be considered.

TABLE 1. *Abundances of fragment and parent ions at 300 K*

		AP eV*	11.26 eV*	11.6–11.8 eV**
			Photon Energy	
***n*–C_4H_{10}**	$C_4H_{10}^+$		0.63	0.34
	$C_3H_7^+$	11.11	.20	.53
	$C_3H_6^+$	11.09	.13	.13
***i*–C_4H_{10}**	$C_4H_{10}^+$		0.21	0.10
	$C_3H_7^+$	11.15	.11	.38
	$C_3H_6^+$	10.89	.68	.52
***n*–C_5H_{12}**	$C_5H_{12}^+$		0.43	0.32
	$C_4H_9^+$	10.95	.041	.072
	$C_4H_8^+$	10.84	.031	.032
	$C_3H_7^+$	11.04	.064	.18
	$C_3H_6^+$	10.89	.42	.37
***i*–C_5H_{12}**	$C_5H_{12}^+$		0.24	0.18
	$C_4H_9^+$	10.97	.066	.18
	$C_4H_8^+$	10.68	.20	.15
	$C_3H_7^+$	11.14	.017	.055
	$C_3H_6^+$	10.74	.47	.35
***neo*–C_5H_{12}**	$C_5H_{12}^+$		0.0006	
	$C_4H_9^+$	10.55	.86	0.89
	$C_4H_8^+$	10.37	.14	.11

*Reference [5].
**This work.

3.2. Bimolecular Reactions

a. Alkene Ions

The fractional intensities of the $C_3H_6^+$ ions produced in the photoionization of *i*-C_4H_{10}, *n*-C_4H_{10}, *n*-C_5H_{12}, and *i*-C_5H_{12} decrease linearly as a function of pressure. Therefore, we may assume that this ion has only one structure, $CH_3CHCH_2^+$, at the time of reaction. The total rate constants for reaction of $C_3H_6^+$ with the various alkanes given in table 2 agree well with those obtained for reaction of $C_3D_6^+$ formed by photoionization of propylene-d_6 with 10 eV photons [1b] in the presence of C_4 and C_5 alkanes. In the case of *i*-butane, for which two reaction channels are possible:

$$C_3H_6^+ + i\text{-}C_4H_{10} \rightarrow C_3H_7 + C_4H_9^+ \quad (1)$$

$$\rightarrow C_3H_8 + C_4H_8^+ \quad (2)$$

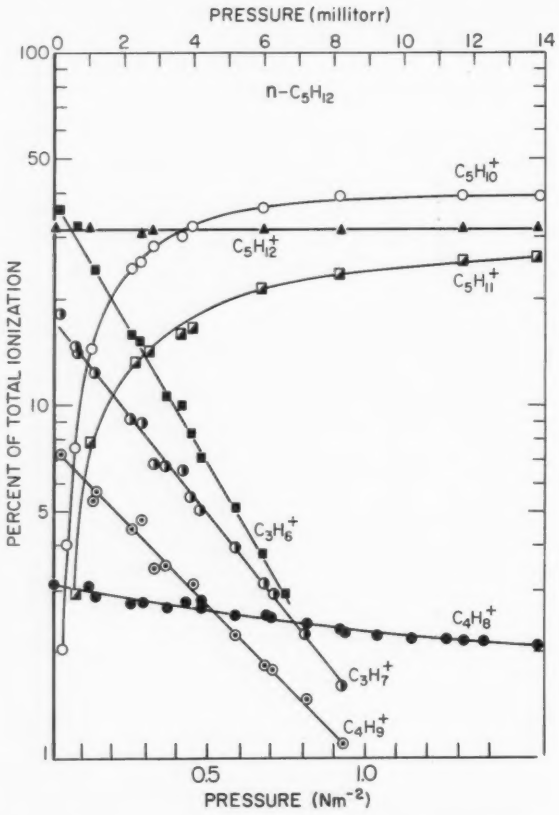

FIGURE 4. *Composite mass spectrum obtained from the photoionization (106.7–104.8 nm) of* n-C_5H_{12} *versus pressure of* n-C_5H_{12}.

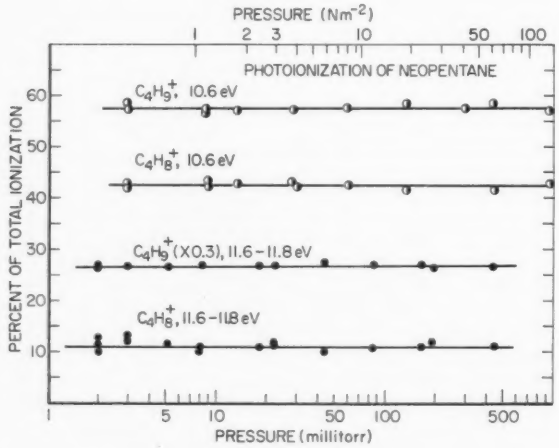

FIGURE 5. *Composite mass spectrum obtained from the photoionization of neopentane at 116.5 nm and at 106.7–104.8 nm versus pressure.*

TABLE 2. *Rate constants (cm³/molecule-second × 10¹⁰)*

		Mass spectrometric		Neutral product analysis
		Photoionization*	Electron impact**	Electron impact***
i-C_4H_{10}	*sec*-$C_3H_7^+$	3.3	4.0	3.1
	$C_3H_6^+$	4.9	6.7	.....
n-C_4H_{10}	*sec*-$C_3H_7^+$	4.4	3.9	4.1
	cyclo-$C_3H_7^+$	.....	.....	0.9
	$C_3H_6^+$	4.9	5.1	.....
i-C_5H_{12}	*sec*-$C_3H_7^+$	4.7		5.5
	$C_3H_6^+$	7.6		.....
	sec-$C_4H_9^+$	3.8		2.9
	t-$C_4H_9^+$	.....		0.46
	$C_4H_8^+$ (2 or more structures)	< 0.5		.....
n-C_5H_{12}	*sec*-$C_3H_7^+$	5.2	.....	7.3
	cyclo-$C_3H_7^+$	.....		1.7
	$C_3H_6^+$	7.9		.....
	sec-$C_4H_9^+$	3.7		4.1
	t-$C_4H_9^+$	.....		< 0.007
	$C_4H_8^+$ (2 or more structures)	0.4		.....

*This work. **Reference [2]. ***Reference [3].

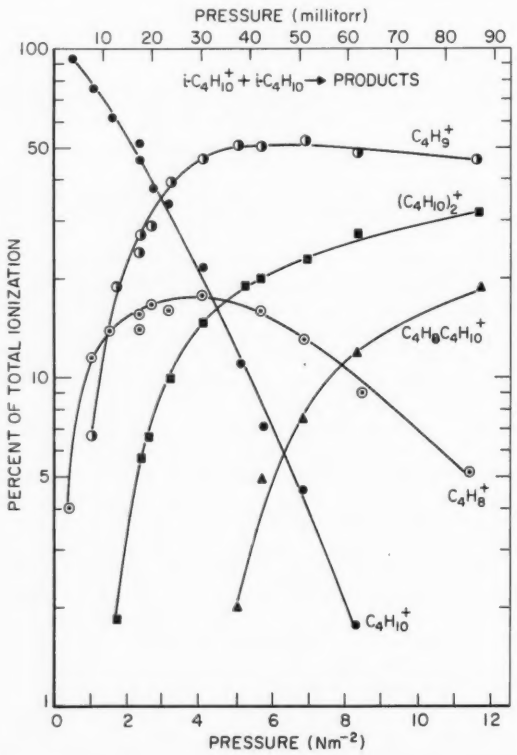

FIGURE 6. *Composite mass spectrum obtained from the photoionization of* i-C_4H_{10} *at 116.5 nm versus pressure.*

the ratio $k(H^-)/k(H_2^-)$ was found to be 1.26 in the present study, and 1.30 in the previous investigation involving $C_3D_6^+$. Assuming that k_1/k_2 is dependent on the internal energy of the propylene ion (a dependence on kinetic energy has been established [9]) this agreement would indicate that the internal energy content of the propylene ion resulting from the unimolecular decomposition of butane does not differ appreciably from that formed in the photoionization of propylene at 123.6 nm.

Rate constants for reaction of $C_3H_6^+$ with the butane isomers were also obtained in a previous study [2b] in which $C_3H_6^+$ was formed by dissociation of butane following impact with high energy electrons (800 eV). It is apparent from table 2 that the values obtained in that investigation also agree well with those obtained in the present experiments.

The overall reactivity of the $C_4H_8^+$ ions resulting from the fragmentation of i-C_5H_{12} and n-C_5H_{12} is more than an order of magnitude less than that found for $C_3H_6^+$. No reaction was found between $C_4H_8^+$ and neopentane at pressures as high as ~ 1 torr, indicating an upper limit of 10^{-14} cm^3/molecule-second for the rate constant. Previous studies have also shown that propylene ions are equally unreactive towards neopentane.

While the majority of the $C_4H_8^+$ ions formed in the fragmentation of neopentane

$$(CH_3)_4C^+ \rightarrow CH_4 + i\text{-}C_4H_8^+ \qquad (3)$$

have a branched structure [4], it may be expected that the majority of the butene ions formed in the decomposition of i-C_5H_{12} and n-C_5H_{12} are linear. Radiolysis experiments have shown [4] that 1-$C_4H_8^+$ ions are more reactive towards n-C_5H_{12} than the 2-$C_4H_8^+$ ions, which were, in fact, not found to react in a static system. The negligible slope in the $C_4H_8^+$ yield curve versus pressure of n-C_5H_{12} above 10 millitorr (fig. 4) may well be due to a nonreactive 2-$C_4H_8^+$ component among the butene ions.

b. Alkyl Ions

It is well established [10] that a reactive collision between an alkyl ion and an alkane molecule results exclusively in the transfer of a hydride ion. This overall process may be represented as:

$$C_mH_{2m+1}^+ + C_nH_{2n+2} \rightarrow C_mH_{2m+2} + C_nH_{2n+1}^+. \qquad (4)$$

$C_3H_7^+$. At 11.6–11.8 eV, $C_3H_7^+$ ions are formed in the fragmentation of i-C_4H_{10}, n-C_4H_{10}, i-C_5H_{12}, and n-C_5H_{12}. However, one would anticipate [4] exclusive formation of $C_3H_7^+$ with the secondary structure only in the dissociation of the two branched alkane ions (reactions 5 and 6):

$$[i\text{-}C_4H_{10}^+]^* \rightarrow sec\text{-}C_3H_7^+ + CH_3 \qquad (5)$$

$$[i\text{-}C_5H_{12}]^* \rightarrow sec\text{-}C_3H_7^+ + C_2H_5. \qquad (6)$$

The production of $C_3H_7^+$ with a well-defined structure in isobutane is supported by the fact that the $C_3H_7^+$ decay curve in figure 3 is linear over the pressure range where 95 percent of these ions have reacted. Also, the rate constants for reaction of sec-$C_3H_7^+$ ions with i-C_4H_{10} and i-C_5H_{12} as determined in the photoionization mass spectrometer are in good agreement with those derived from an analysis of the CD_3CDHCD_3 product in radiolysis experiments in which the sec-$C_3D_7^+$ ions were produced by irradiating i-C_4D_{10} in the presence of various alkanes (reaction7):

$$sec\text{-}C_3D_7^+ + RH \rightarrow CD_3CDHCD_3 + R^+. \qquad (7)$$

Finally, the rate constant obtained for reaction of sec.$C_3H_7^+$ with i-C_4H_{10} in an electron impact mass spectrometer agrees well with that obtained in the present study, even though the electron impact value is based on $C_3H_7^+$ ion currents at pressures above 200 millitorr and our value is derived from measurements at pressures below 10 millitorr (fig. 1). In the former study pronounced curvature was noted in the $C_3H_7^+$ plot, indicating that $C_3H_7^+$ was formed as well as consumed by ionic reactions in butane. No curvature could be detected in our study in the photoionization of either n-butane or i-butane. Therefore, it must be concluded that if $C_3H_7^+$ is indeed a product of a reaction between a fragment ion and the neutral butane molecule, then the precursor must be among those ions which are only formed at energies above 11.8 eV.

It was recently shown that dissociation of n-alkane [3, 4] ions may yield two or more isomeric forms of $C_3H_7^+$. For example, the $C_3H_7^+$ ions resulting from the unimolecular dissociation

$$[n\text{—}C_4H_{10}^+] \rightarrow CH_3 + C_3H_7^+ \qquad (8)$$

were shown to acquire the sec-propyl and protonated cyclopropane structures prior to reaction. It was further demonstrated that the relative abundance of the two isomers varies with the internal energy content of the $C_3H_7^+$ ion. Because the two isomer ions seem to react at rates which differ by nearly a factor of four (sec-$C_3H_7^+$ being the more reactive isomer), it is not surprising that a distinct curvature is observed in the decay of $C_3H_7^+$ in n-butane (fig. 2). The reactivity indicated by the initial slope corresponds most closely to that found for the sec-$C_3H_7^+$ ion. In n-C_4H_{10}, the best straight line drawn through the points obtained up to a pressure of 5 millitorr yields a rate constant of 4.4×10^{-10} cm^3/molecule second, which is in good agreement with value obtained in previous studies (see table 2). The agreement with the electron impact mass spectrometric investigation is somewhat fortuitous since as mentioned above, $C_3H_7^+$ ions of an undetermined structure were also formed as a result of an ion-molecule collision in those experiments.

The variations in the reactivity found for sec-$C_3H_7^+$ with various isomeric alkanes, which are consistent with those observed in earlier radiolysis experiments, can be rationalized in terms of the ΔH of reaction [6] as well as statistical and steric considerations. For example, the increase in the rate constant associated

with an increase in molecular weight in an homologous series may be largely, although not exclusively, ascribed to increased exothermicity. On the other hand, the higher rate constant for reaction of *sec*-$C_3H_7^+$ with *n*-C_4H_{10} when compared to isobutane must be accounted for by other factors. It is well established that *sec*-$C_3H_7^+$ reacts to remove a hydride ion exclusively from the secondary and tertiary position in *n*-butane and isobutane, respectively. These hydride transfer reactions may be written as follows:

$$sec\text{-}C_3H_7^+ + n\text{-}C_4H_{10} \rightarrow C_3H_8 + sec\text{-}C_4H_9^+ \qquad \Delta H = -4 \text{ kcal} \qquad (9)$$

$$\text{sec-}C_3H_7^+ + i\text{-}C_4H_{10} \rightarrow C_3H_8 + t\text{-}C_4H_9^+ \qquad \Delta H = -18 \text{ kcal} \qquad (10)$$

The observation that the more exothermic process (reaction 10) exhibits a lower rate constant then reaction 9 is reasonable since four secondary *H* atoms are available in *n*-C_4H_{10} while only a single tertiary *H* atoms in *i*-C_4H_{10} is available for transfer to *sec*-$C_3H_7^+$ via reaction 10. In addition, the four reactive sites in *n*-C_4H_{10} are sterically more accessible than in the single reactive site in *i*-C_4H_{10}, i.e., reaction 10 would be expected to exhibit a lower entropy of activation.

$C_4H_9^+$. It has been demonstrated [4] that the $C_4H_9^+$ ions resulting from the fragmentation of normal alkanes may have either the *sec*-$C_4H_9^+$ structure or the thermodynamically more stable *t*-$C_4H_9^+$ configuration. However, although initial C——C cleavage in *n*-alkanes will result in a linear structure, there is an energy barrier estimated at 0.67 eV [11] for isomerization to the branched configuration. Because the maximum energy available from the argon resonance lines is only 0.85 eV above the appearance potential of the $C_4H_9^+$ ion, which Semeluk and Lossing [12] have shown to have the *sec*-$C_4H_9^+$ ion structure, the fraction of *t*-$C_4H_9^+$ ions should be quite low in photoionized *n*-C_5H_{12}.

Recent appearance potential measurements [12], as well as mass spectral cracking patterns of deuterium labeled isopentanes, have revealed that the $C_4H_9^+$ ion is formed through a simple C-C cleavage process chiefly with the secondary structure at low energies.

The linear decay curves for the $C_4H_9^+$ ions derived from *n*- and *i*-C_5H_{12} substantiate our view that the majority of the $C_4H_9^+$ ions are of the secondary structure. Participation of *t*-$C_4H_9^+$ can be rules out on the basis of the rate constants given in table 2. Comparison of these data indicates that the rate constants found for the reaction of $C_4H_9^+$ in the present study are in reasonable agreement with those obtained by consideration of the $CD_3CDHCD_3CD_3$ product formed in radiolysis experiments [3] via the well-defined reaction:

$$sec\text{-}C_4D_9^+ + RH \rightarrow CD_3CD_2CDHCH_3 + R^+. \qquad (11)$$

Neutral end-product analysis has confirmed that *t*-$C_4H_9^+$ is much less reactive than *sec*-$C_4H_9^+$ (table 2) and the presence of such ions would yield a pronounced curvature in the $C_4H_9^+$ plots of figures 3 and 4.

The $C_4H_9^+$ ions resulting from the decomposition of neopentane are exclusively of the *t*-$C_4H_9^+$ configuration. The yield of these exhibits no variation with pressure up to the maximum values of 500 to 1000 millitorr covered in the present study (fig. 5). From this result an upper limit of 10^{-14} cm^3/molecule-second may be estimated for the rate constant of the endothermic reaction:

$$t\text{-}C_4H_9^+ + neo\text{-}C_5H_{12} \rightarrow i\text{-}C_4H_{10} + C_5H_{11}^+. \qquad (12)$$

c. Parent Ions

In previous studies we have shown [1] that thermal $C_2H_5^+$ and $C_3H_8^+$ ions react with C_2H_6 and C_3H_8, respectively, to form the corresponding dimer ions [1e, 1f]. Experiments were carried out to determine if dimeric ions were also formed in the butanes and pentanes. The reactions of the isomeric butane and pentane molecular ions with their parent molecules were investigated using 10.6 eV photons from a krypton resonance lamp. This energy is insufficient to induce fragmentation of the parent ion; consequently, reactions of the parent ions may be studied unambiguously. The photoionization of *i*-C_4H_{10} as a function of pressure at 10.6 eV is shown in figure 6. At low pressures (< 20 millitorr) the $C_4H_{10}^+$ ions react slowly with *i*-C_4H_{10} to yield $C_4H_9^+$. The rate constant for this slow bimolecular reaction is $\leq 5 \times 10^{-11}$ cm^3/molecule-second. As the total pressure is increased further, $C_4H_9^+$ ions appear to react slowly with *i*-C_4H_{10} via a H^- transfer reaction to yield $C_4H_9^+$:

$$C_4H_8^+ + i\text{-}C_4H_{10} \rightarrow C_4H_9^+ + C_4H_9. \qquad (13)$$

The analogous reaction has been reported for the $C_3H_6^+ - C_3H_8$ reaction pair [4]. At pressures greater than approximately 15 millitorr the formation of the dimeric ion $(C_4H_{10})_2^+$ was also detected. At the highest pressure (~ 90 millitorr) this ion constituted approximately 30 percent of the composite mass spectrum in photoionized *i*-C_4H_{10}. The $C_4H_8 - C_4H_{10}^+$ collision complex also appeared to be stabilized to some extent at higher densities.

Although a careful search was made for dimeric ions in *n*-C_4H_{10} and the pentanes at pressures up to approximately 0.5 torr, the formation of species analogous to $(C_4H_{10})_2^+$ in *i*-C_4H_{10} was not detected. The only reaction found in any other system was the formation of $C_5H_{11}^+$ in *i*-C_5H_{12} with a rate constant $\leq 2 \times 10^{-12}$ cm^3/molecule-second. The *n*-$C_4H_{10}^+$ and *n*-$C_5H_{12}^+$ ions were found to be unreactive towards their parent molecules.

4. References

[1] (a) Sieck, L. W., Searles, S. K., and Ausloos, P., J. Am. Chem. Soc. **91**, 7627 (1969); (b) Sieck, L. W., and Searles, S., J. Am. Chem. Soc. **92**, 2937 (1970); (c) Sieck, L. W., and Searles, S. K., J. Chem. Phys. **53**, 2601 (1970); (d) Searles, S. K., and Sieck, L. W., **53**, 794 (1970); (e) Searles, S. K., Sieck, L. W., and Ausloos, P., J. Chem. Phys. **53**, 849 (1970); (f) Sieck, L. W., Searles, S. K., and Ausloos, P., J. Chem. Phys. (in press).

[2] (a) Munson, M. S. B., Franklin, J. L., and Field, F. H., J. Phys. Chem. **68**, 3098 (1964); (b) Munson, M. S. B., J. Am. Chem. Soc. **89**, 1772 (1967).

[3] (a) Scala, A. A., Lias, S. G., and Ausloos, P., J. Am. Chem. Soc. **88**, 5701 (1966); (b) Ausloos, P., Structure and Reactivity of Hydrocarbon Ions, Ion-Molecule Reactions, Ed., J. L. Franklin (Plenum Press, New York, 1970); (c) Ausloos, P., and Lias, S. G., J. Am. Chem. Soc. **92**, 5037 (1970).
[4] (a) Lias, S. G., Rebbert, R. E., and Ausloos, P., J. Am. Chem. Soc., **22**, 6430 (1970); (b) Lias, S. G., and Ausloos, P., J. Am. Chem. Soc. **92**, 1840 (1970).
[5] Steiner, B., Giese, C. F., and Inghram, M. G., J. Chem. Phys. **34**, 189 (1961).
[6] Franklin, J. L., Dillard, J. G., Rosenstock, H. M., Herron, J. T., Draxl, K., and Field, Nat. Stand. Ref. Data Ser., Nat. Bur. Stand. (U.S.), 26, 289 pages (1969).
[7] Chupka, W. A., and Berkowitz, J., J. Chem. Phys. **47**, 2921 (1967).
[8] Vestal, M., in Fundamental Processes in Radiation Chemistry, Ed., Ausloos, P. (Interscience, New York, 1969).
[9] Abramson, F. P., and Futrell, J. H., J. Phys. Chem. **71**, 1233 (1967).
[10] (a) Field, F. H., and Lampe, F. W., J. Am. Chem. Soc. **80**, 5587 (1958); (b) For a review see, Futrell, J. H., in Fundamental Processes in Radiation Chemistry, Ed., Ausloos, P. (Interscience, New York, 1969).
[11] Saunders, M., Hagen, E. L., and Rosenfeld, J., J. Am. Chem. Soc. **90**, 6882 (1968).
[12] Lossing, F. P., and Semeluk, G. P., Can. J. Chem. **48**, 955 (1970).

(Paper 75A3–658)

JOURNAL OF RESEARCH of the National Bureau of Standards—A. Physics and Chemistry
Vol. 75A, No. 3, May–June 1971

An Alumina Standard Reference Material for Resonance Frequency and Dynamic Elastic Moduli Measurement I. For Use at 25 °C

R. W. Dickson and J. B. Wachtman, Jr.

Institute for Materials Research, National Bureau of Standards, Washington, D.C. 20234

(February 3, 1971)

Bars of sintered polycrystalline alumina were machined to nominal dimensions of 12.7 by 1.27 by 0.32 cm. Surfaces were machined flat and parallel. The mass, dimensions, and resonance frequencies (flexural and torsional) were measured at 25 °C. The exact frequency is specified for each bar and is typically about 2030 Hz for flexural resonance and 11250 Hz for torsional resonance. The effect of suspension loading on resonance frequency was determined and a correction made. Each bar can be used as a frequency standard with an uncertainty for values measured in air of about ±0.03 Hz for flexure and ±0.08 Hz for torsion. The effect of atmosphere on resonance frequency was determined and a correction was made for this effect. The uncertainty for resonance frequencies in vacuum is about ±0.06 Hz for flexure and ±0.18 Hz for torsion. Each bar can also be used as a dynamic elasticity standard with an uncertainty estimated to be about 0.2 percent for the shear modulus and 0.4 percent for Young's modulus.

Key words: Alumina; elastic modulus; resonance frequency; shear modulus; standard reference material; Young's modulus.

1. Introduction

Elastic moduli of solids are of interest both as fundamental data needed in the calculation of many solid state properties and as engineering data [1].[1] Modern sound velocity and resonance techniques permit their determination to high accuracy provided that the mass and demensions of specimens can be accurately determined and provided that care is taken to eliminate or allow for certain loading effects. One popular technique is to determine the frequencies of the fundamental normal modes of vibration by the Forster method [2] in which a slender rod or bar is suspended horizontally on two fine wires or threads passing around the bar near the nodes of vibration. One wire is vibrated by a driver energized by a variable frequency oscillator. The other wire is attached to a detector. The driving frequency is varied until the desired mode of resonance (usually flexural or torsional) is excited and the frequency at resonance is measured. Procedures to identify the mode which is excited and accurate equations for calculating elastic moduli from these frequencies have been described [3].

The simplicity of the Forster method and its adaptability to measurements at high temperature have led to its widespread use. The accuracy with which frequency can be measured with a crystal-controlled counter and the reproducibility of a given resonance frequency in a particular experimental arrangement sometimes obscures the fact that serious systematic errors can be present. The two most gross errors are the improper identification of the vibrational mode of the specimen which is excited or the exciting of a vibration of some part of the apparatus other than the specimen. Such errors may appear unlikely to pass undetected, but experience in consulting with operators just beginning to use the method has shown that such errors do occur. More subtle errors which are usually smaller and may pass unnoticed even by experienced operators include loading effects caused by the suspension or the surrounding atmosphere and temperature errors. The loading effects cause the specimen to resonate at a frequency slightly different from that of free vibration. The free vibration required for the specimen also makes it impossible to contact the specimens with a thermocouple unless the latter is used as one of the suspensions. This is usually undesirable because of the mechanical characteristics of thermocouple wire. Ordinarily a thermocouple placed very near the specimen is used to measure the temperature. The temperature difference between this couple and the specimen may be appreciable in high temperature measurements. It is, therefore, very useful for an operator to have a standard specimen with accurately known resonance frequencies and to have the temperature de-

[1] Figures in brackets indicate the literature references at the end of this paper.

pendence of these frequencies in order to estimate the magnitude of these errors in his apparatus. The calculation of elastic moduli from resonance frequencies is sufficiently complicated that an example is useful for this purpose also. The complexity in these calculations arises because for a complete determination of the two independent moduli an iteration process is required to solve the simultaneous equations.

The foregoing are the primary reasons leading to the development of a dynamic elasticity standard. A secondary motivation is the possibility of using the same bars also as a standard for static measurement of Young's modulus in flexure. The static (isothermal) moduli should be less than the dynamic (adiabatic) moduli by a small amount calculable from an equation given, for example, by Nye [4]. For alumina the difference for Young's modulus is only 0.2 percent. Static flexural measurements, when carefully made and correctly analyzed show good agreement with dynamic measurements when this small difference is allowed for. Sources of error (up to several percent) exist in static measurement techniques which are difficult to locate and eliminate. Thus, dynamic standards might be useful for debugging static measurements.

The present elasticity standards were chosen to meet the following criteria: (1) They should be in a size range normally used for dynamic elasticity measurements. (2) They should permit very accurate values of resonance frequencies at 25 °C to be certified for use in checking room temperature measurement procedure. (3) Their size and shape should permit accurate values of elastic moduli at 25 °C to be calculated and certified. (4) The material used for the standard should be stable over the temperature range 25 to 1000 °C to permit certification of the ratio of frequency at elevated temperature to frequency at 25 °C over this temperature range (from this information the frequencies themselves and the elastic moduli can be calculated over this temperature range).

2. Material

A standard elasticity bar should certainly be stable under normal use. The most likely sources of trouble with these bars are mechanical abrasion and thermal effects. A standard elasticity bar should always be handled with care so that damage from abrasions is not likely, but it is desirable that the material of the bar be sufficiently hard so that it would not be scratched by contact with metals. The bar should withstand heating in air to 1000 °C without change. These requirements suggest the use of a hard, dense oxide.

Fused silica was considered for this use and would apparently be quite suitable at 25 °C. It possesses the advantages of elastic isotropy and of a high degree of homogeneity. However, the density changes slowly with time at 903 °C [5] so that the temperature range for use would be limited to somewhat below 900 °C. Furthermore, devitrification at the surface occurs slowly at temperatures near 1000 °C; its rate may depend on atmosphere and surface condition. Fused silica was therefore not chosen despite its homogeneity and ready availability because of the uncertainty about the temperature limit which would certainly have to be below 900 °C.

Polycrystalline alumina is elastically isotropic if formed by a process which does not produce a preferred orientation. It is even harder than fused silica so that it is very abrasion resistant. Polycrystalline alumina is normally porous; this reduces the elastic moduli but is not objectional unless the amount of porosity varies sufficiently with position to cause an unacceptable degree of inhomogeneity. A process for the production of nearly pore-free polycrystalline alumina has been developed and thin pieces are available commercially [6–9]. This process requires the presence of a small amount of MgO to reduce the rate of grain growth. The amount of MgO used (typically 0.25 wt %) is chosen to be within the range of solid solubility at the sintering temperature (typically 1850 °C). The extent of solid solubility depends on atmosphere and grain size; more importantly, the limit of solid solubility decreases with decreasing temperature below 1730 °C [10]. Alumina produced by this process will apparently be in a metastable state at temperatures sufficiently below the sintering temperature. No work on the rate of precipitation of excess MgO at 1000 °C has been located, but the strong temperature dependence of diffusion rates in alumina suggests that at temperatures below 1200 °C precipitation would be too slow to be significant in a period of 1000 hours. Polycrystalline alumina was therefore chosen and is believed to be sufficiently stable at 1000 °C for the present purposes although its behavior over extremely long times is not known. After consultation with R. C. Anderson [11] and P. J. Jorgensen [12] it was decided to use 0.1 percent MgO and to isostatically cold press and sinter a single block of nominal dimensions $2\frac{1}{4}$ by $2\frac{5}{8}$ by $4\frac{7}{8}$ in from which 40 specimen bars would be machined. The single-block approach offered the advantages of chemical homogeneity of the starting powder and of lower cost. Regions near the center of an isostatically cold pressed and sintered block are typically more porous than those near the surface, and it was recognized that the large size chosen might result in appreciable total porosity and some variation in porosity throughout the block. It was believed, however, that these effects would be small enough to be acceptable, and the single block was manufactured. Sintering was carried out under the direction of P. J. Jorgensen [12].

The sintered block was diamond ground to produce flat surfaces with opposite surfaces parallel and adjacent surfaces perpendicular. The density was determined from the mass (corrected for air bouyancy) and the dimensions (measured after overnight equilibration in a constant temperature room at 23.9 °C). The result was 3.933 ± 0.002 gm/cm^3 where the uncertainty is the gross standard deviation calculated from the individual standard deviations of the mass and length determinations. The density of pure single crystal alumina is 3.986 gm/cm^3 as determined by hydrostatic weighing [13] or 3.987 gm/cm^3 from x-ray parameter measure-

ment [14]. On this basis, the average porosity of the block was 1.3 percent.

The block was marked off into individual specimens as shown in figure 1 and specimen numbers A1, A2, . . .

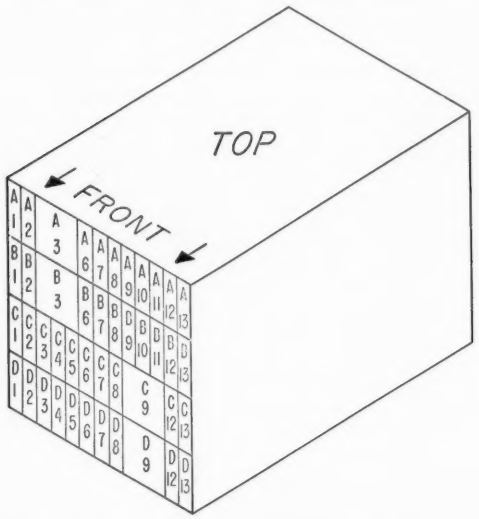

FIGURE 1. *Pattern of resonance bars machined from original cold-pressed and sintered alumina block.*

D13 were lightly inscribed on one end with a diamond point scriber. The block was then diamond sawed into bars in accordance with this pattern. The four large bars A3, B3, C9, and D9 were reserved for possible machining of cylinders and the remaining 40 bars were prepared as elasticity standards. Each bar was given a fine diamond grind to produce flat surfaces with opposite sides parallel and adjacent sides perpendicular. The mass (corrected for air bouyancy) and the dimensions of each bar are given in table 1.

Bars A3 and B3 were examined by x-ray techniques. The prime concern was the possible existence of a preferred orientation of the crystallites which would cause the specimens to be anisotropic. Back-reflection x-ray patterns showed no such preferred orientation [15]. They also yielded the information that the average crystallite size (determined from the number of spots for a given reflection, the beam size, and the adsorption) was 24 μm. High-resolution high-intensity diffractometer patterns showed almost exclusively the α-alumina phase as expected. A very weak pattern, identified as due to the presence of $MgAl_2O_4$ (spinel), was also present; the intensity, however, indicated that the proportion of $MgAl_2O_4$ was much less than one percent.

3. Experimental Procedure and Frequency Corrections

The general procedure for exciting a resonance and probing the vibrational pattern with a pickup to identify the vibrational mode has been described by Spinner and Tefft [3], who also describe the electronic components required. The following specific items of equipment were used in the present work but many similar components exist and would presumably be equally satisfactory. The driver was an Astatic model M 41–8 phonograph record recording head. It was driven by a Hewlett-Packard 463–A precision amplifier driven in turn by a General Radio frequency synthesizer Model 1163–AR7C with automatic sweep unit. The frequency was monitored with a Beckman timer Model 6147 which in turn was standardized with the NBS 100 kHz frequency so that the driving frequency measurement should be accurate to 1 part in 10^6. The pickup was an Astatic L–121 crystal phonograph cartridge for use in air or an Astatic 51–3 ceramic phonograph cartridge for use at reduced pressures. The signal was amplified by an Applied Cybernetics System Model 1A260V battery-powered low-noise amplifier. The signal was continuously monitored on a Dumont Model 304–AR oscilloscope which was supplemented for measurements of response to automatic frequency sweep by a Tektronix type 564 storage oscilloscope with a type 3A72 dual-trace plug-in amplifier and a type 2B67 plug-in time base. The use of a frequency synthesizer having a sweep unit is very desirable for this work which requires the combined capabilities of searching over wide frequency ranges (to find the resonances) and of very precise tuning (to determine the frequency of a resonance response as little as 0.1 Hz broad). The automatic feature of the sweep unit used allowed smooth frequency change (typically 1 Hz frequency change in 10 seconds) in locating the exact maximum of the vibrational amplitude corresponding to resonance. Even with very low sweep rates the slow response of the specimens caused a shift of the maximum amplitude of response from the resonance frequency, but by sweeping in both directions, recording the amplitudes on the storage oscilloscope, and noting how the maximum responses approached each other as the sweep rate was lowered this effect could be overcome.

Each bar was suspended horizontally using fine silk thread and the loop method of suspension [16] in which both the thread from the driver needle and the thread from the pickup needle are cemented to their respective needles at two points. Each thread then forms a continuous loop and supports the specimen without a knot at any point. Approximate values of the flexural and torsional resonance frequency were determined with the thread placed symmetrically some distance from the nodes. The vibrational pattern was probed to verify the identification of the nodes as previously described [3]. The measured internal friction of low-loss specimens is strongly affected by the suspension position [17]; the resonance frequency is affected to an extent which is much smaller but which is still significant for the present accurate frequency determinations. As in the previous work [17], a specimen was suspended with the driver and pickup threads positioned symmetrically. To obtain a correction for the effect of the suspension one of the specimens was suspended at several pairs of symmetrically located

418-535 OL - 71 - 2

TABLE 1. *Properties of alumina standard reference bars for frequency and dynamic elastic moduli at 25 °C in vacuum* [a]

Bar Number	Mass	Length	Width	Thickness	Density	Flexural Frequency	Torsional Frequency	Young's Modulus	Shear Modulus	Poisson's Ratio
	Grams	*cm*	*cm*	*cm*	*g/cm³*	*Hz*	*Hz*	*10'' N/m²*	*10'' N/m²*	
A1	20.5174	12.7003	1.271	0.3222	3.944	2037.56	11249.5	3.900	1.581	0.233
A2	20.4679	12.7002	1.271	.3223	3.934	2032.37	11224.3	3.869	1.569	.232
A6	20.4364	12.7000	1.271	.3223	3.928	2027.82	11203.5	3.846	1.561	.232
A7	20.4388	12.7001	1.271	.3223	3.929	2027.46	11200.4	3.844	1.560	.232
A8	20.4458	12.7003	1.271	.3226	3.926	2027.57	11201.8	3.835	1.557	.231
A9	20.4686	12.7003	1.271	.3228	3.929	2030.70	11216.1	3.847	1.562	.232
A10	20.4708	12.7005	1.271	.3225	3.932	2031.64	11220.8	3.860	1.566	.232
A11	20.4972	12.7006	1.271	.3226	3.936	2035.43	11237.8	3.876	1.572	.233
A12	20.5017	12.7008	1.271	.3222	3.941	2037.12	11247.6	3.898	1.580	.233
A13	20.5579	12.7011	1.271	.3223	3.951	2043.29	11279.6	3.928	1.592	.233
B1	20.4863	12.6998	1.271	0.3224	3.937	2030.55	11216.5	3.863	2.568	0.232
B2	20.4270	12.6998	1.271	.3223	3.926	2027.62	11200.6	3.844	1.560	.232
B6	20.2490	12.6995	1.271	.3221	3.894	2002.33	11071.3	3.720	1.513	.230
B7	20.2543	12.6995	1.271	.3225	3.891	2000.70	11062.4	3.702	1.506	.229
B8	20.2694	12.6996	1.271	.3226	3.893	2003.93	11079.0	3.714	1.510	.229
B9	20.2847	12.6996	1.271	.3227	3.895	2005.27	11085.2	3.719	1.513	.230
B10	20.3098	12.6998	1.271	.3226	3.900	2009.27	11107.4	3.741	1.521	.230
B11	20.3535	12.7002	1.271	.3221	3.914	2015.61	11141.7	3.790	1.540	.230
B12	20.4553	12.7005	1.271	.3223	3.931	2029.48	11213.0	3.856	1.566	.231
B13	20.5947	12.7016	1.271	.3226	3.955	2046.57	11298.6	3.937	1.596	.233
C1	20.5713	12.7008	1.271	0.3227	3.949	2044.29	11289.1	3.919	1.590	0.233
C2	20.4124	12.6998	1.271	.3227	3.920	2022.39	11177.9	3.808	1.548	.230
C3	20.2913	12.6996	1.271	.3220	3.905	2008.83	11109.9	3.759	1.529	.230
C4	20.2657	12.6995	1.271	.3224	3.895	2003.08	11079.2	3.717	1.512	.229
C5	20.2505	12.6996	1.271	.3225	3.891	2000.34	11065.0	3.701	1.506	.229
C6	20.2209	12.6996	1.271	.3221	3.890	1998.10	11054.9	3.700	1.506	.229
C7	20.2274	12.6995	1.271	.3221	3.891	1998.73	11058.1	3.705	1.508	.229
C8	20.2634	12.6997	1.271	.3227	3.891	2002.42	11075.3	3.705	1.508	.229
C12	20.4375	12.7005	1.271	.3221	3.932	2026.81	11202.1	3.851	1.564	.231
C13	20.5306	12.6999	1.271	.3227	3.942	2038.65	11258.3	3.892	1.579	.232
D1	20.5638	12.7006	1.271	0.3226	3.950	2043.27	11281.4	3.919	1.589	0.233
D2	20.5251	12.7003	1.271	.3227	3.942	2038.87	11260.4	3.892	1.579	.232
D3	20.5001	12.7004	1.271	.3228	3.935	2035.35	11243.1	3.869	1.570	.232
D4	20.4892	12.7003	1.271	.3226	3.935	2033.30	11234.1	3.866	1.570	.232
D5	20.4838	12.7002	1.271	.3224	3.937	2033.87	11237.6	3.876	1.573	.232
D6	20.4787	12.7004	1.271	.3225	3.935	2031.77	11227.5	3.863	1.569	.231
D7	20.4863	12.7004	1.271	.3227	3.934	2033.46	11234.8	3.863	1.568	.232
D8	20.4796	12.7006	1.271	.3226	3.934	2033.59	11236.1	3.867	1.570	.231
D12	20.5332	12.7013	1.271	.3226	3.942	2039.18	11259.8	3.896	1.580	.233
D13	20.5710	12.7007	1.271	.3227	3.948	2045.14	11290.3	3.923	1.591	.233

[a] For use in air subtract 0.99 Hz from flexural resonance frequency and 2.25 Hz from torsional resonance frequency.

Estimated accuracy is given in terms of standard deviation based on repeated measurements for length, width, and thickness. For other quantities the estimated uncertainty is based on estimates of the accuracy of the instruments involved, the equations used, the correction factors, and the specimen homogeneity as described in the text. The estimated standard deviations are: mass ±0.0001 gm, length ±0.0002 cm, width ±0.0001 cm, thickness ±0.0003 cm, density ±0.004 gm/cm³. The estimated uncertainties are: flexural frequency in vacuum ±0.06 Hz, torsional frequency in vacuum ±0.18 Hz, Young's modulus $\pm 0.016 \times 10^{11}$ N/m², shear modulus $\pm 0.003 \times 10^{11}$ N/m², and Poisson's ratio ±0.005. The values of resonance frequency in air, obtainable as described above, are more accurate than the vacuum values because they were directly determined. The corresponding estimated uncertainties are ±0.03 Hz for the flexural resonance frequency and ±0.08 Hz for the torsional resonance frequency in air at one atmosphere pressure.

points and a series of frequencies determined. The measured values for the fundamental flexural resonance pass through a minimum, taken as the value for free vibration in air, corresponding to suspension position at the nodes of vibration. One position of the suspension (near the nodes) was chosen as a "standard" position and a correction factor determined for this position. All specimens were measured with the suspension at this position and with the same suspension (i.e., the same threads and needles) used for all measurements. The measured frequency was then corrected to give the free resonance frequency of flexure in air at the test temperature by substracting 0.05 Hz. For torsion the equivalent correction was made by subtracting 0.13 Hz.

The temperature dependence in the vicinity of 25 °C

was next determined for two bars. The elastic moduli of alumina are known to vary smoothly with temperature and to be approximately linear near 25 °C [18, 19]. The temperature coefficients for the flexural and torsional resonance frequencies for these two bars were determined to be −0.117 Hz/°C and −0.710 Hz/°C, respectively.

The bars are so nearly identical that the same correction factors for suspension effect and temperature can be used for all bars. As can be seen the correction factors for these suspensions and for minor deviations of the test temperature from 25 °C are small (small enough to be neglected in most elastic moduli measurements), but they are not negligible for the present purpose. Accordingly, the following procedure was adopted. A careful measurement of the flexural and torsional resonance frequencies for each bar was made by suspending the bar within a heavy-walled, acoustically insulated box and allowing it to come to temperature equilibrium. The temperature was read to 0.1 °C and each measured resonance frequency was taken as the average of the value corresponding to the maximum amplitude of vibration for a slow increasing-frequency sweep and a decreasing-frequency sweep. Values were determined to 0.01 Hz. These values, corrected as above for temperature and suspension effect are the free resonance frequencies in air at 25 °C.

The atmosphere is known to affect both the resonance frequency and damping and it is sometimes suggested, especially for damping, that the viscous drag on the moving specimen is responsible. While viscous drag may be important for certain types of internal friction measurements (e.g., the torsion of thin cylinders) it is apparently not the predominant atmospheric effect on the frequencies of specimens of the present size and shape. To determine the cause and size of the effect of atmosphere on frequency, specimens were suspended in a large vacuum chamber which also contained the driver and pickup. The resonance frequency was first measured in air. The chamber was then evacuated and filled in stages with argon. Figures 2 and 3 show the dependence of the flexural and torsional resonance frequencies upon pressure of argon. The straight lines were drawn by a visual fit. Figures 2 and 3 show that the pressure dependence of the resonance frequencies is essentially linear over the entire range of measurement. This differs markedly from the bahavior of the viscosity which changes little down to pressures of about 1 mm of Hg and then decreases rapidly with futher lowering of the pressure. Such a linear dependence upon pressure is, however, to be expected from the variation of the acoustic impedance with pressure. For small acoustical loading the frequency should change in proportion to the acoustic impedance. The latter is proportional to ρc which for an ideal gas is proportional to $(\rho p)^{1/2}$ or to $\gamma^{1/2}M^{1/2}p$ where ρ is density, c is velocity of sound, p is pressure, $\gamma = C_p/C_1$ and M is mean molecular weight [20]. The molecular weights of argon and air are 39.95 and 29.12, respectively [21]; their γ values are 1.668 and 1.403 [20]. Thus the ratio of the shift of resonance frequency in going from vacuum to 1 atm pressure of argon to the same shift for air is predicted to be $(\gamma M)^{1/2}_{\text{argon}}/(\gamma M)^{1/2}_{\text{air}} = 1.277$. The measured frequency shifts are 1.24 Hz and 0.99 Hz for flexure giving a ratio of 1.25; the corresponding values for torsion are 2.90 Hz and 2.25 Hz giving a ratio of 1.29. The

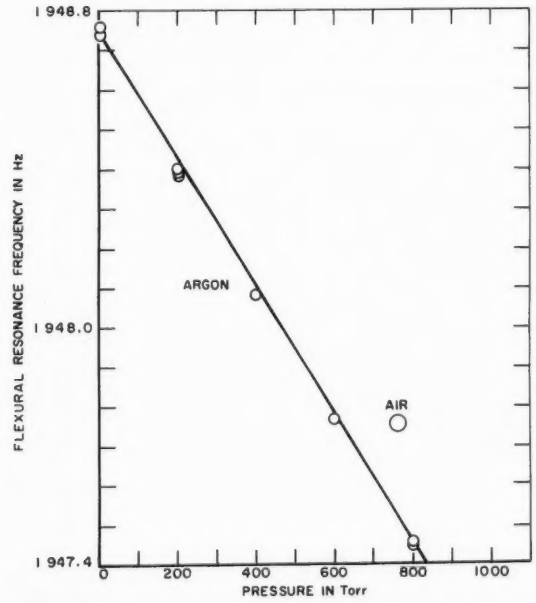

FIGURE 2. *Flexural resonance frequency as a function of pressure of argon.*
Single point is for air at one atmosphere pressure.

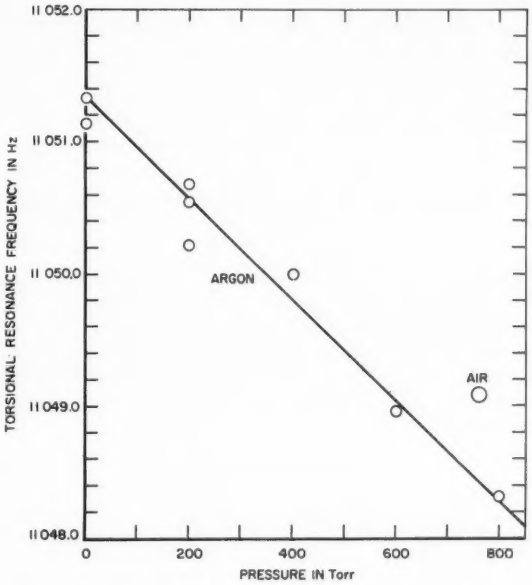

FIGURE 3. *Torsional resonance frequency as a function of pressure of argon.*
Single point is for air at one atmosphere pressure.

bars are sufficiently alike that the same frequency shifts apply to all bars. The free resonance frequency at 25 °C in vacuum is thus given by the free resonance frequency at 25 °C in air plus a correction factor which is 0.99 Hz for flexure and 2.25 Hz for torsion.

4. Calculation of Elastic Moduli and Estimates of Error

Spinner and Tefft [3] have reviewed the equations for calculation of elastic moduli of homogeneous, isotropic material from the resonance frequencies of slender bars. Their recommended equations were used. The shear modulus, G was calculated from the density, ρ, length, l, and fundamental torsional resonance frequency, f_t, using

$$G=\rho R(2lf_t)^2 \tag{1}$$

where R is a shape factor given by

$$R=\left[\frac{1+\left(\frac{b}{a}\right)^2}{4-2.521\,\frac{a}{b}\left(1-\frac{1.991}{\exp\left(\frac{\pi b}{a}\right)+1}\right)}\right]\left[1+\frac{0.00851b^2}{l^2}\right]-0.060\left(\frac{b}{a}\right)^{3/2}\left(\frac{b}{a}-1\right)^2 \tag{2}$$

in which b is width and a is thickness. The flexural motion is in the direction of the thickness.

Spinner and Tefft estimate that this calculation should give G values accurate to within 0.2 percent when $b/l<0.3$ and $b/a<10$ as they are for the present specimens.

Young's modulus, Y, was calculated from

$$Y=0.94642\ (\rho l^4 f_f^2/a^2)T \tag{3}$$

in which f_f is the fundamental flexural resonance frequency and T is a correction factor given by

$$T=1+6.585(1+0.0752\mu+0.8109\mu^2)\left(\frac{a}{l}\right)^2-0.868\left(\frac{a}{l}\right)^4-\frac{8.340(1+0.2023\mu+2.173\mu^2)(a/l)^4}{1+6.338(1+0.14081\mu+1.536\mu^2)(a/l)^2} \tag{4}$$

in which μ is Poisson's ratio.

For each bar a single value of G was calculated which does not require Poisson's ratio in the calculation. An initial value of Y was calculated taking $T=1.000$ which is the value of T for a very thin bar, i.e., for $t/l=0$. A value of Poisson's ratio was then calculated from

$$\mu=(Y/2G)-1 \tag{5}$$

and Y was recalculated using this value of μ. This process was repeated until self consistent values of Y and μ were obtained. The accuracy of this type of calculation for homogeneous bars of the length-to-thickness ratio used here has been judged to be better than 0.1 percent judging from an empirical study with steel specimens by Spinner, Reichard, and Tefft [24].

The above estimates of uncertainty [2] are those of the equations themselves. Additional uncertainty arises from variations in thickness (uncertainties associated with measurements of frequency, mass, length, and width are smaller). For the shear modulus the thickness enters only to the -1 power through the density. An uncertainty of 0.1 percent in the thickness (the probable error based on 5 measurements) is typical and gives an uncertainty (from this source alone) of about 0.1 percent in the shear modulus. For Young's modulus the thickness enters to the -3 power (including its presence in the density) giving an uncertainty (from this source alone) of 0.3 percent in Young's modulus.

The above considerations of error do not include the effect of inhomogeneous distribution of porosity. Porosity differences from bar to bar change elastic moduli values but this is fully taken into account in the calculations and does not introduce additional uncertainty into the moduli values *provided* that the porosity is homogeneously distributed within each bar. Examination of the density values in table 1 shows that the corner bars (A1, A13, D1, and D13 in fig. 1) form the most dense groups followed in order of decreasing density by the following groups: those having a face on the original surface (B1, C1, B13, and C13), those having an edge on the original surface (A2, A6, A7, A8, A9, A10, A11, A12, D2, D3, D4, D5, D6, D7, D8, and D12), and those entirely within the original bar (B2, B6, B7, B8, B9, B10, B11, B12, C2, C3, C4, C5, C6, C7, C8, and C12). As mentioned previously, this type of porosity gradient is commonly observed in cold pressed and sintered bars. If the porosity distribution was the same for all planes parallel to the end of the block shown in figure 1 (no longitudinal component of the gradient); it could probably be ignored. However, there must be a similar gradient from end to end of the original large bar. It is probable that the lengthwise gradient is smallest in the four corner bars because the porosity is least and because these bars have directly experienced the applied pressure. Similarly, it is probable that the lengthwise porosity gradient increases in the order of decreasing density. If this effect introduces systematic error into the calculated moduli, we would expect plots of Young's modulus or the shear modulus as a function of porosity to give a different curve for each of the four groups of bars. In fact, all points fall on the same plot within the random scatter as judged by eye. This scatter is consistent with the above estimates of error due to thickness uncertainty; any

[2] The word "uncertainty," as used in this paper, means an *estimated* total uncertainty derived from the consideration of possible sources of error in all the measurements involved in the determination of the studied property. The estimation is generally based on previous knowledge of the measuring processes involved; the estimates are not expressed in terms of exact statistical measures, such as standard deviations, because they comprise both random and systematic errors and are partly based on judgment rather than on repetitive measurements of the same quantity.

error arising from inaccuracy of the equations would be a systematic error and so not reflected in the scatter on these plots. The maximum deviation from the curve for any bar is 0.3 percent for Young's modulus and 0.2 percent for the shear modulus.

Combining possible errors from the equations and the measurements we thus arrive at estimates of the uncertainty of 0.2 percent for the shear modulus and 0.4 percent for Young's modulus. These uncertainty values refer to the *dynamic* elastic moduli.

The static Young's modulus will be 0.2 percent less than the dynamic Young's modulus because of the change from adiabatic to isothermal conditions as mentioned previously. Determination of static elastic moduli in bending places a very similar, though not identical, stress field on a bar as resonance in the fundamental mode of flexure. We therefore expect inhomogeneous distribution of porosity to have approximately the same effect on the stiffness of a bar in dynamic or static flexure. In dynamic flexure inhonogeneous distribution of porosity could also shift resonance frequency (and therefore calculated moduli) through the change of inertia. As noted above, no appreciable difference in groups of bars of differing porosity ranges was detected so that we believe this dynamic effect is not appreciable and the same uncertainties should hold for static and dynamic moduli measured over the whole length of the bar. We do not recommend cutting a bar into pieces; the reported values may not apply to short pieces within the stated uncertainty limits because of porosity variation along the length of the bar. For very accurate static comparisons we recommend the use of the 8 high density bars (A1, A13, B1, B13, C1, C13, D1, D13) to minimize possible porosity gradient effects.

5. Summary and Recommendations

The resonance frequency of each bar is specified to the nearest 0.1 Hz for the torsional resonance in air at 1 atm pressure with an estimated uncertainty of ± 0.08 Hz (relative uncertainty of 0.0007 percent); for flexural resonance the frequency is specified to the nearest 0.01 Hz with an estimated uncertainty of ± 0.03 Hz (relative uncertainty of 0.0015 percent). These values correspond to free vibration, i.e., the specimen must be supported in such a way that the suspension does not add effective mass or stiffness. In most situations the suspension will affect the resonance frequency, perhaps by a few Hz, unless care is taken. Use of one of the present bars will give the investigator an indication of how much his suspension is affecting the measured resonance frequency. He must not use the difference as a correction factor to apply to other materials, however, because the frequency shift caused by a given suspension may differ markedly for bars of different moduli, density, or size.

Chipping will affect the resonance frequencies. Each bar is quite strong and hard so that no chipping should occur with reasonable care, but impacts must be avoided. The mass of the bar can be redetermined as a confirmation that chipping has not occurred. If a bar is extremely clean and dry, electrostatic charging may cause a fluctuating apparent change in weight, but this effect does not occur in normal practice.

The dynamic elastic moduli are given with an estimated relative uncertainty of 0.2 percent for the shear modulus and 0.4 percent for Young's modulus. These estimates of uncertainty assume the use of the whole bar; cutting the bar into smaller pieces is not recommended because of possible porosity gradients.

Young's modulus in static flexure will be 0.2 percent less than the dynamic value because of the change from adiabatic to isothermal conditions. Use of one of the highest density bars is recommended for accurate work in static flexure.

6. References

[1] Wachtman, J. B., Jr., Elastic Deformation of Ceramics and Other Refractory Materials, pages 139–168 in "Mechanical and Thermal Properties of Ceramics", J. B. Wachtman, Jr., Ed., National Bureau of Standards Special Publication 303, May, 1969.

[2] Forster, F., Ein neues Messverfahren zur Bestimmung des Elastizitatemoduls und der Dampfung (New method for determination of modulus of elasticity and damping), Zeitschrift fur Metallkunde, **29**, 109–115 (1937).

[3] Spinner, S., and Tefft, W. E., A method for determining mechanical resonance frequencies and for calculating elastic moduli from these frequencies, Proc. ASTM **61**, 1221–1238 (1961).

[4] Nye, J. F., Physical Properties of Crystals (Oxford University Press, 1964).

[5] Douglas, R. B., and Isard, J. O., Density changes in fused silica, J. Society Glass Technology **35**, 206–225 (1951).

[6] Coble, R. L., Sintering crystalline solids: I, intermediate and final stage diffusion models, J. Appl. Phys. **32**, 787–792 (1961).

[7] Coble, R. L., Sintering crystalline solids: II, experimental test of diffusion models in powder compacts, J. Appl. Phys. **32**, 793–799 (1961).

[8] Coble, R. L., Sintering alumina: effect of atmospheres, J. Am. Ceram. Soc. **45**, 123–127 (1962).

[9] Jorgensen, P. J., and Westbrook, J. H., Role of solute segregation at grain boundaries during final-stage sintering of alumina, J. Am. Ceram. Soc. **47**, 332–338 (1964).

[10] Roy, S. K., and Coble, R. L., Solubilities of magnesia, titania, and magnesium titanate in aluminum oxide, J. Am. Ceram. Soc. **51**, 1–6 (1968).

[11] Aderson, R. C., General Electric Research and Development Center, Schenectady, N.Y. Private communication with one of the authors (JBW).

[12] Jorgensen, P. J., Stanford Research Institute, Palo Alto, California (formerly with General Electric Research and Development Center, Schenectady, N.Y.). Private communication with one of the authors (JBW).

[13] Wachtman, J. B., Jr., Tefft, W. E., Lam, D. G., Jr., and Stinchfield, R. P., Elastic Constants of Synthetic Single Crystal Corundum at Room Temperature, J. Res. Nat. Bur. Stand. (U.S.), **64A** (Phys. and Chem.), No. 3, 213–228 (May–June 1960).

[14] Swanson, H. E., Cook, Marlene, Isaacs, Thelma, and Evans, Eloise, Standard X-ray Diffraction Powder Patterns, Nat. Bur. Stand. (U.S.), Circ. 539 (1960), p. 3.

[15] Paretzkin, B., National Bureau of Standards, private communication with the authors.

[16] Dickson, R. W., and Spinner, S., An Improved Method for the Determination of Torsional and Flexural Resonance Frequencies of Cylindrical Specimens, Journal of Materials **3**, 716–724 (1968).

[17] Wachtman, J. B., Jr., and Tefft, W. E., Effect of suspension position on apparent values of internal friction determined by Forster's Method, Rev. Sci. Inst. **29,** 517–520 (1958).
[18] Wachtman, J. B., Jr., Tefft, W. E., Lam, D. G., Jr., and Apstein, C. S., Exponential temperature dependence of Young's Modulus for several oxides, Phys. Rev. **122,** 1754–1759 (1961).
[19] Tefft, W. E., Elastic constants of synthetic single crystal corundum, J. Res. Nat. Bur. Stand. (U.S.), **70A** (Phys. and Chem.), No. 4, 277–280 (Mar.–Apr. 1960).
[20] Grey, D. E., Coordinating editor, American Institute of Physics Handbook (McGraw-Hill, 1963). See pages 3–64 and 3–118.
[21] Weast, R. C., editor-in-chief, Handbook of Chemistry and Physics, The Chemical Rubber Company, Forty-eighth edition (1967).
[22] Spinner, S., Stone, L., and Knudsen, F. P., Temperature Dependence of the Elastic Constants of Thoria Specimens of Varying Porosity, J. Res. Nat. Bur. Stand. (U.S.), **67C** (Eng. and Instr.), No. 2, 93–100 (Apr.–June 1963).
[23] Wachtman, J. B., Jr., Scuderi, T. G., and Cleek, G. W., Linear Thermal Expansion of Aluminum Oxide and Thorium Oxide From 100° to 1100 °K, J. Am. Ceram. Soc. **45,** 319–323 (1962).
[24] Spinner, S., Reichard, T. W., and Tefft, W. E., A Comparison of Experimental and Theoretical Relations Between Young's Modulus and the Flexural and Longitudinal Resonance Frequencies of Uniform Bars, J. Res. Nat. Bur. Stand. (U.S.), **64A** (Phys. and Chem.), No. 2, 147–155 (Mar.–Apr. 1960).

(Paper 75A3–659)

JOURNAL OF RESEARCH of the National Bureau of Standards—A. Physics and Chemistry
Vol. 75A, No. 3, May–June 1971

Optical and Mechanical Properties of Some Neodymium-Doped Laser Glasses*

R. M. Waxler, G. W. Cleek, I. H. Malitson, M. J. Dodge, and T. A. Hahn

Institute for Materials Research, National Bureau of Standards, Washington, D.C. 20234

(January 22, 1971)

Studies have been made to evaluate thermo-optic and piezo-optic properties of five laser glasses. Measurements were made at the Cd red line, $\lambda = 0.6438$ μm, over a wide range of temperatures and pressures using interferometric and polarimetric techniques. The refractive index-temperature data show both positive and negative values and small changes with temperature. The changes in index with applied compressive stress are positive in value. Other optical properties evaluated were homogeneity, transmittance, and refractive index as a function of wavelength. An ultrasonic pulse-echo technique was used to determine the elastic constants, Young's modulus, shear modulus, bulk modulus, and Poisson's ratio. Data for thermal expansion, thermal conductivity, density, hardness and chemical composition are also given. Calculations were made of the thermal change of refractive index at constant volume. These data can be used to calculate corrections for the distortions of the wavefront of light generated in lasers.

Key words: Chemical composition; density; glasses; hardness; laser; optical homogeneity; photoelasticity; refractive index; thermal conductivity; thermo-optic properties; transmittance.

1. Introduction

When a glass laser is operated, thermal effects produce optical distortions which virtually preclude diffraction-limited operation even if the materials themselves are of diffraction-limited quality [1].[1] The changes in optical pathlength induced by optical pumping of neodymium-doped glass rods have been studied by several investigators [2–8]. This overall change is caused by changes in certain parameters; thermal expansion alters the physical dimensions of the cavity, and the refractive index varies as a function of the local temperature and stress. Data on these properties are needed to calculate the corrections for the distortion of the wavefront.

Several mechanisms have been proposed in the literature to account for the damage observed in laser materials operated at high power levels [9–12]. These can be properly assessed only when data on the material properties are known.

Compilations of data on the properties of laser materials have been published [13–14], but these are not complete. For the purposes mentioned above, data are presented in this paper on thermal expansion, the elastic constants and the change in refractive index as a function of temperature and stress. Included also are original data on the important laser properties; optical quality, transmittance, refractive index, thermal conductivity, hardness, density, and chemical composition. Measurements were made on specimens of five commercially made neodymium-doped laser glasses, and, for purposes of identification, these have been designed as glasses A, B, C, D, and E.

2. Optical Quality

Each specimen was examined to be sure that the glass contained no gross inhomogeneities, and that the specimen was well annealed. Inclusions and seeds were found by illuminating with a beam of light from the side and viewing normally against a dark background [15]. The optical homogeneity was determined from shadowgraphs and interferograms [16]. The state of anneal was ascertained by measuring the strain birefringence with a sensitive tint plate when the specimen was placed between crossed polarizers [17].

Specimen A was in the form of a cylinder 8 cm in diameter and 2.9 cm thick. Three inclusions that appeared to be metallic and two seeds were found. The specimen was annealed, and the birefringence was reduced to a negligible value except for the very edge of the specimen where a residual path difference of 2 nm/cm remained. The interferogram and shadowgraph are shown in figures 1a and 1b, respectively.

Specimen B, which was cut from a finished oscillator rod, had no seeds or inclusions. It was 5.5 cm

*The work described in this report was sponsored by the Advance Research Projects Agency, Department of Defense.

[1] Figures in brackets indicate the literature references at the end of this paper.

long and 1.6 cm in diameter. The specimen appeared to be well annealed, so that no further heat treatment was considered necessary. The interferogram and shadowgraph are shown in figures 2a and 2b, respectively.

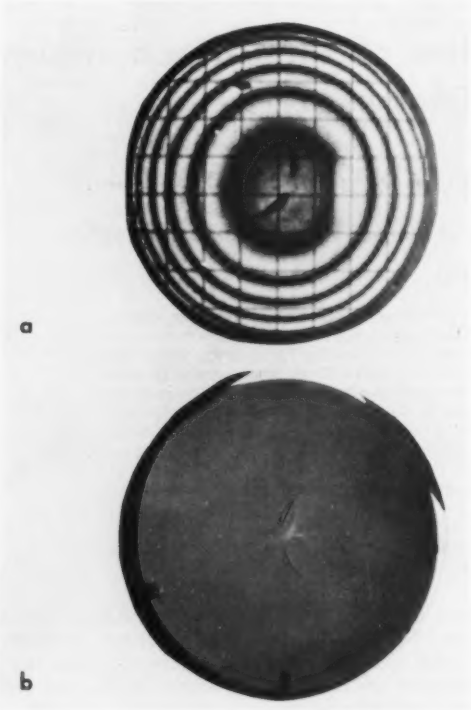

FIGURE 1. (a) *Twyman-Green interferogram of laser glass specimen A*; (b) *shadowgraph of laser glass specimen A.*

Specimens C and D were in the form of rectangular blocks about 4.5 cm × 1 cm × 1 cm. No seeds or inclusions were observed, and the glasses appeared to be well-annealed. The specimens were too small for meaningful interferograms so that only shadowgraphs were taken. The shadowgraph of specimen C is shown in figure 3a and that of specimen D is shown in figure 3b.

Specimen E was in the form of a cylinder 15.2 cm long and 2.5 cm in diameter. There were no seeds or inclusions, and the specimen was well-annealed. The interferogram and shadowgraph are shown in figure 4a and b, respectively.

From the striae that can be observed in the five shadowgraphs, it was concluded that all of the glasses could be regarded as Grade B,[2] or better, according to the military specification for optical glass [15]. The absence of abrupt changes in the fringe pattern of the interferogram was a confirmation that there

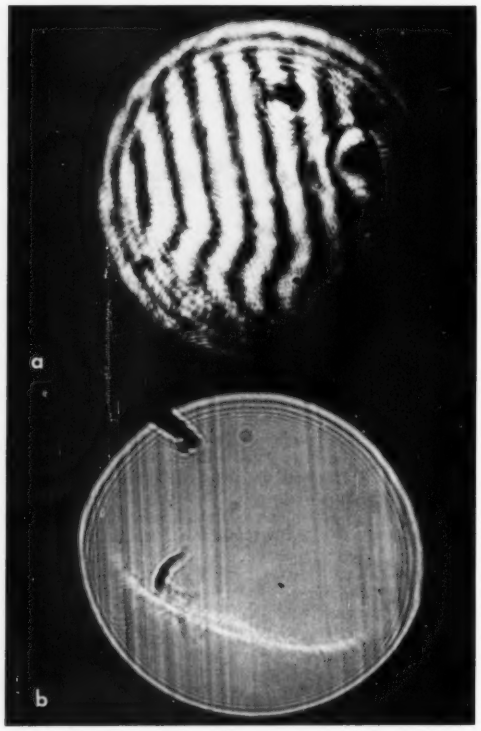

FIGURE 2. (a) *Twyman-Green interferogram of laser glass specimen B*; (b) *shadowgraph of laser glass specimen B.*

were no gross inhomogeneities present. From specimens A through E smaller samples were cut for the various studies of this report.

3. Transmittance

Transmittance curves for neodymium-doped silicate laser glasses have been published [14]. Since only very small variations are found for the different silicate glasses, the transmittance curve for a sample of specimen A is shown in figure 5 as a typical example. The transmittance was measured on a commercial double beam spectrophotometer.

4. Refractive Index

The glass specimens ground and polished for refractive index studies were either in the form of prisms or cuboids.[3] The two prisms had faces approximately 2 cm square and refracting angles near 60° (see table 2). These specimens were measured by means of the classical minimum deviation method using two spectrometers shown schematically in figure 6. The spec-

[2] In reference [15], Grade B glass is defined as glass which contains only striae that are light and scattered when viewed in the direction of maximum visibility when tested by the specified methods.

[3] Specimens B, C, and D were in the form of cuboids because there was insufficient material for prisms.

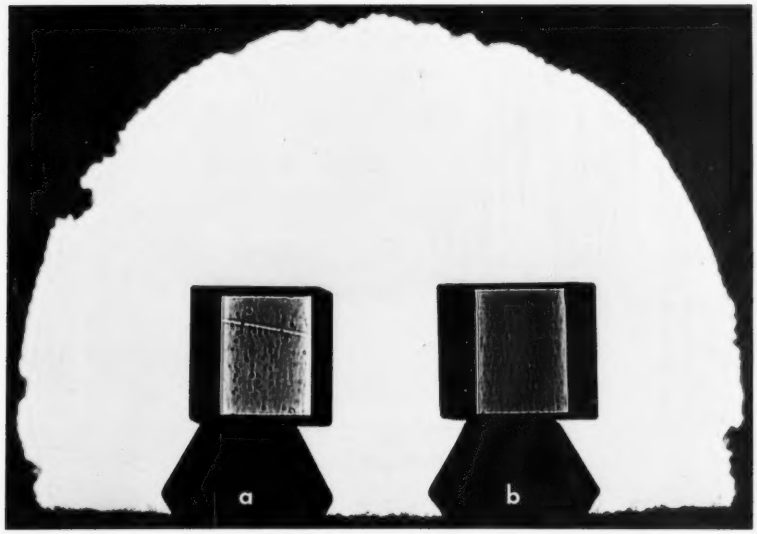

FIGURE 3. (a) *Shadowgraph of laser glass specimen C;* (b) *shadowgraph of laser glass specimen D.*

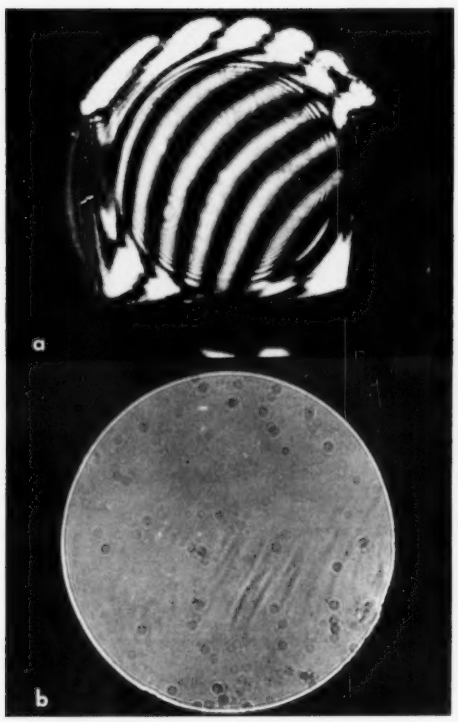

FIGURE 4. (a) *Twyman-Green interferogram of laser glass specimen E;* (b) *shadowgraph of laser glass specimen E.*

trometer shown in Figure 6a is designed for visible-region refractometry. When an infrared image converter is set at the viewing end of the telescope, visual sighting is extended to about 1.1 μm in the near infrared. The spectrometer outlined in figure 6b employs mirror optics and is used for nonvisible-region refractometry. Both instruments and procedures for high-precision refractive index measurements have been described in previous publications [18, 19, 20].

The technique employed for the refractive index measurements of the cuboids was somewhat novel and has been reported in an earlier publication [21]. Briefly, a specimen was optically contacted to a dense flint-glass prism of known refractive index as shown in figure 7. The visual spectrometer (fig. 6a) was used to measure the angles describing the optical path through the combination. Ray tracing equations were derived to compute the refractive index. Index measurements for the five specimens were made at selected wavelengths from 0.4 to 2.3 μm for the prominent emission spectra of mercury, cadmium, and helium at a controlled room temperature near 20 °C.

The indices of refraction of these glasses were represented by a modified Herzberger dispersion equation [22] of the form

$$n = A + BL + D\lambda^2 + E\lambda^4 \qquad (1)$$

where $L = \dfrac{1}{\lambda^2 - C}$ and where λ is expressed in micrometers, μm. The parameters for each glass are given

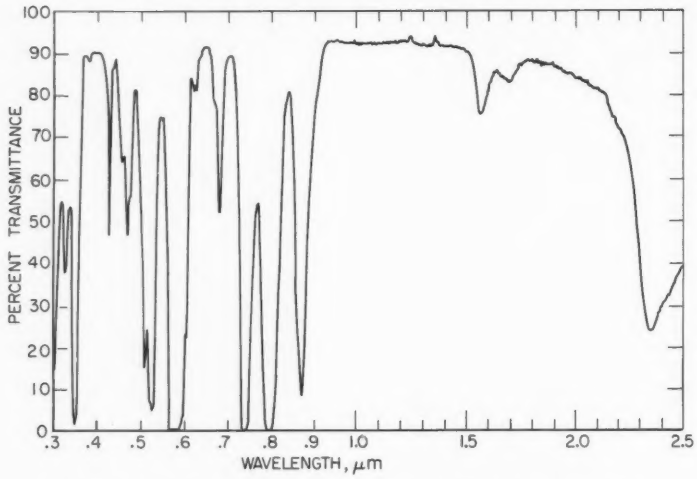

FIGURE 5. *Transmittance curve for laser glass specimen A, 1.882 cm thick.*

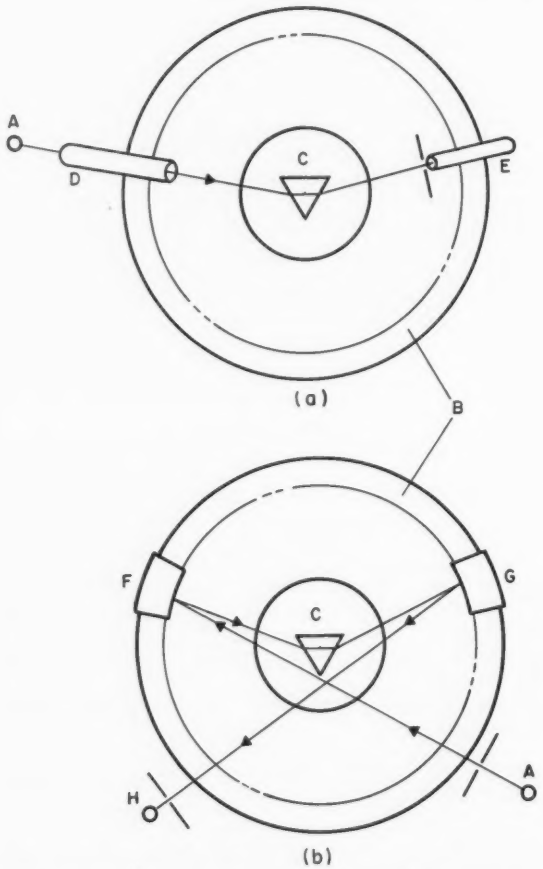

FIGURE 6. (a) *Schematic of spectrometer used for visible-region refractometry. A, source; B, divided circle; C, prism table; D, collimator; E, telescope;* (b) *schematic of spectrometer used for nonvisible-region refractometry. A, source; B, divided circle; C, prism table; F, collimating mirror (fixed): G, movable mirror; H, detector.*

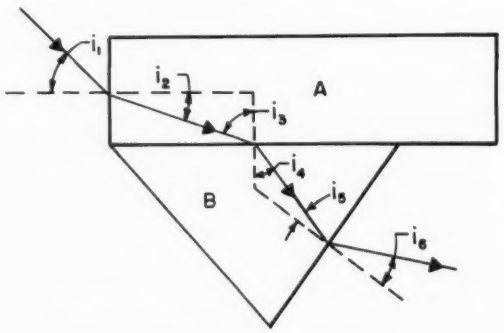

FIGURE 7. *Cuboid-prism combination showing the optical path and angles of refraction. A, Neodymium-doped glass specimen; B, dense flint glass prism.*

in table 1 and were obtained by an iterative process carried out on a time-sharing computer. Each step of iteration consisted of the solving of a set of linear equations.

The original Herzberger equation assigns a fixed value of 0.028 to the parameter C, and consists of five terms which includes a term in L^2. This term in L^2 is also initially included in this modified form, but

TABLE 1. *Parameters of dispersion equations for neodymium-doped laser glasses at 20 °C*

$$n = A + \frac{B}{\lambda^2 - C} + D\lambda^2 + E\lambda^4$$

Parameter	Glass A	Glass B	Glass C	Glass D	Glass E
A	1.507837	1.513668	1.505575	1.509685	1.555067
B	0.003966	0.003812	0.003990	0.003919	0.004406
C	.013919	.017734	.015085	.019009	.012773
D	−.002659	−.005700	−.002919	−.004748	−.002963
E	−.000020	.001510	.000103	.001084	−.000025

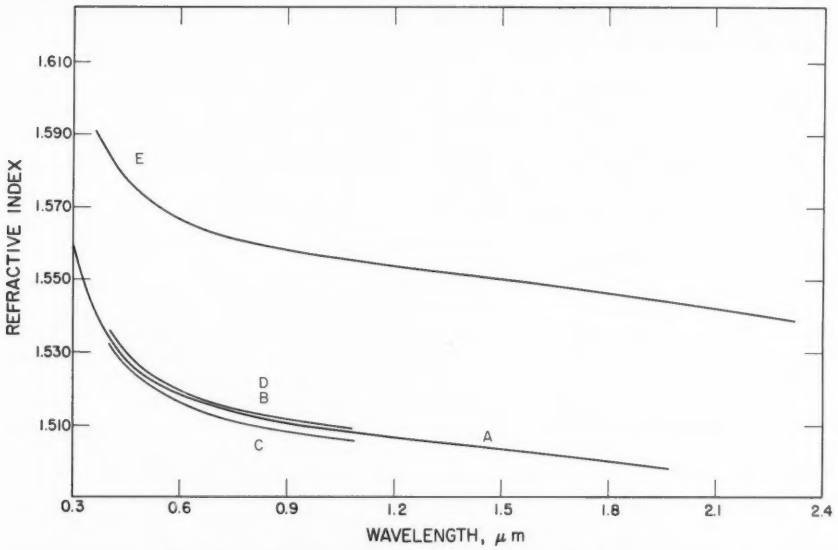

FIGURE 8. *Refractive index of neodymium-doped laser glasses.*

serves only to simplify our adjustment of the parameter C which enters into the formula nonlinearly. The L^2 term drops out of the final equation for relatively small sets of data, as is the case in these experiments, where the wavelength range is primarily over the visible and near-infrared regions of the spectrum.

The average absolute residuals of index for these glasses were from 5 to 10×10^{-6}. The maximum residual, as much as 3×10^{-5}, was obtained at $\lambda = 0.5876$ μm where there is observational uncertainty because of the proximity of this line to a strong absorption band of neodymium. The computed values of index are listed in table 2 and plotted as a function of wavelength in figure 8 (glasses designated B and D are represented by the same curve for sake of clarity). The refractive index at any specific wavelength intermediate to those listed in the table for each glass may be interpolated to five decimal places by means of the dispersion equations.

TABLE 2. *Computed refractive indices of neodymium-doped laser glasses at 20 °C*

Wavelength (μm)	Spectral source	Glass [a] A	Glass [b] B	Glass [b] C	Glass [b] D	Glass [a] E
0.30215	Hg	1.55884	.....	.....	.....	.....
.334148	Hg	1.54811	.....	.....	.....	.....
.340365	Cd	1.54643	.....	.....	.....	.....
.346693	Cd	1.54483	.....	.....	.....	.....
.361248	Cd	1.54150	.....	.....	.....	.....
.365015	Hg	1.54072	.....	.....	.....	1.59125
.404656	Hg	1.53387	1.53888	1.53194	1.53601	1.58376
.435835	Hg	1.52986	1.53479	1.52784	1.53175	1.57937
.467816	Cd	1.52660	.....	1.52452	1.52831	1.57580
.479991	Cd	1.52554	1.53036	1.52344	1.52719	1.57463
.508582	Cd	1.52335	.....	1.52121	1.52488	1.57222
.546074	Hg	1.52099	1.52568	1.51881	1.52240	1.56962
.587561	He	1.51889	1.52354	1.51667	1.52019	1.56729
.643847	Cd	1.51663	1.52116	1.51437	1.51781	1.56480
.667815	He	1.51582	.....	1.51356	1.51696	1.56391
.706519	He	1.51468	1.51912	.....	.....	1.56264
1.01398	Hg	1.50899	.....	1.50662	1.50983	1.55633
1.08297	He	1.50811	1.51235	1.50574	1.50900	1.55536
1.12866	Hg	1.50756	.....	.....	.....	1.55475
1.3622	Hg	.....	.....	.....	.....	1.55187
1.39506	Hg	1.50464	.....	.....	.....	1.55148
1.52952	Hg	1.50321	.....	.....	.....	1.54989
1.6932	Hg	1.50144	.....	.....	.....	1.54791
1.7092	Hg	1.50126	.....	.....	.....	1.54771
1.81307	Hg	1.50009	.....	.....	.....	1.54640
1.97009	Hg	1.49823	.....	.....	.....	1.54433
2.32542	Hg	.....	.....	.....	.....	1.53913

[a] Prism. [b] Cuboid.

5. Thermal Expansion and Thermal Change in Refractive Index

The thermal expansion and the thermal change in refractive index were determined simultaneously by an interferometric method using collimated monochromatic light. The apparatus, described by Saunders [23], records localized Fizeau-type fringes on film. The interferometer assembly is shown in figure 9.

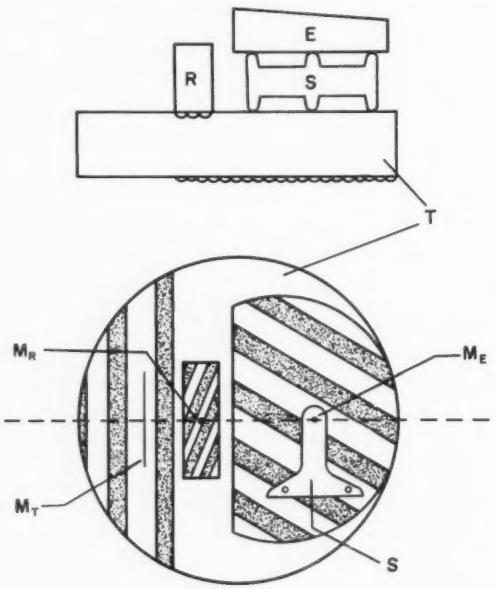

FIGURE 9. *Interferometer assembly for the measurement of thermal expansion and thermal change in refractive index.*

E, an interferometer plate; S, thermal expansion specimen; R, refractive index specimen; T, interference thermometer; M_T, M_R, and M_T, reference lines for the interference fringes of thermal expansion, refractive index change and temperature change.

The set of fringes on the left are obtained between the top and bottom surfaces of the lower fused silica plate, T, and are calibrated in terms of temperature so that they serve as an optical thermometer. The center set of fringes are obtained between the top and bottom surfaces of the index sample, R, and are used to calculate the change in refractive index. Beneath this sample is a frosted area on the lower plate so that no fringes are formed at the interface. The third set of fringes are formed by the slight wedge introduced between the upper plate, E, and the lower plate, T, when they are separated by the expansion sample, S, which is cut from the same material as the index sample, R. These fringes are used to obtain the thermal expansion. The assembly is heated by a vertical tube furnace and the shift in the three sets of fringes are recorded simultaneously on a single strip of 35 mm film as a function of temperature.

The interference pattern generated by the sample of thickness, t, and refractive index, n, is expressed by the equation,

$$N\lambda = 2nt \tag{2}$$

which relates the optical path, nt, and the fringe number, N, when monochromatic light of wavelength, λ, passes twice through the sample at normal incidence. By differentiating with respect to temperature, T, and rearranging, it is found that

$$\frac{\Delta n}{\Delta T} = \frac{\lambda \Delta N}{2t\Delta T} - \frac{n\Delta t}{t\Delta T}. \tag{3}$$

A measurement of the number of fringes that pass a point of reference, and the change in t together with data on the initial index and the temperature interval, permits the calculation of the change in refractive index as a function of temperature [24].

In this experiment, the glass samples were approximately 0.5 cm in thickness. Measurements were made at temperature intervals of about 50 °C using cadmium red radiation, $\lambda = 0.6438$ μm. The recorded fringe shifts from the expansion samples were counted and values of $\Delta t/t$ were calculated. From the recorded fringe shifts of the index samples and the values of $\Delta t/t$, calculations of the values of Δn were made by

TABLE 3. *Increase in length per unit length, Δt/t, as a function of temperature*

Temperature °C	Laser Glasses				
	A	B	C	D	E
0	0.0×10^{-4}	0.0×10^{-4}	0.0×10^{-4}	0.0×10^{-4}	0.0×10^{-4}
10	1.0	1.0	.8	.9	.8
20	1.9	1.9	1.7	1.9	1.6
30	2.9	2.9	2.6	2.9	2.5
40	3.9	4.0	3.5	3.8	3.3
50	4.9	5.0	4.4	4.8	4.2
60	5.9	6.1	5.4	5.8	5.1
70	6.9	7.2	6.4	6.8	6.0
80	7.9	8.3	7.4	7.9	6.9
90	9.0	9.4	8.4	8.9	7.9
100	10.0	10.6	9.4	9.9	8.8
110	11.0	11.8	10.5	11.0	9.8
120	12.1	13.0	11.6	12.1	10.8
130	13.1	14.2	12.7	13.1	11.8
140	14.2	15.4	13.8	14.2	12.8
150	15.2	16.6	14.9	15.3	13.8
160	16.3	17.8	16.0	16.4	14.8
160	17.4	19.1	17.1	17.5	15.9
180	18.4	20.4	18.3	18.6	16.9
190	19.5	21.6	19.4	19.7	18.0
200	20.6	22.9	20.6	20.8	19.0
210	21.6	24.2	21.7	21.9	20.1
220	22.7	25.4	22.9	23.0	21.1
230	23.8	26.7	24.0	24.1	22.2
240	24.9	28.0	25.2	25.2	23.3
250	25.9	29.3	26.3	26.4	24.4
260	27.0	30.6	27.5	27.5	25.5
270	28.1	31.8	28.6	28.6	26.5
280	29.1	33.1	29.7	29.7	27.6
290	30.2	34.4	30.8	30.8	28.7
300	31.3	35.6	32.0	32.0	29.8

TABLE 4. *Change in refractive index, (Δn), as a function of temperature at 0.6438 μm*

Temperature °C	Laser Glasses				
	A	B	C	D	E
0	0.0×10^{-4}	0.0×10^{-4}	0.0×10^{-4}	0.0×10^{-4}	0.0×10^{-4}
10	−.2	−.2	.0	−.5	.3
10	−.4	−.3	.0	−.9	.5
30	−.6	−.5	−.1	−1.3	.8
40	−.8	−.7	−.1	−1.7	1.1
50	−.9	−.8	−.2	−2.0	1.4
60	−1.0	−1.0	−.2	−2.3	1.7
70	−1.1	−1.2	−.3	−2.6	2.0
80	−1.2	−1.3	−.3	−2.8	2.3
90	−1.2	−1.5	−.4	−3.0	2.6
100	−1.3	−1.7	−.5	−3.2	2.9
110	−1.3	−1.9	−.5	−3.4	3.2
120	−1.3	−2.0	−.6	−3.5	3.6
130	−1.2	−2.2	−.6	−3.6	3.9
140	−1.2	−2.4	−.7	−3.7	4.3
150	−1.1	−2.5	−.7	−3.7	4.7
160	−1.1	−2.7	−.8	−3.8	5.0
170	−1.0	−2.8	−.8	−3.8	5.5
180	−.9	−3.0	−.8	−3.8	5.9
190	−.7	−3.1	−.8	−3.7	6.3
200	−.6	−3.3	−.9	−3.7	6.8
210	−.4	−3.4	−.8	−3.6	7.2
220	−.2	−3.6	−.8	−3.6	7.7
230	−.1	−3.7	−.8	−3.5	8.2
240	.1	−3.8	−.7	−3.4	8.8
250	.4	−3.9	−.7	−3.3	9.3
260	.6	−4.0	−.6	−3.1	9.9
270	.8	−4.1	−.5	−3.0	10.5
280	1.1	−4.2	−.3	−2.8	11.1
290	1.4	−4.3	−.2	−2.7	11.7
300	1.6	−4.3	0.0	−2.5	12.4

means of eq (3). The data were fitted by computer to a cubic equation and values of both $\Delta t/t$ and Δn at temperature intervals of 10 °C were obtained. Values of thermal expansion and change in refractive index for the five glasses are given from 0 to 300 °C in tables 3 and 4. Guided by the theory of dispersion for dn/dT in solids [25, 26], it has been assumed that the values of dn/dt are very close at the wavelengths of 0.6438 μm and 1.06 μm, the lasing wavelength of neodymium-doped glasses.

It was estimated that shifts could be measured to one-tenth of an interference fringe. Calculations showed that the sensitivity of measurement of $\Delta t/t$ and Δn were within 0.05×10^{-4} and 0.2×10^{-4}, respectively. The standard deviation for each value of $\Delta t/t$ and Δn was found to be within 0.2×10^{-4}.

6. Photoelastic Constants

When a uniaxial stress is applied to a specimen of glass of refractive index, n, there is a change in refractive index, Δn_1, for polarization along the line of stress and another change, Δn_2, for polarization perpendicular to the stress direction [24]. The two changes are related to the change in stress, ΔP, by the equations,

$$\Delta n_1 = \frac{n^3}{2}[q_{11}]\Delta P \tag{4}$$

and

$$\Delta n_2 = \frac{n^3}{2}[q_{12}]\Delta P, \tag{5}$$

where the q_{ij} are known as the piezo-optic constants. There are corresponding relationships between the state of strain existing in the glass and changes in the refractive index and, in this case, the constants are called the elasto-optic constants, p_{ij}. The p_{ij} are given by

$$p_{11} = C_{11}q_{11} + 2C_{12}q_{12} \tag{6}$$

and

$$p_{12} = C_{11}q_{12} + C_{12}(q_{11} + q_{12}), \tag{7}$$

where the C_{ij} are the elastic constants.

The piezo-optic constants of a neodymium-doped laser glass have been determined from the optical path difference introduced into a specimen by uniaxial stress and the equation,

$$(\Delta n_2 - \Delta n_1) = \frac{n^3}{2}[q_{12} - q_{11}]\Delta P, \tag{8}$$

in combination with the measured change in index from applied hydrostatic pressure, and the equation

$$\Delta n = \frac{n^3}{2}[q_{11} + 2q_{12}]\Delta P. \tag{9}$$

The elasto-optic constants were then evaluated by using eqs (6) and (7). The studies were made using the cadmium red line at 0.6438 μm.

6.1. Hydrostatic Pressure

In this experiment localized interference fringes were observed in a plate of the glass approximately 1 cm × 1 cm × 0.5 cm which had plane, polished, nearly parallel faces. The fringes were viewed in reflection using collimated light at normal incidence. Equation (2) still applies. Application of hydrostatic pressure will cause a shift in the interference fringes, because of the changes induced in n and t. By differentiating eq (2) with respect to pressure and rearranging, it is found that

$$\frac{\Delta n}{\Delta P} = \frac{\Delta N\lambda}{2t\Delta P} - \frac{n\Delta t}{t\Delta P}. \tag{10}$$

A measurement of the number of fringes that pass a point of reference, and the thickness together with data on the initial index and the linear compression, $\Delta t/t$, permits calculation of the change in index [27].

The specimen was immersed in oil in a pressure vessel equipped with glass windows. Hydrostatic pressure was generated by compressing the liquid, and the number of interference fringes passing a fixed ref-

erence mark was determined visually. The specimen was subjected to a maximum pressure of about 1×10^8 N/m^2 and the pressure was measured with a Heise pressure gauge.

6.2. Uniaxial Loading

A specimen in the form of a parallelepiped with dimensions approximately 1 cm × 1 cm × 3 cm was subjected to uniform compression along the long dimension. The specimen was placed in a 45 degree position between crossed polarizers, and the relative retardation introduced between the light rays with electric vectors parallel and perpendicular to the direction of stress was measured with a Babinet-Soliel compensator. The induced birefringence can be related to the induced optical path difference by

$$\frac{(\Delta n_2 - \Delta n_1)}{\Delta P} = \frac{(\Delta N_2 - \Delta N_1)\lambda}{t\Delta P} \tag{11}$$

where ΔN_1 and ΔN_2 are respectively the changes in fringe number parallel and perpendicular to the direction of stress.

A loading frame was used where a yoke with suspended weights brings a piston to bear on the specimen [28]. To insure uniformity of loading, steel caps were machined to fit over the specimen at either end. A small depression was machined in the center of each cap to accommodate a steel ball where the load was applied. Similar depressions were machined at the end of the piston and on the loading frame where the specimen rested. Six calibrated fifty pound weights were used so that the total load was three hundred pounds. The compressive stress on the sample was about 0.13×10^8 N/m^2. Information was also obtained on the effect of wavelength variation upon the stress-induced birefringence. Apparatus which included a continuous light source, a monochromator and a pull rod with a lever arm for exerting stress upon the specimen was employed [29]. In this way data on $(q_{12} - q_{11})$ from 0.300 μm to 1.300 μm were obtained (see fig. 10).

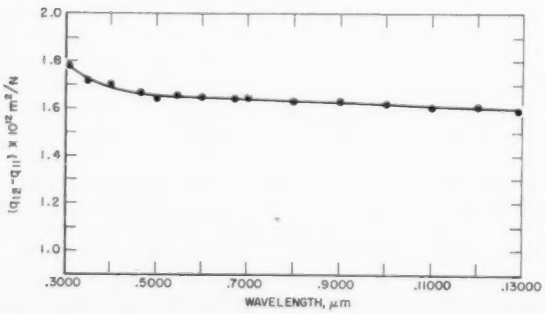

FIGURE 10. *Difference in the piezo-optic constants of laser glass specimen A as a function of wavelength.*

6.3. Results

The q_{ij} and p_{ij} which were evaluated from the data are reported in table 5. The constants obtained for these neodymium-doped laser glasses seem to be in conformity with other reported values for silica-based optical glasses [30]. The relative stress optical coefficient, C, an often used parameter is defined as

$$C = \frac{n^3}{2}(q_{12} - q_{11}).$$

In the experiments involving the relative change in optical path the accuracy is 1 percent or better. In determining the absolute change in optical path with applied hydrostatic pressure, duplicate measurements agreed to within 0.1 interference fringe. However, in this case, the major portion of the path change is due to change in thickness of the specimen which is calculated from the elastic constants (see following section). These latter values are estimated to have an accuracy of ± 2 percent, so the values of the photoelastic constants reported in table 5 can be no better than this.

In figure 10, it can be seen that $(q_{12} - q_{11})$ is nearly constant over an extended wavelength range with a slight rise near the absorption edge. This fact has a bearing upon whether the data measured at 0.6438 μm pertain at the lasing wavelength of 1.060 μm (see sec. 5). There are no data in the literature on the absolute values of the photoelastic constants of any material in this region. It is assumed here that absolute values of the constants at the two wavelengths are very close.

TABLE 5. *The photoelastic constants of neodymium-doped laser glasses*

Glass	q_{11}	q_{12}	p_{11}	p_{12}
	× 10^{12}m^2/N			
A	0.53	2.16	0.134	0.225
B	.54	2.04	.139	.218
C	.58	2.18	.139	.222
D	.78	2.36	.153	.232
E	.12	1.21	.105	.184

7. Elastic Constants

The elastic constants were determined by an ultrasonic pulse-echo technique [31]. Pulses with a frequency of 14 MHz and a duration of 0.5 to 1.0 μs produced by a pulsed oscillator, were passed through an attenuator to a quartz transducer to which the specimen was coupled with resin 276-V9. Signals representing the first transit and subsequent echoes from a second quartz transducer on the opposite end of the specimen were amplified with a wideband amplifier, and transit times were determined by an oscilloscope

with a dual trace unit which also displayed the input pulse.

Elastic moduli were calculated from the following equations:

$$\text{Young's; modulus, } E=\rho V_T^2\left(\frac{3V_L^2-4V_T^2}{V_L^2-V_T^2}\right) \tag{12}$$

$$\text{Shear modulus, } G=\rho V_T^2 \tag{13}$$

$$\text{Bulk modulus, } K=\rho\frac{(3V_L^2-4V_T^2)}{3} \tag{14}$$

$$\text{Poisson's ratio, } \gamma=\frac{V_L^2-2V_T^2}{2(V_L^2-V_T^2)} \tag{15}$$

where V_T=transverse wave velocity, and V_L=longitudinal wave velocity.

The measured values for the five glasses are listed in table 6. These values are estimated to be reproducible to ±2 percent.

TABLE 6. *Elastic Constants of Neodymium-Doped Laser Glasses*

	Glass				
	A	B	C	D	E
Young's Modulus, E	6.81×10^{10}N/m^2	6.58×10^{10}N/m^2	6.41×10^{10}N/m^2	6.15×10^{10}N/m^2	9.08×10^{10}N/m^2
Shear Modulus, G	2.79	2.66	2.61	2.51	3.62
Bulk Modulus, K	4.03	4.16	3.94	3.75	6.14
Poisson's Ratio, γ	0.218	0.236	0.229	0.226	0.255

8. Self-Focusing Induced by Temperature Change and Electrostriction

The measurements of the change of refractive index with temperature and hydrostatic pressure permit the calculation of the temperature-induced change in refractive index at constant volume according to the equation,

$$dn/dT=\left[\rho\left(\frac{\partial n}{\partial\rho}\right)_T\frac{1}{\rho}\left(\frac{d\rho}{dT}\right)+\left(\frac{\partial n}{\partial T}\right)_\rho\right], \tag{16}$$

where ρ represents density. The term, $\frac{1}{\rho}\left(\frac{d\rho}{dT}\right)$, is equal to the negative of the volume coefficient of thermal expansion which, in turn, is equal to three times the linear coefficient of thermal expansion. The parameters, dn/dT and $(\partial n/\partial T)_\rho$, are important in calculating the thermal self-focusing of laser beams [32]. The first part of the laser pulse heats the glass and causes a change in the refractive index. dn/dT is important when there is sufficient time for thermal expansion of the glass to take place. In considering a Q-switched laser pulse which passes before the acoustic relaxation takes place, $(\partial n/\partial T)_\rho$ is the parameter of interest. Data on $\rho\left(\frac{\partial n}{\partial\rho}\right)_T$ are needed to calculate the self-focusing induced by electrostriction [33]. Calculations of $\frac{1}{\rho}\left(\frac{d\rho}{dT}\right)$, $\rho\left(\frac{\partial n}{\partial\rho}\right)_T$, $\frac{dn}{dT}$ and $\left(\frac{\partial n}{\partial T}\right)_\rho$ have been made for the five neodymium-doped laser glasses at 25 °C and the results are presented in table 7.

TABLE 7. *Parameters for calculating self-focusing of laser light in neodymium-doped laser glasses at 0.6438 μm at 25 °C*

	A	B	C	D	E
$\frac{1}{\rho}\left(\frac{d\rho}{dT}\right)\times10^6$	−29.4/°C	−30.1	−26.5	−29.0	−25.2
$\rho\left(\frac{\partial n}{\partial\rho}\right)_T$	0.34	0.34	0.34	0.36	0.30
$\frac{dn}{dT}\times10^6$	−1.8/°C	−1.6	−0.3	−4.0	2.8
$\left(\frac{\partial n}{\partial T}\right)_\rho\times10^6$	8.2/°C	8.6	8.7	6.4	10.3

9. Thermal Conductivity

The thermal conductivity measurements [34] were carried out on a sample cut from specimen E in the apparatus in figure 11. This apparatus utilizes a steady-state longitudinal heat flow method in which the electrically generated heat input to the specimen heater (A) flows perpendicularly from both sides of the heater through the specimens (B) to the cold plates (C). The average thermal conductivity of the two specimens was determined from the measured power to the heater, the measured temperature drops in the two specimens, and the geometry.

Measurements were made between 0 and 100 °C on a section cut from the cylindrical specimen. Since

there appeared to be a discrepancy between the first set of measurements and the values obtained independently in another laboratory, a second set of measurements were made. The largest difference between the measurements at the same point was 1.1 percent, and this was well within the expected error of about 2 percent. A parabola was fitted to the data, and the results for the smoothed thermal conductivity values at 0, 50, and 100 °C are shown in table 8.

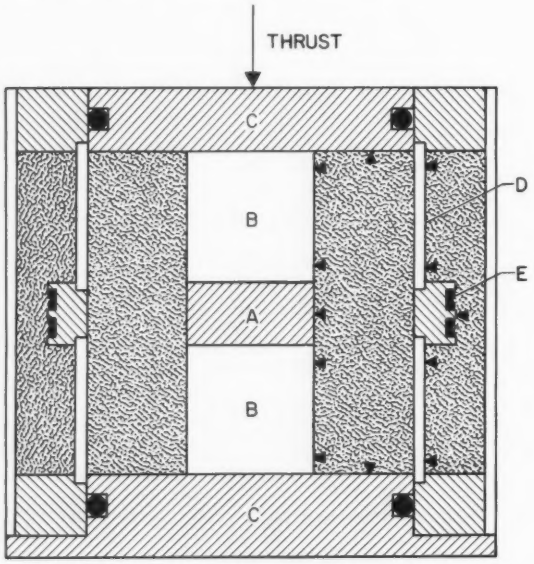

FIGURE 11. *Apparatus for measuring thermal conductivity.*
A, heater; B, specimens; C, cold plates; D, coaxial guard cylinder; E, guard heater.

TABLE 8. *Thermal conductivity of neodymium-doped laser glass, sample E*

Temperature, °C	Thermal conductivity $Wm^{-1}\,°C^{-1}$
0	1.19_7
50	1.29_0
100	1.34_8

10. Knoop Hardness

It is important that laser glasses have sufficient hardness to accept and retain good optical surfaces. The Knoop Hardness values for two of the glass specimens (B and E) were measured with indenting loads of 25, 50, 100, and 200 gram-force. The measuring microscope had a 4.0 mm objective, 0.85 N.A. (numerical aperture), and a 12.5X filar ocular [35]. The hardness tester was a MO Tukon, dash-pot rate at indenter, 0.2 mm/min. The indenter was a Wilson Knoop, No. 2054, with $C_p = 0.7060 \times 10^{-1}$. The Knoop Hardness values were read from a table containing a correction for the Abbe resolution error [35]. The values for the glasses are given in table 9.

TABLE 9. *Knoop hardness values for two neodymium-doped laser glasses*

Glass B

Observation	Indenting Load, gram weight			
	25	50	100	200
1	491	482	457	431
2	476	482	467	438
3	476	482	441	435
4	459	453	457	443
5	466	474	467	426
6	484	474	462	438
7	456	482	458	428
8	466	478	436	440
9	443	465	453	423
10	459	474	430	438
Average	467.6	474.6	452.8	434.0
0.6745 S.D.	3.1	2.0	2.7	1.4

Glass E

Observation	Indenting Load, gram weight			
	25	50	100	200
1	627	545	575	537
2	622	557	564	552
3	622	557	585	550
4	622	454	553	544
5	611	567	569	537
6	587	590	557	543
7	550	567	569	543
8	611	577	540	543
9	611	477	562	543
10	596	590	562	544
Average	605.9	567.2	563.6	543.6
0.6745 S.D.	5.0	3.5	2.6	1.0

Note 1—Indentations were spaced at 0.5 mm intervals for Glass B and at 1 mm intervals for Glass E.
Note 2—S.D. is the standard deviation of the mean.

11. Density

The density of samples from each of the five glasses was determined by the well known buoyancy method [36] using distilled water as the immersion liquid. The values for the five neodymium-doped glasses are given in table 10, where the limit of reproducibility is estimated to be 3 in the fourth decimal place.

TABLE 10. *Density of neodymium-doped laser glasses*

Glass	Density, g/cm³
A	2.6012
B	2.6206
C	2.5935
D	2.5996
E	2.5490

12. Chemical Composition

Chemical analyses were made on samples from each of the five laser glasses. A preliminary general spectrochemical analysis was conducted to determine the elements present. The results are given in table 11. From this table it is seen that all of the glasses are silicates and that Glass A, B, C, and D are mixed alklai glasses. Glass E is different in that it contains a single alkali, lithium.

On the basis of the preliminary spectrochemical analysis, determinations of glass composition with respect to individual elements were made, classing those elements indicated to be at the 0.1 to 1 percent level or higher as major constituents. Table 12 summarizes the pertinent analytical data on the major constituents of the five laser glasses, along with the analytical methods employed in each case. The errors in the values of the major constituents of the glasses are estimated to be no greater than ± 1 in the last significant figure. The trace amounts of Fe_2O_3 found in the glasses are reported in this table because the absorption in the vicinity of the lasing wavelength is usually attributed to the Fe_2O_3 content. These values are believed to have a relative precision of ± 20 percent.

Neutron activation analyses were also made on a sample of each of the glasses, primarily to determine trace impurities, but also as a check on other methods. The results obtained are given in table 13. Here, again, the errors in the values of the major constituents are

TABLE 11. *Spectrochemical analyses of neodymium-doped laser glasses, weight percent*

Element	Glass A	Glass B	Glass C	Glass D	Glass E
Ag	–	–	–	–	–
Al	1–10	1–10	0.1–1	0.1–1	1–10
As	–	–	–	–	–
Au	–	–	–	–	–
B	–	–	<.001	<.001	<.001
Ba	1–10	1–10	1–10	1–10	0.001–0.01
Be	–	–	–	–	–
Bi	–	–	–	–	–
Ca	0.01–0.1	0.01–0.1	0.01–0.1	0.01–0.1	1–10
Cd	–	–	–	–	–
Ce	–	–	–	–	–
Co	–	–	–	–	–
Cr	–	–	–	–	–
Cs	?	?	–	–	–
Cu	<.001	<.001	<.001	<.001	–
Fe	.001–.01	.001–.01	.001–.01	.001–.01	.001–.01
Ga	–	–	–	–	–?
Ge	–	–	–	–	–
Hf	–	–	–	–	–
Hg	–	–	–	–	–
In	–	–	–	–	–
K	1–10	1–10	1–10	1–10	<.001
La	–	–	–	–	–
Li	.1–1	.1–1	<.001	<.001	1–10
Mg	<.001	<.001	<.001	<.001	<.001
Mn	–	–	–?	–?	–?
Mo	–	–	–	–?	–
Na	1–10	1–10	1–10	1–10	.01–.1
Nb	–	–	–	–	–
Nd	1–10	1–10	1–10	1–10	1–10
Ni	–	–	–	–	–
Os	–	–	–	–	–
Pb	–	–	1–10	1–10	–
Pt	–	–	–	–	–
Rb	.001–.01	.001–.01	.001–.01	.001–.01	–
Sb	.1–1	.1–1	.1–1	1–10	–
Si	>10	>10	>10	>10	>10
Sr	–	–	–	–	–?
Ta	–	–	–	–	–
Th	–	–	–	–	–
Ti	.1–1	.1–1	.1–1	.1–1	–
U	–	–	–	–	–
V	–	–	–	–	–
W	–	–	–	–	–
Zn	–	–	–	–	–
Zr	–	–	–	–	–

TABLE 12. *Major constituents of neodymium-doped laser glasses, weight percent*

Oxide	Glass A	Glass B	Glass C	Glass D	Glass E	Method
SiO_2	66.6	61.3	67.8	66.3	66.1	Gravimetric
Li_2O	1.0	1.0			14.5	Flame Emission Spectrometry
Na_2O	6.7	6.2	7.9	3.4		Flame Emission Spectrometry
K_2O	10.0	17.2	13.8	18.2		Flame Emission Spectrometry
CaO					10.1	Flame Emission Spectrometry
BaO	5.5	3.0	3.3	3.5		Flame Emission Spectrometry
PbO			1.1	1.8		Atomic Absorption Spectrometry
ZnO	1.6	1.8				Atomic Absorption Spectrometry
Al_2O_3	1.8	1.9			4.4	Flame Emission Spectrometry
Nd_2O_3	5.4	5.8	5.5	3.5	3.4	Spectrophotometry
Sb_2O_3	0.8	0.8	.9	3.2		Atomic Absorption
CeO_2					0.5	Neutron Activation
Fe_2O_3	0.011	0.010	0.0070	0.0090	0.0055	Spectrophotometry
TiO_2			0.19	0.39		Spectrophotometry
	99.4	99.0	100.3	99.9	99.0	

TABLE 13. *Neutron activation analyses of neodymium-doped laser glasses, weight percent*

Oxide	Glass A	Glass B	Glass C	Glass D	Glass E
Na_2O,	6.85	6.39	7.83	3.19	0.044
K_2O	9.21	17.1	13.8	16.6	< 0.04
Sb_2O_3	0.90	0.93	0.86	2.54	0.0015
Nd_2O_3	5.52	5.73	5.84	3.53	3.52
BaO	5.06	2.83	3.27	3.46	< 0.3
CeO_2	< 0.006	< 0.006	< 0.005	< 0.006	0.52
			Parts per million		
La_2O_3,	< 0.9	7.8	10.2	17.8	< 0.8
Pr_2O_3	< 3	8.4	< 3	< 3	< 2
Eu_2O_3	29.7	1.1	0.6	≤ 0.1	< 0.5
Sm_2O_3	0.37	2.2	0.2	0.2	0.03

estimated to be no greater than ±1 in the last significant figure. For the amounts reported in parts per million, the standard deviation is estimated to be about ±5 percent in most cases. For the lower reported values of Sm there is severe interference from Nd and these values are probably no better than ±20 percent. For the lower reported values for Eu and Ce the signal-to-background ratio was poor and these values also are probably no better than ±20 percent. All results are reported as the oxide rather than the element to facilitate comparison with results from other methods.

13. Summary

As an aid in laser design, measurements have been made on important physical and chemical properties of five commercially available, neodymium-doped laser glasses. The measurements include thermo-optic properties, photoelasticity, refractive index, optical homogeneity, transmittance, thermal conductivity, hardness, density, and chemical composition. Calculations have been made of the thermal change in refractive index at constant volume, because this parameter is important in the study of self-focusing of laser light.

The combined facilities of the Inorganic Materials, Optical Physics, Polymers, Building Research, Mechanics and Chemistry Divisions within the National Bureau of Standards were utilized for making the measurements and compiling the data included in this report. The authors acknowledge the contribution of colleagues as follows: F. W. Rosberry for measurements of homogeneity, G. Dickson for determining the elastic constants, A. Feldman and D. Horowitz for determining the wavelength variation of the stress-induced birefringence, D. Flynn and W. L. Carroll for measurements of thermal conductivity, E. G. Hawkins for density measurements and D. R. Tate for determining the Knoop hardness. In addition, the workers who collaborated in making the chemical analyses were B. A. Thompson, B. B. Bendigo, T. A. Rush, T. C. Rains, E. R. Deardorff, and V. C. Stewart.

14. References

[1] Quelle, F. W., Jr., Appl. Optics **5,** 633 (1966).
[2] Blume, A. E., and Tittel, K. F., Appl. Optics **3,** 527 (1964).
[3] Sims, S. D., Stein, A., and Roth, C., Appl. Optics **5,** 621 (1966).
[4] Sims, S. D., Stein, A., and Roth, C., Appl. Optics **6,** 579 (1967).
[5] Epstein, S., J. Appl. Phys. **38,** 2715 (1967).
[6] Baldwin, G. D., and Riedel, E. P., J. Appl. Phys. **38,** 2726 (1967).
[7] Dishington, D. H., Hook, W. R., and Hilberg, R. P., Proc. IEEE **55,** 2038 (1967).
[8] Welling, H., and Bickart, C., J. Opt. Soc. Amer. **56,** 611 (1966).
[9] Guiliano, C. R., Appl. Phys. Letters **5,** 137 (1964).
[10] Chiao, R. Y., Townes, C. H., and Stoichéff, B. P., Phys. Rev. Letters **12,** 592 (1964).
[11] Olness, D., J. Appl. Phys. **39,** 6 (1968).
[12] Davit, J., J. Appl. Phys. **39,** 6052 (1968).
[13] Thornton, J. R., Fountain, W. D., Flint, G. W., Crow, T. G., Appl. Optics **8,** 1087 (1969).
[14] Snitzer, E., Appl. Optics **5,** 1487 (1966).
[15] Military Specification, Glass, Optical, MIL-G-174A, 5 Nov. 1963.
[16] Rosberry, F. W., Appl. Optics **5,** 961 (1966).
[17] Rogers, A. F., and Kerr, P. F., Optical Mineralogy (McGraw-Hill Book Co., Inc., New York and London, 1942).
[18] Weir, C., Spinner, S., Malitson, I. H., Rodney, W., J. Res. Nat. Bur. Stand. (U.S.), **58,** 189–194 (April 1957) RP2751.
[19] Rodney, W. S., and Spindler, R. J., J. Res. Nat. Bur. Stand. (U.S.), **53,** 185–189 (Sept. 1954) RP2531.
[20] Tilton, L. W., J. Res. Nat. Bur. Stand. (U.S.), **2,** 909–930 (1929) RP64.
[21] Dodge, M. J., Malitson, I. H., and Mahan, A. I., Appl. Opt. **8,** 1703 (1969).
[22] Private communication. L. E. Sutton, Institute of Basic Standards, National Bureau of Standards, Washington, D.C.
[23] Saunders, J. B., J. Res. Nat. Bur. Stand. (U.S.), **35,** 157–218 (Sept. 1945) RP 1668.
[24] Krishnan, R. S. Progress in Crystal Physics, Vol. **I** (Interscience Publishers, New York and London, 1958).
[25] Ramachandran, G. N., Proc. Ind. Acad. Sci. [A] **25,** 498 (1947).
[26] Ramachandran, G. N., Proc. Ind. Acad. Sci. [A] **25,** 286 (1947).
[27] Waxler, R. M., and Weir, C. E., J. Res. Nat. Bur. Stand. (U.S.), **69A,** (Phys. and Chem.), No. 4, 325–333 (July–Aug. 1965).
[28] Waxler, R. M., and Napolitano, A., J. Res. Nat. Bur. Stand. (U.S.), **59,** 121–125 (Aug. 1957) RP 2779.
[29] Feldman, A., Phys. Rev. **150,** 748 (1966).
[30] Vedam, K., Proc. Ind. Acad. Sci. [A] **31,** 450 (1950).
[31] Dickson, G., and Oglesby, P. L., J. Dent. Res. **46,** [6] Part 2, 1475 (1967).
[32] Quelle, F. W., Damage in Laser Glass, ASTM STP 469 (American Society for Testing and Materials, 1969) pp. 110–116.
[33] Kerr, E. L., IEEE J. Quantum Electronics **QE-6,** 616 (1970).
[34] Wachtman, J. B., Jr., Mechanical and Thermal Properties of Ceramics, Nat. Bur. Stand. (U.S.), Spec. Publ. 303, 272 pages (May 1969).
[35] Brock, T. W., Draft of Tentative Method of Test for Knoop Indentation Hardness of Glass. Being considered for approval as an ASTM method by ASTM Committee C14.04.
[36] Glaze, F. W., Young, J. C., and Finn, A. N., J. Res. Nat. Bur. Stand. (U.S.), **9,** 799–805 (1932) RP 507.

(Paper 75A3–660)

JOURNAL OF RESEARCH of the National Bureau of Standards—A. Physics and Chemistry
Vol. 75A, No. 3, May–June 1971

Effect of Environment on Viscous Flow in Inorganic Oxide Glasses

Joseph H. Simmons and Pedro B. Macedo*

Institute for Materials Research, National Bureau of Standards, Washington, D.C. 20234

(February 9, 1971)

Results from viscosity and shear structural relaxation measurements conducted above the liquid-liquid phase transition of a series of immiscible inorganic oxide glasses are analyzed. A model is proposed which relates the temperature dependence of the complex modulus and viscosity to the behavior of microstructure in the glass resulting from supercritical fluctuations in composition. It is suggested that the critical microstructure induces differences in local environment in the glass which in turn cause the appearance of distributions of relaxation times. The model is formulated using elementary fluctuation theory and the resulting equations are successfully compared to the data.

Key words: Critical point theories; immiscibility; phase transitions; structural relaxation; transport phenomena; viscous flow.

1. Introduction

The investigation of viscous flow in glass-forming liquids has been approached from a variety of directions. These can be classified into the empirical equation of Fulcher [1],[1] the thermodynamic approaches of Gibbs [2], Turnbull and Cohen [3], and Goldstein [4], and the kinetic approaches recently characterized by consideration of the structural relaxation mechanisms [5–7]. In the case of inorganic oxide glasses, the investigations of structural relaxation have been undertaken by means of ultrasonic spectroscopy. Recently, ultrasonic [8] and viscosity [9] measurements on vitreous B_2O_3 have yielded evidence conflicting with the predictions of the thermodynamic approaches, and thus have indicated the need for systematic studies of viscous flow by structural relaxation in such glass-formers [9]. Before examining this evidence, let us first introduce the concept of a distribution of relaxation times.

Viscous relaxation investigations by means of ultrasonic spectroscopy consist of studying the interaction of high frequency sound waves with matter as a function of the time of interaction. As the observation time, which is the inverse of the ultrasonic frequency, approaches the structural relaxation time, interaction between the flowing, or moving species and the sound waves leads to a frequency-dependent complex modulus. The frequency-dependent shear viscosity is given by the imaginary part of the shear modulus, $G^*(\omega)$ as follows [10]:

$$\eta'(\omega) = \omega^{-1} \operatorname{Im} [G^*(\omega)] \tag{1}$$

where ω is the angular frequency. The frequency-dependent modulus may in turn be expressed in terms of a sum of relaxation functions. This implies that the stresses are additive. In the case of liquids having simple distributions of relaxation times, such as those in this paper, the relaxation phenomena may be characterized in terms of two independent parameters which are the width and the most probable value of time of any existing distribution of relaxation times. While the choice of additive stresses appears arbitrary at first, we will show later that it is consistent with the physical interpretation of our model. The viscosity is now written as follows:

$$\eta'(\omega) = G_\infty \int_{-\infty}^{\infty} \frac{\tau}{1 + (\omega\tau)^2} g(\ln \tau) d \ln \tau \tag{2}$$

where G_∞ is the instantaneous shear modulus, τ is a relaxation time, and $g(\ln \tau)$ is known as the distribution of relaxation times. The "static" viscosity, η_s, is the zero-frequency limit of $\eta'(\omega)$,

$$\eta_s = G_\infty \int_{-\infty}^{\infty} \tau g(\ln \tau) d \ln \tau. \tag{3}$$

The instantaneous shear modulus and the distribution of relaxation times can be investigated by shear ultra-

*Also at the Vitreous State Laboratory, Catholic University of America, Washington, D.C. 20017.

[1] Figures in brackets indicate the literature references at the end of this paper.

sonic spectroscopy provided the material is fluid enough to relax in a time scale comparable to the period of the ultrasonic waves, and one is equipped with instruments sensitive enough to detect the highly damped shear waves.

The evidence conflicting with the thermodynamic approaches first came from ultrasonic measurements [8]. Log-Gaussian distributions of relaxation times were found to represent the data well for vitreous B_2O_3. At high temperatures, when the static viscosity followed an Arrhenian behavior, it was seen that attributing a single relaxation time to the flow units was sufficient to account for the frequency dependence of the modulus. As the temperature was reduced, however, the shear viscosity departed from the Arrhenius curve, and a broadening distribution of relaxation times was required to fit the data. It was seen that the broadening occurred concurrently with the departure of the viscosity from Arrhenian behavior. Use of the Eyring Rate-Equation led to an analysis of the distribution of activation energies. The latter was found to be Gaussian and to broaden with decreasing temperature as did the distribution of relaxation times. The mean activation energy, however, did not change with temperature over the range of measurements. In conclusion, contrary to the assumption implicit in most phenomenological equations of the thermodynamic approaches, the non-Arrhenian behavior of the viscosity was not associated with an increase in the average activation energy with decreasing temperature, but rather with the appearance of a distribution of energies; some indeed higher, but others lower than the average. These lower activation energies could not be explained within the framework of existing viscosity theories.

Further support for these conclusions came from measurements of the viscosity of B_2O_3 in the range 10^{10} to 10^{14} P [9], in which the viscosity appeared to revert to Arrhenian behavior at low temperatures. The authors could find no reasonable fits of this extended data by any of the viscosity theories, as the parameter $[\partial \ln \eta_s/\partial(1/T)] = E_{app}$ representing an apparent activation energy, approached a temperature-independent behavior near T_g, while all existing theories predicted a continued increase with decreasing temperature. In this case, a temperature-independent apparent activation energy implies Arrhenian viscosity behavior. They thus concluded that the temperature dependence of the viscosity was not controlled by structural effects, such as free volume, and configurational entropy, but rather by some activation energy effects, represented by $[\partial \ln \eta_s/\partial(1/T)]$. A successful theory would have to lead to a constant parameter $[\partial \ln \eta_s/\partial(1/T)]$, or activation energy spectrum near T_g. It became apparent that a microscopic model was needed which could explain the appearance of a symmetric distribution of activation energies, and give physical significance to both the distribution of relaxation times and the temperature dependence of the viscosity.

In analyzing the origin of a spectrum of relaxation times, one cannot differentiate between the occurrence of the same nonexponential relaxation for all flow units, and the weighted sum of varying but exponential relaxation effects caused by a varying environment [11]. This problem was considered in the analysis of annealing experiments on several inorganic glasses [12, 13]. In the case of a borosilicate crown glass [12] both volume relaxation and ionic conduction were measured. Of the various models present in the literature, only a modified version of Fröhlich's model [14] attributing the existence of a distribution of activation energies to a distribution of environments, could fit both sets of data consistently. In these measurements, it was found that if the distribution were represented by two relaxation times, the fast volume relaxation could be related to the fast electrical conductivity relaxation. The results implied that there are definite regions in these materials which are associated with the different relaxations.

The connection between a distribution of activation energies and a distribution of environments was postulated long ago by Fröhlich, but until recently, due to a lack of sufficiently detailed electron micrographs and high temperature x-ray instrumentation, no structure was observed in molten oxide glasses with known distributions of relaxation times. The model presented in the annealing investigations ruled out the possibility of nonexponential decays, but only indicated the possibility of applying some environmental model to the analysis of structural relaxation in inorganic oxide glasses. The problem in interpreting ultrasonic and other relaxation experiments arises from the fact that a distribution of relaxation times does not necessarily indicate any particular molecular relaxation process. As Goldstein [11] clearly suggested, calculation of a distribution of relaxation times in the analysis of a response function is only a mathematical transform and cannot carry physical significance by itself. One must first begin with a model for the molecular mechanisms for structural relaxation and then derive a resulting set or distribution of relaxation times. For this reason, we have chosen to investigate the viscous relaxation process in a series of inorganic oxide glasses with predictable distributions of environments and to attempt to analyze the results in terms of the related microstructure.

Microstructure in molten oxides can best be controlled by selective doping, or by approaching the critical point of an immiscible system. Since x-ray data or electron micrographs describing the structure of normal glasses are lacking, immiscible systems offer the best solution due to the possibility of specifying the temperature dependence of the structure from analysis of the supercritical composition fluctuations.

The immiscibility phase transition is quite widespread in oxide glasses. Liquid-liquid phase separations occur in such systems by changes in composition associated with phases of widely different viscosities. Phase separation at the concentration which has the highest transition temperature, T_c (top of the immiscibility dome), occurs by means of a pseudo second-order phase transition which is characterized by the continuity of the free energy and its first derivatives

across the transition boundary. As a consequence, the thermodynamically unstable fluctuations which lead to demixing below T_c, do not end abruptly when one raises the temperature to the critical point. These fluctuations in fact extend far into the supercritical ($T > T_c$) region, where they are thermodynamically metastable, with associated well defined wavelengths and lifetimes. The resulting transient domains have some structural relationship to the subcritical immiscible phases, and thus are characterized by large viscosity differences.

These supercritical composition fluctuations drastically change the environment of the flow species as the temperature is varied. Consequently, the presence of these fluctuations in composition is expected to have large effects on the viscous flow processes of the materials. Recently, light scattering and x-ray diffraction experiments have observed such fluctuations above the critical point [15, 16]. The effect is usually referred to as critical opalescence.

Theoretical analyses first derived to describe gas-liquid critical point phenomena, were applied to liquid-liquid phase transitions by replacing density fluctuations with fluctuations in composition [15].

Equations are thus available to describe the wavelengths, Λ, and lifetimes, τ_f, of the existent fluctuations as a function of temperature for $T > T_c$. The wavelength, or range of fluctuations varies from very small values far from the critical point, to macroscopic extent near T_c. The range of fluctuations, $\Lambda(T/T_c)$, is expressed as:

$$\Lambda = l/(T/T_c - 1)^{1/2}. \tag{4}$$

The classical exponent of ½ is shown here, but there has been strong evidence that a larger value such as 0.6 may be more appropriate for some liquids. Such a small difference has little effect on our model, so we will follow the classical equation. The parameter l is a constant of the material, and has been shown to vary little among liquid-liquid nonpolymeric systems (see table 4 of ref. [17]). Taking the average value of 11 Å, which also coincides with results from low angle x-ray scattering measurements on $PbO\text{-}B_2O_3\text{-}Al_2O_3$, we may plot the most probable fluctuation wavelength as a function of reduced temperature in figure 1, and thus predict the size of the microstructure present in such critical systems above the solution temperature. It is now possible to investigate the effect of environmental microstructure on viscous flow by conducting structural relaxation measurements above the critical point of some immiscible oxide mixtures, and analyzing the resulting parameters in terms of reduced temperatures.

We have recently reported results from an experimental investigation of the behavior of the viscosity [18] and the frequency-dependent modulus [19] above the critical temperature of a series of immiscible oxide glasses. We will review, here, the salient features of these results and then proceed to analyze the observed supercritical effects in terms of a proposed mechanism for the interaction between the viscous flow process and the supercritical fluctuations in composition.

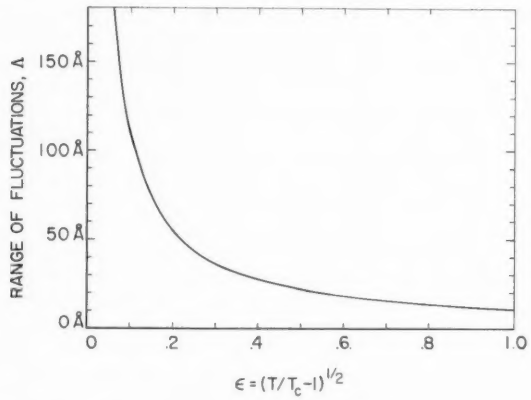

FIGURE 1. *Fluctuation wavelength, Λ, plotted as a function of reduced temperature for $l = 11$ Å.*

2. Results from Viscous Relaxation Measurements on Critical Oxides

The samples chosen for this study are four sodium-borosilicate oxides with similar high-temperature structures but widely varying critical temperatures. These characteristics were chosen to allow separation of effects due to the presence of supercritical composition fluctuations from the noncritical material behavior. Sample 1, with a composition of 70.5 percent SiO_2, 22.7 percent B_2O_3, and 6.8 percent Na_2O by mole is the critical composition (top of the dome) of its system [20], and has a critical temperature of 752 °C. Samples 2, 3, and 4 were made by adding 2.1 mol percent CaO; 1.8 mol percent Al_2O_3; and 1.05 mol percent CaO + 0.9 mol percent Al_2O_3 respectively to the concentrations of sample 1. Samples 2, 3, and 4 have resulting transition temperatures of 830, 643, and 741 °C respectively. These samples clearly provide many advantages. First, the viscosities of the separated phases differ by several orders of magnitude, so that the composition fluctuations can be expected to induce effects of large magnitude on the shear viscous relaxation parameters. Then, the critical temperatures of the samples occur at such high viscosities as to allow investigation of the distribution of shear relaxation times by ultrasonic relaxation spectroscopy.

The shear viscosity was measured by a rotation viscometer [21]. The results [18] were found to vary somewhat, between the samples, at high temperatures, reflecting the effect of doping (log viscosities of 2.41, 2.32, 2.71, and 2.46 at 1300 °C for samples 1, 2, 3, and 4 respectively). The viscosity curves were therefore normalized by the values at 1300 °C, in order to study only the critical point effects. This normalized viscosity:

$$\eta^*(T) \equiv \eta_s(T)/\eta_s(1300\ °C) \tag{5}$$

was calculated for each sample, and is plotted against temperature in figure 2. It is evident from the figure

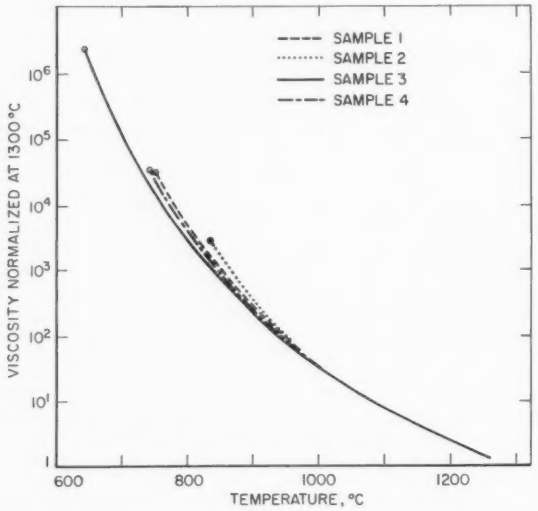

FIGURE 2. *Viscosity normalized by value at 1300 °C for the 4 samples.*
The critical point of each sample is denoted by a circle on the appropriate viscosity curve.

that each curve departs from the curve of sample 3 as the respective critical points are approached from above. This indicates that the growing microstructure in the samples has a definite interaction with the viscous flow process. Further analysis of this excess viscosity was made possible by assuming that the noncritical viscosity behavior could be represented by the values of sample 3 since this sample had a critical temperature lower than the others (samples 1, 2, and 4) by 106, 187, and 98 °C respectively. A normalized excess viscosity was then defined as follows:

$$\Delta\Phi(T) \equiv \Delta\eta^*(T)/\eta_0^*(T) = [\eta^*(T) - \eta_0^*(T)]/\eta_0^*(T) \tag{6}$$

where the noncritical viscosity, $\eta_0^*(T)$, is represented by the viscosity of sample 3. The normalized excess viscosity is shown in figure (3) plotted against reduced temperature: $(T/T_c - 1)^{1/2}$. It is seen that when the excess viscosity $\Delta\eta^*(T)$ is normalized by the noncritical viscosity, $\eta_0^*(T)$, the result, $\Delta\Phi(T)$, has the same reduced-temperature behavior for all samples. The supercritical excess viscosity reached a value of twice the noncritical viscosity ($\Delta\eta^* \approx 2\eta_0^*$) near the transition temperature, but it should be noticed that there are no indications of a divergence down to $T/T_c \approx 1.0009$.

Ultrasonic relaxation measurements were also conducted on the same series of glasses to investigate the distributions of relaxation times, and the parameters which control the viscous flow [19]. The measurements showed that the isothermal frequency dependence of the moduli could be best represented

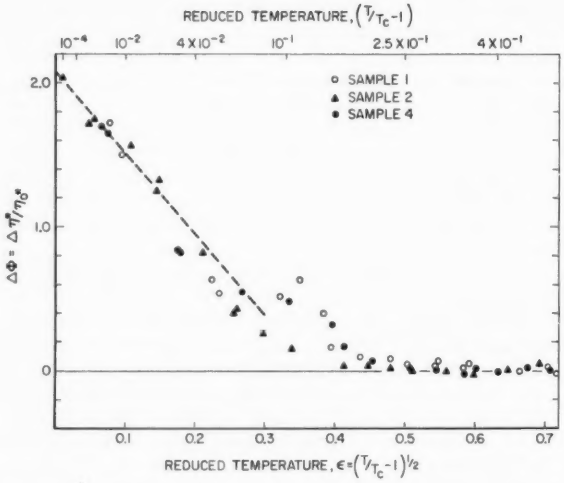

FIGURE 3. *Normalized excess viscosity plotted as a function of reduced temperature.*
The solid horizontal line represents sample 3.

by log-Gaussian distributions of relaxation times down to temperatures close to $T_c(T/T_c \approx 1.0045)$.

Substitution of the structural relaxation distributions so determined into the equation calculating static viscosity, eq (3), yields values within 10 percent of the measured static viscosity. Since this is within the experimental accuracy of the ultrasonic results, we concluded that no additional relaxation process occurring at frequencies lower than the structural relaxation was present in the frequency-dependent description of the shear modulus and viscosity. Such a low frequency process (mode-mode coupling) has been proposed [22] to account for the supercritical excess viscosity and is seen to be inapplicable to the systems studied herein. Therefore, the entire critical-point effect on the shear flow mechanism is contained in the structural relaxation processes rather than in some separate interaction process such as proposed [22] by the mode-mode coupling models. We have shown however, in a separate publication [23], that a low frequency process similar to the mode-mode coupling occurs in the *volume* relaxation mechanism of sample 1.

In order to further investigate the effect of the static microstructure on the relaxation and viscous processes we must consider the relationship between the viscosity and the parameters obtained in the ultrasonic spectroscopy. Since the structural distribution of relaxation times [$g(\ln\tau)$ in eq 2] was found to be log-Gaussian, the static viscosity may be written as:

$$\eta_s(0) = \lim_{\omega\to 0}\left\{G_\infty \int_{-\infty}^{\infty}\left(\frac{\tau}{1+(\omega\tau)^2}\frac{d\ln\tau}{(2\pi\Theta)^{1/2}}\exp\right.\right.$$
$$\left.\left.[-ln^2\,(\tau/\tau')/(2\Theta)]\right)\right\} \tag{7}$$
$$= G_\infty\bar{\tau} = G_\infty\tau'\exp(\Theta/2)$$

where $\bar{\tau}$ is the average and τ' the most probable relaxation times, and Θ is the width or variance $[\Theta \equiv < (\Delta \ln \tau)^2 >]$ of the distribution.

Further analysis of the ultrasonic data yielded the behavior of the three parameters which control the shear viscosity. These are the instantaneous shear modulus, G_∞ the most probable relaxation time, τ', and the width of the distribution of relaxation times, Θ, as per eq (7). The first two parameters, G_∞ and τ', did not appear to be subject to critical point effects and thus seem to be independent of the change in size of the microstructure as T_c is approached. It was found, however, that the width of the distribution of relaxation times was greatly affected by the approach of the transition temperature, and thus by the changing microstructure. As shown in figure 4, the samples have narrow distributions at high temperatures where the fluctuations are small. The distributions then broaden drastically as the temperature is lowered to the phase transition. Finally, the broadening saturates as the width appears to approach a finite value close to T_c, where the fluctuations have grown to macroscopic sizes. The large increase in the width is related to the viscosity anomaly and represents some interaction between the composition fluctuations and the shear viscous relaxation process. The saturation of this broadening very close to T_c indicates that the interaction is weakening when T_c is approached and the fluctuation wavelengths are large.

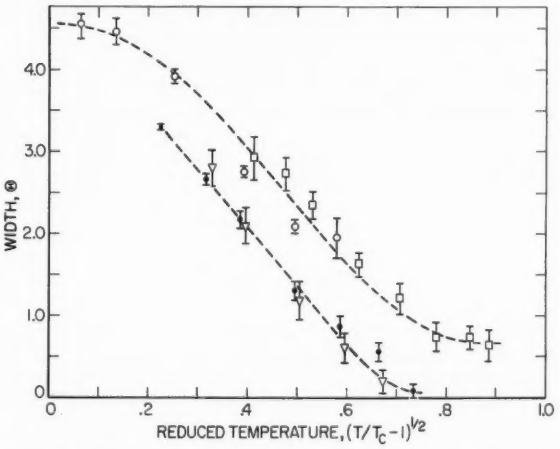

FIGURE 4. *Width of the distribution of relaxation times for sample 1 (solid circles), sample 2 (open circles), sample 3 (squares), and sample 4 (triangles) as a function of reduced temperature.*
The curves were drawn to emphasize the general behavior of the materials.

3. Analysis of the Environmental Relaxation Model

3.1. Development of the Model

In this discussion of the model we will be concerned with presenting physical arguments followed by a mathematical formulation of the behavior of the distributions of relaxation times and activation energies in terms of the appearance and growth of local microstructure in the melt. These distributions, therefore, will be related to a distribution of the molecular environments. The latter is then to be estimated in terms of the supercritical probability for the occurrence of composition fluctuations in a local region defined in the model by the range of forces controlling structural relaxation of the flow units.

The results from the supercritical, shear relaxation experiments indicate that while the distribution of relaxation times is narrow at high temperatures, a large broadening occurs as the critical point is approached from above. Figure 4 shows that all four curves follow the same general behavior within the range of measurements, despite the vastly different critical temperatures of the oxide mixtures, when the width is analyzed in terms of the reduced temperature.

Recent analysis of measurements of the volume structural relaxation properties [23] of sample 1 resulted in the determination of the average concentration fluctuation lifetime, $\bar{\tau}_f$, whose magnitude is compared in figure 5 with the most probable volume, τ'_v, and shear, τ'_s, relaxation times. While τ'_v approaches the concentration fluctuation lifetimes at high temperatures, the shear distribution centered at τ'_s is always shorter than $\bar{\tau}_f$. The shear structural relaxation process, therefore, occurs in an apparently static environment, and the composition fluctuations only interact with the

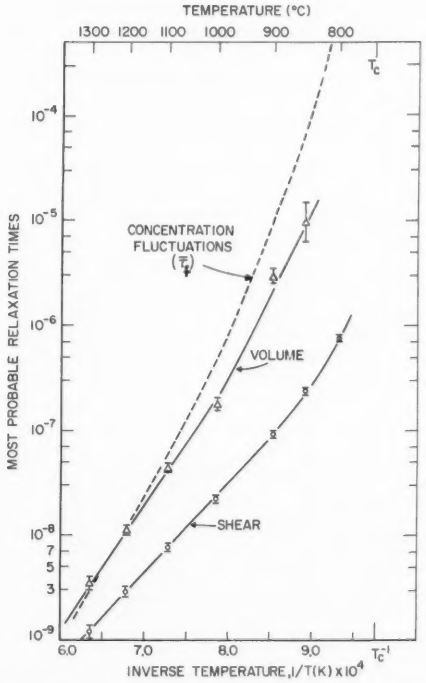

FIGURE 5. *Average concentration fluctuation lifetime compared to the most probable volume and shear relaxation times (Reprinted from Ref. [23]).*

shear flow process through the resulting temperature-dependent distribution of local environments.

A molecule rearranges its position to respond to a stress in a manner which is strongly dependent upon its environment. The large increase in the width of the distribution of relaxation times therefore could be related to the change in the local configuration of the material resulting from the supercritical fluctuations in composition. Furthermore, the broadening in the distribution of relaxation times then would result from the change in the distribution of local environments. Since it has been demonstrated that there is no direct mode-mode coupling between the shear relaxation mechanisms and the fluctuations in concentration, the flow process does not exchange energy with the fluctuations and only samples the presence of the resulting microstructure. The problem therefore reduces to the analysis of structural relaxation occurring in a temperature-dependent but quasi-static environment, because the concentration fluctuation times are longer than the shear structural relaxation times at all temperatures.

Assuming a direct relationship between distributions of environments and relaxation times, we may analyze the effect of the critical microstructure. A system will exhibit a single relaxation time if all its molecules or flowing species have equivalent neighborhoods. As a number of different configurations become available to the molecules, the relaxation process will vary spatially, and a distribution of times will appear which broadens as either the number of configurations or the variation of relaxation times among the neighborhoods increases. It is clear from our results that these two types of behavior are evident in our distribution of relaxation times as T_c is approached. However, as the fluctuations grow to macroscopic sizes, we see that the number of configurations increases, becoming very large as the material phase-separates. The resulting divergence is however inconsistent with our results.

We note that a relaxing species cannot be subject to the nature of its environment without limit. As intermolecular forces have ranges, so must the relaxation mechanism. Thus, we postulate that the relaxation mechanism of a molecule is further characterized by a range (which we will call r_0) within which the number of configurations affect the relaxation time of the molecule. Changes in the number of configurations outside this range will be considered irrelevant in determining the relaxation time of the molecule. This concept results in a saturation of the broadening of the distribution very close to T_c, as the flowing species are insensitive to further changes in the environment. The magnitude of r_0 is characteristic of the relaxation process in a particular material, and is independent of critical phenomena. While it is quite possible that r_0 varies with temperature, in order to maintain the undetermined parameters to a manageable number, we will assume that its magnitude remains constant over the range of our measurements. This assumption is well justified since the changes in r_0 are expected to be small in the temperature range of interest to us, and the introduction of a finite range for the effective environment in structural relaxations carries a far greater effect than changes in the range itself. In order to formulate the relationship between the composition fluctuations and the distribution of relaxation times, let us turn to elementary fluctuation theory.

3.2. Formulation of the Model

The supercritical state of liquid mixtures is characterized by fluctuations in the local composition of the material. Since we are interested in the analysis of the width of a distribution of relaxation times in terms of composition fluctuations, we will consider the width, $\Theta = \langle(\Delta \ln \tau)^2\rangle$, as a dependent function of the mean-square composition change, $\langle(\Delta c)^2\rangle$ [24]. Thus, we let the width of the relaxation time spectrum be dependent upon the fluctuations in local composition as follows:

$$\ln \tau = \ln \tau_0 + c(\partial \ln \tau/\partial c). \tag{8}$$

This expression implies that $(\partial \ln \tau/\partial c)$ has been chosen to be independent of τ and c with the result:

$$\Theta = \langle(\Delta \ln \tau)^2\rangle = (\partial \ln \tau/\partial c)^2\langle(\Delta c)^2\rangle. \tag{9}$$

This formulates the connection between the critical-point related changes in the distribution of relaxation times and the environmental changes brought about by the supercritical microstructure.

Assuming that the probability density for composition fluctuations is a normal or Gaussian function, then it follows from eqs (8) and (9) that the corresponding distribution of relaxation times is a log-Gaussian function of time of the form:

$$g(\ln \tau) = \left[2\pi\left(\frac{\partial \ln \tau}{\partial c}\right)^2 \langle(\Delta c)^2\rangle\right]^{-1/2} \exp\left[-\frac{(\Delta \ln \tau)^2}{2\left(\frac{\partial \ln \tau}{\partial c}\right)^2\langle(\Delta c)^2\rangle}\right]. \tag{10}$$

Since the ultrasonic measurements have shown that $g(\ln \tau)$ is indeed a Gaussian in $(\ln \tau)$ in the critical oxide mixtures, then the choice of $\langle(\Delta \ln \tau)^2\rangle$ rather than another time expression such as $\langle(\Delta\tau)^2\rangle$ for the dependent function of eq (8) is justified. The assumption that $(\partial \ln \tau/\partial c)$ is independent of τ and c, at any temperature, therefore leads to a distribution consistent with the measured function $g(\ln \tau)$.

The change in the number of available configurations for relaxation resulting from supercritical fluctuations is written as the change in the mean-square composition fluctuation. The latter represents the average deviation of local composition in the supercritical mixture from the composition in a similar but homogeneous system. This is obtained by integrating the supercritical correlation function, $G(r)$, over the local volume, V_0. $G(r)$ is the increased probability above average of finding two particles of the same component at a distance r apart and thus gives a measure of the

probability of having deviations from the homogeneous composition [24].

$$G(r) = \frac{1}{c_0^2} \langle [c(r_1) - \overline{c(r_1)}][c(r_2) - \overline{c(r_2)}] \rangle - \delta(r_1 - r_2) \tag{11}$$

c_0 is the average density of the component of interest, the subscripts 1 and 2 represent two locations in space at r_1 and r_2, separated by a distance r, and the averaging is a space average. $\delta(r_1 - r_2)$ is a "delta" function expressing the certainty of finding a particle at r_2 when $r_2 = r_1$. The supercritical pair correlation function, $G(r)$, varies from zero, far from the critical point, where no composition fluctuations are present, to one at the critical point.

The supercritical deviation in local composition may now be calculated by integrating the clustering or ordering probability represented by $G(r)$ over a local volume, defined by a cutoff function $f(r)$.

$$\langle [\Delta c]^2 \rangle_f = \int G(r) f(r) dV / \int f(r) dV \tag{12}$$

where the local composition deviation is represented by $\langle [\Delta c]^2 \rangle_f$ in order to indicate that it is associated with the cutoff function $f(r)$. The screening function represents the limitation of the range of interaction in the structural relaxation process, and thus is used to limit the integration to a local volume. As discussed earlier, this cutoff or screening function, $f(r)$, is necessary here, since the ultrasonic and viscosity results show a saturation in the interaction of the viscous relaxation process with the composition fluctuations at temperatures close to the critical where the fluctuations grow to macroscopic sizes. The specific form of this function cannot be derived at this time, since the microscopic mechanism of structural relaxation is not known. In earlier papers [25, 17], the authors denoted $f(r)$ by a step function:

$$f(r) = \begin{cases} 1 \text{ for } r < r_0 \\ 0 \text{ for } r > r_0. \end{cases} \tag{13}$$

However, in order to take into account the gradual decrease in influence as the distance from the flow unit is increased, a Gaussian screening function is used herein.

$$f(r) = \exp(-r^2/2r_0^2). \tag{14}$$

Little difference results from this choice, except that the final equation may be solved in closed form. The range of this function is r_0, and events which occur at $r > r_0$ have little effect on the behavior of the flow unit at the center.

The choice of a functional form for the pair correlation function, $G(r)$, presents a further problem. A popular form, to date, has been the Ornstein-Zernike-Debye (OZD) pair correlation function [24]:

$$G(r)_{OZD} = k_B T \alpha_0 \frac{e^{-r/\Lambda}}{r} \tag{15}$$

where Λ is the range of interaction and α_0 is a material constant. The Fourier transform of this expression has had some success with light scattering [15], and low angle x-ray scattering [16] at small wave numbers, k, and is written as:

$$g(k)_{OZD} = \alpha_{0k} k_B T / (a + bk^2). \tag{16}$$

The OZD pair correlation function is applicable only at large distances since the validity of the Fourier transform in eq (16) is limited to small k. As a result, $G(r)_{OZD}$ has an unacceptable divergence at the origin, and cannot represent the critical correlation function at small distances. This failure of the OZD function to suitably represent the supercritical correlation function has been demonstrated in various x-ray measurements [16, 26] for large k-values, as the inverse intensity departs drastically from a k^2-dependence (eq (16)). Following our model, we see that at temperatures close to the critical point, the correlation length Λ is of the order of r_0, and the integration of eq (12) weighs heavily the intermediate portion of the pair correlation function. It has been shown in a previous paper [25] that, as a result, the OZD function fails to describe adequately the data near T_c. In order to improve this present model let us choose a function which satisfies the same asymptotic conditions as the OZD function for small k and large r, and has a better behavior where the latter fails at large k and intermediate distances. The conditions which must be met are that the Fourier transform of the correlation function follow a k^2-dependence at low k-values, and that the function be finite at the origin ($r = 0$). The well-known Gaussian function satisfied these requirements.

$$G'(r) = \alpha_0' k_B T \exp(-r^2/2\Lambda^2) \tag{17}$$

with a Fourier transform:

$$g'(k) = \alpha_{0k}' k_B T \exp(-k^2/2k^2) \tag{18}$$

where $\kappa = 1/\Lambda$. The Fourier transform of the Gaussian expression may be expanded into a series at small wave numbers:

$$\lim_{k \to 0} g'(k) = \alpha_{0k}' k_B T / [1 + \tfrac{1}{2}(k/\kappa)^2 + \tfrac{1}{4}(k/\kappa)^4 + \ldots] \tag{19}$$

thus having the same asymptotic behavior $(a + bk^2)$ as the OZD function. Furthermore, the additional positive k^4-term which appears for larger k-values is consistent with an upward bend in the intensity curves (I^{-1} versus k^2) resulting from low-angle x-ray scattering measurements. In addition, the Gaussian pair-correlation function remains finite at the origin, and therefore can be normalized to one—a necessary property since the correlation function is a probability density. We have chosen this particular form for the correlation function only as a means of analyzing our results. Although the Gaussian function appears to satisfy a number of conditions for suitability, since we cannot

formulate the functional form of the screening function, $f(r)$, from microscopic considerations, we by no means intend to propose that agreement of the model with data should suggest the Gaussian expression as a new universal supercritical correlation function.

The local deviation in composition is now given by the integration of the pair-correlation function as per eq (12).

$$\langle(\Delta c)^2\rangle_{\text{Gauss}} = \alpha_0' k_B T \left[\frac{\Lambda^2}{\Lambda^2 + r_0^2}\right]^{3/2}. \tag{20}$$

Defining the ratio of the structural relaxation range, r_0, to the correlation length, Λ, by $\mathscr{R}$, and using the temperature dependence of Λ discussed earlier,

$$\begin{aligned}\mathscr{R} &\equiv r_0/\Lambda = (r_0/l)\,(T/T_c - 1)^{1/2} \\ &= \mathscr{R}_0 (T/T_c - 1)^{1/2}\end{aligned} \tag{21}$$

we may write the local deviation in composition in terms of reduced temperature:

$$\langle(\Delta c)^2\rangle_{\text{Gauss}} = \alpha_0' k_B T \left[\frac{1}{1 + \mathscr{R}_0^2 (T/T_c - 1)}\right]^{3/2}. \tag{22}$$

The expression is now inserted into eq (9) and once a suitable value of $(\partial \ln \tau/\partial c)$ is obtained, the distribution of relaxation times or activation energies may be expressed in terms of the reduced temperature.

4. Calculations

The factor $(\partial \ln \tau/\partial c)$ presents the final problem. Throughout the paper, we have discussed the relaxation properties in terms of the natural logarithm of time, $\ln \tau$, instead of the time. A useful transform is accomplished by the Eyring Rate Equation.

$$\tau = A e^{-S/k_B} e^{E/k_B T}. \tag{23}$$

Therefore:

$$\tau/\tau' = \frac{A}{A'} e^{(E-E')/k_B T} e^{-(S-S')/k_B}. \tag{24}$$

This transformation allows the use of "activation energy" distributions instead of distributions in $\ln \tau$. The activation energy format is used here for convenience and to calculate $(\partial \ln \tau/\partial c)$. We are not concerned with whether shear structural relaxation occurs by a simple rate process in the strict Eyring sense, in these glasses, although some indication to that effect is seen in the Arrhenian behavior of the most probable relaxation time at temperatures above 900 °C.

Some data [27] is available on the relative behavior of the activation entropy and energy as a function of composition in a borosilicate system where B_2O_3 replaces SiO_2. Since this process occurs during the phase separation of the oxides investigated herein, we will use the relative magnitudes of $\left(\frac{\partial E}{\partial c}\right)$ and $\left(\frac{\partial S}{\partial c}\right)$ to deduce the proper temperature dependence of $\left(\frac{\partial \ln \tau}{\partial c}\right)$ in our system, according to the following equation.

$$\left(\frac{\partial \ln \tau}{\partial c}\right) = \frac{1}{A}\left(\frac{\partial A}{\partial c}\right) + \left(\frac{1}{k_B T}\right)\left(\frac{\partial E}{\partial c}\right) - \left(\frac{1}{k_B}\right)\left(\frac{\partial S}{\partial c}\right). \tag{25}$$

In order to compare the equation with the data [27] we combine the first and third terms:

$$\left(\frac{\partial \ln \tau}{\partial c}\right) = \frac{1}{k_B T}\left(\frac{\partial E}{\partial c}\right) - \frac{1}{k_B}\left(\frac{\partial S^*}{\partial c}\right). \tag{26}$$

Measurements of viscosity at high temperatures in the Arrhenius temperature range yield both terms of eq (26). Figure 6 represents the temperature dependence of the subsequently calculated $\left(\frac{\partial \ln \tau}{\partial c}\right)$. The

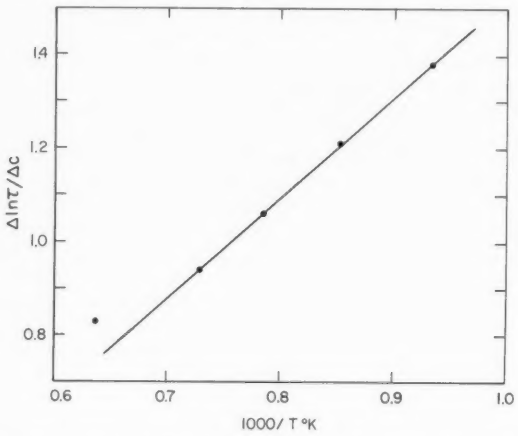

FIGURE 6. *Plot of* $(\partial \ln \tau/\partial c)$ *typical of the immiscible system studied here.*
These points were calculated from the data of Ref. [27].

activation energy term appears to dominate in the temperature range of interest to us and the factor $\left(\frac{\partial \ln \tau}{\partial c}\right)$ is found to change inversely with temperature. Thus we may write:

$$\left(\frac{\partial \ln \tau}{\partial c}\right) = \left[2.15\left(\frac{1000}{T}\right) - 0.627\right]. \tag{27}$$

The width of the relaxation time spectrum $g(\ln \tau)$ consequently becomes:

$$\langle(\Delta \ln \tau)^2\rangle = \langle(\Delta E)^2\rangle/(k_B T)^2.$$

$$= \alpha_0'\left[2.15\left(\frac{1000}{T}\right) - 0.627\right]^2 (k_B T)\left[\frac{1}{1 + \mathscr{R}^2}\right]^{3/2} \tag{28}$$

Before comparing the results with our model, we note from figure 4, that two of the samples investigated (samples 2 and 3) follow curves which appear to be shifted from the others. In the case of sample 3, there may be a high temperature residual width responsible for the shift. Since we are only interested in analyzing the broadening attributed to the change in structure resulting from the composition fluctuations, we subtract this width, and consider only the fractional change in width. A lack of high temperature data prevents a similar analysis of the data from sample 2, therefore, we will assume that it also has a residual width.

The data in the form:

$$\Delta = \langle (\Delta \ln \tau)^2 \rangle \left\{ \alpha_0' k_B T \left[2.15 \left(\frac{1000}{T} \right) - 0.627 \right]^2 \right\}^{-1} = \left[\frac{1}{1+\mathscr{R}^2} \right]^{3/2} \qquad (29)$$

is plotted in figure 7 for all four samples. The individual deviations from the composite curve are of the order of the experimental uncertainty, as can be seen from the error bars on the data. At this point, the equation proposed above can be fitted to the data, with α_0' and $\mathscr{R}_0$ as undetermined variables. The results are shown in figure 7. The proposed function describes the three regions in the curve. Of particular interest are the large increase in width and the saturation of the width near T_c. Using the value of 11 Å for l, the range of interaction for structural relaxation, r_0, is calculated to be 41 Å. In a previous paper, using the OZD function, we calculated r_0 to be 56 Å [25]. This shows that while the form of the pair-correlation function influences the value obtained, its order of magnitude is well established by the data in relation to the three regions measured in $\langle (\Delta \ln \tau)^2 \rangle$. Such a large value for r_0 indicates that shear viscous flow is truly a wide ranging process!

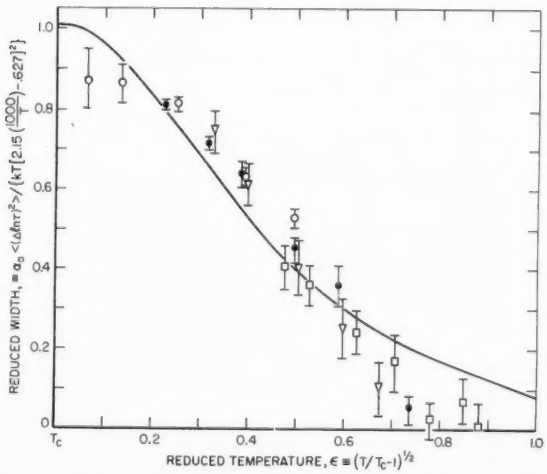

FIGURE 7. *Comparison of the critical increase in width, with the proposed model, (solid line).*

5. Summary and Conclusion

5.1. Treatment of Supercritical Relaxation Experiments by the Environmental Relaxation Model

A model is proposed which indicates that systems with a broad continuous distribution of mobilities will exhibit large supercritical effects. The model predicts that the supercritical effect will manifest itself in the width of the distribution of relaxation times. The relaxation mechanism is assumed to be characterized by a distance, r_0, which represents a finite range for the interactions which lead to relaxation. This range is characteristic of the material and independent of critical point phenomena. The dependence of width on reduced temperature, ϵ, consists of three regions characterized by the relative sizes of Λ, the range of fluctuations, and r_0 the range of structural influence, as shown in figure 8 where we have represented the

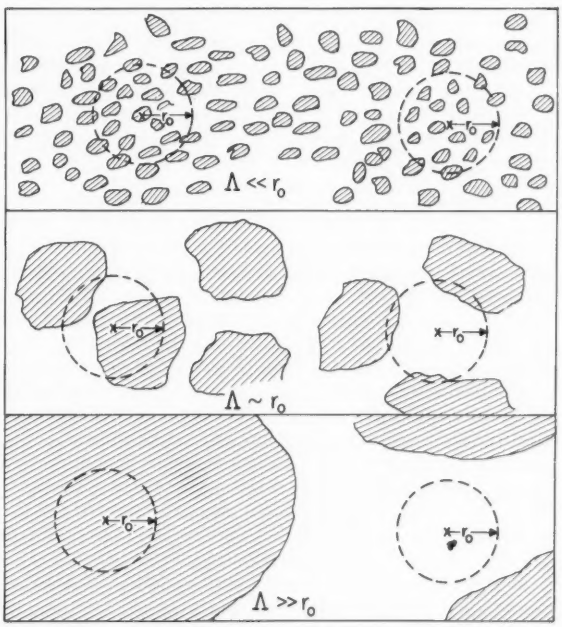

FIGURE 8. *Typical microstructure expected to produce the three regions in the distribution of relaxation times, as a function of the relative sizes of r_0 and $\Lambda(\epsilon)$.*

distribution of mobilities by two distinct phases for simplicity. Region I, in which $\Lambda(\epsilon) \ll r_0$, represents high temperatures, far above T_c, and shows that due to space averaging within $V_0 = 4/3\ \pi r_0^3$, all relaxing species interact with similar neighborhoods and the distribution of relaxation times is narrow, and in simple liquids is single. The distribution is temperature independent and Arrhenian viscosity behavior is observed. In Region II, as one approaches the critical temperature, Λ approaches r_0. Now, large differences in environment appear as relaxing species begin to be surrounded by different local environments. The

width of the relaxation time spectrum increases as the temperature approaches the critical point and the viscosity no longer follows Arrhenian behavior. An anomalous excess viscosity appears. In Region III, $\Lambda(\epsilon) \gg r_0$, the temperature is close to the critical point, and the fluctuations are large. Relaxing species are well imbeded within the fluctuations so that further changes in $\Lambda(\epsilon)$ have little effect on the local compositions. The width of the relaxation time spectrum saturates, changing little as one approaches T_c. This is reflected in a saturation of the anomalous excess viscosity despite a divergence of the correlation length Λ. The viscosity appears to revert to Arrhenian behavior because, although a broad distribution of relaxation times remains at temperatures near T_c, the character of the distribution ceases the change with temperature that gave rise to the non-Arrhenian behavior. Actual Arrhenian behavior is however only observed if the most probable relaxation time, τ', is also Arrhenian. The Gaussian function proposed fits all three regions well and has the proper asymptotic behavior near and far from T_c. The range of structural influence, r_0, is quite large with a value of 41 to 56 Å, and spans over many molecular diameters. This explains why, in some oxide glasses, the addition of small amounts of impurities changes the relaxation properties: an addition of 5 ppm of Na_2O to pure SiO_2 changes the viscosity by a factor of two [28].

5.2. Generalization to Other Materials

The work presented herein has been concerned with explaining the origin of distributions of relaxation times observed above the critical points of a series of immiscible oxide mixtures. For this reason, we have been primarily concerned with describing the microstructure in the environment in terms of supercritical composition fluctuations. Microstructure in the environment may, however, arise from other causes: association, density and various other ordering phenomena. The analysis presented here would also apply in such cases in qualitative terms. The three regions described previously would be expected to occur in an analysis of the spectral width as the order parameter varies in size relative to the range of structural influence, r_0.

Boron trioxide glass, for example, has a log-Gaussian shear distribution of relaxation times [8] but has no composition fluctuations. Yet its relaxation time spectrum and its distribution of activation energies broaden as the temperature is lowered, exhibiting not only higher activation energy values as expected, but also lower ones as well. This apparent paradox is easily explained by the present relaxation model, as we attribute the appearance of lower and higher activation energies to the formation of a distribution of regions in the melt with varying degrees of association, some low and some high (low E and high E). A temperature dependent spectrum of relaxation times also occurs in GeO_2 glass at temperatures near its transformation region [13]. According to the model, this would indicate that there is a degree of microheterogeneity whose size is of the order of r_0 at the transformation region in this glass. Since r_0 is a property of the material, it is likely to vary little among simple oxide glassformers so that the model suggests a value of 50 Å to the size of the microstructure in GeO_2 in the transformation region. Electron micrographs on GeO_2 [29] have revealed that, indeed, there is microheterogeneity in GeO_2 in the transformation region of the order of 25 to 50 Å.

Although, the environmental relaxation model can give a qualitative description of the behavior of the width of the relaxation time spectrum in terms of the size of the order parameter (i.e., Regions I, II, and III), a description in terms of temperatures is not possible for normal glasses. An analysis of the temperature dependence of the order parameter, and the form of the pair correlation function are needed before a treatment similar to the immiscible melts can be carried out on normal or single component molten oxides.

6. References

[1] Fulcher, G. S., J. Am. Ceram. Soc. **8,** 339 (1925).
[2] Gibbs, J. H., Modern Aspects of the Vitreous State, Vol. **1,** J. D. Mackenzie, Ed. (Butterworths, London, 1960).
[3] Turnbull, D., and Cohen, M. H., J. Chem. Phys. **34,** 120 (1961).
[4] Goldstein, M., J. Chem. Phys. **51,** 3728 (1969).
[5] Litovitz, T. A., Non-Crystalline Solids, V. D. Frechette, Ed. (John Wiley, New York, 1960).
[6] Montrose, C. J., and Litovitz, T. A., J. Acous. Soc. Am. **47,** 1250 (1970).
[7] Isakovich, M. A., and Chaban, I. A., Soviet Phys. Doklady **10,** 1053 (1966); Sov. Phys. JETP **23,** 893 (1966).
[8] Tauke, J. Litovitz, T. A., and Macedo, P. B., J. Am. Ceram. Soc. **51,** 158 (1968).
[9] Macedo, P. B., and Napolitano, A., J. Chem. Phys. **49,** 1887 (1968).
[10] Herzfeld, K. F., and Litovitz, T. A., Absorption and Dispersion of Ultrasonic Waves (Academic Press, New York, N.Y., 1959).
[11] Goldstein, M., Modern Aspects of the Vitreous State, Vol. **3,** J. D. Mackenzie, Ed. (Butterworth, Washington, 1964).
[12] Macedo, P. B., and Napolitano, A., J. Res. NBS **71A,** 231 (1967).
[13] Napolitano, A., and Macedo, P. B., J. Res. NBS **72A,** 425 (1968); Boesch, L., Napolitano, A., and Macedo, P. B., J. Am. Ceram. Soc. **53,** 148 (1970).
[14] Fröhlich, H., Theory of Dielectrics (Clarendon Press, Oxford, 1949).
[15] Chu, B., J. Am. Chem. Soc. **86,** 3557 (1964); Fisher, M., J. Math. Phys. **5,** 944 (1964).
[16] Debye, P., Caulfield, D., and Bashaw, J., J. Chem. Phys. **41,** 3051 (1964).
[17] Macedo, P. B., Simmons, J. H., and Haller, W., Phys. Chem. Glasses **9,** 156 (1968).
[18] Simmons, J. H., Napolitano, A., and Macedo, P. B., J. Chem. Phys. **53,** 1165 (1970).
[19] Simmons, J. H., and Macedo, P. B., J. Chem. Phys. **53,** 2914 (1970).
[20] Haller, W., Blackburn, D. H., Wagstaff, F. E., and Charles, R. J., J. Am. Ceram. Soc. **53,** 34 (1970).
[21] Napolitano, A., Macedo, P. B., and Hawkins, E. G., J. Res. NBS **69A,** 449 (1965).
[22] Kawasaki, K., Phys. Rev. **150,** 291 (1966); Kadanoff, L. P., Swift, J., Phys. Rev. **166,** 89 (1968); Ferrell, R., Phys. Rev. Letters **24,** 1169 (1970).
[23] Simmons, J. H., and Macedo, P. B., Conference on the Physics of Non-Crystalline Solids, Sheffield, England, September, 1970.
[24] Landau, L. D., and Lifshitz, E. M., Statistical Physics (Addison-Wesley Publishing Co., Reading, Mass. 1958).
[25] Simmons, J. H., and Macedo, P. B., J. Chem. Phys. **54,** 1325 (1971).
[26] Munster, A., Small Angle X-Ray Scattering, (Gordon and Breach, 1967) p. 401.
[27] Riebling, E. F., J. Am. Ceram. Soc. **47,** 478 (1964).
[28] Hagy, H., private communication.
[29] Zarzycki, J., and Mezard, R., Phys. Chem. Glasses **3,** 163 (1962).

(Paper 75A3–661)

JOURNAL OF RESEARCH of the National Bureau of Standards—A. Physics and Chemistry
Vol. 75A, No. 3, May–June 1971

Phase Relations in the SrO–IrO_2–Ir System in Air

C. L. McDaniel and S. J. Schneider

Institute for Materials Research, National Bureau of Standards, Washington, D.C. 20234

(February 3, 1971)

The equilibrium phase relations for the SrO–IrO_2–Ir system were determined in an air environment at atmospheric pressure. A ternary equilibrium phase diagram was constructed indicating selected oxygen reaction lines and tie lines. A binary representation is given for the ternary system in air. Of the nine phases detected in this study, three are stable and six are probably metastable under atmospheric conditions. The stable compounds, $4SrO \cdot IrO_2$, $2SrO \cdot IrO_2$, and $SrO \cdot IrO_2$ dissociate at 1540, 1445, and 1205 °C, respectively. The metastable phases include low-$4SrO \cdot IrO_2$, $2SrO \cdot 3IrO_2$, $xSrO \cdot IrO_2 (x > 2)$, $ySrO \cdot IrO_2 (4 > y > 2)$, $zSrO \cdot IrO_2 (2 > z > 1)$, and $3SrO \cdot 2IrO_2$. The specific composition of the metastable phases could not be ascertained with certainty. The x-ray patterns of all phases detected in this study were indexed with the exception of that of the $zSrO \cdot IrO_2 (2 > z > 1)$ compound. A summary of x-ray data is given for all known phases occurring in the system.

Key words: Dissociation; equilibrium; phase relations; SrO:IrO_2 compounds; SrO–IrO_2–Ir system.

1. Introduction

The present study is part of a program [1, 2, 3][1] to obtain a better understanding of the behavior of various Pt-group metals and metal oxides when heated together in an oxidizing environment. Considering the fact that several of these metals are used as secondary standards on the International Practical Temperature Scale (IPTS 1968[2]) [4] as well as for container materials for high temperature applications, knowledge of the phase relations between these metals and other materials becomes important. This work presents the results of an investigation of the equilibrium relationships between the condensed phases in the system SrO–IrO_2–Ir in air.

Strontium oxide (SrO) has a cubic, sodium chloride-type structure with $a = 5.1602$ Å [5]. The melting point of SrO has been reported to be 2424 °C [6].

Iridium (Ir) has a face-centered cubic, copper-type structure with $a = 3.8394$ Å [7]. Its freezing point, 2447 °C, is listed as a secondary reference point on the IPTS (1968).

Iridium has a strong tendency to form iridium dioxide (IrO_2) when heated in air at moderate temperatures. The unit cell dimensions of IrO_2 are reported as (tetragonal) $a = 4.4983$ Å and $c = 3.1544$ Å [8]. However, above 1021 °C [2] Ir metal is the only solid phase that exists in equilibrium with air.

Even though Ir oxidizes to IrO_2 when heated in air, complete oxidation of the entire sample is often difficult to obtain. By utilizing IrO_2 rather than Ir as starting material, an approach to equilibrium could be achieved more readily. The study will still reflect, however, the behavior of the metal in air.

2. Experimental Procedure

Specimens were prepared from 0.4 g batches of various combinations of strontium carbonate ($SrCO_3$) and IrO_2, each having a purity of at least 99.8 percent. Calculated amounts of these end members, corrected for ignition loss, were weighed to the nearest milligram. Each batch was thoroughly hand mixed and calcined in a muffle furnace at a minimum temperature of 800 °C or heated directly at the temperature of interest. Specimen containers employed in this study were open or sealed gold tubes, open or sealed platinum tubes, and open fused silica tubes. Portions of each calcined batch were refired in a platinum alloy wire-wound quench furnace at various temperatures for different periods of time. The specimens were quenched in air, ice water, or liquid nitrogen. Temperatures in the quench furnace were measured with a Pt versus 90 percent Pt-10 percent Rh calibrated thermocouple. All reported temperatures pertaining to quench furnace data are considered accurate to within ±5 °C. The precision of the measurements was estimated to be ±2 °C.

Equilibrium was assumed to have been achieved when the x-ray pattern showed no change after successive heat treatments of the specimen or when the data were consistent with the results from a previous set of experiments. An attempt was made on various compositions to obtain equilibrium by increasing the oxygen pressure of the environment exposed to the specimen. The specimen was placed in an open gold tube and heated at moderate temperatures to decom-

[1] Figures in brackets indicate the literature references at the end of this paper.
[2] This scale (IPTS 1968) applies to all temperatures listed in this paper.

pose the $SrCO_3$. The open gold tube containing the specimen was then placed into a larger platinum tube containing a calculated amount of finely divided platinum dioxide (PtO_2). The platinum tube was then sealed by welding and heat treated at a given temperature. As the temperature was raised the PtO_2 decomposed and increased the oxygen pressure, calculated to be approximately 30 atm (3.03975×10^6 N/m^2). The container materials did not appear to influence or react with the various oxide samples. All phases detected in this study were formed in air using gold as well as Pt for container materials.

All specimens were examined by x-ray diffraction at room temperature using a high-angle-recording Geiger counter diffractometer and Ni-filtered Cu radiation. The scanning rate was $\frac{1}{4}°2\theta$/min. Unit cell dimensions were refined by a least-squares computer program and are estimated to be accurate to at least 2 in the last decimal place listed.

3. Results and Discussion

3.1. Phase Diagram

The equilibrium phase diagram for the SrO-IrO_2-Ir system in air is given in figure 1. The diagram was con-

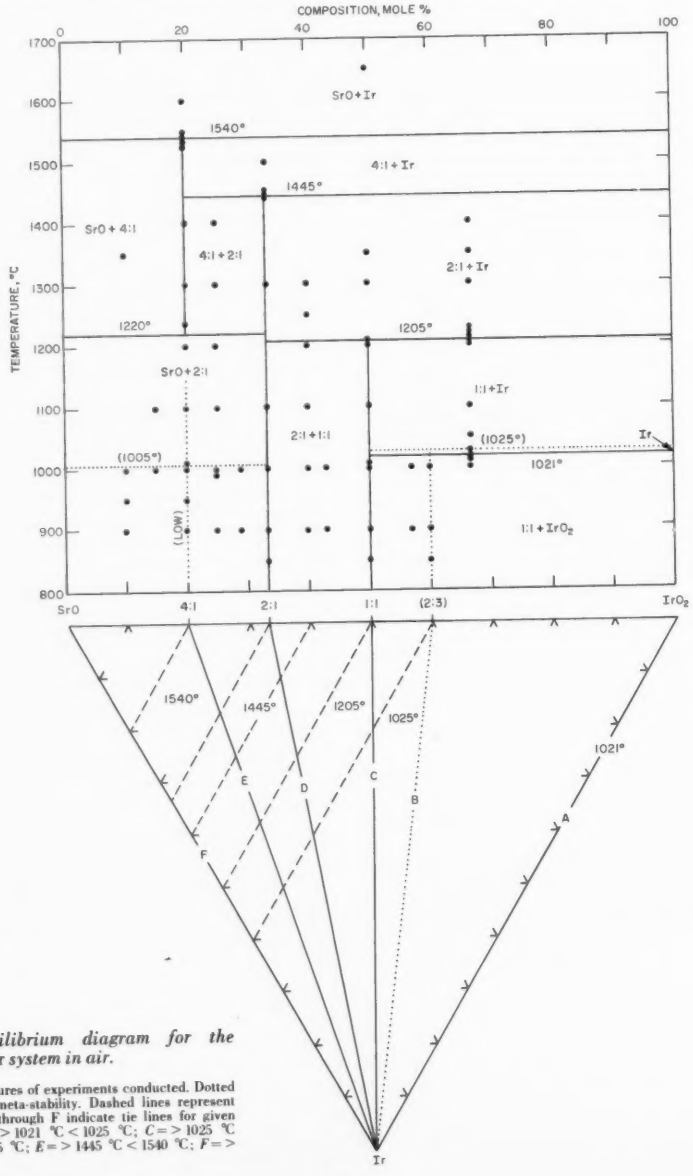

FIGURE 1. *Phase equilibrium diagram for the* SrO-IrO_2-Ir *system in air.*

●—compositions and temperatures of experiments conducted. Dotted lines and parentheses indicate meta-stability. Dashed lines represent oxygen reaction lines. Lines A through F indicate tie lines for given temperatures. A = 1021 °C, B = > 1021 °C < 1025 °C; C = > 1025 °C < 1205 °C; D = > 1205 °C < 1445 °C; E = > 1445 °C < 1540 °C; F = > 1540 °C.

structed from the data listed in table 1. The solid circles illustrate the compositions and temperatures of the experiments conducted. The dotted lines and parentheses indicate metastability. In the ternary plot the dashed lines represent oxygen reaction lines. Lines A through F indicate tie lines. The three phase triangular areas with listed temperatures represent invariant situations in which three condensed phases co-exist in equilibrium at those specified temperatures. The oxygen reaction lines connect compositions on the SrO-IrO_2 join and the final compositions attained upon dissociation of the oxide mixtures. The dissociation products are Ir and one of the following: $SrO \cdot IrO_2$, $2SrO \cdot IrO_2$, $4SrO \cdot IrO_2$, or SrO. It should be emphasized that these dissociation products are the condensed phases of the system and are always in equilibrium with oxygen. The tie lines (A–F) represent joins for a given temperature or series of temperatures for any series of intersecting oxygen reaction lines.

Consider for instance a 50:50 mole percent mixture on the SrO-IrO_2 join. At temperatures below 1205 °C, the mixture contains one solid phase, the 1:1 compound. As this phase is heated to higher temperatures, oxygen loss occurs, producing a situation in which two

TABLE 1. *Experimental data for compositions in the* SrO–IrO_2–Ir *system*

Composition		Heat treatment[a]		X-ray diffraction analyses[g]	Remarks
SrO	IrO_2	Previous[h]	Final		
Mol%	*Mol%*	*°C–h*	*°C–h*		
90	10		700–68	$SrCO_3 + xSrO \cdot IrO_2$ $(x > 2)$	Nonequilibrium.
			[e] 900–3	$SrCO_3 + IrO_2$	No reaction; nonequilibrium.
			900–3	$SrCO_3 + xSrO \cdot IrO_2$ $(x > 2)$	Nonequilibrium.
			[e] 900–18	$SrCO_3 + IrO_2$	No reaction; nonequilibrium.
			[f] 950–272	$4SrO \cdot IrO_2 + xSrO \cdot IrO_2$ $(x > 2)$	Nonequilibrium.
			1000–2	$SrO + xSrO \cdot IrO_2$ $(x > 2) + 4SrO \cdot IrO_2 + \text{low} - 4SrO \cdot IrO_2$	Nonequilibrium.
		[f] 900–3	[d] 1000–4	$\text{low} - 4SrO \cdot IrO_2 + SrCO_3$	Nonequilibrium.
		1350–2	[f] 1000–96	$4SrO \cdot IrO_2 + SrO$	
			[f] 1000–72	$4SrO \cdot IrO_2 + SrO + xSrO \cdot IrO_2$ $(x > 2) + \text{low} - 4SrO \cdot IrO_2$	Nonequilibrium.
			[f] 1000–168	$4SrO \cdot IrO_2 + SrO$	
			1350–2	$4SrO \cdot IrO_2 + SrO$	
85	15		800–18	$SrCO_3 + ySrO \cdot IrO_2$ $(4 > y > 2) + \text{low} - 4SrO \cdot IrO_2$	Nonequilibrium.
		800–18	1000–21	$\text{low} - 4SrO \cdot IrO_2 + SrO$	Nonequilibrium.
		800–18, 1000–21	1100–66	$4SrO \cdot IrO_2 + SrO$	
80	20	[f] 800–67, [f] 1000–20, [f] 1000–20, 1400–3	800–18	$4SrO \cdot IrO_2$	
			[f] 800–67	$\text{low} - 4SrO \cdot IrO_2 + SrCO_3 + xSrO \cdot IrO_2$ $(x > 2)$	Nonequilibrium.
		[f] 900–2	[d] 900–66	$\text{low} - 4SrO \cdot IrO_2 + SrCO_3 + IrO_2$	Nonequilibrium; trace amounts of $SrCO_3$ and IrO_2.
		[f] 800–67, [f] 1000–20, [f] 1000–20, 1400–3	[f] 950–192	$4SrO \cdot IrO_2$	
			[f] 1000–0.5	$\text{low} - 4SrO \cdot IrO_2 + xSrO \cdot IrO_2$ $(x > 2)$	Nonequilibrium.
		900–2	[e] 1000–1	$ySrO \cdot IrO_2$ $(4 > y > 2) + \text{low} - 4SrO \cdot IrO_2 + SrCO_3$	Nonequilibrium.
		[f] 900–2	[d] 1000–2	$\text{low} - 4SrO \cdot IrO_2 + ySrO \cdot IrO_2$ $(4 > y > 2) + SrCO_3$	Nonequilibrium.
		1400–3	1000–18	$4SrO \cdot IrO_2 + 2SrO \cdot IrO_2 + xSrO \cdot IrO_2$ $(x > 2)$	Quenched in liquid nitrogen; nonequilibrium.
		1400–3	[e] 1000–18	$4SrO \cdot IrO_2 + 2SrO \cdot IrO_2$	Quenched in liquid nitrogen; nonequilibrium.
		900–2	[e] 1000–19	$2SrO \cdot IrO_2 + \text{low} - 4SrO \cdot IrO_2 + SrCO_3$	Nonequilibrium.
		1300–2	1000–19	$4SrO \cdot IrO_2 + 2SrO \cdot IrO_2 + xSrO \cdot IrO_2$ $(x > 2)$	Nonequilibrium.
		[f] 800–67	[f] 1000–20	$\text{low} - 4SrO \cdot IrO_2 + 4SrO \cdot IrO_2 + xSrO \cdot IrO_2$ $(x > 2)$	Nonequilibrium.
		[f] 800–67, [f] 1000–20	[f] 1000–20	$4SrO \cdot IrO_2 + \text{low} - 4SrO \cdot IrO_2 + xSrO \cdot IrO_2$ $(x > 2)$	Nonequilibrium.
		1400–3	1000–21	$4SrO \cdot IrO_2 + 2SrO \cdot IrO_2 + xSrO \cdot IrO_2$ $(x > 2)$	Nonequilibrium.
		1400–3	[c] 1000–72	$4SrO \cdot IrO_2 + 2SrO \cdot IrO_2 + xSrO \cdot IrO_2$ $(x > 2)$	Nonequilibrium.
		1400–3	1000–72	$2SrO \cdot IrO_2 +$ unidentified phase	Quenched in ice water; unidentified phase probably a hydrate.
		1400–3	[f] 1000–72	$2SrO \cdot IrO_2 +$ unidentified phase	Quenched in ice water; unidentified phase probably a hydrate.

Footnotes at end of table.

TABLE 1. *Experimental data for compositions in the* $SrO-IrO_2-Ir$ *system*—Continued

Composition		Heat treatment[a]		X-ray diffraction analyses[g]	Remarks
SrO	IrO_2	Previous[b]	Final		
Mol%	*Mol%*	*°C–h*	*°C–h*		
		1400–3	1000–66	$4SrO{\cdot}IrO_2 + 2SrO{\cdot}IrO_2 + xSrO{\cdot}IrO_2$ $(x > 2)$	Nonequilibrium.
		1400–3	[b] 1000–96	$4SrO{\cdot}IrO_2 + 2SrO{\cdot}IrO_2$	Quenched in ice water; nonequilibrium.
		[f] 800–67, [f] 1000–20, [f] 1000–20	1010–20	$4SrO{\cdot}IrO_2 + 2SrO{\cdot}IrO_2$	Nonequilibrium.
		1400–3	[e] 1100–18	$4SrO{\cdot}IrO_2 + 2SrO{\cdot}IrO_2$	Nonequilibrium.
		[f] 800–67, [f] 1000–20, [f] 1000–20, 1400–3	1100–66	$4SrO{\cdot}IrO_2 + 2SrO{\cdot}IrO_2$	Nonequilibrium.
		1400–3	[e] 1200–22	$4SrO{\cdot}IrO_2 + 2SrO{\cdot}IrO_2$	Nonequilibrium.
		[f] 800–67, [f] 1000–20, [f] 1000–20, 1400–3	1200–63	$4SrO{\cdot}IrO_2 + 2SrO{\cdot}IrO_2 + xSrO{\cdot}IrO_2$ $(x > 2)$	Nonequilibrium.
		1400–3	[e] 1235–17	$4SrO{\cdot}IrO_2$	
		1400–0.5	[e] 1300–65	$4SrO{\cdot}IrO_2$	
		1400–2	1400–0.5	$4SrO{\cdot}IrO_2$	Quenched in liquid nitrogen.
		1400–2	1400–0.5	unidentified phase + $2SrO{\cdot}IrO_2$	Quenched in ice water; unidentified phase probably a hydrate.
			1400–2	$4SrO{\cdot}IrO_2$	
		[f] 800–67, [f] 1000–20, [f] 1000–20	1400–3	$4SrO{\cdot}IrO_2$	
		1400–2, 1600–2	1400–18	$4SrO{\cdot}IrO_2$	
		1400–2	1540–2	$4SrO{\cdot}IrO_2 + SrO$	
		1400–2	1550–2	$4SrO{\cdot}IrO_2 + SrO$	
		1400–2	1525–2	$4SrO{\cdot}IrO_2$	
		1400–2	1535–2	$4SrO{\cdot}IrO_2$	
		1400–2	1600–2	$4SrO{\cdot}IrO_2 + SrO$	
75	25	[f] 900–3	[d] 800–17	low $-4SrO{\cdot}IrO_2 + 2SrO{\cdot}3IrO_2 + ySrO{\cdot}IrO_2$ $(4 > y > 2)$	Nonequilibrium.
			[f] 800–20	low $-4SrO{\cdot}IrO_2 + xSrO{\cdot}IrO_2$ $(x > 2) + SrCO_3 + ySrO{\cdot}IrO_2$ $(4 > y > 2)$	Nonequilibrium.
			900–2	low $-4SrO{\cdot}IrO_2 + xSrO{\cdot}IrO_2$ $(x > 2)$	Nonequilibrium.
			900–17	$xSrO{\cdot}IrO_2$ $(x > 2)$ + low $-4SrO{\cdot}IrO_2$	Nonequilibrium.
		[f] 900–3	[d] 900–17	low $-4SrO{\cdot}IrO_2 + 2SrO{\cdot}IrO_2 + ySrO{\cdot}IrO_2$ $(4 > y > 2)$	Nonequilibrium.
		[f] 800–20, [f] 1000–20, [f] 1000–21	900–65	$2SrO{\cdot}IrO_2$ + low $-4SrO{\cdot}IrO_2 + xSrO{\cdot}IrO_2$ $(x > 2)$	Nonequilibrium.
		[f] 900–2	[d] 900–66	low $-4SrO{\cdot}IrO_2 + 2SrO{\cdot}IrO_2 + ySrO{\cdot}IrO_2$ $(4 > y > 2)$	Nonequilibrium.
		900–2	[e] 900–71	low $-4SrO{\cdot}IrO_2 + 2SrO{\cdot}IrO_2$	Nonequilibrium.
		[f] 800–20, [f] 1000–20, [f] 1000–21, 1300–2	990–18	$4SrO{\cdot}IrO_2 + 2SrO{\cdot}IrO_2 + xSrO{\cdot}IrO_2$ $(x > 2)$	Nonequilibrium.
			1000–2	$xSrO{\cdot}IrO_2$ $(x > 2) + 4SrO{\cdot}IrO_2$ + low $-4SrO{\cdot}IrO_2$	Nonequilibrium.
		[f] 900–2	[d] 1000–2	$ySrO{\cdot}IrO_2$ $(4 > y > 2)$ + low $-4SrO{\cdot}IrO_2$	Nonequilibrium.
		1300–2	1000–18	$2SrO{\cdot}IrO_2 + 4SrO{\cdot}IrO_2$	
		1300–2	1000–19	$2SrO{\cdot}IrO_2$ + unidentified phase	Quenched in ice water; unidentified phase probably a hydrate.
		900–2	[e] 1000–19	$2SrO{\cdot}IrO_2$ + low $-4SrO{\cdot}IrO_2$	Nonequilibrium.
		[f] 800–20	[f] 1000–20	low $-4SrO{\cdot}IrO_2 + xSrO{\cdot}IrO_2$ $(x > 2) + 2SrO{\cdot}IrO_2$	Nonequilibrium.
		[f] 800–20, [f] 1000–20	[f] 1000–20	low $-4SrO{\cdot}IrO_2 + xSrO{\cdot}IrO_2$ $(x > 2) + 2SrO{\cdot}IrO_2$	Nonequilibrium.
		[f] 800–20, [f] 1000–20, [f] 1000–20, 1300–2	1000–96	$2SrO{\cdot}IrO_2 + 4SrO{\cdot}IrO_2 + xSrO{\cdot}IrO_2$ $(x > 2)$	Nonequilibrium.
		1000–20	1100–68	$2SrO{\cdot}IrO_2 + xSrO{\cdot}IrO_2$ $(x > 2) + 4SrO{\cdot}IrO_2$	Nonequilibrium.
		[f] 800–20, [f] 1000–20, [f] 1000–20	1100–288	$2SrO{\cdot}IrO_2 + 4SrO{\cdot}IrO_2$	
		[f] 800–20, [f] 1000–20, [f] 1000–20	[e] 1100–288	$2SrO{\cdot}IrO_2 + 4SrO{\cdot}IrO_2$ + low $-4SrO{\cdot}IrO_2$	Nonequilibrium.
		1000–20	1200–2	$2SrO{\cdot}IrO_2 + 4SrO{\cdot}IrO_2$	
		1000–20	1300–2	$2SrO{\cdot}IrO_2 + 4SrO{\cdot}IrO_2$	
		[f] 800–20, [f] 1000–20, [f] 1000–20, 1300–2, 1300–2, 1000–19	1400–2	$2SrO{\cdot}IrO_2 + 4SrO{\cdot}IrO_2$	1000–19 Heat quenched in ice water.
71	29	[f] 900–2	[d] 1000–2	$2SrO{\cdot}IrO_2$ + low $-4SrO{\cdot}IrO_2$	Nonequilibrium.

Footnotes at end of table.

TABLE 1. *Experimental data for compositions in the* $SrO-IrO_2-Ir$ *system*—Continued

Composition		Heat treatment[a]		X-ray diffraction analyses[g]	Remarks
SrO	IrO_2	Previous[h]	Final		
Mol%	*Mol%*	*°C–h*	*°C–h*		
66.6	33.3		[f]800–67	$2SrO{\cdot}3IrO_2 + xSrO{\cdot}IrO_2$ $(x>2)$ + low − $4SrO{\cdot}IrO_2 + ySrO{\cdot}IrO_2$ $(4>y>2)$	Nonequilibrium.
		[f]800–20	[f]800–19	$2SrO{\cdot}3IrO_2 + ySrO{\cdot}IrO_2$ $(4>y>2)$ + low − $4SrO{\cdot}IrO_2 + xSrO{\cdot}IrO_2$ $(x>2)$	Nonequilibrium.
			[f]800–20	$2SrO{\cdot}3IrO_2 + ySrO{\cdot}IrO_2$ $(4>y>2)$ + low − $4SrO{\cdot}IrO_2 + xSrO{\cdot}IrO_2$ $(x>2)$	Nonequilibrium.
		[f]800–20, [f]800–19	[f]850–20	$2SrO{\cdot}IrO_2$ + low − $4SrO{\cdot}IrO_2 + 2SrO{\cdot}3IrO_2$	Nonequilibrium.
		[f]900–2	[d]900–17	$2SrO{\cdot}IrO_2 + 2SrO{\cdot}3IrO_2$	Nonequilibrium.
		[f]900–2	[d]1000–2	$2SrO{\cdot}IrO_2 + 2SrO{\cdot}3IrO_2$	Nonequilibrium.
		[f]800–67	[f]1000–20	$2SrO{\cdot}IrO_2$	
		[f]800–67, [f]1000–20	[f]1000–20	$2SrO{\cdot}IrO_2$	
		[f]800–67, [f]1000–20, [f]1000–20, 1500–2	1000–22	$2SrO{\cdot}IrO_2 + 4SrO{\cdot}IrO_2 + Ir$	Nonequilibrium.
			1100–0.5	$2SrO{\cdot}IrO_2$	
		[f]800–67, [f]1000–20, [f]1000–20	1100–20	$2SrO{\cdot}IrO_2$	
		[f]800–67, [f]1000–20, [f]1000–20	1300–63	$2SrO{\cdot}IrO_2$	
		[f]800–67, [f]1000–20, [f]1000–20	1440–2	$2SrO{\cdot}IrO_2$	
		[f]800–67, [f]1000–20, [f]1000–20	1445–2	$2SrO{\cdot}IrO_2 + 4SrO{\cdot}IrO_2$	
		[f]800–67, [f]1000–20, [f]1000–20	1450–2	$2SrO{\cdot}IrO_2 + 4SrO{\cdot}IrO_2$	
		[f]800–67, [f]1000–20, [f]1000–20	1500–2	$4SrO{\cdot}IrO_2 + 2SrO{\cdot}IrO_2 + Ir$	Nonequilibrium.
60	40	[f]900–3	[d]800–17	$2SrO{\cdot}3IrO_2$ + low − $4SrO{\cdot}IrO_2$	Nonequilibrium.
			[f]800–20	$2SrO{\cdot}3IrO_2 + xSrO{\cdot}IrO_2$ $(x>2)$ + low − $4SrO{\cdot}IrO_2 + ySrO{\cdot}IrO_2$ $(4>y>2)$	Nonequilibrium.
			[f]800–408	$2SrO{\cdot}3IrO_2 + xSrO{\cdot}IrO_2$ $(x>2) + ySrO{\cdot}IrO_2$ $(4>y>2)$	Nonequilibrium.
		[f]900–3	[d]900–17	$2SrO{\cdot}3IrO_2 + 3SrO{\cdot}2IrO_2$ + low − $4SrO{\cdot}IrO_2$	Nonequilibrium.
		[f]800–20, [f]1000–20, [f]1000–21	900–65	$3SrO{\cdot}2IrO_2 + SrO{\cdot}IrO_2 + zSrO{\cdot}IrO_2$ $(2>z>1)$	Nonequilibrium.
		[f]900–2	[d]900–66	$2SrO{\cdot}3IrO_2 + 2SrO{\cdot}IrO_2 + xSrO{\cdot}IrO_2$ $(x>2)$	Nonequilibrium.
			[f]1000–2	$zSrO{\cdot}IrO_2$ $(2>z>1) + SrO{\cdot}IrO_2$	Nonequilibrium.
		1300–2	1000–18	$2SrO{\cdot}IrO_2 + SrO{\cdot}IrO_2$	
		[f]800–20	[f]1000–20	$3SrO{\cdot}2IrO_2 + SrO{\cdot}IrO_2 + zSrO{\cdot}IrO_2$ $(2>z>1)$	Nonequilibrium.
		[f]800–20, [f]1000–20	[f]1000–21	$3SrO{\cdot}2IrO_2 + SrO{\cdot}IrO_2 + zSrO{\cdot}IrO_2$ $(2>z>1)$	Nonequilibrium.
		[f]800–20, [f]1000–20, [f]1000–21	1100–68	$3SrO{\cdot}2IrO_2 + SrO{\cdot}IrO_2 + zSrO{\cdot}IrO_2$ $(2>z>1)$ + $2SrO{\cdot}IrO_2$	Nonequilibrium.
		[f]800–20, [f]1000–20, [f]1000–21	1100–288	$3SrO{\cdot}2IrO_2 + 2SrO{\cdot}IrO_2 + zSrO{\cdot}IrO_2$ $(2>z>1)$	Nonequilibrium.
		[f]800–20, [f]1000–20, [f]1000–21	[e]1100–288	$3SrO{\cdot}2IrO_2 + 2SrO{\cdot}IrO_2 + SrO{\cdot}IrO_2$	Nonequilibrium.
		[f]800–20, [f]1000–20, [f]1000–21	1200–2	$3SrO{\cdot}2IrO_2 + zSrO{\cdot}IrO_2$ $(2>z>1) + SrO{\cdot}IrO_2$	Nonequilibrium.
		[f]800–20, [f]1000–20, [f]1000–21	1250–42	$2SrO{\cdot}IrO_2 + Ir$	
			1300–2	$2SrO{\cdot}IrO_2 + Ir$	
57	43		[f]800–408	$2SrO{\cdot}3IrO_2 + xSrO{\cdot}IrO_2$ $(x>2) + ySrO{\cdot}IrO_2$ $(4>y>2)$	Nonequilibrium.
			900–3	$2SrO{\cdot}3IrO_2 + 2SrO{\cdot}IrO_2 + 3SrO{\cdot}2IrO_2 + zSrO{\cdot}IrO_2$ $(2>z>1) + SrO{\cdot}IrO_2$	Nonequilibrium.
		[f]900–2	[d]900–66	$2SrO{\cdot}3IrO_2 + 2SrO{\cdot}IrO_2$	Nonequilibrium.
		900–3	[e]1000–19	$SrO{\cdot}IrO_2 + 3SrO{\cdot}2IrO_2$	Nonequilibrium.
50	50		750–17	$2SrO{\cdot}3IrO_2 + SrO{\cdot}IrO_2$	Nonequilibrium.
			[f]800–19	$2SrO{\cdot}3IrO_2 + SrO{\cdot}IrO_2$	Nonequilibrium.
			[f]800–67	$2SrO{\cdot}3IrO_2 + SrO{\cdot}IrO_2$	Nonequilibrium.
			[f]850–20	$2SrO{\cdot}3IrO_2 + SrO{\cdot}IrO_2$	Nonequilibrium.
		[f]900–2	[d]900–17	$2SrO{\cdot}3IrO_2 + ySrO{\cdot}IrO_2$ $(4>y>2)$ + $SrO{\cdot}IrO_2$	Nonequilibrium.
		[f]900–2	[d]1000–2	$SrO{\cdot}IrO_2 + 2SrO{\cdot}3IrO_2$	Nonequilibrium.

Footnotes at end of table.

418-535 OL - 71 - 4

TABLE 1. *Experimental data for compositions in the* $SrO-IrO_2-Ir$ *system*—Continued

Composition		Heat treatment[a]		X-ray diffraction analyses[g]	Remarks
SrO	IrO_2	Previous[b]	Final		
Mol%	*Mol%*	*°C–h*	*°C–h*		
		[f] 800–67	[f] 1000–20	$SrO \cdot IrO_2 + 2SrO \cdot 3IrO_2$	Nonequilibrium.
		[f] 800–67, [f] 1000–20	[f] 1000–20	$SrO \cdot IrO_2$	
		[f] 800–67, [f] 1000–20, [f] 1000–20	[f] 1000–288	$SrO \cdot IrO_2$	
		[f] 800–67, [f] 1000–20, [f] 1000–20, 1350–2	1005–17	$SrO \cdot IrO_2$	$SrO \cdot IrO_2$ reformed from dissociation products.
		[f] 800–67, [f] 1000–20, [f] 1000–20	1100–20	$SrO \cdot IrO_2$	
		[f] 800–67, [f] 1000–20, [f] 1000–20	1100–288	$SrO \cdot IrO_2$	
		[f] 800–67, [f] 1000–20, [f] 1000–20	[e] 1100–288	$SrO \cdot IrO_2$	
		[f] 800–67, [f] 1000–20, [f] 1000–20	1200–2	$SrO \cdot IrO_2$	
		[f] 800–67, [f] 1000–20, [f] 1000–20	1205–2	$SrO \cdot IrO_2 + 2SrO \cdot IrO_2 + Ir$	
		[f] 800–67, [f] 1000–20, [f] 1000–20	[e] 1300–2	$2SrO \cdot IrO_2 + Ir$	
		[f] 800–67, [f] 1000–20 [f] 1000–20	1300–18	$2SrO \cdot IrO_2 + Ir$	
		[f] 800–67, [f] 1000–20, [f] 1000–20	1300–63	$2SrO \cdot IrO_2 + Ir$	
		[f] 800–67, [f] 1000–20, [f] 1000–20	1350–2	$2SrO \cdot IrO_2 + Ir$	
		1000–18	1650–4	$Ir + SrO + SrCO_3$	Nonequilibrium; $SrCO_3$ formed on cooling.
47	53		800–18	$2SrO \cdot 3IrO_2 + SrO \cdot IrO_2$	Nonequilibrium.
43	57	[f] 900–2	[f] 1000–2	$2SrO \cdot 3IrO_2 + SrO \cdot IrO_2$	Nonequilibrium.
			[f] 1000–168	$SrO \cdot IrO_2 + IrO_2$	
40	60		700–18	$2SrO \cdot 3IrO_2 + IrO_2$	Nonequilibrium.
		700–18	700–18	$2SrO \cdot 3IrO_2 + IrO_2$	Nonequilibrium.
		700–18, 700–18	700–19	$2SrO \cdot 3IrO_2 + IrO_2$	Nonequilibrium.
		700–18, 700–18, 700–19	700–66	$2SrO \cdot 3IrO_2 + IrO_2$	Nonequilibrium; trace amount of IrO_2.
		700–18, 700–18, 700–19, 700–66	700–456	$2SrO \cdot 3IrO_2 + IrO_2$	Nonequilibrium; trace amount of IrO_2.
			[f] 800–20	$2SrO \cdot 3IrO_2 + IrO_2$	Nonequilibrium.
			850–17	$SrO \cdot IrO_2 + 2SrO \cdot 3IrO_2 + IrO_2$	Nonequilibrium.
		[f] 900–2	[d] 900–17	$2SrO \cdot 3IrO_2 + IrO_2 + SrO \cdot IrO_2$	Nonequilibrium.
			[e] 900–19	$2SrO \cdot 3IrO_2 + IrO_2 + SrO \cdot IrO_2$	Nonequilibrium.
		[f] 800–20	[f] 1000–20	$2SrO \cdot 3IrO_2 + IrO_2$	Nonequilibrium.
		[f] 800–20, [f] 1000–20	[f] 1000–21	$2SrO \cdot 3IrO_2 + IrO_2 + SrO \cdot IrO_2$	Nonequilibrium.
		[f] 800–20, [f] 1000–20, [f] 1000–21	[e] 1000–312	$2SrO \cdot 3IrO_2 + IrO_2 + SrO \cdot IrO_2$	Nonequilibrium.
		[f] 800–20, [f] 1000–20, [f] 1000–21	1000–408	$SrO \cdot IrO_2 + IrO_2$	
33.3	66.6		[f] 800–67	$2SrO \cdot 3IrO_2 + IrO_2$	Nonequilibrium.
		[f] 800–67	[f] 1000–20	$2SrO \cdot 3IrO_2 + IrO_2$	Nonequilibrium.
		[f] 800–67, [f] 1000–20	[f] 1000–20	$2SrO \cdot 3IrO_2 + IrO_2$	Nonequilibrium.
		[f] 800–67, [f] 1000–20, [f] 1000–20	1015–2	$2SrO \cdot 3IrO_2 + IrO_2$	Nonequilibrium.
		[f] 800–67, [f] 1000–20, [f] 1000–20	1020–2	$2SrO \cdot 3IrO_2 + IrO_2$	Nonequilibrium.
		[f] 800–67, [f] 1000–20, [f] 1000–20	1025–2	$2SrO \cdot 3IrO_2 + SrO \cdot IrO_2 + Ir + IrO_2$	Nonequilibrium.
		[f] 800–67, [f] 1000–20, [f] 1000–20	1050–2	$SrO \cdot IrO_2 + Ir$	
		[f] 800–67, [f] 1000–20,			

Footnotes at end of table.

TABLE 1. *Experimental data for compositions in the* $SrO-IrO_2-Ir$ *system*—Continued

Composition		Heat treatment[a]		X-ray diffraction analyses[g]	Remarks
SrO	IrO_2	Previous[h]	Final		
Mol%	*Mol%*	*°C–h*	*°C–h*		
		[f]1000–20	1100–20	$SrO \cdot IrO_2 + Ir$	
		[f]800–67, [f]1000–20,			
		[f]1000–20	1200–2	$SrO \cdot IrO_2 + Ir$	
		[f]800–67, [f]1000–20,			
		[f]1000–20	1205–2	$3SrO \cdot 2IrO_2 + Ir$	Nonequilibrium.
		[f]800–67, [f]1000–20,			
		[f]1000–20	1210–2	$3SrO \cdot 2IrO_2 + Ir$	Nonequilibrium.
		[f]800–67, [f]1000–20,			
		[f]1000–20	1215–2	$3SrO \cdot 2IrO_2 + Ir$	Nonequilibrium.
		[f]800–67, [f]1000–20,			
		[f]1000–20	1225–2	$3SrO \cdot 2IrO_2 + Ir + 2SrO \cdot IrO_2$	Nonequilibrium.
		[f]800–67, [f]1000–20,			
		[f]1000–20	1300–2	$3SrO \cdot 2IrO_2 + Ir$	Nonequilibrium.
		[f]800–67, [f]1000–20,			
		[f]1000–20	1300–18	$3SrO \cdot 2IrO_2 + 2SrO \cdot IrO_2$	Nonequilibrium.
		[f]800–67, [f]1000–20,			
		[f]1000–20	1350–2	$2SrO \cdot IrO_2 + Ir$	
		[f]800–67, [f]1000–20,			
		[f]1000–20	1400–2	$2SrO \cdot IrO_2 + Ir$	

[a] All specimens were heat treated in open platinum tubes and air quenched unless otherwise indicated. All temperatures listed applies to (IPTS 1968).

[b] Sealed gold tube container; quenched in ice water.

[c] Open fused silica tube container; air quenched.

[d] Specimen was placed in an open gold tube, which was placed into a larger platinum tube containing a calculated amount of PtO_2. The platinum tube was then sealed. Oxygen pressure calculated to be approximately 30 atm (3.03975×10^6 N/m^2).

[e] Sealed platinum tube container; quenched in ice water.

[f] Open gold tube container; air quenched.

[g] Phases identified are given in order of the relative amount present at room temperature; of those intermediate phases listed the following are believed to be metastable in air at atmospheric pressure, low $4SrO \cdot IrO_2$, $xSrO \cdot IrO_2$ $(x > 2)$, $ySrO \cdot IrO_2$ $(4 > y > 2)$, $zSrO \cdot IrO_2$ $(2 > z > 1)$, $3SrO \cdot 2IrO_2$, and $2SrO \cdot 3IrO_2$.

[h] No entry under "previous" column indicates the specimen received no prior heat treatment.

or three solid phases are in equilibrium for a given temperature. By following the oxygen reaction lines in figure 1, the specific phases in equilibrium can be established. For example, at 1205 °C, three phases (2:1, 1:1, Ir) exist in equilibrium and for temperatures greater than 1205 °C and less than 1445 °C, two phases (2:1, Ir) exist as illustrated by tie line D. The behavior of any arbitrary mixture, e.g., 60:40, can be established in a similar manner by following the appropriate oxygen reaction line.

The binary-type phase diagram given in the top portion of figure 1 is a projection of certain elements of the three dimensional ternary system $SrO-IrO_2-Ir$ on a two dimensional plane figure. The diagram in effect represents a composite of the SrO-Ir and $SrO-IrO_2$ systems. As the temperature is increased, the compositions of the solid phases change by an apparent oxygen loss to those indicated by the SrO-Ir join. By illustrating a dissociation as a type of phase transition or decomposition in which the vapor phase is ignored, a simple binary representation of the phase relations of the ternary system can be given. This method of illustration has been employed by a number of investigators [9, 10]. The diagram can be interpreted as a binary system and the application of the lever law is valid.

It was found in earlier work that IrO_2 dissociates to Ir metal and oxygen at 1021 °C in air at atmospheric pressure [2]. This dissociation is a reversible process. Other investigators [11, 12] have reported that IrO_2 combines with oxygen to form IrO_3, which is stable only in the gaseous state. Stoichiometric IrO_2 apparently is the only condensed Ir-oxide phase stable in an air environment at atmospheric pressure. Furthermore, this study did not detect any evidence for solid solutions in the system which would indicate oxygen-deficient oxides or oxygen-rich metal phases.

3.2. Compounds

a. Stable Phases

Randall and Katz [13] previously reported that $4SrO \cdot PtO_2$ and $4SrO \cdot IrO_2$ (4:1) have the same type structure (K_4CdCl_6 type) but give no specific x-ray data on the Ir compound. Table 2 gives the x-ray diffraction powder pattern of the $4SrO \cdot IrO_2$ compound indexed on the basis of a hexagonal (rhombohedral) cell with $a = 9.736$ Å and $c = 11.886$ Å.

The 4:1 compound is stable only between 1220 and 1540 °C. At the higher temperature, the phase dissociates to SrO, Ir, and oxygen, while at temperatures below the minimum, 1220 °C, the phase slowly decomposes during prolonged heat treatments. The decomposition products generally are the $2SrO \cdot IrO_2$ (2:1) compound and another metastable phase $xSrO \cdot IrO_2$ $(x > 2)$. The stability of the 4:1 compound was established by heating a specimen first above and

then below the dissociation temperature. The 4:1 compound always reformed from the dissociation products.

TABLE 2. *X-ray diffraction powder data for the* $4SrO \cdot IrO_2$ *and low* $4SrO \cdot IrO_2$ *compounds* (CuKα *Radiation*)[a]

$4SrO \cdot IrO_2$[b]				Low $4SrO \cdot IrO_2$[c]			
d(Å)				d(Å)			
hkl	obs	calc	I/I_0	*hkl*	obs	calc	I/I_0
110	4.87	4.87	74	002	9.43	9.39	4
012		4.86		100	8.56	8.54	11
202	3.440	3.439	3	102	6.316	6.318	15
113	3.075	3.073	52	111	4.769	7.768	15
300	2.812	2.811	100	004	4.699	4.697	10
122		2.809		112	4.367	4.365	16
024	2.430	2.429	54	200	4.269	4.269	6
131	2.295	2.295	14	113	3.872	3.873	11
214	2.175	2.173	50	114	3.400	3.400	3
223	2.075	2.074	30	210	3.228	3.227	7
042	1.987	1.987	5	212	3.053	3.052	4
006	1.981	1.981	7	115	2.990	2.988	82
125	1.905	1.906	4	106	2.940	2.940	5
134	1.837	1.838	21	300	2.845	2.846	100
116	1.835	1.835	24	214	2.660	2.660	4
404	1.719	1.719	6	116	2.642	2.643	26
051	1.668	1.670	9	206	2.523	2.525	7
413		1.669		221	2.443	2.444	7
330	1.621	1.623	35	304	2.434	2.434	9
502		1.622		310	2.369	2.368	3
324		1.621		311	2.350	2.350	4
241	1.5791	1.5794	3	008		2.348	
422	1.5389	1.5391	7	312	2.296	2.296	5
226	1.5362	1.5365	12	216	2.246	2.247	19
511	1.5019	1.5023	3	314	2.114	2.115	3
333		1.5017		306	2.106	2.106	3
054	1.4667	1.4667	12	402	2.082	2.082	6
018	1.4630	1.4633	14	225	2.061	2.061	38
600	1.4054	1.4053	17	320	1.960	1.959	4
208	1.4017	1.4013	14	226	1.936	1.937	13
137	1.3739	1.3741	3	0, 0, 10	1.878	1.879	6
520	1.3498	1.3502	14	411	1.854	1.854	3
34		1.3500		308	1.811	1.811	6
416	1.3481	1.3482	11	413	1.786	1.786	2
128	1.3470	1.3467	17	219	1.753	1.753	6
425	1.3235	1.3236	3	415,	1.669	1.669	22
161	1.2783	1.2784	7	326	1.661	1.661	8
523		1.2780		330	1.643	1.643	16
119	1.2746	1.2746	6	421	1.608	1.608	4
612	1.2566	1.2568	6	416	1.601	1.601	11
318	1.2538	1.2541	5	3, 0, 10	1.567	1.568	13
048	1.2145	1.2145	3	334	1.550	1.551	4
532	1.1805	1.1806	4	510	1.533	1.534	3
238	1.1782	1.1783	10	511	1.529	1.529	3
229	1.1610	1.1608	4	2, 2, 10	1.493	1.494	5
615	1.1310	1.1310	3	513	1.490	1.490	5
704	1.1164	1.1163	13	600	1.4231	1.4231	10
508	1.1147	1.1148	7	3, 0, 12	1.3715	1.3717	5
624	1.0881	1.0881	5	338	1.3463	1.3464	3
541	1.0753	1.0752	2	509	1.3218	1.3217	4
419	1.0730	1.0729	3	2, 2, 12		1.3215	
630	1.0625	1.0623	6	525	1.2847	1.2849	5
452		1.0622		0, 0, 15	1.2527	1.2524	4
158	1.0605	1.0606	5	519	1.2361	1.2359	6
1,3,10	1.0596	1.0596	5	1, 1, 15	1.2135	1.2139	4
446	1.0370	1.0370	2	3, 0, 14		1.2138	
271	1.0263	1.0263	2	4, 1, 12	1.1986	1.1986	2
722	1.0150	1.0150	4	528	1.1814	1.1816	1
084	0.9936	0.9934	4	445	1.1711	1.1711	3
274	.9734	.9733	3	446	1.1468	1.1468	3
900	.9368	.9369	6	3,3,12	1.1337	1.1335	5
372		.9368		2,2,15	1.1163	1.1166	3
538	.9357	.9357	7	3,1,15	1.1069	1.1071	2
3,0,12	.9343	.9342	11	3,2,14		1.1070	
820	.9200	.9200	3	5,2,10	1.1054	1.1055	3
268	.9188	.9189	4	715	1.0830	1.0830	3
651	.8815	.8815	3	630	1.0758	1.0758	4
740	.8745	.8744	3	716	1.0635	1.0637	3
4,1,12	.8722	.8722	4	6,0,12	1.0531	1.0530	2
808	.8597	.8597	7	4,1,15	1.0390	1.0394	3
654	.8473	.8472	6	3,3,14		1.0394	
3,3,12	.8455	.8455	8				
915	.8285	.8285	2				
384	.8227	.8227	5				
660	.8113	.8114	2				
6,0,12	.8096	.8096	6				
924	.8001	.8001	6				

[a] d-Interplanar spacing, I/I_0—relative intensity.

[b] X-ray pattern obtained from specimen heat treated at 1400 °C for 2 h. Indexing based on hexagonal cell with $a = 9.736$ and $c = 11.886$ Å.

[c] X-ray pattern obtained from specimen heat treated at 900 °C for 66 h. Indexing based on hexagonal cell with $a = 9.860$ and $c = 18.786$ Å; Low $4SrO \cdot IrO_2$ is probably metastable.

It has been reported that $4SrO \cdot PtO_2$ hydrolyzes readily on contact with water [13]. This study did not detect any hydrolysis of the 4:1 Ir compound when in contact with water at temperature up to 140 °C. However, the x-ray powder pattern of a specimen having 4:1 composition heated at 1440 °C and quenched in water indicated only the 2:1 compound and an unidentified phase (probably a hydrate). A similar experiment utilizing liquid nitrogen instead of water showed only the 4:1 compound.

Randall, Katz, and Ward [14] previously have reported the existence of a $2SrO \cdot IrO_2$ compound having the body-centered tetragonal, K_2NiF_4 type-structure with $a = 3.89$ Å and $c = 12.92$ Å. The cell dimensions for the 2:1 compound in this study are in accord. The 2:1 compound is stable in air at atmospheric pressure up to 1445 °C, the dissociation temperature. The dissociation products when heated at 1100 °C reform the 2:1 compound indicating that it is a stable phase.

An atmospheric pressure form of $SrO \cdot IrO_2$ (1:1) was reported by Longo and Kafalas [15], who indexed its x-ray pattern on the basis of a unit cell with monoclinic symmetry and the following cell dimensions: $a = 5.60$ Å, $b = 9.62$ Å, $c = 14.17$ Å, and $\beta = 93°16'$.

The x-ray diffraction data obtained in the present study indicates good agreement with the cell dimensions reported. The 1 : 1 compound is stable in air below 1205 °C, the dissociation temperature.

b. Metastable Phases

The phase listed as low $4SrO \cdot IrO_2$ (fig. 1) formed readily in air at temperatures of 800 to 1000 °C and was detected at several compositions rich in SrO. Various experiments failed to produce a completely single phase specimen and residual amounts of other phases always persisted. The composition of the compound considered most likely is 4 : 1 since this mixture always produced the greatest quantity of the phase. In all probability this phase is metastable and forms only on heating. Prolonged heat treatments of the stable 4 : 1 compound up to 8 days at 950 °C, failed to reform the low 4:1 compound. Indexing of the x-ray pattern of the phase was accomplished by a trial and error method after a literature search did not reveal any compounds structurally similar to the low $4SrO \cdot IrO_2$. The x-ray powder pattern is given in table 2. It was indexed on the basis of a hexagonal cell with $a = 9.860$ Å and $c = 18.786$ Å. The low 4:1 compound metastably decomposes at 1005 °C in air forming the 4 : 1 and 2 : 1 compounds. It is somewhat unusual that the metastable low 4 : 1 decomposes to the 4 : 1 compound which itself is metastable at 1005 °C.

The $3SrO \cdot 2IrO_2$ (3:2) compound forms (probably metastable) in combination with other phases in air at atmospheric pressure between 1000 and 1200 °C. The phase also occurs as a dissociation product when a mixture $SrO:2IrO_2$ is heated at 1300 °C. Longo and Kafalas [15] have reported previously the existence of $3SrO \cdot 2IrO_2$, as a high pressure phase (synthesized at 10 kbar (1.0×10^9 N/m²) 1000 °C) with perovskite-related structure and a body-centered tetragonal unit cell with $a = 3.90$ Å and $c = 20.90$ Å. This phase is apparently similar to $3SrO\ 2TiO_2$, the structure of which has been proposed by Ruddlesden and Popper [16, 17]. The values obtained in the present study are in good agreement with those reported by Longo and Kafalas [15]. Several attempts to reform the 3:2 compound from the dissociation products were unsuccessful, indicating perhaps it is a metastable phase in air.

The $xSrO \cdot IrO_2 (x > 2)$ compound forms (probably metastable) in air over a wide range of compositions and always in combination with other phases. The specific composition of the $xSrO \cdot IrO (x > 2)$ compound is unknown; however mixtures richer in SrO than the 2:1 molar ratio yielded the greatest quantity of the phase. Its x-ray diffraction pattern, given in table 3, was indexed on the basis of a hexagonal cell with $a = 10.307$ Å and $c = 12.634$ Å. Trace amounts of the $xSrO \cdot IrO_2 (x > 2)$ compound form as one of the decomposition products when the 4:1 compound is given prolonged heat treatment at 1000 °C.

Table 3 gives the x-ray diffraction pattern for the $ySrO \cdot IrO_2 (4 > y > 2)$ compound indexed on the basis of a hexagonal cell with $a = 9.805$ Å and $c = 23.699$ Å. It exists at 900 to 1000 °C at various compositions and always occurs in combination with other phases. Attempts to prepare single phase specimens were not successful. The specific composition of the

TABLE 3. *X-ray diffraction powder data for the* $xSrO \cdot IrO_2$ $(x > 2)$ *and* $ySrO \cdot IrO_2$ $(4 > y > 2)$ *phases* (CuKα *radiation*) [a]

$xSrO \cdot IrO_2$ $(x > 2)$ [b]				$ySrO \cdot IrO_2$ $(4 > y > 2)$ [c]			
	d(Å)				d(Å)		
hkl	obs	calc	I/I_0	*hkl*	obs	calc	I/I_0
111	4.774	4.772	46	100	8.51	8.49	19
003	4.211	4.211	22	102	6.90	6.90	18
201		4.208		004	5.93	5.92	6
112	3.994	3.993	6	110	4.908	4.903	13
203	3.062	3.063	5	112	4.532	4.530	33
212	2.975	2.976	76	200	4.251	4.246	7
300		2.975		202	3.999	3.997	3
301	2.896	2.896	100	006	3.952	3.950	4
221	2.524	2.525	16	114	3.781	3.777	5
303	2.429	2.430	12	210	3.211	3.210	12
311		2.430		116	3.076	3.076	69
214	2.307	2.306	2	206	2.893	2.892	3
401	2.197	2.198	3	300	2.831	2.830	100
304	2.167	2.166	2	108	2.798	2.797	6
402	2.103	2.104	27	304	2.553	2.554	7
				118	2.536	2.536	28
				216	2.490	2.491	6
				305	2.429	2.430	7
				208		2.429	
				222	2.400	2.400	3
				310	2.356	2.355	5
				312	2.310	2.310	4
				225	2.178	2.177	13
				218		2.177	
				1,1,10	2.134	2.134	5
				226	2.082	2.083	30
				308	2.046	2.046	4
				1,1,11	1.973	1.972	3
				320	1.948	1.948	5
				228	1.888	1.889	12
				324	1.851	1.851	4
				318	1.843	1.843	4
				412	1.831	1.831	10
				3,0,10	1.817	1.817	5
				326	1.747	1.747	3
				2,2,10	1.703	1.704	3
				416	1.677	1.678	13
				330	1.634	1.634	9
				504	1.633	1.633	13
				332	1.619	1.619	6
				418	1.570	1.571	10
				2,2,12	1.537	1.538	4
				510	1.524	1.525	3
				600	1.415	1.415	8
				522	1.3507	1.3509	4
				526	1.2857	1.2857	5
				528	1.2354	1.2358	4

[a] d-Interplanar spacing, I/I_0 – relative intensity.

[b] X-ray pattern obtained from $3SrO:IrO_2$ mixture heat treated at 900 °C for 17 h. Indexing based on hexagonal cell with $a = 10.307$ and $c = 12.634$ Å; $xSrO \cdot IrO_2$ $(x > 2)$ is probably metastable.

[c] X-ray pattern obtained from $3SrO:IrO_2$ mixture heat treated at 1000 °C for 2 h. Indexing based on hexagonal cell with $a = 9.805$ and $c = 23.699$ Å; $ySrO \cdot IrO_2$ $(4 > y > 2)$ is probably metastable.

$ySrO \cdot IrO_2 (4 > y > 2)$ compound is unknown, however the x-ray patterns indicate its composition is probably between the 4:1 and 2:1 molar ratios. The $ySrO \cdot IrO_2 (4 > y > 2)$ compound forms only on heating and probably is metastable in air at atmospheric pressure.

The $zSrO \cdot IrO_2 (2 > z > 1)$ compound formed (probably metastable) predominately at the 3:2 molar ratio between 1000 and 1100 °C. This phase, always in combination with other phases, formed only on heating. Various experiments failed to produce a single phase specimen and the specific composition of the compound is also unknown. The unindexed x-ray diffraction powder pattern for the $zSrO \cdot IrO_2 (2 > z > 1)$ compound is given in table 4.[3]

The $2SrO \cdot 3IrO_2$ (2:3) compound was formed most readily and was detected during the preparation of almost every composition at 800 °C although never as single phase. Powder x-ray diffraction data for this phase is given in table 4. The pattern was indexed on the basis of a body-centered cubic cell with $a = 9.344$ Å. At 1025 °C the 2:3 compound dissociates to the 1:1 compound and Ir. Prolonged heating of the dissociation products failed to reform the 2:3 compound, indicating perhaps it is a metastable phase that forms only on heating. However, a mixture of the 1:1 compound and amorphous IrO_2 did form small amounts of the 2:3 phase, whereas crystalline IrO_2 and the 1:1 compound did not react. All experiments conducted in an effort to produce single phase specimens were unsuccessful. The composition considered most likely for the body-centered cubic phase is the 2:3 molar ratio. This mixture yielded the greatest quantity of the phase. Longo[4] has pointed out that the $2SrO \cdot 3IrO_2$ compound has similar intensities and unit cell dimensions to $La_4Re_6O_{19}$ [18]. However, the discrepancy in oxygen content has not been explained.

c. Compound Summary

Table 5 summarizes the x-ray and stability data for the intermediate phases detected in this study and those reported in the literature for the $SrO\text{-}IrO_2$ pseudobinary system. Of the eleven intermediate phases tabulated, nine were identified in this study. Three stable and six probably metastable phases occur in air at atmoshperic pressure.

Other investigators have generally used Ir metal as a starting material for the preparation of mixtures in the $SrO\text{-}IrO_2$ system. Several of the metastable phases detected in this study had a tendency to form only on heating and when utilizing amorphous IrO_2 as a starting material. For this reason others may not have detected the metastable phases.

Longo and Kafalas reported a series of compounds in the $SrO\text{-}IrO_2$ system with closely related perovskite-

TABLE 4. *X-ray diffraction powder data for* $zSrO \cdot IrO_2 (2 > z >)1$ *and* $2SrO \cdot 3IrO_2$ *(CuKα Radiation)*[a]

$zSrO \cdot IrO_2$ $(2 > z > 1)$[b]		$2SrO \cdot 3IrO_2$[c]			
		d(Å)			
d(Å)	I/I_0	hkl	obs	calc	I/I_0
7.2367	4	110	6.62	6.61	52
6.9154	6	200	4.68	4.67	37
5.6647	27	211	3.82	3.81	10
5.3326	4	220	3.307	3.303	14
[d]4.9374	19	310	2.957	2.955	100
4.6840	4	222	2.699	2.697	18
4.4734	12	321	2.498	2.497	74
3.8274	7	400	2.337	2.336	12
3.3445	6	330	2.202	2.202	7
3.2372	5	420	2.089	2.089	2
3.1486	7	422	1.906	1.907	12
[d]2.8482	100	510	1.833	1.832	44
2.8254	18	521	1.705	1.706	5
2.6859	17	530	1.602	1.602	15
2.5707	16	600	1.556	1.557	26
2.5149	3	611	1.5154	1.5157	13
2.2939	4	620	1.4771	1.4773	7
2.2435	4	541	1.4413	1.4417	4
2.1974	3	631	1.3778	1.3776	14
2.1435	4	444	1.3488	1.3486	5
2.1367	6	550	1.3213	1.3214	9
2.0882	5	640	1.2952	1.2957	2
2.0606	6	730	1.2269	1.2269	6
1.9997	6	651	1.1864	1.1866	8
1.9653	5	800	1.1679	1.1679	2
1.9517	8	741	1.1501	1.1501	1
1.9286	3	653	1.1165	1.1168	5
1.8656	7	660	1.1010	1.1011	6
1.7471	4	743	1.0862	1.0862	12
1.6695	3	910	1.0317	1.0318	3
[d]1.6466	7	761	1.0077	1.0075	4
1.6420	7	932	0.9637	0.9637	4
		941	.9438	.9438	4
		860	.9342	.9343	1
		10,2,2	.8990	.8991	3
		10,3,1	.8910	.8909	5
		961	.8602	.8601	4
		10,4,2	.8530	.8529	4
		11,1,0	.8459	.8459	5
		963	.8324	.8324	2
		970	.8194	.8195	2
		10,4,4	.8132	.8132	3
		972	.8072	.8072	4

[a] *d*-Interplanar spacing, I/I_0 relative intensity.

[b] X-ray pattern obtained from specimen $3SrO : 2IrO_2$ heat treated at 1000 °C for 2 h; $zSrO \cdot IrO_2 (2 > z > 1)$ is probably metastable.

[c] X-ray pattern obtained from specimen heat treated at 900 °C for 17 h. Indexing based on body-centered cubic cell with $a = 9.344$ Å; $2SrO \cdot 3IrO_2$ is probably metastable.

[d] These *d*-spacings in decreasing order may correspond to the hexagonal indices (110), (300), (330) based on $a = 9.87$ Å.

[3] The x-ray diffraction powder patterns for all the low temperature metastable hexagonal phases appear to be quite similar. An attempt was made to index the x-ray pattern for $zSrO \cdot IrO_2 (2 > z > 1)$ based on a hexagonal cell with $a = 9.87$ Å, assuming the *d* values indicated in table 4 correspond to the (110), (300), and (330) reflections. Although the *c* value necessary to account for all the data was unreasonable large, it seems possible the phase also has hexagonal symmetry.

[4] Personal communication.

TABLE 5. *Compounds in the* $SrO\text{-}IrO_2$ *system*

Composition	Symmetry	Unit cell (Å) a	b	c	β	Stability data	References
$4SrO \cdot IrO_2$	hexagonal (rhombohedral)	9.736		11.886		Stable in air at atmospheric pressure between 1220 and 1540 °C (dissociation temperature).	Present work.
Low $4SrO \cdot IrO_2$	hexagonal	9.860		18.786		Forms (probably metastable) in air at atmospheric pressure up to 1005 °C (metastable phase transformation).	Present work.
$xSrO \cdot IrO_2 (x > 2)$	hexagonal	10.307		12.634		Forms (probably metastable) in combination with other phases in air at atmospheric pressure at 900 °C.	Present work.
$ySrO \cdot IrO_2 (4 > y > 2)$	hexagonal	9.805		23.699		Forms (probably metastable) in combination with other phases in air at atmospheric pressure at 800 °C.	Present work.
$2SrO \cdot IrO_2$	tetragonal[a] (body-centered)					Stable in air at atmospheric pressure up to 1445 °C (dissociation temperature).	Present work.
		3.89		12.92			Randall, Katz, and Ward [14].
$zSrO \cdot IrO_2 (2 > z > 1)$	unindexed					Forms (probably metastable) in combination with other phases in air at atmospheric pressure at 1000 °C.	Present work.
$3SrO \cdot 2IrO_2$	tetragonal[a] (body-centered)	3.90		20.90		Synthesized at 10 kbar (1.0×10^9 N/m²) 1000 °C. Forms (probably metastable) in combination with other phases in air at atmospheric pressure at 1000 °C. Also occurs as a dissociation product when a mixture $SrO:2IrO_2$ is heated at 1300 °C.	Longo and Kafalas [15]. Present work.
$4SrO \cdot 3IrO_2$	tetragonal (body-centered)	3.93		28.4		Synthesized at 35 kbar (3.5×10^9 N/m²) 1000 °C. Phase not detected in air at atmospheric pressure.	Longo and Kafalas [15]. Present work.
$SrO \cdot IrO_2$	monoclinic[a]					Stable in air at atmospheric pressure up to 1205° (dissociation temperature).	Present work.
		5.60	9.62	14.17	93°16′		Longo and Kafalas [15].
High $SrO \cdot IrO_2$	orthorhombic	5.58	5.60	7.89		Synthesized at 45 kbar (4.5×10^9 N/m²) 1000 °C. Phase not detected in air at atmospheric pressure.	Longo and Kafalas [15]. Present work.
$2SrO \cdot 3IrO_2$	cubic (body-centered)	9.344				Forms (probably metastable) in air at atmospheric pressure up to 1025 °C (dissociation temperature).	Present work.

[a] Cell dimensions obtained in the present study are in good agreement.

type structure [15]. The structural series extends between the $SrO \cdot IrO_2$ and $2SrO \cdot IrO_2$ compounds and includes in addition to the end members, the $4SrO \cdot 3IrO_2$ and $3SrO \cdot 2IrO_2$ phases. Of these perovskite-related compounds the 1:1 and 4:3 apparently can be formed only at high pressures and thus were not detected in the present study.

With the exception of the 2:3 compound, all the low temperature metastable phases detected here have hexagonal or pseudohexagonal symmetry with a similar

a-dimension. It is possible that some undetermined structural relationship exists between these phases which could include the 2:3 compound as a member of the series. If this is true, the cubic symmetry designated for the 2:3 compound would represent a pseudocell and the true symmetry may be hexagonal.

4. References

[1] Schneider, S. J., Waring, J. L., and Tressler, R. E., J. Res. Nat. Bur. Stand. (U.S.), **69A** (Phys. and Chem.), No. 3, 245–254 (May–June 1965).

[2] McDaniel, C. L. and Schneider, S. J., J. Res. Nat. Bur. Stand. (U.S.), **71A** (Phys. and Chem.), No. 2, 119–123 (Mar.–Apr. 1967).

[3] McDaniel, C. L. and Schneider, S. J., J. Res. Nat. Bur. Stand. (U.S.), **72A** (Phys. and Chem.), No. 1, 27–37 (Jan.–Feb. 1968).

[4] Barber, C. R., Metrologia **5** [2], 35–44 (1969).

[5] Swanson, H. E., Gilfrich, N. T., and Ugrinic, G. M., Nat. Bur. Stand. (U.S.), Circ. 539, 68 pages (1955).

[6] Schumacher, E. E., J. Am. Chem. Soc. **48,** 396–405 (1926).

[7] Swanson, H. E., Fuyat, R. K., and Ugrinic, G. M., Nat. Bur. Stand. (U.S.), Circ. 539, 10 pages (1955).

[8] Swanson, H. E., Morris, M. C., and Evans, E. H., Nat. Bur. Stand. (U.S.), Monogr. 25, Sect. 4, 85 pages (1965).

[9] Muan, A., Am. J. Sci. **256,** 171–207 (1958).

[10] Negas, T. and Roth, R. S., J. Res. Nat. Bur. Stand. (U.S.), **73A** (Phys. and Chem.), No. 4, 431–442 (Nov.–Dec. 1969).

[11] Schafer, H. and Heitland, H. J., Z. Anorg. Allgem. Chem. **304,** 249 (1960).

[12] Cordfunke, E. H. P. and Meyer, G., Rec. Trav. Chim. **81,** 495–504 (1962).

[13] Randall, J. J. and Katz, L., Acta Cryst. **12,** 519–21 (1959).

[14] Randall, J. J., Katz, L., and Ward, R., J. Am. Chem. Soc. **79,** 266–7 (1957).

[15] Longo, J. M., Kafalas, J. A., and Arnott, R. J., J. Solid State Chem. **3,** (1971).

[16] Ruddlesden, S. N. and Popper, P., Acta Cryst. **10,** 538 (1957).

[17] Ruddlesden, S. N. and Popper, P., Acta Cryst. **11,** 54 (1958).

[18] Longo, J. M. and Sleight, A. W., Inorg. Chem. **7,** 108–111 (1968).

(Paper 75A3–662)

JOURNAL OF RESEARCH of the National Bureau of Standards—A. Physics and Chemistry
Vol. 75A, No. 3, May–June 1971

The Crystal Structure of $BaCa(CO_3)_2$ (barytocalcite)

B. Dickens and J. S. Bowen*

Institute for Materials Research, National Bureau of Standards, Washington, D.C. 20234

(February 3, 1971)

The barytocalcite phase of $BaCa(CO_3)_2$ crystallizes in the monoclinic unit cell $a=8.092(1)$ Å, $b=5.2344(6)$ Å, $c=6.544(1)$ Å, $\beta=106.05(1)°$ at 25 °C with cell contents of $2[BaCa(CO_3)_2]$. The structure previously reported by Alm is correct in its coarse details but has been redetermined here and refined to $R_w=0.028$, $R=0.023$ in space-group $P2_1/m$ using 1652 observed reflections. Corrections were made for absorption, isotropic extinction, and anomalous dispersion.

The structure of barytocalcite has an . . . ABCABC . . . stacking of cation layers and repeat every 3 layers. The calcite phase of $CaCO_3$ has an ABC cation layer sequence and repeats every 6 layers. The orientations of the CO_3 groups in barytocalcite are like the CO_3 group orientation in the aragonite phase of $CaCO_3$, and are rotated about 30° from the CO_3 group orientation in calcite. The cation layer sequence in aragonite is . . . ABAB . . . and the structure repeats every 2 layers.

The Ca ion in barytocalcite is coordinated to seven oxygens, including an edge of a CO_3 group, with Ca . . . O distances in the range 2.305(2) Å to 2.518(2) Å. The Ba ion is coordinated to five edges and one apex of the CO_3 groups with Ba . . . O distances ranging from 2.729(3) Å to 3.140(2) Å. The distances of the C atoms in the CO_3 groups from the planes of the O atoms are 0.025(5) Å and 0.022(4) Å for C(1) and C(2), respectively.

Key words: Aragonite; barium calcium carbonate; calcium carbonate; crystal structure; single crystal x-ray diffraction.

1. Introduction

The crystal structure of the barytocalcite phase of $BaCa(CO_3)_2$ has been redetermined in our program of structural investigations [1][1] on calcium carbonates, calcium phosphates, associated hydrates, and related compounds. The structural features in these compounds have important applications in understanding possible epitaxy, syntaxy, and substitutional solid solution in biological minerals such as hydroxyapatite ($Ca_5(PO_4)_3OH$) and calcite, aragonite and vaterite, the three phase of anhydrous $CaCO_3$.

From a consideration of the morphologies, *d*-spacings and possible space-groups of barytocalcite and calcite, Gossner and Mussgnug [2] gave a structure for barytocalcite which is a rearrangement of the calcite structure. They assumed the space-group to be $P2_1$. Alm [3] used a relatively large (0.3 mm) single crystal of barytocalcite and unfiltered Cu radiation to collect photographic data from the *h*0*l*, *h*1*l*, *hk*0 and *hkh* levels. He also assumed the space-group to be $P2_1$, rather than $P2_1/m$, on steric considerations which are invalid. The structure he gave for barytocalcite differs from that given by Gossner and Mussgnug in the orientations of the CO_3 groups. However, Alm made no corrections for what must have been considerable absorption, gave no standard deviations on any parameters and used limited film data. The structure of barytocalcite was, therefore, poorly known by modern standards, and has been redetermined here.

2. Data Collection and Structure Refinement

The crystal used in the data collection is an approximate sphere, radius 0.094(3) mm, ground from a crystal from mineral sample R13868 (from Cumberland, England) obtained from the National Museum of Natural History, Smithsonian Institution, Washington, D.C., and supplied by J. S. White, Jr. It was mounted in our usual way [4].

formula (ideal): $BaCa(CO_3)_2$ (barytocalcite phase).
cell: monoclinic
$a=8.092(1)$ Å at 25 °C
$b=5.2344(6)$ Å
$c=6.544(1)$ Å
$\beta=106.05(1)°$
volume = 266.4 Å^3
space-group $P2_1/m$; cell contents $2[BaCa(CO_3)_2]$
reciprocal lattice extinctions, $0k0: k=2n+1$
calculated density 3.72 g·cm^{-3}; observed density 3.71 g·cm^{-3} [5].

In the determination of the unit cell and in the collection and processing of data, the general procedure

*Research Associate of the American Dental Association at the National Bureau of Standards, Washington, D.C. 20234.

[1] Figures in brackets indicate the literature references at the end of this paper.

in reference [4] was followed. In the present case, 3379 reflections were collected from the $\pm h+k+l$ and $\pm h-k+l$ quadrants and merged into a unique set of 1772, of which 1652 are "observed" and 120 are "unobserved." The R factor

$$\sum_{hkl} |F^i_{hkl} - F^j_{hkl}| / \sum F^i_{hkl}$$

with $i<j$ between pairs F^i_{hkl} and F^j_{hkl} of observed equivalent reflections F_{hkl} was 0.018 calculated over 1189 pairs. i and j are the sequence numbers in the list of equivalent reflections. Absorption corrections for a sphere with $\mu = 85.6$ cm^{-1} were applied. The maximum and minimum transmission factors were 0.347 and 0.317, respectively.

The $\theta-2\theta$ scans were carried out on an automated Picker[2] diffractometer at 2°/min for 2θ; backgrounds were counted for 20 s each. Because the least significant digit in all counts was dropped by the Picker hardware, standard deviations, σ_{hkl}, of the structure factors, F_{hkl}, were estimated from $\sigma_{hkl} = F_{hkl}/5.7$ for $F_{hkl} < 5.7$; $\sigma_{hkl} = 1$ for $5.7 < F_{hkl} < 30$; and $\sigma_{hkl} = F_{hkl}/30$ for $F_{hkl} > 30$ where F_{max} on this arbitrary scale is 113. The scattering factors used were those for the neutral atoms in reference 6 for the x-ray 67 refinements and those in references 7 and 8 for the extinction and anomalous dispersion refinements.

The quasi-normalized structure factor statistics on our barytocalcite data indicate that the structure is acentric, since $<|E|> = 0.885$, $<E^2> = 1.00$ (fixed), $<|E^2-1|> = 0.709$; the corresponding theoretical values are 0.886, 1.000, 0.736 for the acentric case and 0.798, 1.000, 0.968 for the centric case. E is the quasi-normalized structure factor [9]. The fraction of E values greater than 1.0, 2.0 and 3.0, respectively, was found to be 0.405, 0.0027 and 0.0000; the corresponding theoretical values are 0.368, 0.0183, 0.0001 for the acentric case and 0.317, 0.0455, 0.0027 for the centric case. The statistical procedure suggested an average temperature factor, B, of about 2.5 Å^2 and an exponent of 1.00 for $\sin\theta/\lambda$. Our experience has been that the quasi-normalized structure factor statistics are normally much closer to the theoretical values and the exponent of $\sin\theta/\lambda$ is closer to 2.00 than was calculated here for barytocalcite.

Because of the presence of the strongly scattering Ba ions, this indication that the space-group is the acentric $P2_1$ was not considered to be reliable. The structure of barytocalcite was redetermined by us from a sharpened Patterson function calculated with (E^2-1) coefficients and an F_0 Fourier electron density synthesis phased from the positions of the Ba and Ca ions. The y coordinate of Ba was set equal to zero to define the origin along b. The structure was refined isotropically in space-group $P2_1$ to $R_w = 0.65$, $R = 0.057$ and then anisotropically in $P2_1$ to $R_w = 0.036$, $R = 0.028$ using the x-ray 67 system of computing programs [10]. The least-squares refinements used the full matrix, minimized $\Sigma w(|F_o| - |F_c|)^2$, and included those unobserved reflections for which F_{hkl} calculated more than $2\sigma(F_{hkl})$.

The highest peak in an electron density difference synthesis calculated after anisotropic refinement was equivalent to about 1/3 of an electron and was 0.49 Å from Ba. When the space-group is assumed to be $P2_1$ the largest correlation coefficients are 0.90 to 0.95 between (i) x of O(1) and x of O(2), (ii) z of O(1) and z of O(2), (iii) x of O(4) and x of O(5) and (iv) z of O(4) and z of O(5); 0.80 to 0.90 between (i) B_{11} of O(1) and B_{11} of O(2), (ii) B_{13} of O(4) and B_{13} of O(5), and (iii) B_{23} of O(4) and B_{23} of O(5). There are 48 correlation coefficients greater than 0.50.

The isotropic extinction parameter, r, where $F^2 = F^2_{unc}(1+\beta r F^2_{unc})$ and F_{unc} is the structure factor uncorrected for extinction, was then refined together with the structural and scale parameters using the least-squares program RFINE written by L. W. Finger of the Carnegie Institution of Washington; these refinements included only the observed reflections. The resulting R values were $R_w = 0.027$, $R = 0.022$. The structure obtained had essentially the symmetry $P2_1/m$; subsequent anisotropic refinement in $P2_1/m$ gave $R_w = 0.036$, $R = 0.028$ without extinction refinement and $R_w = 0.028$, $R = 0.025$ in refinements in which r refined to 0.000100(4) cm. All unconstrained parameters were varied. Finally, three cycles of refinement including corrections for anomalous dispersion and extinction gave $R_w = 0.028$, $R = 0.023$; r became 0.000100(5) cm. The largest change in the other parameters was an increase of ~ 0.1 Å^2 in all B_{ii} parameters of Ca. In the final cycle, the average shift/error was 0.02, and the standard deviation of an observation of unit weight, $[\Sigma w(F_o - F_c)^2/(1652-56)]^{1/2}$, was 0.43.

The final R_w values for the centric and acentric cases are near the limit of the experimental data. The weighting scheme is arbitrary, though reasonable. Further, there are large correlation coefficients in the acentric refinement. From the first two considerations, the authors feel that the ratio test [11] on $\Sigma w(F_o - F_c)^2$, the numerator of the R_w term, is not really applicable in this border-line case, even though it appears from this test that refinement in the acentric $P2_1$ is to be preferred at a confidence level greater than 99.5 percent. Because refinement in the centric space-group $P2_1/m$ gives essentially the same result as refinement in $P2_1$ but has more restraints which remove the high correlation coefficients, the space-group of barytocalcite is assumed here to be $P2_1/m$. This is consistent with the symmetry of 2/m in the observed crystalline forms of the mineral [12]. With refinement in $P2_1/m$, the largest correlation coefficients were removed, and only six were greater than 0.50. The four largest were about 0.60 and were between the scale factor and the extinction parameter, and between the scale factor and B_{11}, B_{22}, and B_{33} of Ba.

Because Sr has been reported [13] in the alstonite phase of $BaCa(CO_3)_2$, a refinement of barytocalcite in which the cation positions were considered to be occupied by Sr^{2+} in solid solution was carried out using Finger's least-squares program. The occupan-

[2] Certain commercial equipment, instruments, or materials are identified in this paper in order to adequately specify the experimental procedure. In no case does such identification imply recommendation or endorsement by the National Bureau of Standards, nor does it imply that the materials or equipment identified is necessarily the best available for the purpose.

TABLE 1. *Atomic parameters for barytocalcite* $BaCa(CO_3)_2$

Atoms	x	y	z	B_{11}*	B_{22}	B_{33}	B_{12}	B_{13}	B_{23}
Ba	0.14740(3)	0.25	0.28824(3)	0.883(6)	0.646(6)	0.652(6)	.....	0.399(4)	.....
Ca	.62320(8)	.25	.19855(9)	.64(2)	.50(2)	.58(1)	.....	.21(1)	.....
C(1)	.8972(5)	.75	.2483(5)	.83(8)	.65(8)	.55(7)	.....	.17(8)	.....
O(1)	1.0057(4)	.75	.1393(4)	1.44(9)	1.31(9)	1.03(8)	.....	.77(7)	.....
O(2)	0.8457(3)	.9620(4)	.3089(3)	1.45(6)	0.85(6)	1.25(6)	0.50(5)	.45(6)	0.03(5)
C(2)	.6149(4)	.25	.7468(5)	0.68(8)	.74(8)	0.61(7)	.....	.27(6)	.....
O(3)	.6383(4)	.25	.5644(4)	2.4(1)	1.9(1)	.80(7)	.....	.97(8)	.....
O(4)	.6066(2)	.4604(4)	.8474(3)	1.29(6)	0.61(5)	1.00(6)	.16(4)	.52(4)	−.04(4)

Figures in parentheses are standard errors in the last significant figure quoted, and were computed in the final cycle of full-matrix least-squares refinements.

*Thermal parameters have the form exp $[-1/4(a^{*2}B_{11}h^2 + b^{*2}B_{22}k^2 + c^{*2}B_{33}l^2 + 2a^*b^*B_{12}hk + 2a^*c^*B_{13}hl + 2b^*c^*B_{23}kl)]$.

cies, 1.003(13) and 1.004(4), for Ba and Ca respectively, suggest that there is no solid solution of Sr ions in this sample of barytocalcite.

The atomic parameters from the final extinction refinement in space-group $P2_1/m$ are given in table 1. The observed structure factors are given in table 2.

3. Description of the Structure

The structure of barytocalcite (fig. 1) consists of Ba . . . CO_3 chains and Ca . . . CO_3 chains, both parallel to [001], in which the cations are coordinated to an edge of one neighboring CO_3 group in the chain, and to an apex of the other CO_3 group. The $C(2)O_3$ group is in the $CaCO_3$ chain with its plane parallel to (100). The $C(1)O_3$ group is in the $BaCO_3$ chain, with its plane nearly parallel to (101), and is pushed out of the line of the chain because of the large ionic radius of the Ba ion. The chains lie in layers parallel to (210), a perfect cleavage in $BaCa(CO_3)_2$. The structure may also be considered to consist of layers of CO_3 groups coordinated to layers of cations, and is related in this way to the calcite [14] phase of $CaCO_3$, with (201) of barytocalcite corresponding to (001) of calcite.

3.1. The Barium Ion Environment

The Ba ion is coordinated (fig. 1, table 3) to 11 oxygen atoms with Ba . . . O distances less than 3.2 Å, i.e., in the normal range. These oxygens consist of 5 edges of CO_3 groups, O(2, 2^I), O(1^I, 2^{II}), O(1^{II}, 2^{III}), O(3, 4), O(3^I, 4^I) and one apex, O(1). The Ba ion is more extensively coordinated than it is in the witherite phase of $BaCO_3$, where it has a coordination of 9 oxygens. The structure of witherite resembles that of the aragonite phase of $CaCO_3$.

TABLE 3. Ba *environment in barytocalcite,* $BaCa(CO_3)_2$

Atoms	Distance, Å
Ba, O(1)	2.729(3)
Ba, O(4, 4^I)	2.833(2)
Ba, O(2, 2^I)	2.847(2)
Ba, O(2^{II}, 2^{III})	2.904(2)
Ba, O(1^I, 1^{II})	2.914(1)
Ba, O(3, 3^I)	3.140(2)
Ba, C(1)	3.152(3)
Ba, C(2)	3.294(2)

In all tables of interatomic distances and angles, the quantities in parentheses are standard errors in the last significant figure and were computed from the standard errors in the atomic positional parameters and in the cell parameters. They include contributions from the variance covariance matrix. The atom labels refer to atoms in figure 1.

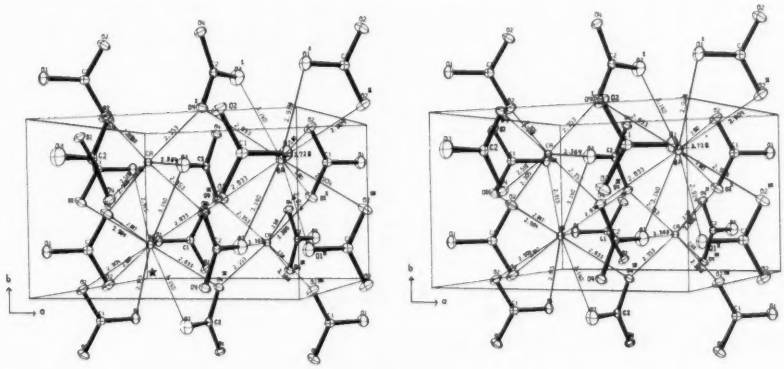

FIGURE 1. *The crystal structure of barytocalcite,* $BaCa(CO_3)_2$, *and the environments of the* Ba *and* Ca *ions.*

The origin of the crystallographic coordinate system is marked by *. The labels refer to atoms in tables 3 and 4.

Table 2. Observed structure factors for barytocalcite, $BaCa(CO_3)_2$

Columns are ℓ, and $10F_o$. F_o's are on an absolute scale. "Unobserved" reflections are marked by *.

3.2. The Calcium Ion Environment

The Ca ion is coordinated (fig. 1, table 4) to seven oxygen atoms, including one edge, O(4^{II}, 4^{III}), of a CO_3 group, with Ca . . . O distances in the normal range. The five apex oxygen atoms lie in a square pyramid. The center of the coordinated edge of the CO_3 group is near the remaining octahedral position. The coordination of Ca in barytocalcite is thus intermediate between the octahedral coordination of six CO_3 apexes with no shared edges in the calcite phase of $CaCO_3$ and the nine-fold coordination of three shared CO_3 edges and three apexes in the aragonite phase of $CaCO_3$.

TABLE 4. Ca *environment in barytocalcite*, $BaCa(CO_3)_2$

Atoms	Distance, Å
Ca, O(2^{I}, 2^{IV})	2.305(2)
Ca, O(4^{I}, 4^{V})	2.353(2)
Ca, O(3)	2.364(3)
Ca, O(4^{II}, 4^{III})	2.518(2)

The atomic labels refer to atoms in figure 1.

3.3. The Carbonate Groups and Their Environments

There are two crystallographically different CO_3 groups in the structure. One (table 5, fig. 2) is in the Ba . . . CO_3 chains and the other (table 5, fig. 2) is in the Ca . . . CO_3 chains. The former, the C(1) CO_3 group, coordinates with all edges to Ba ions, and coordinates one apex, O(1), to another Ba ion. The two remaining apexes O(2, 2^{I}) are coordinated to Ca ions.

The C(2) CO_3 group coordinates the edge containing the O(4, 4^{I}) atoms to Ca^{II} and the remaining two edges, O(3, 4) and O(3, 4^{I}), to ions Ba^{V} and Ba^{IV}, respectively. The average values of the C–O bond distance in the C(1) and C(2) CO_3 groups, 1.283 Å and 1.283 Å, respectively, compare well with the C–O bond lengths ob-

TABLE 5. *The carbonate anions and their environments in barytocalcite*, $BaCa(CO_3)_2$

CO_3 groups	Distance or angle
C(1), O(1)	1.275(4) Å
C(1), O(2, 2^{I})	1.286(2)
O(1), O(2)	2.221(3)
O(2), O(2^{I})	2.220(4)
O(1), C(1), O(2)	120.3(2)°
O(2), C(1), O(2^{I})	119.3(3)
C(2), O(3)	1.259(4) Å
C(2), O(4, 4^{I})	1.294(2)
O(3), O(4)	2.229(3)
O(4), O(4^{I})	2.203(4)
O(3), C(2), O(4)	121.6(1)°
O(4), C(2), O(4^{I})	116.6(3)
O environments	**Distance, Å**
O(1), Ba	2.729(3)
O(1), (Ba^{I}, Ba^{II})	2.915(1)
O(2), Ca^{III}	2.305(2)
O(2), Ba^{III}	2.847(2)
O(2), Ba^{II}	2.904(2)
O(3), Ca^{I}	2.364(3)
O(3), (Ba^{IV}, Ba^{V})	3.140(2)
O(4), Ca^{III}	2.353(2)
O(4), Ca^{II}	2.518(2)
O(4), (Ba^{V})	2.833(2)

The atomic labels refer to atoms in figure 2.

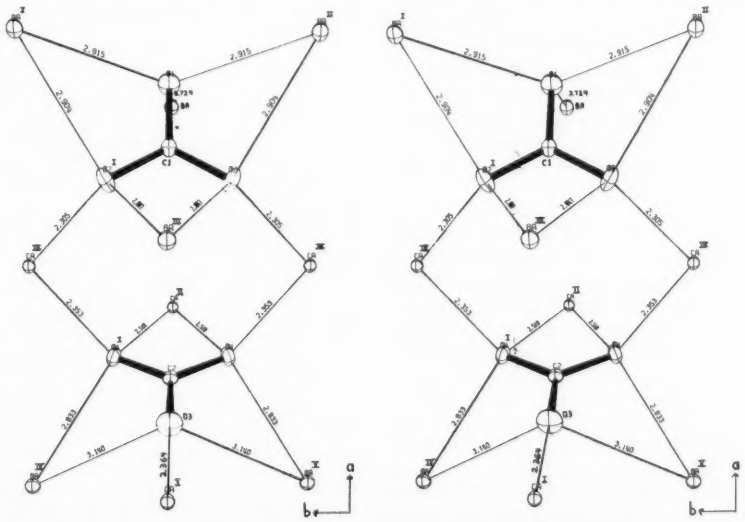

FIGURE 2. *The CO_3 environments in barytocalcite*, $BaCa(CO_3)_2$.
The labels refer to atoms in table 5.

served in the calcite (1.283(2) Å [14]) and aragonite (1.288(2) and 1.283(1) Å [4]) phases of $CaCO_3$.

The two CO_3 groups are nonplanar in barytocalcite. The displacements of C from the plane of the oxygen atoms are 0.025(5) Å for C(1) and 0.022(4) Å for C(2). Both displacements are toward the two central Ca ions Ca^{III} and Ca^{IV} in figure 2, and probably arise from polarization of the O atoms by these Ca ions. Similarly distorted CO_3 groups have been found in aragonite [15, 4] and $Ca_2Na_2(CO_3)_3$ [1]. (In calcite, the CO_3 group point symmetry is constrained to 32 by the choice of $R\bar{3}c$ as the space-group.)

The different C–O bond lengths in the CO_3 groups (table 5) are consistent with the observed features in the structure. O(1) is bonded to three Ba ions. O(2) is bonded to two Ba ions and one Ca ion. Thus O(2) experiences stronger interaction with its cation neighbors, which is compatible with the C(1)–O(2) distance being longer than C(1)–O(1). Similarly, O(4) is coordinated to two Ca ions and one Ba ion, whereas O(3) is coordinated to one Ca ion and two Ba ions. Thus, the C(2)–O(4) bond distance is expected to be longer than the C(2)–O(3) distance. Because the O(4, 4′) edge is coordinated to Ca whereas the O(3, 4) and O(3, 4′) edges are coordinated to Ba, the O(4), C(2), O(4′) angle is expected to be less than 120°. Both these effects are realized.

Although O(2) and O(3) have similar environments, comparison of the lengths of the bonds C(1)–O(2) and C(2)–O(3) is not fruitful. Such a superficial comparison only applies when the oxygen atoms are competing in their bonding to the same central atom or when the other oxygens in the CO_3 groups also have similar environments.

4. Discussion

Alm [3] showed that the structure given by Gossner and Mussgnug [2] is incorrect. The general features of the structure given by Alm for barytocalcite are correct to within ~ 0.3 Å. The details given here are, however, far more precise. Gossner and Mussgnug and Alm gave the space-group of barytocalcite as $P2_1$ in their limited analyses of the structure. Our more extensive analysis shows, however, that barytocalcite can be refined equally well, within the limits of the data, in the centrosymmetric space-group $P2_1/m$.

Barytocalcite is related to the calcite and aragonite phases of $CaCO_3$. There are pseudo-hexagonal layers of cations parallel to (101) in the barytocalcite structure. If the difference between Ca and Ba is ignored, a pseudo-cell may be defined with $a' \sim 8.7$ Å (along $[10\bar{1}]$), $b' = 5.2$ Å (along [010]), $c' \sim 9.2$ Å (along [101]) and $\beta' \sim 95°$. In this pseudo-cell, the cation layers repeat every third layer along c' as they do in calcite. The pseudo-cell of barytocalcite compares well with the orthohexagonal cell 8.641, 4.989, 17.062 Å of calcite. The orientations of the CO_3 groups in the two compounds calcite and barytocalcite differ by a rotation of ~ 30° (the $C(2)O_3$ group in barytocalcite further differs in that it makes an angle of ~ 20° with the (101) plane), and the cell repeat, 17.062 Å, perpendicular to the layers in calcite encompasses six cation layers whereas barytocalcite repeats every three cation layers. As regards the . . . ABCABC . . . sequence of cation layers, barytocalcite is like calcite. However, the rotation of the CO_3 groups by ~ 30° relative to the CO_3 positions in calcite relates barytocalcite to the aragonite phase of $CaCO_3$. Thus the detailed coordinations of the CO_3 groups are like those in aragonite, which also has CO_3 groups rotated by ~ 30° from the CO_3 positions in calcite, because all CO_3 edges in both compounds are shared in coordination to neighboring cations and all apexes are further coordinated to cations. The coordinations of the cations in barytocalcite are however different from the coordination of Ca in aragonite, partly because in the former there are two differently sized cations.

W. E. Brown suggested the problem and gave helpful discussions; P. B. Kingsbury gave technical assistance. This investigation was supported in part by research grant DE–00572 to the American Dental Association from the National Institute of Dental Research and is part of the dental research program conducted by the National Bureau of Standards, in cooperation with the American Dental Association; the United States Army Medical Research and Development Command; the Dental Sciences Division of the School of Aerospace Medicine, USAF; the National Institute of Dental Research and the Veterans Administration.

5. References

[1] Dickens, B., Hyman, A., and Brown, W. E., The crystal structure of $Ca_2Na_2(CO_3)_3$, (shortite), J. Res. Nat. Bur. Stand. (U.S.), **75A** (Phys. and Chem.), No. 2, 129–135 (Mar.–Apr. 1971).

[2] Gossner, B., and Mussgnug, F., Uber Alstonite und Milarit. Zbl. Mineral. Geol Palaont. **A1930,** 220 (1930); Beitrag zur Kenntnis des Baryto-calcites und seiner strukturellen Beiziehungen zu anderen Stoffen., Ibid. **A1930,** 321 (1930).

[3] Alm, K. F., The crystal structure of barytocalcite, $BaCa(CO_3)_2$, Arkiv for Mineralogi och Geologi **2,** (1960) 399–410.

[4] Dickens, B., and Bowen, J. S., Refinement of the crystal structure of the aragonite phase of $CaCO_3$, J. Res. Nat. Bur. Stand. **75A** (Phys. and Chem.), No. 1, 27–32 (Jan.–Feb. 1971).

[5] Kreutz, S., Parallel growths of different substances, Min. Mag. **15,** 232–237 (1909).

[6] International Tables for X-ray Crystallography, **3,** (The Kynoch Press, Birmingham, England, 1962) p. 202.

[7] Cromer, D. T., and Mann, J. B., X-ray scattering factors computed from numerical Hartree-Fock wave functions, Acta Cryst. **A24,** 321–324 (1968).

[8] Cromer, D. T., Anomalous dispersion corrections computed from self-consistent field relativistic Dirac-Slater wave functions, Acta Cryst. **18,** 17–23 (1965).

[9] Dickinson, C., Stewart, J. M., and Holden, J. R., A direct determination of the crystal structure of 2,3,4,6-tetranitroaniline, Acta Cryst. **21,** 663–670 (1966).

[10] Stewart, J. M., editor, X-ray 67 program system for x-ray crystallography, Technical report 67–58, University of Maryland, College Park, Maryland 20742, December 1967.

[11] Hamilton, W. C., Significance tests on the crystallographic *R* factor, Acta Cryst. **18,** 502–510 (1965).

[12] Palache, C., Berman, H., and Frondel, C., Dana's system of mineralogy, vol. **II,** 7th edition (John Wiley and Sons, Inc., New York, 1963) pp. 220 and 221.

[13] Chang, L. L. Y., Subsolidus phase relations in the systems $BaCO_3$-$SrCO_3$, $SrCO_3$-$CaCO_3$ and $BaCO_3$-$CaCO_3$, J. Geol. **73,** 346–368 (1965).
[14] Chessin, H., Hamilton, W. C., and Post, B., Position and thermal parameters of oxygen atoms in calcite, Acta Cryst. **18,** 689–693 (1965).
[15] de Villiers, J. P. R., The crystal structures of aragonite, strontianite and witherite, Ph.D. Thesis, University of Illinois (1969).

(Paper 75A3–663)

JOURNAL OF RESEARCH of the National Bureau of Standards—A. Physics and Chemistry
Vol. 75A, No. 3, May–June 1971

Ionization of Hydrofluoric Acid at 25 °C*

P. R. Patel, E. C. Moreno,** and J. M. Patel****

Institute for Materials Research, National Bureau of Standards, Washington, D.C. 20234

(January 11, 1971)

The ionization constant, K_1, for the reaction $HF \rightleftarrows H^+ + F^-$ was calculated on the basis of potentiometric measurements in the cell Ag; AgCl, Cl^-, $F^-||LaF_3||NaF$, HCl, $H_2O|KCl(Satd.)$, Hg_2Cl_2; Hg at 25 °C. A least squares procedure was applied to the experimental data yielding a best estimate for K_1 of 5.85×10^{-4} with a standard error of 0.03×10^{-4}.

Key words: Hydrofluoric acid; ionization constant; lanthanum fluoride electrode; least squares procedure; potentiometric measurements.

1. Introduction

The chemical properties of dilute aqueous solutions of hydrofluoric acid are described [1, 2, 3][1] by the equilibria

$$HF \rightleftarrows H^+ + F^-;\ K_1 = \frac{(H^+)(F^-)}{(HF)} \qquad (1)$$

$$F^- + HF \rightleftarrows HF_2^-;\ K_2 = \frac{(HF_2^-)}{(F^-)(HF)} \qquad (2)$$

in which parentheses indicate activities of the various chemical species. Most of the evidence for the presence of the various species involved in the above equilibria has been obtained from studies [3, 4] at high constant ionic strengths. Unfortunately, the values for the apparent equilibrium constants derived from such studies are of limited use.

Thermodynamic values of K_1 and K_2 have been reported on the basis of potentiometric [5, 6] or conductance measurements [7]. However, there are uncertainties in the values of the constants originating from the graphical approximations [5, 6] used in the calculations, or from the assumptions regarding the species responsible for the transport of current [7].

The present investigation was prompted by the observation of small but consistent discrepancies between the values of fluoride ion activities obtained with a lanthanum fluoride membrane electrode and those calculated on the basis of the reported ionization constants of hydrofluoric acid. Potentiometric measurements were made in the ternary system NaF-HCl-H_2O. The use of the thermodynamic value of K_1 derived from such measurements eliminated the discrepancy between measured and calculated fluoride ion activities. The least squares procedure used in the present study obviates the uncertainties inherent to graphical methods and permits the estimation of errors on a sound statistical basis.

2. Experimental Methods and Procedures

2.1. NaF-HCl-H_2O Systems

All the chemicals used in the present study were reagent grade. Stock solutions of sodium fluoride were prepared by weighing the salt which was dried at 100 °C for 24 h; the salt was dissolved with conductivity water in borosilicate volumetric flasks and immediately transferred to polyethylene bottles for storage. The systems used in the potentiometric measurements were made by taking 100 ml of sodium fluoride solutions of suitable concentrations and adding various aliquots of standard hydrochloric acid. In this way it was possible to obtain systems with a wide concentration range in both sodium fluoride and hydrochloric acid. The estimated standard error in the concentrations of sodium fluoride and hydrochloric acid was ± 1.3 percent of the amount present.

2.2. Potentiometric Measurements

The cell used in these measurements may be schematically represented by

*This investigation was supported in part by research grant DE–02659–02 to the American Dental Association from the National Institute of Dental Research and is part of the dental research program conducted by the National Bureau of Standards, in cooperation with the Council on Dental Research of the American Dental Association; the United States Army Medical Research and Development Command; the Dental Sciences Division of the School of Aerospace Medicine, USAF; the National Institute of Dental Research; and the Veterans Administration.

**Research Associates of the American Dental Association at the National Bureau of Standards, Washington, D.C. 20234. Present address for Dr. E. C. Moreno, Forsyth Dental Center, Boston, Mass. 02100.

[1] Figures in brackets indicate the literature references at the end of this paper.

418-535 OL - 71 - 5

$$Ag;\ AgCl,\ Cl^-(0.1),\ F^-(0.1)\,||\,LaF_3\,||\,\text{test solution}\,|\ KCl(\text{satd.}),\ Hg_2Cl_2;\ Hg.$$

The lanthanum fluoride membrane electrode has been described in the literature [8, 9] and its Nernstian behavior was confirmed in our laboratories. The calomel electrode was encased in a polytetrafluoroethylene (PTFE) jacket; only the fibre tip was in direct contact with the test solution. This precaution was indispensable to obtain reproducible measurements. The measurements were made with a commercially available pH meter (claimed relative accuracy ± 0.1 mV). Polyethylene beakers containing the solutions and the electrodes were thermostated in a water bath at 25 ± 0.05 °C. The solutions were constantly stirred with magnetic stirrers except during the measurement. Precautions were taken to minimize evaporation and contamination with the atmosphere. A reading was considered to represent equilibrium conditions when the EMF remained constant, within ± 0.1 mV for about 20 min. A minimum of three such readings were obtained for each system. For the purpose of calculations a conservatively estimated standard error of 0.15 mV was adopted. Measurements of pH with glass and calomel electrodes were made only on the standard sodium fluoride solutions (pH values above 6.2). No reliable measurements of pH could be obtained in the NaF-HCl-H_2O systems, presumably because of the attack of hydrofluoric acid on the glass electrode. The ionic strengths of all the systems were in the range of 0.008 to 0.03 M.

3. Calculative Procedures

As mentioned in the introduction, discrepancies were observed in this study between the measured fluoride ion activities, $(F^-)_m$, and those calculated, $(F^-)_c$, on the basis of the available ionization constants for hydrofluoric acid. In the next two sections, details will be given concerning the methods used to derive these activities. The statistical procedure used for the estimation of K_1, on the basis of the potentiometric measurements reported here, will be given in section 3.3.

3.1. Calculation of Fluoride Ion Activities

Fluoride ion activities in the systems NaF-HCl-H_2O were calculated from the cubic equation

$$(F^-)_c^3\left\{\frac{K_2}{K_1 f_1 f_2}\right\} + (F^-)_c^2\left\{\frac{2K_2[H]_T}{K_1 f_2} + \frac{1}{K_1 f_1} - \frac{K_2[F]_T}{K_1 f_2}\right\} + (F^-)_c\left\{\frac{[H]_T}{K_1} + \frac{1}{f_1 f_3} - \frac{[F]_T}{K_1}\right\} - \frac{[F]_T}{f_3} = 0 \qquad (3)$$

in which $[F]_T$ and $[H]_T$ represent total concentrations of sodium fluoride and hydrochloric acid respectively, and f_i represent molar ionic activity coefficients; in this paper subscripts 1, 2, 3 and 4 refer to the species F^-, HF_2^-, H^+, and OH^-, respectively. In the present calculations it was assumed that $f_1 = f_2$ and that the activity coefficient for the undissociated species, HF, was unity. The values for K_1 and K_2 reported by Broene and DeVries were used in eq (3) to calculate the fluoride ion activity in the ternary system.

The ionic strength, I, in the systems considered here is defined by

$$I = 0.5\left\{[Na^+] + \frac{(H^+)}{f_3} + \frac{K_w}{(H^+)f_4} + \frac{(F^-)}{f_1} + \frac{K_2(H^+)(F^-)^2}{K_1 f_2} + [Cl^-]\right\} \qquad (4)$$

in which $[Na^+]$ is the sodium ion concentration, equal to $[F]_T$; $[Cl^-]$ is the chloride ion concentration, equal to $[H]_T$, and K_w is the ionization constant of water (1.008×10^{-14} [10]).

The activity of hydrogen ion appearing in eq (4) was calculated from

$$(H^+) = [H]_T \Big/ \left(\frac{1}{f_3} + \frac{(F^-)_c}{K_1} + \frac{K_2(F^-)_c^2}{K_1 f_2}\right). \qquad (5)$$

The ionic activity coefficients were calculated from the Debye-Hückel equation

$$f_i = \exp\left(-2.303 A Z_i^2 \sqrt{I}/(1 + B a_i \sqrt{I})\right) \qquad (6)$$

in which A and B are temperature dependent constants, Z_i is the valence of the ith ion and a_i is its ion size parameter.[2]

The calculations were performed by an iterative procedure in which initial values of unity were taken for all f_i; approximate solutions for eqs (3) and (5) and their substitution into eq (4) yielded an approximate value of I which was then used to obtain f_i from eq (6). The new values of f_i were cycled in a similar fashion until convergence in the value of I, which required from 3 to 4 cycles.

3.2. Measured Fluoride Ion Activities

Fluoride ion activities, $(F^-)_s$, for the standard sodium fluoride solutions were calculated from the quadratic equation

$$(F^-)_s^2\left\{\frac{2K_2(H^+)}{K_1 f_2}\right\} + (F^-)_s\left\{\frac{1}{f_1} + \frac{(H^+)}{K_1}\right\} - [F]_T = 0. \qquad [3](7)$$

In the pH range of these solutions (6.2 to 6.8), differences of up to 30 percent in the values of K_1 and K_2 do not affect the calculated fluoride ion activities in the standard sodium fluoride solutions. Standard curve was obtained by least squares fitting of the equation

$$E_s = a + b \log (F^-)_s \qquad (8)$$

[2] The values used for A and B in eq (6) were 0.5115 and 0.3291×10^8 [11], respectively. The ion size parameters were $a_1 = a_2 = a_4 = 3.5 \times 10^{-8}$ cm and $a_3 = 9 \times 10^{-8}$ cm [12].

[3] This equation is used instead of equation (3) because the values for (H^+) are readily obtained from pH determinations in the standard solutions.

in which E_s represents potential measurements of the standard solutions and a and b are the parameters to be estimated. In table 1 typical results for the potential measurements in standard sodium fluoride solutions are given. The concentrations of the standard solutions covered a range 1×10^{-1} to 2.5×10^{-5} molar in sodium fluoride. When eq (8) was fitted to the data in table 1, the best estimates of the parameters obtained were $a = -173.032 \pm 0.176$ and $b = -57.9066 \pm 0.0610$. Frequent checks were made to ascertain the invariability of these parameters; these were found to be constant for the course of the experiments reported in this paper.

TABLE 1. *Electromotive force measurements for the standard sodium fluoride solutions*

Standard number	$[NaF]_T \times 10^3$ mol. l^{-1}	Log $(F^-)_s$ [a] mol. l^{-1}	E_s mV
1	100.0	−1.118	−108.4
2	75.0	−1.231	−101.6
3	50.0	−1.392	−92.4
4	25.0	−1.670	−76.1
5	10.0	−2.046	−54.6
6	7.50	−2.165	−48.0
7	5.00	−2.335	−37.8
8	2.50	−2.627	−20.7
9	1.00	−3.016	1.5
10	0.500	−3.313	18.8
11	.250	−3.612	35.8
12	.100	−4.015	59.2
13	.750	−4.137	67.1
14	.0250	−4.627	94.9

[a] Activities of standard sodium fluoride solutions were calculated from eq (7). Linear least squares fitting of eq (8) yielded the best estimates of parameters a (-173.032 ± 0.176) and b (-57.9066 ± 0.0610).

Fluoride ion activities in the systems NaF–HCl–H_2O were obtained from the potential measurements, E_m, by the use of equation

$$(F^-)_m = \exp\,(2.303\ (E_m - a)/b). \tag{10}$$

Estimations of the variances, $\sigma^2_{(F^-)m}$, were obtained from Ref. [13]

$$\sigma^2_{(F^-)m} = (2.303\ (F^-)_m)^2 \cdot \sigma^2_{\log (F^-)m} \tag{11}$$

in which

$$\sigma^2_{\log (F^-)m} = \frac{\sigma_s^2}{b^2}\left\{\frac{1}{i} + \frac{1}{j} + \frac{(E_m - \bar{E}_s)^2 \cdot \sigma_b^2}{b^2 \sigma_s^2}\right\}. \tag{12}$$

In eq (12), i and j are the number of measurements per sample and the number of points in the standard curve respectively; $\bar{E}_s$ is the mean value of the potential measurements for the standard curve, and σ_b^2 is the variance in the parameter b as obtained from the least squares fitting of eq (8).

The calculated standard errors, $\sigma_{(F^-)m}$, for all the systems lay between 0.65 and 0.70 percent of the measured activity.

3.3. Least Squares Procedure for Estimation of the Equilibrium Constants

This procedure entails the simultaneous adjustment of the weighted observables – i.e.,

$$[F]_T,\ [H]_T,\ \text{and}\ (F^-)_m$$

– and the determination of two parameters which yield best estimates of K_1 and K_2. The main features of the method follow the general least squares adjustment discussed by Deming [14] and they are similar to those reported in connection with the calculation of diffusion coefficients [15]. The adjustment of the observables was made subject to the condition function ϕ,

$$\phi = \bar{n}_m - \bar{n}_c = 0. \tag{13}$$

In eq (13), $\bar{n}_m$ is defined by

$$\bar{n}_m = \frac{[F]_T - (F^-)_m/f_1}{[H]_T} \tag{14}$$

and it is a function often used in ion association studies [3, 16]. The term $\bar{n}_c$ is an alternative definition involving the equilibrium constants K_1 and K_2,

$$\bar{n}_c = \left\{\frac{(F^-)_m/K_1 + 2K_2(F^-)_m^2/K_1 f_2}{1/f_3 + (F^-)_m/K_1 + K_2(F^-)_m^2/K_1 f_2}\right\}. \tag{15}$$

The weights of the observables were calculated from

$$W_{\text{obs}} = \frac{\sigma^2_{\text{int}}}{\sigma^2_{\text{obs}}} \tag{16}$$

in which σ_{obs} is the standard deviation for the observable in question and σ_{int} is an arbitrary constant conveniently selected for calculating purposes. The aim of the procedure is to compute adjustments of the observables and the corrections for the initial estimates of the equilibrium constants in such a way that

$$\phi([F]_T^*,\ [H]_T^*,\ (F^-)_m^*,\ k_1,\ k_2) \approx 0 \tag{17}$$

in which k_1 and k_2 are the final estimates of the equilibrium constants and the starred quantities represent adjusted observables. The adjustment of the observables is done subject to the criterion that the weighted sum of squares of the residuals (observed value – adjusted value) be a minimum.

The procedure is an iterative one in which new estimates of the equilibrium constants are substituted as initial estimates until their values converge to a constant value. Also, it allows one to calculate the standard errors in the final estimates of the equilibrium constants.

Although the calculations based upon this procedure are of a general nature and permit the estimation of best values (in the least squares sense) for K_1 and K_2, in the concentration ranges used here, there was

significant information only about K_1. For this reason, a fixed value of 3.86 for K_2 [5] was adopted and the least squares procedure was applied to estimate K_1. As shown in section 5, the best estimate for K_1 derived from the present data is relatively insensitive to substantial variations in the value of K_2.

In the iterative procedure described in this section, each new estimate of K_1 was used to recalculate the ionic species distribution, ionic strength, and activity coefficients. The total number of cycles, using $K_1 = 6.71 \times 10^{-4}$ as an initial estimate, was from 6 to 7, over the whole concentration range.

4. Results

The measured fluoride ion activities together with concentrations of sodium fluoride and hydrochloric acid are shown in table 2.

The quantity R (5th column of table 2) is defined as $R = (F^-)_m/(F^-)_c$, i.e., the ratio of the fluoride ion activity measured with the lanthanum fluoride membrane electrode to the activity calculated from eq (3) in section 3.1. The equilibrium constants given by Broene and DeVries [5] were used for this calculation. It is apparent that as the concentration of hydrochloric acid increases relative to that of sodium fluoride the value of R departs substantially from unity. As indicated in the Discussion, the most probable cause for the departure of R from unity is the value of K_1 used in the calculation of $(F^-)_c$. Similar calculations were made using the value of K_1 reported here (table 3); the ratio in this case is represented by R*, last column of table 2. The values of R^* are in general close to unity; their departure from unity are anticipated on the basis of the experimental errors in the observables.

Adjusted values of the concentrations for sodium fluoride, hydrochloric acid and measured fluoride ion activities are given in table 3 together with the ionic strength calculated from these adjusted quantities. A comparison with table 2 shows that the adjustments were very small and well within experimental errors in the measurements. The values for K_1 given in column 6 of table 3 were obtained for each individual system using the activities calculated from adjusted observables in eq (1). For this purpose an iterative procedure was used in which an initial distribution of ionic species was obtained from the values of adjusted observables and the best estimate of K_1 obtained from the least squares adjustment; the ionic strength was recalculated and a new value for K_1 was obtained from eq (1); this process was recycled until convergence in the value of the constant.

The near constancy for the value of K_1 in all the systems and the closeness of these values to that of the overall estimate of K_1 further substantiates the soundness of the statistical treatment of the data.

The best estimate of K_1 as obtained from the least squares adjustment on 46 systems is given at the bottom of column 6 in table 3. The calculation of the error associated with this value (sect. 3.3) takes into consideration all the experimental errors in the observables. Thus, the small magnitude of the error in K_1 reflects the reliability of the experimental data and the validity of the physical model, eqs (1) and (2).

The function $\bar{n}_m$ is plotted against the logarithm of the fluoride ion concentration in figure 1. The points in the figure appear to describe a smooth function; however, since the ionic strength was not the same in all the systems, trends in families of points are discernible

TABLE 2. *Unadjusted measurements in the system* $NaF-HCl-H_2O$ *at 25 °C*

System number	$[F]_T \times 10^3$ mol. l^{-1}	$[H]_T \times 10^3$ mol. l^{-1}	$(F^-)_m \times 10^3$ mol. l^{-1}	R [a]	R^* [a]
1	0.499	0.504	0.318	0.97	1.01
2	.499	1.02	.222	.95	1.02
3	.499	1.52	.168	.94	1.02
4	.498	2.03	.133	.92	1.02
5	.498	2.53	.110	.91	1.01
6	.497	3.04	.0938	.91	1.01
7	.497	3.54	.0819	.90	1.01
8	.496	4.04	.0724	.90	1.01
9	.496	4.54	.0648	.89	1.01
10	.495	5.04	.0584	.89	1.00
11	.999	0.508	.701	.98	1.01
12	.998	1.02	.508	.96	1.00
13	.997	1.52	.389	.94	1.01
14	.996	2.03	.305	.93	1.01
15	.995	2.53	.249	.91	1.00
16	.994	3.04	.209	.90	1.00
17	.993	3.54	.180	.90	1.00
18	.992	4.04	.158	.89	1.00
19	.991	4.54	.136	.86	0.97
20	.990	5.04	.124	.87	.98
21	.990	5.29	.119	.87	.99
22	4.99	1.02	3.77	.99	1.00
23	4.98	2.03	2.97	.97	0.98
24	4.97	3.04	2.29	.96	.98
25	4.96	4.04	1.74	.93	.97
26	4.95	5.04	1.33	.92	.98
27	4.94	6.04	1.04	.92	.99
28	4.93	7.03	0.846	.93	1.02
29	4.92	8.02	0.696	.92	1.02
30	4.91	9.00	.586	.92	1.03
31	4.90	9.98	.504	.92	1.03
32	9.88	6.04	3.86	.93	0.95
33	9.85	7.52	3.05	.94	.97
34	9.83	8.51	2.40	.88	.92
35	9.80	9.98	1.93	.92	.99
36	9.79	11.0	1.50	.85	.92
37	9.76	12.4	1.28	.91	1.00
38	9.74	13.4	1.03	.85	0.94
39	9.71	14.8	0.927	.92	1.02
40	9.69	15.8	.771	.86	0.96
41	9.66	17.2	.710	.92	1.03
42	9.62	19.6	.570	.92	1.04
43	9.57	21.9	.477	.91	1.04
44	9.52	24.2	.407	.91	1.03
45	9.48	26.5	.355	.91	1.03
46	9.43	28.8	.315	.91	1.04

[a] For the definition of R and R^*, see section 4.

TABLE 3. *Adjusted measurements in the system* NaF–HCl—H_2O, *ionic strength, and ionization constant of hydrofluoric acid at 25 °C*

System number	$[F]_T^* \times 10^3$ mol. l^{-1}	$[H]_T^* \times 10^3$ mol. l^{-1}	$(F^-)_m^* \times 10^3$ mol. l^{-1}	$I \times 10^3$ mol. l^{-1}	$K_1 \times 10^4$ mol. l^{-1}
1	0.502	0.503	0.318	0.830	5.85
2	.503	1.02	.222	1.25	5.85
3	.502	1.51	.168	1.69	5.85
4	.500	2.02	.133	2.17	5.85
5	.500	2.53	.110	2.65	5.85
6	.499	3.03	.0937	3.14	5.85
7	.499	3.53	.0818	3.63	5.85
8	.497	4.03	.0723	4.12	5.85
9	.496	4.54	.0648	4.61	5.85
10	.494	5.05	.0584	5.10	5.85
11	1.00	0.508	.700	1.24	5.85
12	0.996	1.02	.508	1.55	5.85
13	.999	1.52	.389	1.93	5.85
14	.996	2.03	.305	2.35	5.85
15	.993	2.53	.249	2.80	5.85
16	.992	3.04	.209	3.26	5.85
17	.990	3.55	.180	3.73	5.85
18	.989	4.05	.158	4.21	5.85
19	.974	4.61	.137	4.69	5.84
20	.978	5.09	.124	5.18	5.85
21	.981	5.33	.119	5.42	5.85
22	4.97	1.02	3.77	5.13	5.87
23	4.92	2.04	2.98	5.33	5.86
24	4.91	3.06	2.29	5.61	5.86
25	4.91	4.07	1.74	6.01	5.85
26	4.91	5.07	1.33	6.54	5.85
27	4.92	6.05	1.04	7.21	5.85
28	4.95	7.01	0.845	7.96	5.85
29	4.95	7.98	.695	8.79	5.85
30	4.94	8.95	.585	9.65	5.85
31	4.93	9.92	.503	10.5	5.85
32	9.65	6.12	3.87	10.7	5.86
33	9.75	7.57	3.05	11.1	5.86
34	9.60	8.65	2.41	11.5	5.84
35	9.75	10.0	1.93	12.3	5.85
36	9.59	11.2	1.50	12.9	5.84
37	9.75	12.4	1.28	13.9	5.85
38	9.57	13.6	1.03	14.7	5.84
39	9.76	14.7	0.926	15.9	5.85
40	9.58	16.0	.772	16.8	5.85
41	9.73	17.1	.709	18.0	5.85
42	9.71	19.4	.569	20.3	5.85
43	9.67	21.7	.476	22.5	5.85
44	9.61	24.0	.406	24.7	5.85
45	9.56	26.3	.354	26.9	5.85
46	9.52	28.5	.314	29.2	5.85

[a] $k_1 = 5.85 \pm 0.03 \times 10^{-4}$

[a] Best estimate for K_1 and its standard error as obtained by least squares procedure. Fixed value of $K_2 = 3.86$.

in this plot. The maximum value of the $\bar{n}_m$ was 0.922; reliable information on the value of K_2 can be obtained only from systems with $\bar{n}_m$ values in the neighborhood of 1.5; this would require high concentrations of sodium fluoride and hydrochloric acid and the calculation of ionic activity coefficients would be questionable.

5. Discussion

The lack of agreement between the calculated fluoride ion activities and the measurements reported here must be attributed to the value of the constant K_1 used in the calculations and not to the measurements, because: (a) the specific fluoride electrode used in this investigation displays a normal behavior in standard solutions at relatively high pH as well as in acidic solution [6, 8]; (b) the contribution of liquid junction potential [3] to the potential measurements in the standard NaF solutions and the dilute NaF-HCl-H_2O systems should be approximately constant since identical cells and dilute solutions were used in this study; the standard curves, equation (8), should absorb this contribution and it should not be reflected in the fluoride ion activities, $(F^-)_m$, obtained from eq (10); (c) the highest ionic strength in the present systems was 0.0292 *M*; for this reason the Debye-Hückel theory eq (6), used in the calculations, should be quite adequate for the calculation of f_i; (*d*) the relatively low standard errors in the observables vouch for the quality of the experimental data.

Although both the values of K_1 and K_2 are involved in the calculations of the fluoride ion activity, only the former affects the value of $(F^-)_c$ in the experimental ranges reported here. Indeed, when the value of K_1 obtained from the least squares procedure was used to calculate the fluoride ion activity, the discrepancies were eliminated (see values for R^* in table 2). In this connection it is pertinent to mention that, whereas forty-two values of R (out of forty-six) are significantly different from unity at the 0.05 confidence level, only four values of R^* are significantly different from unity. For the significance test (two sided normal test), the error in $(F^-)_m$ was obtained as explained in section 3.2 and the error in $(F^-)_c$ was obtained by propagation [17] in eq (3).

The generalized least squares procedure described in section 3.3 can be applied to the present data for the simultaneous estimation of the equilibrium constants. When this was done, the best estimates for K_1 and K_2 were $5.91 \pm 0.04 \times 10^{-4}$ and 8 ± 2, respectively. Whereas the value of K_1 obtained in this fashion is in reasonably good agreement with that reported in table 3, the estimate for K_2 is substantially different from that used in the reported calculations. This is a clear indication that the experimental data are inadequate for the estimation of a reliable value for K_2. Such a limitation is to be anticipated on the basis of the values of $\bar{n}_m$ calculated from the experimental data and plotted in figure 1. In physical terms, the experimental systems are essentially defined by the

[3] The type of cells used in this study have a liquid junction formed by a contact between saturated KCl in the reference electrode and the test solution. A liquid junction potential arises because of the different nature of the electrolytes at the two boundaries of the junction [Bates, R. G., Determination of pH Theory and Practice, Chapter 3 (John Wiley and Sons, Inc., New York, New York, 1965)].

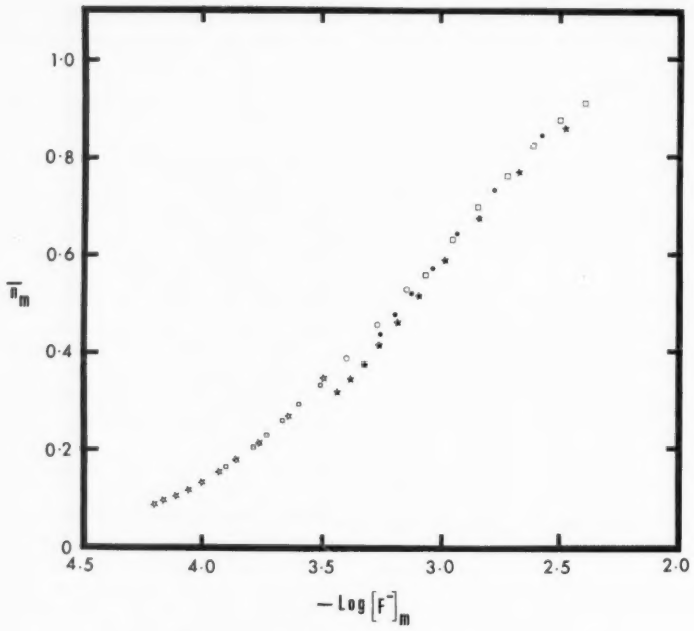

FIGURE 1. *Plot of* $\bar{n}_m$ *versus* $-log\ [F^-]_m$.
Experiments with similar ionic strengths are represented by the same symbol.

equilibrium given in eq (1). For this reason substantial changes in the value of K_2 should not affect significantly the best estimate of K_1.

Broene and DeVries reported [5] a value of 6.71×10^{-4} for K_1, obtained from EMF measurements using a lead fluoride electrode. The calculations involved graphical approximations. In addition, the solubility of lead fluoride is sufficient [18] to open to question their measurements at least in the most dilute systems. Ellis reported [7] a value, 6.60×10^{-4}, for K_1 calculated from conductance data. In his calculations, Ellis had to make questionable assumptions regarding the ionic species responsible for the current transport. Recently, Vanderborgh has reported [6] a value of 6.46×10^{-4} for K_1, calculated from EMF measurements using a lanthanum fluoride membrane electrode. This value was obtained by extrapolation to zero ionic strength of apparent equilibrium constants at finite ionic strengths. However, the plot used for this purpose (fig. 1 in reference [6]) is in error. The values for the apparent equilibrium constants given by Vanderborgh (table 1 in reference [6]) are plotted against the square root of the ionic strength in figure 2; the full line is a least squares fit of this data. It is apparent that the intercept of this line, $pK_1=3.21\pm0.03$, which corresponds to a value of $K_1=6.17\pm0.43\times10^{-4}$, is in reasonable agreement with the value of K_1, $5.85\pm0.03\times10^{-4}$, reported here. Furthermore, if the point corresponding to $\sqrt{I}=0.224$ in figure 2 is disregarded then the remaining three points extrapolate even closer to the value obtained in the present study at zero ionic strength (shown by the open square). This agreement substantiates the validity of the assumption used in this study regarding the liquid junction potential since in both Vanderborgh's and the present investigation the potential measurements were made using comparable cells except that the liquid junction potentials were eliminated in his study by a special experimental design.

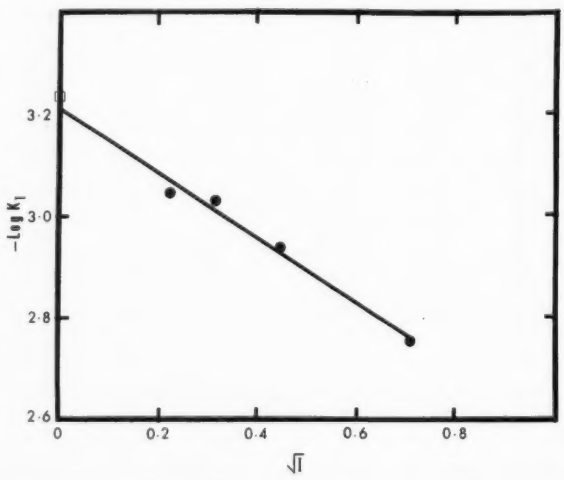

FIGURE 2. *Plot of* pK_1 *versus square root of ionic strength.*
•, points from table 1 of reference [6]; □, $pK_1=3.23$ corresponding to the value $K_1=5.85\times10^{-4}$ reported in this paper.

6. References

[1] Wooster, C. B., J. Amer. Chem. Soc. **60,** 1609 (1938).
[2] Ciavatta, L., Arkiv Kemi **21,** 129 (1963).
[3] Srinivasan, K., and Rechnitz, G. A., Anal. Chem. **40,** 509 (1968).
[4] Farrer, H. N., and Rossotti, F. J. C., J. Inorg. Nucl. Chem. **26,** 1959 (1964).
[5] Broene, H. H., and DeVries, T., J. Amer. Chem. Soc. **69,** 1644 (1947).
[6] Vanderborgh, N. E., Talanta **15,** 1009 (1968).
[7] Ellis, A. J., J. Chem. Soc. 4300 (1963).
[8] Frant, M. S., and Ross, J. W., Science **154,** 1553 (1966).
[9] Lingane, J. J., Anal. Chem. **40,** 935 (1968).
[10] Harned, H. S., and Owen, B. B., The Physical Chemistry of Electrolytic Solutions, p. 645, equation 15–3–7a (Reinhold Publishing Corp., 3d ed., New York, New York, 1958).
[11] Robinson, R. A., and Stokes, R. H., Electrolyte Solutions, p. 468 (Academic Press, 2d ed., New York, New York, 1959).
[12] Kielland, J., J. Amer. Chem. Soc. **59,** 1675 (1937).
[13] Bennett, C. A., and Franklin, N. L., Statistical Analysis in Chemistry and Chemical Industry, p. 232 (John Wiley & Sons, Inc., New York, New York, 1954).
[14] Deming, W. E., Statistical Adjustment of Data, pp. 49–58 (John Wiley & Sons, Inc., New York, New York, 1943) (Reprinted by Dover Publications, New York, New York, 1964).
[15] Patel, P. R., Moreno, E. C., and Gregory, T. M., J. Res. Nat. Bur. Stand. (U.S.), **73A** (Phys. and Chem.), No. 1, 43–49 (Jan.–Feb. 1969).
[16] Bjerrum, J., Metal Ammine Formation in Aqueous Solution (P. Haase and Son, Copenhagen, 1957).
[17] Margenau, H., and Murphy, G. M., The Mathematics of Physics and Chemistry, p. 515 (D. Van Nostrand Company, Inc., 2d ed., Princeton, New Jersey, 1956).
[18] Carter, R. H., Ind. Eng. Chem. **20,** 1195 (1928).

(Paper 75A3–664)

JOURNAL OF RESEARCH of the National Bureau of Standards—A. Physics and Chemistry
Vol. 75A, No. 3, May–June 1971

Vapor Pressure Equation for Water in the Range 0 to 100 °C

Arnold Wexler and Lewis Greenspan

Institute for Basic Standards, National Bureau of Standards, Washington, D.C. 20234

(February 19, 1971)

Some precise measurements of the vapor pressure of liquid water at seven temperatures in the range 25 to 100 °C were reported recently by H. F. Stimson of NBS. These measurements have an estimated standard deviation of 20 ppm or less, except at 25 °C where the estimated standard deviation is 44 ppm. We have derived a formula which yields computed values of vapor pressure agreeing with Stimson's measurements to within 7 ppm.

We integrated the Clausius-Clapeyron equation using the accurate calorimetric data of Osborne, Stimson, and Ginnings and the Goff and Gratch formulations for the virial coefficients of water vapor to obtain an equation that has a rational basis. This equation was then adjusted to bring it into closer accord with Stimson's pressure measurements. Two tables are given of the vapor pressure, expressed in pascals, as a function of temperature at 0.1-deg intervals over the range 0 to 100 °C, one on the International Practical Temperature Scale of 1948 and the other on the International Practical Temperature Scale of 1968.

Key words: Clausius-Clapeyron equation; saturation vapor pressure over water; vapor pressure; vapor pressure of water; water vapor; steam; virial coefficients.

1. Introduction

In establishing and maintaining humidity standards, in calibrating hygrometers, and in making precision humidity measurements, an accurate equation for the vapor pressure of water is essential. Such an equation also plays a vital role in steam power technology. It is important in the fields of meteorology and air conditioning where precise calculations relating to the water vapor content of atmospheric air are often made. It is employed in chemical thermodynamics, where the vapor pressure of the pure water substance is used as a reference standard in calibrating boiling point apparatus, in comparative vapor pressure measurements, in ebulliometry and in evaluating vapor pressure data of organic liquids.

It has been the practice at NBS to use the Goff and Gratch vapor pressure formulation [1][1] in all work pertaining to hygrometry. Recently, H. F. Stimson [2] published the results of some precise measurements of the vapor pressure of water at seven temperatures from 25 to 100 °C. These vapor pressures, obtained with the steam boiler and precision manometer used at NBS in the 1940's to calibrate standard platinum resistance thermometers [3], have an estimated standard deviation of 20 ppm or less except at 25 °C where the estimated standard deviation is 44 ppm. Although vapor pressures calculated using the Goff and Gratch formulation are in reasonably good accord with Stimson's measurements, differing at most, at 25 °C, by 95 ppm, we concluded that it would be desirable to have a formulation that was in closer agreement with Stimson's measurements, preferably within the estimated uncertainty of the latter. The purpose of this paper is to present such a formulation. We shall limit our considerations to temperatures 0 to 100 °C.

[1] Figures in brackets indicate the literature references at the end of this paper.

2. Derivation

We start with a modified version of the Clausius-Clapeyron equation [4]

$$\frac{dp}{dT}=\frac{\gamma}{Tv} \tag{1}$$

where p is the pressure of the saturated vapor, v is the specific volume of the saturated vapor, T is the absolute thermodynamic temperature, γ is an experimentally measured calorimetric quantity, and dp/dT is the derivative of the vapor pressure with respect to the absolute thermodynamic temperature. The quantity γ [4] is the heat supplied to water to evaporate a unit mass of water isothermally and withdraw its vapor from the calorimeter. It differs from the latent heat of vaporization, L, by a small quantity, β, that is,

$$\gamma=L+\beta \tag{2}$$

where

$$\beta=\frac{v'}{v-v'}L \tag{3}$$

and v' is the specific volume of the saturated liquid. The quantity β may be pictured as the heat necessary to vaporize water to fill the space no longer filled with liquid in the γ experiment.

The virial equation of state for water vapor, expressed as a power series in p,

$$pv = RT[1 + B'p + C'p^2 + \ldots] \tag{4}$$

when substituted into eq (1) yields

$$\frac{dp}{p} = \frac{\gamma}{RT^2 Z}\, dT \tag{5}$$

where

$$Z = 1 + B'p + C'p^2 + \ldots \tag{6}$$

Z is the compressibility factor, R is the gas constant for water vapor, B' is the second pressure-series virial coefficient, and C' is the third pressure-series virial coefficient. For temperatures up to 100 °C, fourth and higher virial coefficients affect Z by less than 12 ppm and therefore will be neglected.

Performing some simple mathematical manipulations and integrations, eq (5) becomes

$$\int_{p_0}^{p} d(\ln p) = \int_{T_0}^{T} \frac{\gamma}{RT^2}\, dT - \int_{T_0}^{T} \frac{\gamma}{RT^2}\left(\frac{Z-1}{Z}\right) dT \tag{7}$$

where p_0 and p correspond to vapor pressures at temperatures T_0 and T, respectively. The first integral on the right-hand side of the equation provides the major contribution to the vapor pressure. The second integral on the right-hand side of the equation accounts for the deviation of water vapor from ideal gas behavior.

We shall show later that the quantity γ can be represented with high precision by the polynomial equation

$$\gamma = a + bT + cT^2 + dT^3 \tag{8}$$

which, when substituted into the first integral on the right-hand side of eq (7) yields

$$\int_{p_0}^{p} d(\ln p) = \frac{1}{R}\left[-a\left(\frac{1}{T} - \frac{1}{T_0}\right) + b \ln \frac{T}{T_0} + c(T - T_0) + \frac{d}{2}(T^2 - T_0^2)\right] - \frac{1}{R}\int_{T_0}^{T} \frac{\gamma}{T^2}\left(\frac{Z-1}{Z}\right) dT. \tag{9}$$

Equation (9) reduces to

$$\int_{p_0}^{p} d(\ln p) = -\frac{a}{RT} + \frac{b}{R} \ln T + \frac{c}{R} T + \frac{d}{2R} T^2 + e - \frac{1}{R}\int_{T_0}^{T} \frac{\gamma}{T^2}\left(\frac{Z-1}{Z}\right) dT \tag{10}$$

where

$$e = +\frac{a}{RT_0} - \frac{b}{R} \ln T_0 - \frac{c}{R} T_0 - \frac{d}{2R} T_0^2. \tag{11}$$

The derivation of eq (10) is similar in some respects to that of Goff and Gratch [5, 6].

In 1939, Osborne, Stimson and Ginnings [7] reported weighted mean values of γ from 0 to 200 °C based on precise calorimetric measurements in the range 0 to 100 °C and on similar measurements made in the same laboratory during 1930–32 in the range 50 to 270 °C [8] and in 1937 in the range 100 to 374 °C [9]. We fitte ' eq (8) to these weighted means by the method of least squares, retaining the units international joules per gram for γ and temperature t in degrees C based on the International Temperature Scale of 1927 (ITS–27) but letting the absolute temperature $T_{48} = t + 273.15$. In our range of interest, 0 to 100 °C, t has the same numerical value on the International Temperature Scale of 1927 (ITS–27) [10], the International Temperature Scale of 1948 (ITS–48) [11], and the International Practical Temperature Scale of 1948 (IPTS–48) [12]. Therefore, we will use t interchangeably on these scales as may prove convenient. However, the absolute temperature T_{48}, due to the choice of 273.15 conforms to IPTS–48. The coefficients of eq (8) have the following numerical values: $a = 3.4660697 \times 10^3$, $b = -5.6067899$, $c = 1.0963233 \times 10^{-2}$, and $d = -1.2366148 \times 10^{-5}$. The residual standard deviation[2] is 0.231 international joules per gram, about 1 part in 10,000.

Virial coefficients for steam are usually derived from p-v-t measurements [13, 14, 15, 16]. Unfortunately, there are no p-v-t measurements for steam (water vapor) in the range 0 to 100 °C.

The early experiments of Knoblauch, Linde and Klebe [17], which were performed at temperatures from 100 to 180 °C, are suspect because of the static method used which leads to systematic errors due to the adsorption of water vapor on the walls of the container [13]. The experiments of Keyes, Smith, and Gerry [13], made by a continuous flow-method, cover the range 195 to 460 °C. These, too, are suspect below the critical temperature because of possible adsorption effects [16]. Other investigators have provided data at higher temperatures and pressures. It is possible to extrapolate the virial coefficients obtained at higher temperatures to lower temperatures [13, 14], but such extrapolations do not give values with the requisite accuracy for our purpose. Alternately, calorimetric data can be employed to obtain enthalpy coefficients, which, when integrated with respect to temperature, yield virial coefficients. This procedure was employed by Goff and Gratch [5, 6], who used the 38 to 125 °C throttling experiment data of Collins and Keyes [18] and the γ data of Osborne, Stimson and Ginnings [7] to derive second and third pressure-series virial coefficients valid for the range 0 to 100

[2] The residual standard deviation is given by

$$\left(\frac{\sum_{i=1}^{n} r_i^2}{n-4}\right)^{1/2}$$

where r_i is the difference between the weighted mean and the corresponding computed value, n is the number of fitted points, $n-4$ is the number of degrees of freedom and 4 is the number of coefficients in eq (8).

°C [5, 6, 19]. Because the Goff and Gratch empirical relationships for the pressure-series virial coefficients are based on experimental data in the range of temperatures of interest to us, and because, of the various virial coefficients we tried, the Goff and Gratch virial coefficients yielded values of vapor pressure in closest agreement with Stimson's experimental values, we chose to use them. We converted the Goff and Gratch relationships [19] to SI units compatible with eqs (4) and (6) to obtain

$$B' = \left[+ \frac{0.4086}{T_{48}} - \left(\frac{665.19}{T_{48}^2}\right) \times 10^{\frac{72000}{T_{48}^2}} \right] \times 10^{-5} \qquad (12)$$

and

$$C' = 2.374 \left[+ \frac{0.4086}{T_{48}} - \left(\frac{665.19}{T_{48}^2}\right) \times 10^{\frac{72000}{T_{48}^2}} \right]^3 \times 10^{-8} \qquad (13)$$

where B' is in units of reciprocal pressure, 1/pascal,[3] C' is in units of the square of the reciprocal pressure, (1/pascal)^2, and T_{48} is based on IPTS–48. The equations as derived by Goff and Gratch presumably were in terms of absolute temperature on ITS–27. Over the range 0 to 100 °C, the errors arising in B', C', Z, and $Z-1$ from using T_{48} without conversion are negligible.

The Clausius-Clapeyron equation is an exact thermodynamic expression in which T is the absolute thermodynamic temperature. It therefore follows that the temperature T in eq (10), which was derived from the Clausius-Clapeyron equation, is also the absolute thermodynamic temperature. We will assume that T_{48} is a reasonably close approximation to the absolute thermodynamic temperature T and reserve for later discussion the reasons for this assumption. We inserted into eq (10) the coefficients of eq (8) on the basis of T_{48}, and the virial coefficients given by eqs (12) and (13) as functions of T_{48}. We selected as lower limits of integration for substitution into eqs (10) and (11) the pressure $p_0 = 101325.0$ pascals, which is one standard atmosphere, and the temperature $T_0 = 373.15$ K, which is the absolute temperature assigned to the steam point at one standard atmosphere on T_{48}. The gas constant for water vapor, R, is 0.46151 joules per gram kelvin and was derived from the NAS–NRC recommended value [20] of 8.3143 joules per mol kelvin for the universal gas constant and 18.01534 grams for the molar mass of water vapor on the unified carbon-12 scale. The units of the quantity γ were made consistent with R by the conversion factor 1 international joule = 1.000165 (absolute) joule [21]. After inserting the appropriate constants and conversion factor, eq (10) becomes

$$\int_{p_0}^{p} d(\ln p) = \sum_{i=0}^{3} A_i T_{48}^{i-1} + B \ln T_{48} + C \int_{373.15}^{T_{48}} \frac{\gamma}{T_{48}^2} \left(\frac{Z-1}{Z}\right) dT \qquad (14)$$

where $A_0 = -7.51152 \times 10^3$, $A_1 = 85.0869143$, $A_2 = 2.3759056 \times 10^{-2}$, $A_3 = -1.399697 \times 10^{-5}$, $B = -12.150799$, $C = -2.1671578$, p is expressed in pascals, $T_{48} = t_{48} + 273.15$ in kelvins, and t_{48} is in degrees Celsius on IPTS–48.

Because eq (14) is implicit in p we calculated p by iteration, numerically evaluating the integral at 1/4-deg intervals by means of the trapezoidal rule [22]. Iteration at each interval was terminated when successive values of p differed by less than one ppm. Evaluating the integral at 1/4-deg intervals was considered satisfactory. A check calculation at 80 °C showed that decreasing the interval to 0.025 deg produced a change in p of much less than one ppm from that obtained using 1/4-deg intervals.

The calculation of p by eq (14) is best accomplished with the aid of a high-speed digital computer. For desk-type calculations, an explicit equation without the integral is desirable. Equation (14) was converted into such an explicit form. A polynomial of the fourth degree was fitted, by the method of least squares, to numerical values of the integral at 1-deg intervals from 0 to 100 °C to give

$$C \int_{373.15}^{T_{48}} \frac{\gamma}{T_{48}^2} \left(\frac{Z-1}{Z}\right) dT = \sum_{i=0}^{4} D_i T_{48}^i \qquad (15)$$

where $D_0 = -5.2075843 \times 10^{-2}$, $D_1 = -5.769527 \times 10^{-5}$, $D_2 = 3.2537152 \times 10^{-6}$, $D_3 = -1.6189993 \times 10^{-8}$, and $D_4 = 2.381486 \times 10^{-11}$. Substituting eq (15) into eq (14), integrating the left-hand side of eq (14), and combining terms yielded

$$\ln p = \sum_{i=0}^{5} E_i T_{48}^{i-1} + B \ln T_{48}. \qquad (16)$$

The coefficients are listed in table 1.

On plotting the very small differences between $\ln p$ given by eq (16) and Stimson's measurements as a function of temperature, we observed that the course of the curve was smooth. A polynomial of the fourth degree was fitted to this difference curve. By adding the corresponding coefficients of like powers in T_{48} to eq (16) we obtained

$$\ln p = \sum_{i=0}^{5} E_i T_{48}^{i-1} + B \ln T_{48} \qquad (17)$$

which is identical to eq (16), except that the numerical values of the coefficients E_1 through E_5 are slightly different. The coefficients are listed in table 1.

We investigated the feasibility of simplifying eq (17). Numerous formulas have been proposed for empirically representing the functional relationship between vapor pressure and temperature [23, 24, 25, 26]. A procedure often followed is to select the formula with the least number of terms that not only best fits the vapor pressure data but also yields derivatives that are smooth and regular. We chose the equation

$$\ln p = \sum_{i=0}^{n} E_i T_{48}^{i-1} + B \ln T_{48} \qquad (18)$$

[3] 1 pascal = 1 newton/m^2 = 10^{-5} bar = 10^{-2} mb = 7.50062×10^{-3} mm Hg.

TABLE 1. *Coefficients to vapor pressure equations on IPTS–48*

	Eq (16) $n=5$	Eq (17) $n=5$	Eq (18a) $n=2$	Eq (18b) $n=3$	Eq (18c) $n=4$
E_0	-7.51152×10^{3}	-7.51152×10^{3}	-7.2465822×10^{3}	-6.7777203×10^{3}	-7.7847207×10^{3}
E_1	9.65609269×10^{1}	9.65389644×10^{1}	7.7641232×10^{1}	5.4409359×10^{1}	1.1670432×10^{2}
E_2	2.3701361×10^{-2}	2.3998970×10^{-2}	5.7447142×10^{-3}	$-8.0404143 \times 10^{-3}$	5.1177435×10^{-2}
E_3	$-1.0145982 \times 10^{-5}$	$-1.1654551 \times 10^{-5}$		7.1544503×10^{-6}	-5.438695×10^{-5}
E_4	$-1.6189993 \times 10^{-8}$	$-1.2810336 \times 10^{-8}$			3.189024×10^{-8}
E_5	$2.3816486 \times 10^{-11}$	$2.0998405 \times 10^{-11}$			
B	-1.2150799×10^{1}	-1.2150799×10^{1}	-8.2470402	-3.8358214	-1.6463576×10^{1}

because it is analogous in form to our derived eq (17) and fitted it for $2 \leqq n \leqq 4$ by the method of least squares to values of vapor pressure generated at 1-deg intervals from 0 to 100 °C by eq (17). The coefficients are listed in table 1. For convenience in identifying the several versions of eq (18), each has been designated with a letter a through c corresponding to $n = 2$, 3, and 4, respectively.

3. Results

The measurements made at the Physikalisch-Technische Reichsanstalt by Holborn and Henning [27] in 1908 from 50 to 200 °C and by Scheel and Heuse [28] in 1910 from 0 to 50 °C have, until now, constituted the major sources of data for the vapor pressure of water in the 0 to 100 °C range. In 1919, PTR published revised values of the vapor pressure [29] and these have served as the input data for many empirical formulations [30, 31].

The steam point has been used as one of the defining fixed points for the several successive practical temperatures scales that have been adopted internationally [10, 11, 12, 32]. Because of this, the vapor pressure near the steam point has been investigated in great detail [33, 34, 35, 36, 37, 38]. Most of these measurements were made over narrow temperature spans around 100 °C. The largest temperature range, 73 to 130 °C, was covered in 1939 by Moser and Zmaczynski [37] who used both a static and a dynamic method in their determinations. Beattie and Blaisdell in 1937 [36] and Michels, Blaisse, Ten Seldam and Wouters in 1943 [38] limited their observations to several degrees below and above 100 °C.

Douslin and McCullough in 1963 [39] and Douslin in 1970 [40], using an inclined dead-weight piston gage, made vapor pressure measurements from 0 to 20 °C.

The above series of measurements, plus the measurements of Stimson, comprise the most important determinations covering the 0 to 100 °C span.

We compared our formulation with these experimental data and with other formulations in order to obtain a general perspective on the degree of accord achieved. However, because of the high precision and internal consistency of the Stimson measurements we judged the efficacy of our vapor pressure equations primarily on their agreement with the Stimson data.

3.1. Comparisons With Stimson's Measurements

Differences in vapor pressure between Stimson's measurements and eqs (14), (16), (17), and (18) are given in table 2. The standard deviation of Stimson's values are also shown. Equation (14) yields values which agree with Stimson's measurements to within one standard deviation of the latter, except at 50 and 80 °C where the agreement is within two standard deviations. The maximum difference is 32 ppm and occurs at 25 °C. The conversion of eq (14), an implicit equation, to eq (16), an explicit equation, has little effect on the differences. Equation (17), which was

TABLE 2. *Comparison between calculated vapor pressures and Stimson's measurements on IPTS–48*

Temperature IPTS–48	Stimson's measurements			Eq (14)		Eq (16) $n=5$		Eq (17) $n=5$		Eq (18a) $n=2$		Eq (18b) $n=3$		Eq (18c) $n=4$	
	Vapor pressure	Standard deviation													
°C	*pascals*	*pascals*	*ppm*	*pascal*	*ppm*	*pascal*	*ppm*	*pascal*	*ppm*	*pascal*	*ppm*	*pascal*	*ppm*	*pascal*	*ppm*
25	3167.0	0.14	44	+0.1	+32	+0.1	+32	0.0	0	0.0	0	0.0	0	0.0	0
40	7377.27	.15	20	+ .11	+15	+ .08	+11	− .05	−7	− .14	−19	− .02	−3	− .07	−9
50	12338.30	.18	15	+ .22	+18	+ .18	+14	+ .09	+7	− .15	−12	+ .10	+8	+ .05	+4
60	19924.22	.16	8	− .15	− 8	− .17	−	− .12	−6	− .33	−17	− .13	−7	− .18	−9
70	31166.15	.22	7	− .20	− 6	− .20	−	+ .15	+5	+ .40	+12	+ .16	+5	+ .05	+2
80	47363.9	.52	11	− .7	−15	− .9	−19	− .2	−4	+ .9	+19	0.0	0	− .4	−8
100	101325.0	1.59	16	+ .1	+ 1	+ .2	+ 2	0.0	0	−5.3	−52	− .5	−5	− .4	−4

obtained by making a minor adjustment to the coefficients of eq (16), is in closer accord with Stimson's measurements. The maximum difference is 7 ppm. Of the three variants of eq (18), which are least square fits to values generated by eq (17), eqs (18b) and (18c) are in excellent agreement with Stimson's measurements, differing at most by 9 ppm. The differences for eq (18a) are larger, becoming as great as 52 ppm at 100 °C. There does not appear to be any reason for choosing any one equation from eqs (17), (18b), and (18c) on the basis of the difference between calculated vapor pressures and Stimson's measurements.

Using eq (17) as a base line, differences between eqs (18a) through (18c) and eq (17) were computed and plotted in pascals on figure 1 and in ppm on figure 2. The differences between Stimson's measurements and eq (17) are also shown. As n decreases from 4 to 2 the differences increase. Equation (18c) deviates systematically from eq (17) by 3 ppm. The differences between eq (18b) and (17) and eqs (18a) and (17) show oscillatory patterns; they do not exceed 9 ppm for eq (18b) but reach 52 ppm for (18a). Equations (18c) and (18b) offer a reduction in terms without a significant loss in accuracy. If a lower order of accuracy is acceptable, then eq (18a) could be used. In our opinion, eq (17) is preferable because it has a thermodynamic origin and, therefore, may inspire more confidence for interpolation and extrapolation. However, eq (17) has seven terms and where a simpler formula is desired, eq (18b), with five terms, would be our choice.

3.2. Comparisons With Douslin's Measurements

Douslin [39, 40] has made two sets of vapor pressure measurements over liquid water at temperatures below 25 °C using an inclined-piston dead-weight pressure gage.[4] The earlier measurements are as much as 4 pascals (30 microns) higher at some temperatures which Douslin attributed to incomplete degassing of his water sample in the earlier work. In the later work, the measurements were made in two series, Series I with the piston unweighted and Series II with the piston weighted. The two series overlap in temperature. We have compared Douslin's later measurements [40] with eq (17). The differences are given in table 3. Douslin's vapor pressures, measured on IPTS–68, were adjusted to IPTS–48 for this comparison. He reported that his estimated maximum systematic error varied from 0.32 pascal at 0 °C to 0.81 pascal at 20 °C, or, in relative terms, from 520 to 350 ppm. There is a systematic difference between Douslin's measurements and our calculations, his observed values deviating from our computed values by two to three times his estimated maximum systematic error. It must be emphasized that eq (17) was adjusted to fit Stimson's measurements in the range 25 to 100 °C and that our calculations below 25 °C are therefore, in part, extrapolations and may not necessarily fit other experimental measurements with comparable accuracy.

[4] We wish to thank Dr. D. R. Douslin for permission to quote from his second paper prior to publication.

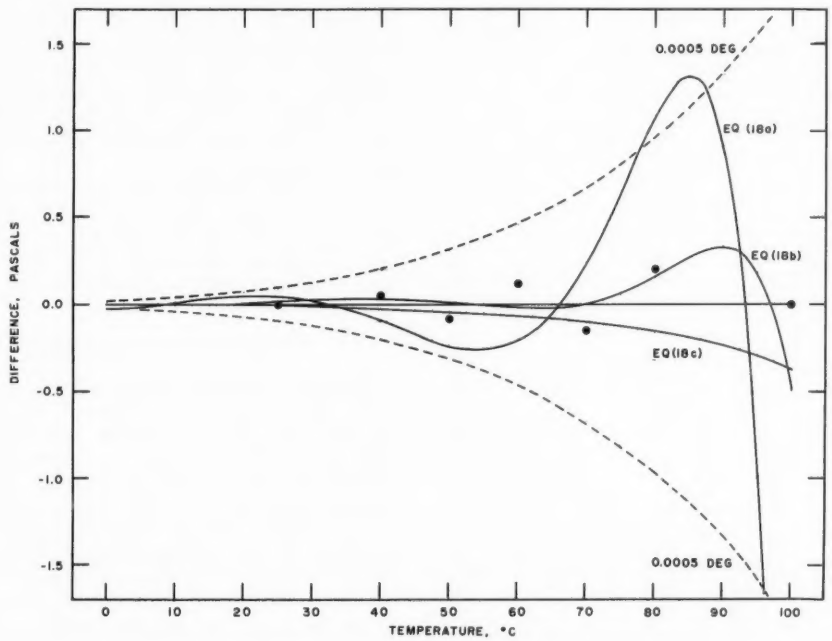

FIGURE 1. *Comparison of equations.*

Vapor pressure difference [other − eq (17)] in pascals between eqs (18a), (18b), and (18c) and eq (17). Vapor pressure difference between Stimson's measurements and eq (17) shown by solid circles. Dashed lines are difference curves for a temperature deviation of ± 0.0005 deg.

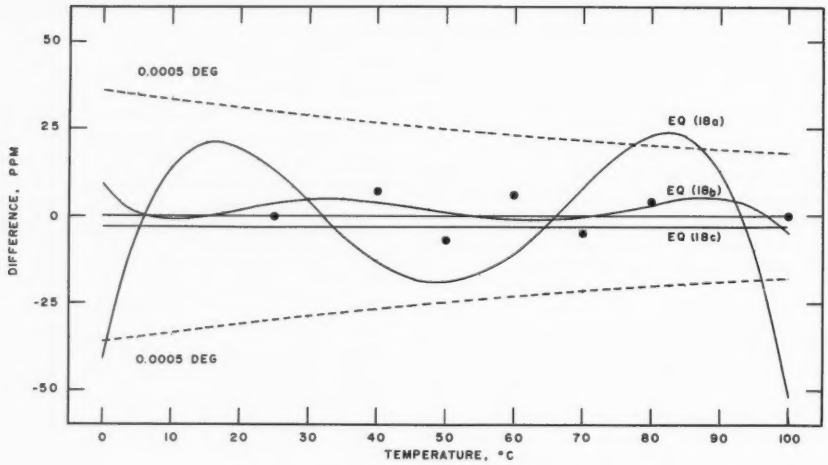

FIGURE 2. *Comparison of equations.*

Relative vapor pressure difference $\left[\frac{\text{other}-\text{eq (17)}}{\text{eq (17)}} \times 10^6\right]$ in ppm between eqs (18a), (18b), and (18c) and eq (17). Relative vapor pressure difference between Stimson's measurements and eq (17) shown by solid circles. Dashed lines are difference curves for a temperature deviation of ± 0.0005 deg.

TABLE 3. *Comparison between calculated vapor pressures and Douslin's measurements on IPTS–48*

Temperature IPTS–48	Douslin's Adjusted Measurements			Vapor Pressure Difference Douslin – Eq (17)	
	Vapor pressure	Maximum systematic error			
°C	pascals	pascals	ppm	pascals	ppm
		Series I			
0	[a] 611.5	0.32	520	+0.7	+1140
0.01	612.2	.33	540	+1.0	+1630
1	657.4	.35	530	+0.8	+1220
2	706.2	.35	490	+0.7	+ 990
3	758.6	.36	470	+1.1	+1450
4	813.7	.37	460	+0.8	+ 980
5	873.0	.39	440	+1.1	+1260
7.5	1037.2	.43	410	+1.0	+ 960
10	1228.8	.45	370	+1.6	+1300
15	1706.1	.57	340	+1.7	+1000
		Series II			
7.5	1036.8	0.43	410	+0.6	+580
12.5	1448.2	.61	420	−0.4	−280
17.5	2000.1	.73	370	+1.1	+550
20	2338.7	.81	350	+1.4	+600

[a] Metastable state; vapor pressure with respect to supercooled water.

3.3. Comparisons at the Ice and Triple Points

In table 4 we have compared several Physikalisch-Technische Reichsanstalt measurements of vapor pressure at 0 °C [28, 41, 42], Prytz's measurement at the triple point [43], and steam table values at both the ice and triple points [16, 44, 48] with corresponding values calculated with eq (17). It may be noted that the ice and triple points should not be subject to any temperature scale uncertainty as may be the case at other temperatures with data from the early 1900's. To complete the tabulation, Douslin's values at 0° and 0.01 °C [40] are repeated here.

At 0 °C, the PTR data are lower and Douslin's measurement is higher than our calculated value. At the triple point, Prytz's and Douslin's measurements are higher than our calculated value. We are in very good agreement with the steam table values.

3.4. Comparisons at and below the Steam Point

We have compared the Moser and Zmaczynski data [37],[5] the Beattie and Blaisdell data [36], and the Michels, Blaisse, Ten Seldam and Wouters data [38] with eq (17). This is shown as a plot of vapor pressure differences, in pascals, in figure 3 and as a plot of relative vapor pressure differences, in ppm, in figure 4. Moser and Zmaczynski fitted their data to a polynomial equation of the fourth degree in temperature. We, therefore, have included a curve of the differences between the Moser and Zmaczynski equation and eq (17). There is a varying negative difference between the

[5] The Moser and Zmaczynski data extend over the temperature range 73 to 130 °C. We have limited our consideration of these data to the temperature span 73 to 103 °C, the upper end corresponding to the highest temperature of the Beattie and Blaisdell data.

TABLE 4. *Ice point and triple point vapor pressures comparisons*

Source	Reference	Ice point, 0°			Triple point, 0.01 °C		
		Vapor pressure[a]	Difference Other-Eq (17)		Vapor pressure	Difference Other-Eq (17)	
		pascal	*pascal*	*ppm*	*pascal*	*pascal*	*ppm*
Eq (17)		610.75			611.20		
Experimental Measurements							
Thiesen and Scheel (1900)	[41]	610.46	−0.29	− 480			
Scheel and Heuse (1909)	[42]	610.46	−0.29	− 480			
Scheel and Heuse (1910)	[28]	610.11	−0.64	−1050			
Prytz (1931)	[43]				611.52	+0.32	+ 530
Douslin (1970)	[40]	611.5	+0.75	+1200	612.2	+1.0	+1640
Steam Tables							
IST (1963)	[44]	610.8	+0.05	+ 80	611.2	0.0	0
NEL (1964)	[44]	610.7	−0.05	− 80	611.2	0.0	0
IFC (1967)	[48]	610.8	+0.05	+ 80	611.2	0.0	0
Keenan, Keyes, et al. (1969)	[16]	610.8	+0.05	+ 80	611.3	+0.1	+160

[a] Metastable state; vapor pressure with respect to supercooled water.

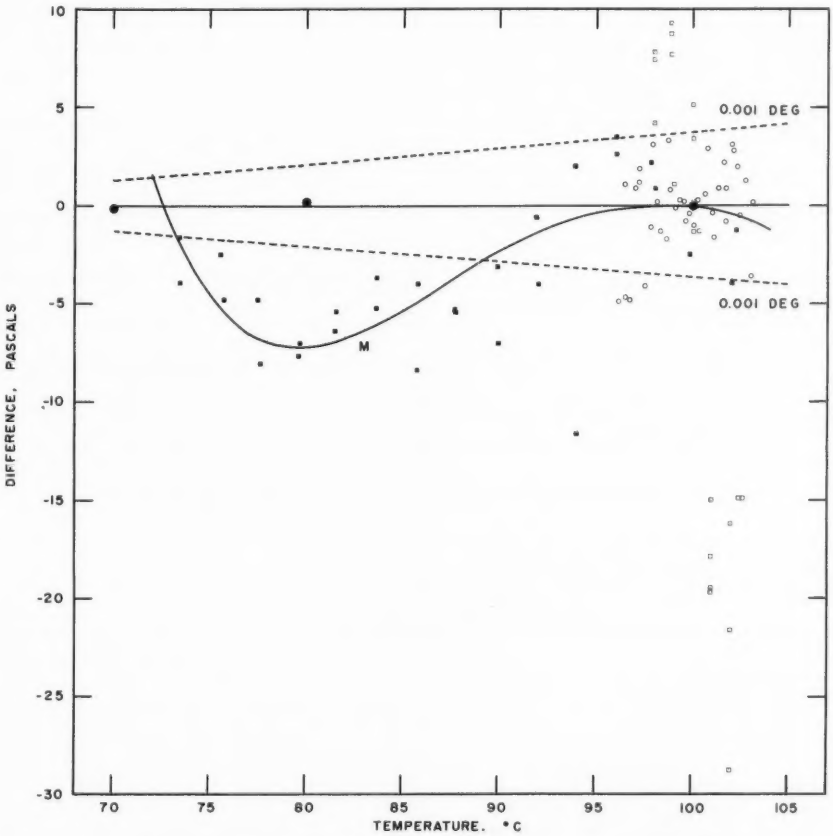

FIGURE 3. *Comparison with experimental data at and below the steam point.*

Vapor pressure difference [measurement − eq (17)] in pascals between measurement and eq (17).

● Stimson
■ Moser and Zmaczynski
○ Beattie and Blaisdell
□ Michels, Blaisse, Ten Seldam and Wouters
M Moser and Zmaczynski equation

Dashed lines are difference curves for a temperature deviation of ± 0.001 deg.

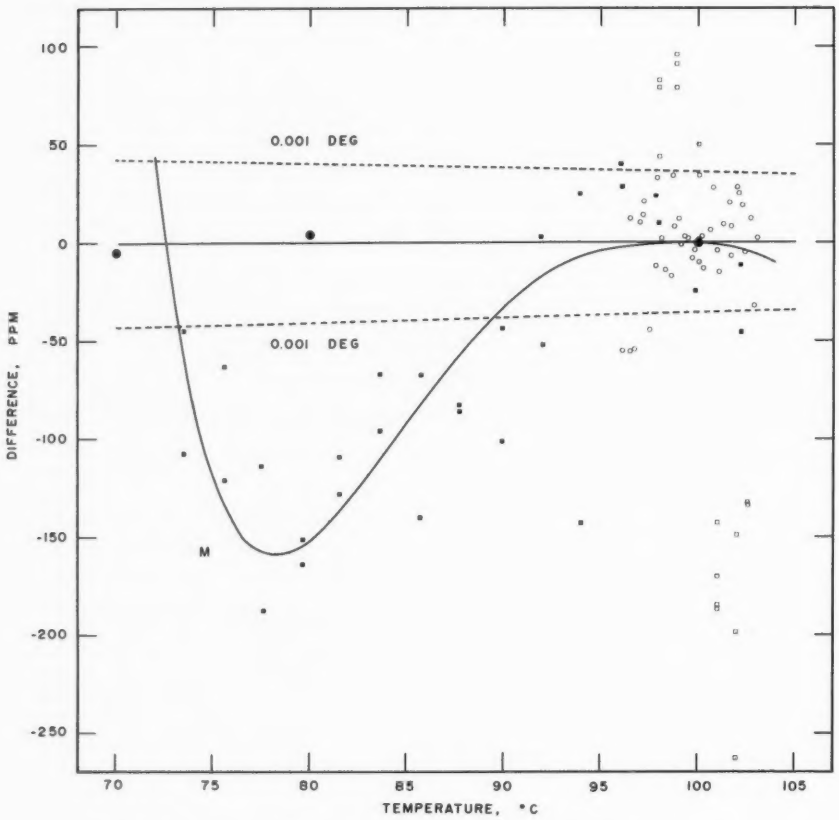

FIGURE 4. *Comparison with experimental data at and below the steam point.*

Relative vapor pressure difference $\left[\frac{\text{measurement} - \text{eq (17)}}{\text{eq (17)}} \times 10^6\right]$ in ppm between measurement and eq (17).

● Stimson
■ Moser and Zmaczynski
○ Beattie and Blaisdell
□ Michels, Blaisse, Ten Seldam and Wouters
M Moser and Zmaczynski equation

Dashed lines are difference curves for a temperature deviation of ±0.001 deg.

Moser and Zmaczynski data and eq (17), reaching a maximum at 78 °C of −8 pascals (−190 ppm). The Beattie and Blaisdell data cover only the very narrow temperature range of 96 to 103 °C. The differences appear to be random with respect to sign and magnitude. The residual standard deviation (based on n-7 degrees of freedom where 7 is the number of coefficients in eq (17)) is 1.55 pascals (17 ppm). The Michels et al. data extend from 98 to 102.6 °C. The differences vary linearly with temperature from about + 9.3 pascals (+ 100 ppm) at 98 °C to about − 27.7 pascals (− 260 ppm) at 102.6 °C.

3.5. Comparisons With Other Formulations

There have been numerous attempts to formulate vapor pressure equations for the pure water substance. Some of the equations are based on theoretical considerations, others are empirical. Since Sonntag [45] has summarized the extensive literature on the vapor pressure of water, we will not attempt to repeat it here. However, we will compare vapor pressures computed from several formulas which are in current use with vapor pressures computed from eq (17) over the range 0 to 100 °C. We have chosen for this purpose the equations due to Gerry [44, 46], Goff and Gratch [1], American Petroleum Institute [47], 1967 IFC [48], Bridgeman and Aldrich [49], and Gibson and Bruges [50].

The Gerry equation is an empirical formula derived from Physikalisch-Technische Reichsanstalt data. It was adopted by the Third International Conference on Steam Tables in 1934 [51] and has been used in successive formulations of the International Skeleton Tables.

The Goff and Gratch equation is based on integration of the Clausius-Clapeyron equation. It was adopted in 1947 by the Twelfth Conference of Directors of the International Meteorological Organization and by the Joint International Committee on Psychrometric Data in 1949 [19]. Tables of vapor pressure were published in the ASHRAE Guide [52] and in the Smithsonian Meteorological Tables [53]. Goff transposed this equation from the absolute ITS–48 to the absolute IPTS–48 [1] in which form it was adopted by the World Meteorological Organization [54]. It is this latter version which we use for our comparison.

The American Petroleum Institute Research Project 44 values of vapor pressure were calculated from the Antoine equation using several sets of constants, each set valid for a narrow range of temperatures. These constants were derived by fitting the Antoine equation to vapor pressures obtained from the Osborne and Meyers formulation [31] to which were added the "Cragoe-Stimson" corrections. The latter were obtained from vapor pressure measurements made at NBS in 1942 which had received limited private circulation but had remained unpublished until 1967 [50]. These 1942 measurements, augmented by a more extensive series of measurements made during the years 1947 through 1949, were finally published in 1969 by Stimson [2].

At the Sixth International Conference on the Properties of Steam an International Formulation Committee (IFC) was established to develop for use with computers a thermodynamically consistent formulation of the properties of steam within the tolerances of the International Skeleton Table of 1963. The result was the 1967 IFC Formulation for Industrial Use. Values of vapor pressure calculated using the vapor pressure equation given by the 1967 IFC are tabulated in the 1967 ASME Steam Tables [48].

In 1964, Bridgeman and Aldrich published an equation and tables of vapor pressure for water. Keenan et al. [16] used the Bridgeman and Aldrich values to derive an alternate equation. We used the logarithm of the vapor pressure given by Bridgeman and Aldrich in their tables [49] and converted this to vapor pressure.

Gibson and Bruges [50] derived two empirical vapor pressure equations using Chebyshev polynomials. One equation, which we will designate by a, reproduces the entries in table 1 of the 1964 NEL Steam Tables [44] which, in turn, are derived from the Gerry equation [44, 46], for 0 to 100 °C and from the Osborne and Meyers formulation [31] above 100 °C. The second equation, which we will designate by b, is based on APIRP–44 values [47] between 0 and 100 °C, and on the Osborne and Meyers formulation above 100 °C.

We have calculated the differences in vapor pressure between each of the above formulations and eq (17) and plotted these in pascals on figure 5 and in ppm on figure 6. Also included on these figures are the differences between Stimson's measurements and eq (17). These figures show the degree of accord of the several formulations with eq (17) as well as with the Stimson vapor pressures.

3.6. Conversion to IPTS-68

In 1968 the International Practical Temperature Scale of 1968 (IPTS-68) was adopted [32] as a replacement for IPTS-48. We have converted eq (17) from IPTS-48 to IPTS-68. Let the difference between these two scales be designated by μ, that is,

$$T_{68} - T_{48} = \mu. \tag{19}$$

Douglas [55] has shown that from 0 to 630.74 °C, μ is given by

$$\mu = \frac{4.904(10^{-7})t_{68}(t_{68} - 100)}{1 - 2.939(10^{-4})t_{68}} + \varphi(t_{68}) \tag{20}$$

where

$$\varphi(t_{68}) = 0.045\left(\frac{t_{68}}{100}\right)\left(\frac{t_{68}}{100} - 1\right)\left(\frac{t_{68}}{419.58} - 1\right)\left(\frac{t_{68}}{630.74} - 1\right) \tag{21}$$

and t_{68} is in Celsius degrees on IPTS-68. Expanding eq (20) into a polynomial, converting t_{68} to T_{68}, where $T_{68} = t_{68} + 273.15$, and neglecting higher order terms in T_{68}, we obtain

$$\mu = \sum_{i=0}^{4} \alpha_i T_{68}^i \tag{22}$$

where $\alpha_0 = 1.1314914$, $\alpha_1 = -9.9294171 \times 10^{-3}$, $\alpha_2 = 3.0306087 \times 10^{-5}$, $\alpha_3 = -3.9043313 \times 10^{-8}$ and $\alpha_4 = 1.7044968 \times 10^{-11}$. Equations (19) and (22) are now substituted into eq (17) which, after appropriate algebraic manipulations, and neglecting higher order terms in μ, becomes

$$\ln p = \sum_{i=0}^{9} F_i T_{68}^{i-2} + B \ln T_{68} \tag{23}$$

418-535 OL - 71 - 6

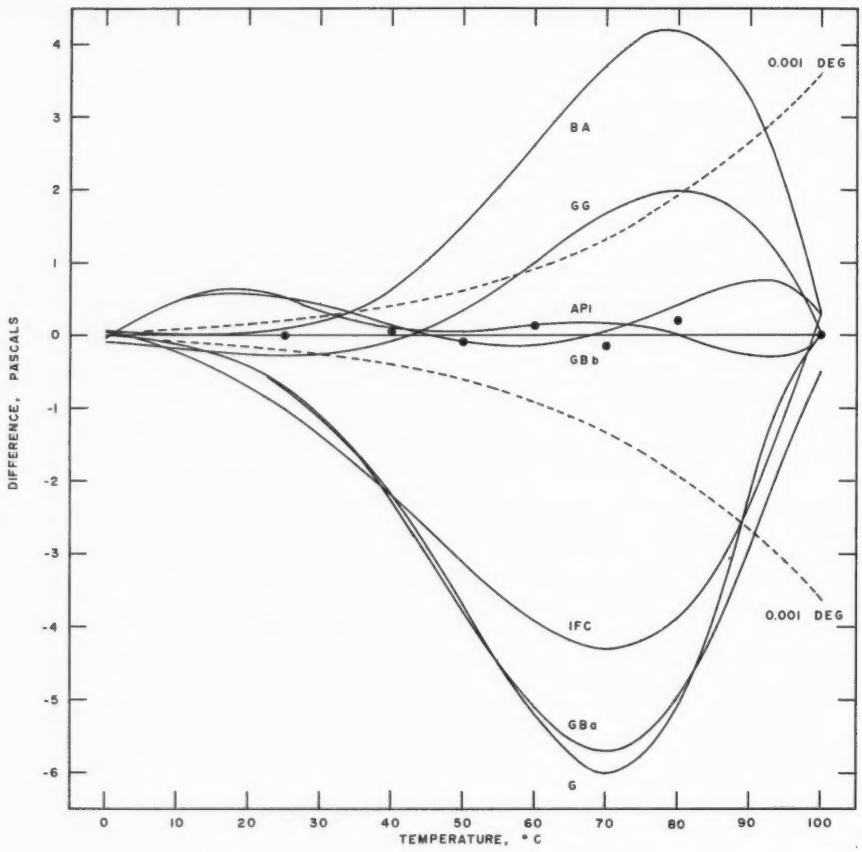

FIGURE 5. *Comparison with other formulations.*

Vapor pressure difference [other − eq (17)] in pascals between other formulations and eq (17).

API	American Petroleum Institute Research Project 44
BA	Bridgeman and Aldrich
G	Gerry
GBa	Gibson and Bruges, eq (a)
GBb	Gibson and Bruges, eq (b)
GG	Goff and Gratch
IFC	International Formulation Committee

Dashed lines are differences curves for a temperature deviation of ±0.001 deg.

where $F_0 = -8.49922 \times 10^3$, $F_1 = -7.4231865 \times 10^3$, $F_2 = 96.1635147$, $F_3 = 2.4917646 \times 10^{-2}$, $F_4 = -1.3160119 \times 10^{-5}$, $F_5 = -1.1460454 \times 10^{-8}$, $F_6 = 2.1701289 \times 10^{-11}$, $F_7 = -3.610258 \times 10^{-15}$, $F_8 = 3.8504519 \times 10^{-18}$, $F_9 = -1.4317 \times 10^{-21}$, and $B = -12.150799$.

In the range 0 to 100 °C, the numerical values of temperature on IPTS-48 are larger than on IPTS-68. Therefore, at the same numerical values of temperature, the corresponding vapor pressures are smaller on IPTS-48. For example, at $t_{48} = 50$ °C, the vapor pressure, calculated by eq (17), is 12338.39 pascals whereas at $t_{68} = 50$ °C, the vapor pressure, calculated by eq (23), is 12344.73 pascals.

We investigated the feasibility of simplifying eq (23). We fitted the equation

$$\ln p = \sum_{i=0}^{n} G_i T_{68}^{i-1} + H \ln T_{68} \qquad (24)$$

for $2 \leqq n \leqq 4$ by the method of least squares to values of vapor pressure generated at 1-deg intervals from 0 to 100 °C by eq (23). The results are comparable to that obtained for T_{48}. We, therefore, only present the results for $n = 3$ where the largest difference between eqs (23) and (24) is 8 ppm. The coefficients are as follows: $G_0 = -6898.2434$, $G_1 = 59.38385$, $G_2 = -5.797662 \times 10^{-3}$, $G_3 = 6.2223854 \times 10^{-6}$, and $H = -4.7406885$. Equation (24) on IPTS-68 with these coefficients is equivalent to eq (18b) on IPTS-48.

3.7. Tabulations

Using eqs (17) and (23) we computed vapor pressure in pascals, as a function of temperature, in degrees Celsuis, at 0.1-deg intervals, from 0 to 100 °C, These computed values are given in table 5 on IPTS-48 and in table 6 on IPTS-68.

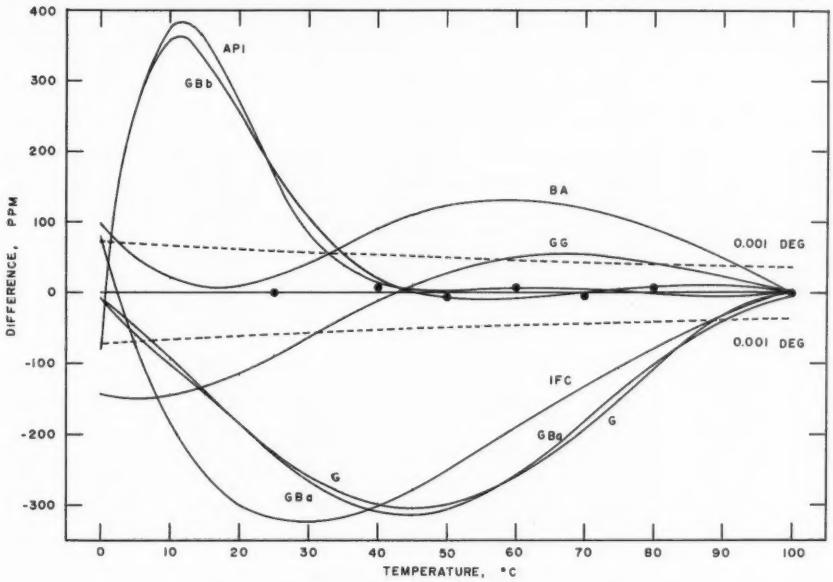

FIGURE 6. *Comparison with other formulations.*

Relative vapor pressure difference $\left[\frac{\text{other} - \text{eq (17)}}{\text{eq (17)}} \times 10^6\right]$ in ppm between other formulations and eq (17).

API	American Petroleum Institute Research Project 44.
BA	Bridgeman and Aldrich
G	Gerry
GBa	Gibson and Bruges, eq (a)
GBb	Gibson and Bruges, eq (b)
GG	Goff and Gratch
IFC	International Formulation Committee

Dashed lines are difference curves for a temperature deviation of ±0.001 deg.

TABLE 5. *Saturation vapor pressure over water (IPTS-48)*

Temperature deg C	0.0	0.1	0.2	0.3	0.4	0.5	0.6	0.7	0.8	0.9
	pascals	*pascals*	*pascals*	*pascals*	*pascals*	*pascals*	*pascals*	*pascals*	*pascals*	*pascals*
0	[a] 610.752	615.205	619.686	624.196	628.736	633.304	637.902	642.529	647.187	651.874
1	656.591	661.338	666.116	670.924	675.763	680.633	685.534	690.466	695.429	700.425
2	705.451	710.510	715.601	720.724	725.879	731.068	736.289	741.542	746.829	752.150
3	757.504	762.891	768.313	773.768	779.258	784.782	790.341	795.934	801.563	807.227
4	812.926	818.660	824.431	830.237	836.079	841.958	847.873	853.825	859.814	865.840
5	871.903	878.004	884.142	890.318	896.533	902.785	909.076	915.406	921.775	928.183
6	934.630	941.117	947.643	954.209	960.816	967.462	974.150	980.878	987.647	994.457
7	1001.31	1008.20	1015.14	1022.11	1029.13	1036.20	1043.30	1050.45	1057.64	1064.87
8	1072.15	1079.47	1086.84	1094.25	1101.70	1109.20	1116.75	1124.34	1131.97	1139.65
9	1147.38	1155.15	1162.97	1170.83	1178.75	1186.71	1194.71	1202.77	1210.87	1219.02
10	1227.22	1235.46	1243.76	1252.10	1260.50	1268.94	1277.43	1285.98	1294.57	1303.22
11	1311.91	1320.66	1329.45	1338.30	1347.20	1356.15	1365.16	1374.22	1383.33	1392.49
12	1401.71	1410.98	1420.30	1429.68	1439.11	1448.60	1458.14	1467.74	1477.39	1487.10
13	1496.87	1506.69	1516.57	1526.50	1536.49	1546.54	1556.65	1566.81	1577.04	1587.32
14	1597.66	1608.06	1618.52	1629.04	1639.62	1650.25	1660.95	1671.72	1682.54	1693.42
15	1704.37	1715.37	1726.44	1737.57	1748.77	1760.03	1771.35	1782.74	1794.19	1805.70
16	1817.28	1828.92	1840.63	1852.41	1864.25	1876.16	1888.13	1900.18	1912.28	1924.46
17	1936.70	1949.02	1961.40	1973.85	1986.37	1998.96	2011.62	2024.34	2037.14	2050.01
18	2062.96	2075.97	2089.05	2102.21	2115.44	2128.74	2142.12	2155.57	2169.09	2182.69
19	2196.36	2210.11	2223.93	2237.83	2251.80	2265.85	2279.98	2294.18	2308.47	2322.83
20	2337.26	2351.78	2366.37	2381.05	2395.80	2410.63	2425.55	2440.54	2455.62	2470.77
21	2486.01	2501.33	2516.73	2532.22	2547.79	2563.44	2579.18	2595.00	2610.90	2626.90
22	2642.97	2659.13	2675.38	2691.72	2708.14	2724.65	2741.25	2757.94	2774.71	2791.57
23	2808.53	2825.57	2842.70	2859.93	2877.24	2894.65	2912.15	2929.74	2947.42	2965.20
24	2983.07	3001.03	3019.09	3037.24	3055.49	3073.84	3092.28	3110.81	3129.44	3148.17
25	3167.00	3185.93	3204.95	3224.08	3243.30	3262.62	3282.05	3301.57	3321.20	3340.92
26	3360.75	3380.68	3400.72	3420.86	3441.10	3461.44	3481.90	3502.45	3523.11	3543.88
27	3564.75	3585.74	3606.82	3628.02	3649.33	3670.74	3692.26	3713.90	3735.64	3757.49
28	3779.46	3801.54	3823.73	3846.03	3868.44	3890.97	3913.61	3936.37	3959.24	3982.23
29	4005.33	4028.56	4051.89	4075.35	4098.92	4122.61	4146.42	4170.35	4194.40	4218.57
30	4242.86	4267.28	4291.81	4316.47	4341.25	4366.15	4391.18	4416.33	4441.61	4467.01
31	4492.54	4518.20	4543.98	4569.89	4595.93	4622.10	4648.40	4674.82	4701.38	4728.07
32	4754.89	4781.84	4808.93	4836.14	4863.49	4890.98	4918.60	4946.35	4974.24	5002.27
33	5030.44	5058.74	5087.18	5115.76	5144.47	5173.33	5202.33	5231.47	5260.74	5290.17
34	5319.73	5349.44	5379.29	5409.28	5439.42	5469.71	5500.14	5530.72	5561.45	5592.32
35	5623.34	5654.51	5685.83	5717.30	5748.92	5780.69	5812.62	5844.70	5876.93	5909.31
36	5941.85	5974.54	6007.39	6040.40	6073.56	6106.88	6140.36	6173.99	6207.79	6241.75
37	6275.86	6310.14	6344.58	6379.18	6413.95	6448.87	6483.97	6519.23	6554.65	6590.24
38	6626.00	6661.92	6698.02	6734.28	6770.71	6807.31	6844.08	6881.03	6918.15	6955.44
39	6992.90	7030.54	7068.35	7106.34	7144.50	7182.84	7221.36	7260.06	7298.93	7337.99
40	7377.22	7416.64	7456.24	7496.02	7535.98	7576.13	7616.46	7656.98	7697.68	7738.57
41	7779.65	7820.92	7862.37	7904.01	7945.85	7987.87	8030.09	8072.50	8115.10	8157.89
42	8200.88	8244.07	8287.45	8331.02	8374.80	8418.77	8462.94	8507.31	8551.89	8596.66
43	8641.63	8686.81	8732.19	8777.78	8823.57	8869.56	8915.76	8962.17	9008.79	9055.61
44	9102.65	9149.89	9197.35	9245.02	9292.90	9340.99	9389.30	9437.82	9486.56	9535.51
45	9584.69	9634.08	9683.68	9733.51	9783.56	9833.83	9884.32	9935.04	9985.98	10037.14
46	10088.53	10140.14	10191.99	10244.06	10296.35	10348.88	10401.64	10454.63	10507.85	10561.30
47	10614.98	10668.91	10723.06	10777.45	10832.08	10886.95	10942.05	10997.40	11052.98	11108.81
48	11164.88	11221.19	11277.74	11334.54	11391.58	11448.88	11506.41	11564.20	11622.23	11680.52
49	11739.05	11797.84	11856.88	11916.17	11975.72	12035.52	12095.58	12155.89	12216.47	12277.30
50	12338.39	12399.74	12461.35	12523.23	12585.37	12647.77	12710.44	12773.37	12836.57	12900.04
51	12963.77	13027.78	13092.06	13156.61	13221.43	13286.52	13351.89	13417.54	13483.46	13549.66
52	13616.13	13682.89	13749.92	13817.24	13884.84	13952.72	14020.88	14089.33	14158.07	14227.09
53	14296.40	14366.00	14435.89	14506.07	14576.54	14647.30	14718.36	14789.71	14861.36	14933.31
54	15005.55	15078.09	15150.93	15224.07	15297.51	15371.26	15445.31	15519.66	15594.32	15669.29
55	15744.56	15820.15	15896.04	15972.25	16048.76	16125.59	16202.73	16280.19	16357.97	16436.06
56	16514.47	16593.19	16672.24	16751.61	16831.31	16911.32	16991.66	17072.33	17153.32	17234.64
57	17316.29	17398.27	17480.58	17563.22	17646.20	17729.51	17813.15	17897.13	17981.45	18066.11
58	18151.11	18236.45	18322.12	18408.15	18494.51	18581.23	18668.29	18755.69	18843.45	18931.55
59	19020.01	19108.81	19197.97	19287.49	19377.36	19467.58	19558.17	19649.11	19740.41	19832.08

[a] Metastable state; vapor pressure with respect to supercooled water.

TABLE 5. *Saturation vapor pressure over water (IPTS-48)*—Continued

Temperature deg C	0.0	0.1	0.2	0.3	0.4	0.5	0.6	0.7	0.8	0.9
	pascals	*pascals*	*pascals*	*pascals*	*pascals*	*pascals*	*pascals*	*pascals*	*pascals*	*pascals*
60	19924.10	20016.49	20109.25	20202.37	20295.86	20389.71	20483.93	20578.53	20673.50	20768.83
61	20864.55	20960.64	21057.10	21153.94	21251.16	21348.76	21446.74	21545.11	21643.86	21742.99
62	21842.51	21942.41	22042.70	22143.39	22244.46	22345.93	22447.79	22550.04	22652.69	22755.73
63	22859.18	22963.02	23067.27	23171.91	23276.96	23382.41	23488.27	23594.54	23701.21	23808.29
64	23915.79	24023.69	24132.01	24240.75	24349.90	24459.46	24569.45	24679.85	24790.67	24901.92
65	25013.59	25125.69	25238.21	25351.15	25464.53	25578.34	25692.58	25807.25	25922.35	26037.89
66	26153.87	26270.28	26387.13	26504.43	26622.16	26740.34	26858.96	26978.03	27097.54	27217.51
67	27337.92	27458.79	27580.10	27701.88	27824.10	27946.79	28069.93	28193.53	28317.59	28442.11
68	28567.10	28692.55	28818.47	28944.85	29071.71	29199.03	29326.83	29455.10	29583.84	29713.06
69	29842.76	29972.94	30103.59	30234.73	30366.35	30498.46	30631.05	30764.13	30897.70	31031.76
70	31166.31	31301.35	31436.89	31572.92	31709.45	31846.48	31984.01	32122.04	32260.57	32399.61
71	32539.16	32679.21	32819.77	32960.84	33102.43	33244.53	33387.14	33530.27	33673.92	33818.08
72	33962.77	34107.98	34253.72	34399.98	34546.76	34694.08	34841.92	34990.30	35139.21	35288.65
73	35438.63	35589.15	35740.21	35891.80	36043.94	36196.63	36349.86	36503.63	36657.95	36812.83
74	36968.25	37124.23	37280.77	37437.85	37595.50	37753.71	37912.47	38071.80	38231.70	38392.16
75	38553.18	38714.78	38876.94	39039.68	39202.99	39366.88	39531.34	39696.38	39862.01	40028.21
76	40195.00	40362.37	40530.33	40698.87	40868.01	41037.73	41208.06	41378.97	41550.48	41722.59
77	41895.30	42068.61	42242.52	42417.04	42592.16	42767.90	42944.24	43121.19	43298.76	43476.94
78	43655.73	43835.15	44015.18	44195.84	44377.11	44559.02	44741.55	44924.71	45108.49	45292.91
79	45477.96	45663.65	45849.98	46036.94	46224.54	46412.79	46601.67	46791.21	46981.39	47172.22
80	47363.70	47555.83	47748.62	47942.06	48136.16	48330.92	48526.34	48722.42	48919.17	49116.58
81	49314.67	49513.42	49712.84	49912.94	50113.71	50315.16	50517.29	50720.10	50923.59	51127.77
82	51332.63	51538.18	51744.43	51951.36	52158.98	52367.30	52576.32	52786.04	52996.46	53207.58
83	53419.40	53631.93	53845.17	54059.12	54273.78	54489.16	54705.25	54922.05	55139.58	55357.83
84	55576.80	55796.50	56016.92	56238.07	56459.95	56682.57	56905.92	57130.00	57354.82	57580.39
85	57806.69	58033.74	58261.54	58490.08	58719.37	58949.42	59180.21	59411.77	59644.08	59877.15
86	60110.98	60345.57	60580.93	60817.06	61053.95	61291.62	61530.06	61769.27	62009.26	62250.03
87	62491.58	62733.92	62977.04	63220.94	63465.64	63711.12	63957.40	64204.47	64452.34	64701.01
88	64950.48	65200.75	65451.82	65703.71	65956.40	66209.90	66464.22	66719.35	66975.30	67232.06
89	67489.65	67748.06	68007.30	68267.36	68528.26	68789.98	69052.54	69315.93	69580.16	69845.23
90	70111.14	70377.90	70645.50	70913.95	71183.25	71453.40	71724.41	71996.27	72268.99	72542.57
91	72817.02	73092.33	73368.50	73645.55	73923.46	74202.25	74481.92	74762.46	75043.88	75326.18
92	75609.37	75893.44	76178.41	76464.26	76751.00	77038.64	77327.18	77616.62	77906.95	78198.19
93	78490.34	78783.39	79077.36	79372.24	79668.03	79964.73	80262.36	80560.91	80860.38	81160.77
94	81462.10	81764.35	82067.53	82371.65	82676.71	82982.71	83289.64	83597.52	83906.35	84216.12
95	84526.84	84838.51	85151.14	85464.73	85779.28	86094.78	86411.25	86728.69	87047.09	87366.47
96	87686.81	88008.13	88330.43	88653.71	88977.97	89303.22	89629.45	89956.67	90284.88	90614.09
97	90944.29	91275.49	91607.69	91940.89	92275.10	92610.31	92946.53	93283.77	93622.02	93961.29
98	94301.58	94642.88	94985.22	95328.58	95672.96	96018.38	96364.83	96712.32	97060.85	97410.41
99	97761.02	98112.68	98465.38	98819.13	99173.94	99529.80	99886.71	100244.69	100603.73	100963.83
100	101325.01									

TABLE 6. *Saturation vapor pressure over water (IPTS–68)*

Temperature deg C	0.0	0.1	0.2	0.3	0.4	0.5	0.6	0.7	0.8	0.9
	pascals	*pascals*	*pascals*	*pascals*	*pascals*	*pascals*	*pascals*	*pascals*	*pascals*	*pascals*
0	[a] 610.752	615.207	619.690	624.203	628.744	633.315	637.916	642.545	647.205	651.894
1	656.614	661.364	666.144	670.955	675.796	680.669	685.572	690.507	695.473	700.471
2	705.500	710.562	715.655	720.781	725.939	731.130	736.354	741.611	746.901	752.224
3	757.581	762.971	768.396	773.854	779.347	784.874	790.436	796.033	801.664	807.331
4	813.034	818.771	824.545	830.355	836.200	842.082	848.001	853.956	859.948	865.978
5	872.045	878.149	884.291	890.470	896.688	902.945	909.239	915.573	921.945	928.357
6	934.808	941.298	947.828	954.399	961.009	967.660	974.351	981.083	987.856	994.670
7	1001.53	1008.42	1015.36	1022.34	1029.37	1036.43	1043.54	1050.70	1057.89	1065.13
8	1072.41	1079.74	1087.11	1094.52	1101.98	1109.48	1117.03	1124.63	1132.27	1139.95
9	1147.68	1155.46	1163.28	1171.15	1179.07	1187.04	1195.05	1203.11	1211.21	1219.37
10	1227.57	1235.83	1244.13	1252.48	1260.88	1269.32	1277.82	1286.37	1294.97	1303.62
11	1312.32	1321.07	1329.87	1338.73	1347.63	1356.59	1365.60	1374.67	1383.78	1392.95
12	1402.17	1411.45	1420.78	1430.16	1439.60	1449.10	1458.64	1468.25	1477.91	1487.62
13	1497.39	1507.22	1517.11	1527.05	1537.04	1547.10	1557.21	1567.39	1577.62	1587.90
14	1598.25	1608.66	1619.12	1629.65	1640.24	1650.88	1661.59	1672.36	1683.18	1694.08
15	1705.03	1716.04	1727.12	1738.26	1749.46	1760.73	1772.06	1783.45	1794.91	1806.43
16	1818.01	1829.67	1841.38	1853.17	1865.02	1876.93	1888.91	1900.96	1913.08	1925.27
17	1937.52	1949.84	1962.23	1974.69	1987.21	1999.81	2012.48	2025.21	2038.02	2050.90
18	2063.85	2076.87	2089.97	2103.13	2116.37	2129.68	2143.07	2156.53	2170.06	2183.66
19	2197.34	2211.10	2224.93	2238.84	2252.82	2266.88	2281.02	2295.23	2309.52	2323.89
20	2338.34	2352.86	2367.47	2382.15	2396.91	2411.76	2426.68	2441.68	2456.77	2471.93
21	2487.18	2502.51	2517.93	2533.42	2549.00	2564.66	2580.41	2596.24	2612.16	2628.16
22	2644.25	2660.42	2676.68	2693.02	2709.46	2725.98	2742.59	2759.28	2776.07	2792.94
23	2809.91	2826.96	2844.11	2861.34	2878.67	2896.09	2913.60	2931.20	2948.89	2966.68
24	2984.56	3002.54	3020.61	3038.77	3057.03	3075.39	3093.84	3112.39	3131.03	3149.78
25	3168.62	3187.55	3206.59	3225.73	3244.96	3264.30	3283.73	3303.27	3322.91	3342.65
26	3362.49	3382.43	3402.48	3422.63	3442.89	3463.24	3483.71	3504.28	3524.95	3545.73
27	3566.62	3587.62	3608.72	3629.93	3651.25	3672.67	3694.21	3715.86	3737.61	3759.48
28	3781.46	3803.55	3825.75	3848.07	3870.50	3893.04	3915.70	3938.47	3961.36	3984.36
29	4007.48	4030.71	4054.06	4077.53	4101.12	4124.83	4148.65	4172.59	4196.66	4220.84
30	4245.15	4269.58	4294.13	4318.80	4343.60	4368.52	4393.56	4418.73	4444.02	4469.44
31	4494.98	4520.65	4546.45	4572.38	4598.43	4624.62	4650.93	4677.37	4703.95	4730.65
32	4757.49	4784.46	4811.56	4838.79	4866.16	4893.66	4921.29	4949.07	4976.97	5005.02
33	5033.20	5061.52	5089.97	5118.57	5147.30	5176.17	5205.19	5234.34	5263.64	5293.08
34	5322.66	5352.39	5382.25	5412.27	5442.42	5472.73	5503.18	5533.77	5564.52	5595.41
35	5626.45	5657.63	5688.97	5720.46	5752.10	5783.89	5815.83	5847.93	5880.18	5912.58
36	5945.14	5977.85	6010.72	6043.74	6076.92	6110.26	6143.75	6177.41	6211.22	6245.20
37	6279.33	6313.63	6348.09	6382.71	6417.50	6452.44	6487.56	6522.83	6558.28	6593.89
38	6629.66	6665.61	6701.72	6738.00	6774.45	6811.08	6847.87	6884.83	6921.97	6959.28
39	6996.76	7034.42	7072.25	7110.26	7148.44	7186.80	7225.34	7264.06	7302.96	7342.03
40	7381.29	7420.73	7460.35	7500.15	7540.13	7580.30	7620.65	7661.19	7701.92	7742.83
41	7783.92	7825.21	7866.69	7908.35	7950.21	7992.25	8034.49	8076.92	8119.54	8162.36
42	8205.37	8248.57	8291.98	8335.58	8379.37	8423.37	8467.56	8511.95	8556.55	8601.34
43	8646.34	8691.54	8736.94	8782.55	8828.36	8874.38	8920.60	8967.03	9013.67	9060.52
44	9107.58	9154.84	9202.32	9250.01	9297.92	9346.03	9394.36	9442.91	9491.67	9540.65
45	9589.84	9639.25	9688.89	9738.74	9788.81	9839.10	9889.62	9940.36	9991.32	10042.50
46	10093.92	10145.55	10197.42	10249.51	10301.83	10354.38	10407.16	10460.18	10513.42	10566.90
47	10620.61	10674.55	10728.73	10783.15	10837.80	10892.69	10947.82	11003.19	11058.79	11114.64
48	11170.74	11227.07	11283.65	11340.47	11397.54	11454.86	11512.42	11570.23	11628.29	11686.60
49	11745.15	11803.97	11863.03	11922.35	11981.92	12041.74	12101.83	12162.17	12222.76	12283.62
50	12344.73	12406.11	12467.75	12529.65	12591.81	12654.24	12716.93	12779.89	12843.11	12906.61
51	12970.37	13034.40	13098.70	13163.27	13228.12	13293.24	13358.63	13424.30	13490.25	13556.47
52	13622.97	13689.75	13756.81	13824.15	13891.78	13959.68	14027.87	14096.35	14165.11	14234.16
53	14303.49	14373.12	14443.03	14513.23	14583.73	14654.52	14725.60	14796.98	14868.65	14940.62
54	15012.89	15085.45	15158.32	15231.49	15304.96	15378.73	15452.80	15527.18	15601.86	15676.86
55	15752.16	15827.76	15903.68	15979.91	16056.45	16133.31	16210.47	16287.96	16365.76	16443.87
56	16522.31	16601.06	16680.13	16759.53	16839.25	16919.29	16999.65	17080.34	17161.36	17242.71
57	17324.38	17406.39	17488.72	17571.39	17654.39	17737.72	17821.39	17905.40	17989.74	18074.42
58	18159.44	18244.81	18330.51	18416.56	18502.95	18589.69	18676.77	18764.20	18851.98	18940.11
59	19028.59	19117.42	19206.60	19296.14	19386.04	19476.29	19566.90	19657.86	19749.19	19840.88

[a] Metastable state; vapor pressure with respect to supercooled water.

TABLE 6. *Saturation vapor pressure over water (IPTS–68)*—Continued

Temperature deg C	0.0	0.1	0.2	0.3	0.4	0.5	0.6	0.7	0.8	0.9
	pascals	*pascals*	*pascals*	*pascals*	*pascals*	*pascals*	*pascals*	*pascals*	*pascals*	*pascals*
60	19932.93	20025.34	20118.12	20211.26	20304.77	20398.65	20492.90	20587.52	20682.51	20777.87
61	20873.61	20969.72	21066.21	21163.07	21260.32	21357.94	21455.95	21554.33	21653.10	21752.26
62	21851.80	21951.73	22052.04	22152.75	22253.85	22355.33	22457.21	22559.49	22662.16	22765.23
63	22868.70	22972.56	23076.83	23181.50	23286.57	23392.04	23497.92	23604.21	23710.91	23818.01
64	23925.53	24033.45	24141.79	24250.55	24359.72	24469.31	24579.31	24689.74	24800.58	24911.85
65	25023.54	25135.66	25248.20	25361.17	25474.56	25588.39	25702.65	25817.34	25932.46	26048.02
66	26164.02	26280.45	26397.32	26514.64	26632.39	26750.59	26869.23	26988.32	27107.85	27227.83
67	27348.27	27469.15	27590.48	27712.27	27834.52	27957.22	28080.38	28204.00	28328.08	28452.62
68	28577.62	28703.09	28829.03	28955.43	29082.30	29209.64	29337.46	29465.74	29594.50	29723.74
69	29853.45	29983.65	30114.32	30245.47	30377.11	30509.23	30641.84	30774.93	30908.51	31042.59
70	31177.15	31312.21	31447.76	31583.81	31720.35	31857.39	31994.94	32132.98	32271.53	32410.58
71	32550.14	32690.21	32830.78	32971.87	33113.46	33255.57	33398.20	33541.34	33685.00	33829.18
72	33973.88	34119.10	34264.84	34411.11	34557.91	34705.24	34853.09	35001.48	35150.40	35299.85
73	35449.84	35600.37	35751.43	35903.04	36055.19	36207.88	36361.12	36514.90	36669.23	36824.11
74	36979.55	37135.53	37292.07	37449.17	37606.82	37765.03	37923.81	38083.14	38243.04	38403.51
75	38564.54	38726.14	38888.31	39051.05	39214.37	39378.26	39542.72	39707.77	39873.39	40039.60
76	40206.39	40373.76	40541.73	40710.27	40879.41	41049.14	41219.46	41390.38	41561.89	41734.00
77	41906.71	42080.02	42253.93	42428.45	42603.57	42779.30	42955.64	43132.59	43310.16	43488.34
78	43667.13	43846.54	44026.57	44207.22	44388.50	44570.40	44752.92	44936.08	45119.86	45304.27
79	45489.32	45675.00	45861.32	46048.28	46235.87	46424.11	46612.99	46802.52	46992.69	47183.51
80	47374.98	47567.11	47759.89	47953.32	48147.41	48342.16	48537.57	48733.64	48930.38	49127.78
81	49325.85	49524.59	49724.00	49924.09	50124.85	50326.28	50528.40	50731.19	50934.67	51138.83
82	51343.68	51549.22	51755.44	51962.36	52169.97	52378.27	52587.27	52796.97	53007.37	53218.47
83	53430.28	53642.79	53856.01	54069.94	54284.58	54499.93	54716.00	54932.78	55150.29	55368.51
84	55587.46	55807.14	56027.53	56248.66	56470.52	56693.11	56916.43	57140.49	57365.29	57590.82
85	57817.10	58044.12	58271.89	58500.41	58729.67	58959.68	59190.45	59421.97	59654.25	59887.29
86	60121.09	60355.65	60590.98	60827.07	61063.94	61301.57	61539.97	61779.15	62019.11	62259.84
87	62501.36	62743.65	62986.73	63230.60	63475.26	63720.70	63966.94	64213.98	64461.80	64710.43
88	64959.86	65210.09	65461.12	65712.96	65965.61	66219.07	66473.34	66728.43	66984.33	67241.05
89	67498.60	67756.96	68016.15	68276.16	68537.01	68798.68	69061.19	69324.53	69588.71	69853.73
90	70119.59	70386.30	70653.85	70922.24	71191.49	71461.58	71732.54	72004.34	72277.01	72550.53
91	72824.92	73100.17	73376.29	73653.27	73931.13	74209.86	74489.46	74769.94	75051.30	75333.54
92	75616.66	75900.67	76185.57	76471.36	76758.04	77045.61	77334.08	77623.45	77913.72	78204.89
93	78496.96	78789.95	79083.84	79378.65	79674.36	79971.00	80268.55	80567.02	80866.42	81166.74
94	81467.99	81770.16	82073.27	82377.31	82682.29	82988.20	83295.06	83602.86	83911.60	84221.29
95	84531.93	84843.52	85156.07	85469.57	85784.03	86099.44	86415.83	86733.17	87051.49	87370.77
96	87691.03	88012.26	88334.47	88657.66	88981.82	89306.97	89633.11	89960.24	90288.35	90617.46
97	90947.56	91278.66	91610.76	91943.86	92277.97	92613.08	92949.20	93286.34	93624.48	93963.65
98	94303.83	94645.03	94987.26	95330.51	95674.79	96020.09	96366.43	96713.81	97062.22	97411.68
99	97762.17	98113.71	98466.30	98819.94	99174.62	99530.37	99887.16	100245.02	100603.94	100963.92
100	101324.97									

4. Discussion

4.1. Thermodynamic Temperature

IPTS–68 was adopted as a replacement for IPTS–48 on the basis, at least in part, that it approached the thermodynamic temperature scale to within the uncertainty of the latter. Presumably, therefore, the conversion of γ and of B' and C' from IPTS–48 to IPTS–68, and the substitution of these quantities into eqs (10) and (11) should yield a solution giving vapor pressure on IPTS–68. This is not the case. The conversion of γ from IPTS–48 to IPTS–68 introduces a maximum change in γ, which occurs at 50 °C, of about 0.04 joules per gram, a quantity which has negligible effect on p. Similarly, B' and C', and consequently p, are affected insignificantly by the change in temperature scales. The lower limits of integration, p_0 and T_0, remain identical on the two scales. Thus, when temperature scale changes in γ, B' and C' are made, eq (10) still leads to a formulation that yields vapor pressures in substantial agreement with Stimson's vapor pressures on IPTS–48 and *not* on IPTS–68. The inference from these results is that IPTS–48 may be a closer approximation to the thermodynamic temperature scale in the range 0 to 100 °C than IPTS–68. It is for this reason that we based our derivation on IPTS–48 rather than IPTS–68.

4.2. Error Analysis

It is of interest to estimate the uncertainty in calculating p arising from estimated errors in γ, Z, R, T, and T_0, using the Clausius-Clapeyron equation. For purposes of this error analysis, we shall derive a simpli-

fied vapor pressure equation and we shall assume that all variables are independent. Equation (5) serves as a convenient starting point for this analysis:

$$\frac{dp}{p}=\frac{\gamma}{RT^2Z}\,dT \tag{5}$$

The calorimetric quantity γ varies from 2500 to 2257 j/g as t increases from 0 to 100 °C. As an approximation let γ be equal to 2400 j/g and constant. The compressibility factor Z varies from 0.9995 to 0.9845 over the same temperature range. Let Z be approximated by unity. Under these conditions, the integration of eq (5) yields

$$\ln\frac{p}{p_0}=-\left[\frac{\gamma}{RTZ}\right]_{T_0}^{T} \tag{25}$$

or

$$p=p_0\,e^{-\frac{\gamma}{RT_0Z}\left[\frac{T_0}{T}-1\right]}. \tag{26}$$

Differentiating p with respect to each parameter, replacing the differentials by finite increments, and dividing each side by p, we obtain

$$\frac{\Delta p}{p}=-\frac{1}{RT_0Z}\left[\frac{T_0}{T}-1\right]\Delta\gamma \tag{27}$$

$$\frac{\Delta p}{p}=\frac{\gamma}{R^2T_0Z}\left[\frac{T_0}{T}-1\right]\Delta R \tag{28}$$

$$\frac{\Delta p}{p}=\frac{\gamma}{RT_0Z^2}\left[\frac{T_0}{T}-1\right]\Delta Z \tag{29}$$

$$\frac{\Delta p}{p}=\frac{\gamma}{RT^2Z}\,\Delta T \tag{30}$$

$$\frac{\Delta p}{p}=-\frac{\gamma}{RT_0^2Z}\,\Delta T_0. \tag{31}$$

If we let the finite increments represent estimated errors in their respective parameters, then these equations permit us to calculate the corresponding estimated relative error in pressure $\frac{\Delta p}{p}$.

Since p_0 and T_0 are the assigned steam point values of pressure and temperature on IPTS-48, and since our derivation was made on this scale, it will be assumed that both p_0 and T_0 have zero error. The estimated error in γ will be taken as 0.23 j/g, the residual standard deviation of the least square fit of eq (8) to the Osborne, Stimson, and Ginnings data. The estimated error in R, the specific gas constant for water vapor, arises from the estimated errors in the universal molar gas constant and in the molecular weight of water. According to Bain [44], the error limit in R, defined as three times the standard deviation, is 7×10^{-5} j/gK. We will use the standard deviation as our estimate of error in R, i.e., 2.3×10^{-5} j/gK. Goff [19] has assigned tolerances to the Goff and Gratch virial coefficients which he set at twice the probable error. We have converted his tolerances to standard deviations, and computed, as the equivalent estimated error in Z, the quantity 2×10^{-4}, valid from 0 to 100 °C. The absolute temperature T enters into eq (26) as the independent variable so that it is subject neither to experimental nor scale error. Experimental and scale errors in T affect γ and the virial coefficients; however, these temperature errors show up and are contained in the assigned estimated errors in γ and Z.

A summary of the relative errors in p due to the estimated errors in γ, R, and Z is given in table 7. Assuming that the estimated errors in γ, R, and Z are systematic, then the total estimated error in p is at most the arithmetic sum of the estimated errors in p due to $\Delta\gamma$, ΔR, and ΔZ, respectively. This error analysis sets the outer bounds, that is, the estimated maximum error, that might occur in the calculation of p.

TABLE 7. *Estimated uncertainty in thermodynamic computation of vapor pressure*

Temperature	Estimated relative error in vapor pressure due to estimated uncertainties in			Estimated maximum error in vapor pressure	
t	γ	R	Z		
°C	*ppm*	*ppm*	*ppm*	*ppm*	*pascals*
0	490	254	1021	1765	1.08
10	426	221	887	1534	1.88
20	366	190	761	1317	3.08
30	310	161	644	1115	4.73
40	257	133	535	925	6.82
50	208	108	432	748	9.23
60	161	83	335	579	11.54
70	117	61	244	422	13.15
80	76	39	158	273	12.93
90	37	19	77	133	9.32
100	0	0	0	0	0

The deviations of our formulation from Stimson's data may be taken as a measure of the actual error in the calculation of vapor pressure. Therefore, one would expect these deviations to be comparable to the estimated maximum errors in the calculation of p, but they are two orders of magnitude smaller. It is possible that the estimates of uncertainty assigned to γ, R, and Z may be conservative leading to estimated maximum errors in p that are too large. It is also possible that the systematic errors in γ, R, and Z tend to compensate each other whereas we assumed that these are additive. Finally, the Goff and Gratch virial coefficients, which we used to compute Z, are not completely independent parameters. Goff and Gratch derived these virial coefficients using vapor pressure data, first in computing enthalpy coefficients from calorimetric data, that is, from γ, and second, in evaluating the constants of integration that result from integrating enthalpy coefficients to obtain virial coefficients. The effect of this procedure is that the virial coefficients are partially dependent on, and self-consistent with, p and γ. Although the Cragoe-Stimson measurements were available to Goff and Gratch [6], apparently these were used only for comparison with

their vapor pressure equation and not for deriving virial coefficients. On the other hand, the Gerry equation [7], the Osborne and Meyers formulation [31] and the Moser and Zmaczynski vapor pressure measurements [37] were used directly or indirectly.

We have employed virial coefficients due to Keyes [56] and to Czuha as given by Bain [44] and obtained equations which predict vapor pressures significantly different from Stimson's measurements, but well within our estimated maximum error. We ascribe, in part, the close concordance of our formulation with Stimson's measurements to our use of the Goff and Gratch virial coefficients.

It is clear that if the parameters γ, R, and Z were completely independent, then they must be known to an accuracy that is 1 to 2 orders of magnitude better than they are now known if thermodynamic calculations of vapor pressure are to have an uncertainty comparable to Stimson's measurements. Therefore, our formulation should not be taken as a corroboration from completely independent thermodynamic data of Stimson's vapor pressure measurements; rather it should be viewed as a smoothing function that has a theoretical basis. This is particularly true of eq (17) which was adjusted to fit Stimson's measurements. However, it is evident that there is a high level of thermodynamic consistency among the parameters p, γ, and Z.

5. Conclusions

The feasibility of computing the vapor pressure of water to a high order of accuracy by a smoothing function that has a rational basis has been demonstrated. Calculated vapor pressures agree with the very precise measurements of Stimson to within 7 ppm from 25 to 100 °C.

At the ice point the PTR data is in reasonable accord with the value calculated from eq (17); at the triple point and ice point, steam table values are very close to our calculated values. Prytz's triple point measurement is 0.3 pascal (490 ppm) higher than our calculated value.

It should be noted that the triple point, the most stable condition of the pure water substance, which serves as a defining fixed point on the thermodynamic temperature scale and is reproducible in temperature to a very high order of accuracy, has a comparatively inexactly known saturation pressure. A definitive determination of the vapor pressure at the triple point is needed.

Douslin's measurements from 0 to 20 °C are systematically higher than our calculations by 0.6 to 1.7 pascals, roughly of the order of 2 to 3 times his estimated maximum systematic error.

The Moser and Zmaczynski data from 73 to 100 °C are systematically lower than the values predicted by eq (17) whereas the Beattie and Blaisdell data, which only encompass the range 96 to 103 °C, deviate randomly about our curve with an estimated residual standard deviation of 1.55 pascals (17 ppm).

Equation (17) has seven terms, and where a simpler equation is desired, eq (18b) with five terms can be used with little degradation in the accuracy of the computed values. Equation (24) with $n=3$ on IPTS–68 is equivalent to eq (18b) on IPTS–48.

6. References

[1] Goff, J. A., Saturation pressure of water on the new kelvin scale, Humidity and Moisture, Arnold Wexler, Editor-in-chief, vol. **3** (Reinhold Publishing Corporation, New York, 1965) p. 289.

[2] Stimson, H. F., Some precise measurements of the vapor pressure of water in the range from 25 to 100 °C, J. Res. Nat. Bur. Stand. (U.S.), **73A** (Phys. and Chem.) No. 4, 493–496 (Sept.–Oct. 1969).

[3] Stimson, H. F., Precision resistance thermometry and fixed points. Temperature, Its Measurement and Control in Science and Industry, Vol. **2**, American Institute of Physics Symposium, 1939 (New York City, Reinhold Publishing Co.)

[4] Osborne, Nathan S., Calorimetry of a fluid, J. Res. Nat. Bur. Stand. (U.S.), **4**, 609–629 (1930)RP168.

[5] Goff, J. A. and Gratch, S., Thermodynamic properties of moist air. Heating, Piping and Air Conditioning, ASHVE Journal Section **17**, 334 (1945).

[6] Goff, John A. and Gratch, S., Low-pressure properties of water from −160 to 212 F, Trans. ASHVE **52**, 95 (1946).

[7] Osborne, N. S., Stimson, H. F., and Ginnings, D. C., Measurements of heat capacity and heat of vaporization of water in the range 0° to 100 °C, J. Res. Nat. Bur. Stand. (U.S.), **23**, 197–260 (1939)RP1228.

[8] Fiock, E. F. and Ginnings, D. C., Heat of vaporization of water at 50°, 70°, and 90 °C, J. Res. Nat. Bur. Stand. (U.S.), **8**, 321–324 (1932)RP416.

[9] Osborne, N. S., Stimson, H. F., and Ginnings, D. C., Calorimetric determination of the thermodynamic properties of saturated water in both the liquid and gaseous states from 100° to 374 °C, J. Res. Nat. Bur. Stand. (U.S.), **18**, 389–447 (1937)RP983.

[10] Burgess, G. K., The international temperature scale, J. Res. Nat. Bur. Stand. (U.S.), **1**, 635–640 (1928)RP22.

[11] Stimson, H. F., International temperature scale of 1948, J. Res. Nat. Bur. Stand. (U.S.), **42**, 209–217 (1949)RP1962.

[12] Stimson, H. F., International practical temperature scale of 1948. Text revision of 1960, J. Res. Nat. Bur. Stand. (U.S.), **65A** (Phys. and Chem.), No. 3, 139–145 (May–June 1961).

[13] Keyes, F. G., Smith, L. B., and Gerry, H. T., The specific volume of steam in the saturated and superheated condition together with derived values of the enthalpy, entropy, heat capacity and Joule Thompson coefficients. Proc. Am. Acad. Arts Sci. **70**, 319 (1936).

[14] Keyes, F. G., The consistency of the thermodynamic data for water substance vapor phase to 550 °C, J. Chem. Phys. **17**, 923 (1949).

[15] Keyes, F. G., The 1957 status of steam properties, Trans. ASME **80**, 555 (1958).

[16] Keenan, J. H., Keyes, F. G., Hill, P. G., and Moore, J. G., Steam Tables (John Wiley and Sons, Inc., New York, 1969).

[17] Knoblauch, O., Linde, R. and Klebe H., Die thermischen Eigenshaften des gesättigen und des überhitzten Wasserdampfes zwischen 100° und 180 °C, Mittheilung über Forschungsarbeiten d. Ver. d. Ing. **21**, 33 (1905).

[18] Collins, S. C., and Keyes, F. G., The heat capacity and pressure variation of the enthalpy for steam from 38° to 125 °C. Proc. Am. Acad. Arts. Sci. **72**, 283 (1938).

[19] Goff, J. A., Standardization of thermodynamic properties of moist air-final report of the Working Subcommittee, International Joint Committee on Psychrometric Data, ASHVE J. Section, Heating, Piping and Air Conditioning **55**, 118 (1949).

[20] New values for the physical constants, Nat. Bur. Stand. (U.S.), Tech. News Bull. 47 (10) 175 (1963).

[21] ASTM Metric Practice Guide, Nat. Bur. Stand. (U.S.), Handb. 102, 49 pages (1967).

[22] Abramowitz, M., and Stegun, I. A., Handbook of Mathematical Functions, Nat. Bur. Stand. (U.S.), Appl. Math. Ser. 55, 885 (June 1964).

[23] Partington, J. R., An Advanced Treastise on Physical Chemistry, vol. **2** (Longman, London, 1951).
[24] Miller, D. G., Estimating vapor pressures—a comparison of equations, Ind. Eng. Chem. **56,** 46 (1964).
[25] Ambrose, D., Councell, J. F., and Davenport, A. J., The use of Chebyshev polynomials for the representation of vapour pressures between the triple point and the critical point. J. Chem. Thermo. **2,** 283 (1970).
[26] Goodwin, R. D., Nonanalytic vapor pressure equation with data for nitrogen and oxygen. J. Res. Nat. Bur. Stand. (U.S.), **73A,** (Phys. and Chem.) No. 5, 487–491 (Sept.–Oct. 1969).
[27] Holborn, L., and Henning, F. Über das Platinthermometer und den Sättigungsdruck des Wasserdampfes zwischen 50 and 200°, Ann. Physik. IV, **26,** 54 (1908).
[28] Scheel, K., and Heuse, W. Bestimmung des Sättigungsdruckes von Wasserdampf zwischen 0 und +50°, Ann. Physik. IV **31,** 715 (1910).
[29] Holborn, L., Scheel, K., and Henning, F., Wärmetabellen (Vieweg and Sohn, 1919).
[30] Smith, L. B., Keyes, F. G., and Gerry, H. T., The vapor pressure of water, Proc. Am. Acad. Arts and Sci. **69,** 137 (1934).
[31] Osborne, N. S., and Meyers, C. H., A formula and tables for the pressure of saturated water vapor in the range 0 to 374 °C, J. Res. Nat. Bur. Stand. (U.S.), **13,** 1–20 (1934) RP691.
[32] The International Practical Temperature Scale of 1968, Metrologia **5,** 35 (1969).
[33] Volet, Ch., La température d'ébullition d'eau d'après les experiences de P. Chappuis, Travaux et Mémoires du Bureau international des Poids et Measures **18,** 11 (1929).
[34] Zmaczynski, A., and Bonhoure, A., La température d'ébullition de l'eau en fonction de la pression, J. Phys. et Rad. (VII) **1,** 285, (1930).
[35] Moser, H., Eine statische Methode für präzise Dampfdruckmessungen bei höheren Temperaturen und ihre Anwendung zur Sicherung des Hundertpunktes der Temperaturskala, Ann. Phys. (5) **14,** 790 (1932).
[36] Beattie, J. A. and Blaisdell, B. E., An experimental study of the absolute temperature scale. III. The reproducibility of the steam point. The effect of pressure on the steam point, Proc. Am. Acad. Arts Sci. **71,** 361 (1937).
[37] Moser, H. and Zmaczynski, A. Sättigungsdruck von Wasserdampf Zwischen 73 und 130°, Physik. Zeits **40,** 221 (1939).
[38] Michels, A., Blaisse, B., Ten Seldam, C. A. and Wouters, H. M., The vapour pressure of water in the neighborhood of 100 °C. Physica **10,** 613 (1943).
[39] Douslin, D. R. and McCullough, J. P., An inclined-piston deadweight pressure gage, U.S. Bureau of Mines Rept. of Investigation No. 6149 (1963).
[40] Douslin, D. R., Vapor pressure of water from −2.5 to 20 °C, J. Chem. Thermodynamics, in press.
[41] Thiesen, M. and Scheel, K., Bestimmung der Spannkraft des gesättigen Wasserdampfes bei Temperaturen zwischen −12° und +25°, Wiss. Abh. physik-techn. Reichsanst. **3,** 71 (1900).
[42] Scheel, K. and Heuse, W., Bestimmung des Sättigungsdruckes von Wasserdampf unter 0°, Ann. Physik. **29,** 729 (1909).
[43] Prytz, K., Manomètre a contact optique et son emploi pour la determination du triple point d'eau, Mathematisk-fysike meddelelser Danske Videnskabernes Selskab, Copenhagen **11,** No. 2 (1931).
[44] Bain, R. W., N.E.L. Steam Tables, 1964, Her Majesty's Stationery Office, Edinburgh, 1964.
[45] Sonntag, D., Hygrometrie, pp. 91–102 (Akademie-Verlag, Berlin, 1966–1968).
[46] Osborne, N. S., Stimson, H. F. and Ginnings, D. C., Thermal properties of saturated water and steam, J. Res. Nat. Bur. Stand. (U.S.), **23,** 261–270 (1939) RP1229.
[47] APIRP 44 Table 2-1-(1.01)-k, American Petroleum Institute Research Project 44, Texas A and M University, Chemical Thermodynamics Properties Center, Dept. of Chem., College Station, Texas (1964).
[48] Meyer, C. A., McClintock, R. B., Silvestri, G. J., and Spencer, Jr., R. C. 1967 ASME Steam Tables, American Soc. Mech. Eng., New York.
[49] Bridgeman, O. C., and Aldrich, E. W., Vapor pressure tables for water, Trans ASME. J. Heat Transfer Series C-D **86,** 279 (1964).
[50] Gibson, M. R. and Bruges, E. A., New equations for the thermodynamic properties of saturated water in both the liquid and vapor phases, J. Mech. Eng. Science **9,** 24 (1967).
[51] The Third International Conference on Steam Tables, Mech. Eng. **57,** 710 (1935).
[52] ASHRAE Guide and Data Book, Fundamentals and Equipment. 1961, 1965 and 1966, American Society of Heating Refrigerating and Air Conditioning Engineers, Inc., New York.
[53] List, R. J., Smithsonian Meteorological Tables, Sixth revised edition, Smithsonian Institution, Washington (1951).
[54] Resolution 19, IV Congress, World Meteorological Organization, 1963.
[55] Douglas, T. B. Conversion of existing calorimetrically determined thermodynamic properties to the basis of the International Practical Temperature Scale of 1968. J. Res. Nat. Bur. Stand. (U.S.), **73A** (Phys. and Chem), No. 5, 451–470 (Sept.–Oct. 1969).
[56] Keyes, F. G. The thermodynamic properties of water substance 0 to 150 °C. J. Chem. Phys. **15,** 602 (1947).

(Paper 75A3–665)

JOURNAL OF RESEARCH of the National Bureau of Standards—A. Physics and Chemistry
Vol. 75A, No. 3, May–June 1971

Publications of the National Bureau of Standards*

Selected Abstracts

Aquista, N., Schoen, L. J., **Matrix isolation spectrum of the SH radical,** *J. Chem. Phys.* **53,** *No. 3, 1290–1291 (August 1, 1970).*

Key words: Infrared spectrum; isolated SH; low temperature; matrix; SH; ultraviolet.

The free radical SH is produced in sufficient quantities by photodeposition of H_2S in argon matrices at 20 K for observation in the ultraviolet and infrared. Close agreement between the matrix data and the gas-phase work in the electronic region support the assignment.

Adler, I., Walter, L. S., Lowman, P. D., Glass, B. P., French, B. M., Philpotts, J. A., Heinrich, K. F. J., Goldstein, J. I., **Electron microprobe analysis of Apollo 11 lunar samples** (*Proc. Apollo 11 Lunar Science Conf., Houston, Texas*), *Geochim. Cosmochim.* **34,** Suppl. 1, 87–92 (January 30, 1970).

Key words: Analysis; electron probe; lunar samples; microanalysis; minerals; rocks.

Plagioclase feldspar, clinopyroxene and ilmenite in a polished thin section of a "Type A" crystalline rock were analyzed. The clinopyroxene grains are compositionally variable and both high Ca and low Ca phases are present. The plagioclase is compositionally homogeneous. The ilmenite is chemically homogeneous except for occasional, small areas of high local chromium concentration. Accessory minerals are: apatite (containing Cl, F, Y, and Ce), troilite and metallic iron.
Glassy spherules from the lunar soil are mostly similar in composition to the crystalline rocks; however, some appear to have been monomineralic.
The crystalline rock has apparently formed by relatively rapid cooling of a silicate melt under conditions of low partial pressure. Many components of the soil appear to have formed by meteoritic impact.

Anderson, H. J., Brenner, A., **Chemical vapor deposition of rhenium,** *Proc. 2nd Intern. Conf. on Chemical Vapor Deposition, Los Angeles, Calif., May 1970, pp. 356–366 (1970).*

Key words: Chemical vapor deposition; rhenium; rhenium coatings; rhenium oxychlorides.

The chemical vapor deposition (CVD) of rhenium from a variety of compounds was investigated. The reduction of perrhenyl chloride and rhenium oxytetrachloride with hydrogen resulted in the production of deposits which ranged from bright to powdery, the latter being obtained at a temperature above 600 °C. The bright deposits were cracked and exfoliated from the substrate. The only ductile deposits were obtained by thermal decomposition of $ReOCl_4$ at about 1200 °C, which process has been previously described by Russian workers.

Ausloos, P., **Ion-molecule reactions and photoionization of hydrocarbons,** *Chapter in Progress in Reaction Kinetics, G. Porter, Ed., 5, 113–179 (March–April 1970).*

Key words: Hydrocarbons; ion-molecule reactions; radiolysis and photoionization; rate constants; theory.

This is a critical review of the literature on ion-molecule reactions in the radiolysis and photoionization of hydrocarbons.

Ausloos, P., Lias, S. G., **Carbonium ions in radiation chemistry. Reactions of *t*-butyl ions with hydrocarbons,** *J. Am. Chem. Soc.* **92,** *No. 17, 5037–5045 (August 26, 1970).*

Key words: Carbonium ions; ion-molecule reactions; neopentane; radiolysis; rate constants; *t*-butyl ion.

t-Butyl ions, generated by the γ-irradiation of neopentane, undergo hydride transfer reactions with alkanes having tertiary hydrogen atoms

$$t\text{-}C_4H_9^+ + RH \rightarrow iso\text{-}C_4H_{10} + R^+$$

to form isobutane and a tertiary carbonium ion as products. By irradiating neopentane in the presence of mixtures of two reactant molecules, one deuterated and one non-deuterated, the relative rates of the hydride transfer reaction for twenty-two C_5-C_8 alkanes were determined with an unusually high accuracy from the observed ratios of *iso*-C_4H_9D to *iso*-C_4H_{10}. Absolute rate constants for the reactions, based on a determination of the rate of depletion of the isobutane yield when ammonia is added, are given. The rate constants are generally very low (10^{-11} to 10^{-10} cm^3/molecule-s), but are shown to depend on the heat of reaction, which in turn, depends on the structure of the tertiary product ion, R^+. The evidence indicates that the hydride transfer reactions of the *t*-butyl ion have an activation energy, $E_{act} \leq 0.12$ eV.

Branscomb, L. M., **A fully integrated partnership between government laboratory and university,** *Proc. Education on Federal Laboratory-University Relationships Symp., sponsored by the Federal Council for Science and Technology and the American Council on Education, Washington, D.C., October 29–31, 1968, pp. 139–151 (May 1969).*

Key words: Management principles; research management principles.

The pattern of government laboratory-university collaboration inherent in the Joint Institution for Laboratory Astrophysics (JILA) is described, with emphasis on its advantages and shortcomings and the relevant management principles.

Branscomb, L. M., **Discussion,** *Can. J. Chem.* **47,** *No. 10, 1703–1941 (May 15, 1969).*

Key words: Aeronomy; editorial comments.

This manuscript contains the edited comments on invited papers by A. Dalgarno, A. V. Phelps, and E. E. Ferguson which will appear in Transactions of the IAGA (International Association of Geomagnetism and Aeronomy) Symposium on Laboratory Measurements of Aeronomic Interest, September 3–4, 1968, York University, Toronto, Canada. The Transactions are to be published in the Canadian Journal of Chemistry.

Brauer, G. M., Huget, E. F., Termini, D. J., **Plastic modified *o*-Ethoxybenzoic acid cements as temporary restorative materials,** *J. Dental Res.* **49,** *No. 6, 1487–1494 (November–December 1970).*

Key words: Dental restorative materials; EBA cements; plastic reinforced restoratives; restorative materials; temporary dental cements.

To improve the stress-bearing characteristics, powdered polymers of relatively low elastic moduli were incorporated into the powder component of EBA cements. Acrylic and vinyl copolymers appeared to be the most suitable additives for achieving reinforcement. The resultant products exhibited significant increases in tensile strength. These materials possess excellent manipulative qualities. Limited clinical evaluation indicates that some of the polymer-reinforced materials, on the basis of their demonstrated mechanical and palliative properties, appear to be highly useful as long duration temporary restoratives.

Brenner, A., Anderson, H. J., **Chemical vapor deposition of rhenium,** *Proc. Interfinish 1968 7th International Metal Finishing Conf., May 5–9, 1968, Hanover, Germany, pp. 28–31 (1968).*

Key words: Carbonyl; chemical vapor deposition; electrodeposition; hexafluoroacetylacetone; rhenium coatings; trifluorophosphine.

Methods of depositing rhenium coatings are reviewed, and a brief account is given of work now in progress at NBS on the deposition of rhenium. The electrodeposition of rhenium from an aqueous perrhenate bath does not yield a satisfactory coating; work at NBS with various rhenium compounds in both aqueous and nonaqueous solutions did not lead to a better plating process. The chemical vapor deposition (CVD) of rhenium is more promising, particularly the reduction of rhenium hexafluoride with hydrogen. At NBS work has been done with the CVD of rhenium from the carbonyl, the hexafluoroacetylacetone derivative, and work is in progress with the trifluorophosphine derivatives.

Bridges, J. M., Wiese, W. L., **Transition probabilities for the prominent red lines of Ne I,** *Phys. Rev. A.* **2,** *No. 2, 285–293 (August 1970).*

Key words: Neon; spectrum; transition probabilities.

Relative transition probabilities of all 30 lines belonging to the prominent $3s-3p$ transition array of Ne I have been measured in emission with a wall-stabilized arc operating in an argon-neon mixture atmospheric pressure. The data have been normalized to an absolute scale provided by recent lifetime measurements of the $3p$-levels. Our results as well as the data from other emission measurements have been subjected to extensive comparisons and tests, including a check for fullfillment of the J-file sum rule. It is found that our data exhibit a much better consistency than any other set of individual values. On the basis of this as well as our uncertainty estimates we estimate that the accuracy of our individual transition probabilities for this transition array, except for a few weak lines, is of the order of 10% on an absolute basis.

Brinckman, F. E., Wachtman, J. B., Jr., Editors, **Research materials developed under the NBS inorganic materials program,** *Nat. Bur. Stand. (U.S.), Spec. Publ. 333, 71 pages (September 1970) 70 cents, SD Catalog No. C13.10:333.*

Key words: Chemical properties; composition; gases; glasses; liquids; multiphase materials; physical properties; polycrystals; preparation; research.

The National Bureau of Standards develops many specialized materials in the process of carrying out research supporting its measurements, standards, and service activities. These materials include gases, liquids, glasses, single crystals, polycrystals, and various multiphase materials; their compositions (including trace elements in some cases) and physical characteristics are tailored to specific research needs, but the materials are often of use for other research purposes. Production is usually limited to immediate internal needs and samples are not generally available for distribution, but knowledge of production techniques and materials characteristics which may be helpful to other scientists is available. The present listing of research materials developed in the Inorganic Materials Division accordingly gives names of scientific staff members who may be contacted for this type of information as well as giving a brief summary of the nature, method of preparation and properties determined for each material.

Brown, D. W., Lowry, R. E., Wall, L. A., **Radiation-induced copolymerization of tetrafluoroethylene and 3,3,4,4,5,5,5-heptafluoropentene-1 under pressure,** *J. Polymer Sci. Part A-1,* **8,** *No. 9, 2441–2452 (1970).*

Key words: Amorphous polymer; copolymerization; fluoropolymers; glass temperature; 3,3,4,4,5,5,5-heptafluoropentene-1; high pressure; radiation-induced; tetrafluoroethylene.

An investigation was made of the gamma-ray induced copolymerization of tetrafluoroethylene and 3,3,4,4,5,5,5-heptafluoropentene-1. At 22 °C and 5000 and 10,000 atm the polymerization rate changes little between 0 and 75 mole percent tetrafluoroethylene. Above 90 mole percent the rate increases greatly. Molecular weights vary in a fashion similar to the variation in the rates. Between 10,000 and 15,000 atm the viscosity of the pentene increases by a factor of 10^5. A rate maximum occurs in this pressure range; polymerization continues long after irradiation is ended. Both reactivity ratios favor the pentene.
Several copolymer properties were studied. The polymers are amorphous and soluble in perfluoro-ethers, -alkanes, and -aromatics if they contain less than 80% tetrafluoroethylene. The glass temperatures of the amorphous polymers decrease and the thermal and radiation stability increases as the tetrafluoroethylene content increases.

Carrington, T., Garvin, D., **The chemical production of excited states,** *Chapter 3 in Comprehensive Chemical Kinetics Volume* **3.** *The Formation and Decay of Excited Species, pp. 107–181 (1969).*

Key words: Atom-transfer reaction; chemi-excitation; chemical activation; chemical kinetics; gas phase; potential energy surfaces; recombination; review; unimolecular decomposition.

Chemical excitation, the production of molecules in non-equilibrium population distributions in electronic, vibrational and rotational states is described.
The applicable parts of reaction rate theory are reviewed. Typical cases are used as examples of chemi-excitation in combination, group transfer and decompostion reactions. Reactions involving excited electronic states are discussed in terms of the interaction of potential surfaces. Applications to lasers and to the study of unimolecular decompositions are described.

Cezairliyan, A., McClure, J. L., Morse, M. S., Beckett, C. W., **Measurement of heat capacity of tantalum in the range 1900–3000 K by a pulse heating method,** *Proc. 5th Symp. Thermophysical Properties, Newton, Mass., September 30–October 2, 1960, C. F. Bonilla, Ed., pp. 385–390 (American Society of Mechanical Engineers, New York, N.Y., 1970).*

Key words: Heat capacity; high-speed measurements; high temperature; tantalum; thermodynamics.

A technique is described for the high-speed (millisecond resolution) measurement of heat capacity of electrical conductors at high temperatures (above 1900 K). Measurements on heat capacity of tantalum in the temperature range 1900 to 3000 K are reported and are compared with those in the literature. Duration of an individual experiment in which the specimen was heated from room temperature to close to its melting point is less than one second. Temperature measurements were made with a high-speed photoelectric pyrometer. Experimental quantities (voltage, current, temperature) were recorded with a high-speed digital data acquisition system which has a time resolution of 0.4 ms. Estimated inaccuracy of heat capacity measurements in the above temperature range is 2 to 3 percent.

Cezairliyan, A., Morse, M. S., Berman, H. A., **Improvements in oscilloscopic measurements in high-speed experiments,** *Nat. Bur. Stand. (U.S.), Tech. Note 539, 20 pages (Oct. 1970) 30 cents, SD Catalog No. C13.46:539.*

Key words: High-speed measurements; high-speed recording; oscilloscopes.

Two refinements in oscilloscopic recording have been made which improve considerably the recording of isolated events in heavy

current discharge studies, where substantially rectangular pulses are employed. The accuracy of the method employed has been verified experimentally to be in the region of 0.01 to 0.1 percent. The first refinement is a unit for the differential suppression of the incoming signal by an adjustable amount, and the second refinement is a system by which time markers are sent to several oscilloscopes at adjustable time intervals simultaneously with the actual incoming signal.

Chandler, H. H., Bowen, R. L., Paffenbarger, G. C., Mullineaux, A. L., **Clinical investigation of a radiopaque composite restorative material,** *J. Am. Dental Assoc.* **81,** *No. 4, 935–940 (October 1970).*

Key words: Clinical research (dental); composite restorations; diagnosis; physical properties of fillings; x-ray opaque.

A radiopaque composite restorative material was developed using a ternary eutectic dimethacrylate liquid formulation as the binder and a BaF_2-containing glass and fused silica as the reinforcing fillers. One hundred and ten restorations were placed using this newly developed material. The restorations will be observed over a prolonged period. They had sufficient radiopacity and yet were esthetically pleasing. Postoperative radiographs showed comparatively radiolucent areas in and around many of the restorations. These radiolucencies were usually caused by unfilled spaces at the tooth-restoration interface.

Christ, B. W., Smith, G. V., **Effects of nitrogen in lattice solution on the yielding and flow of zone-refined iron polycrystals between 128 and 300 K,** *Trans. Met. Soc. AIME* **1,** *No. 4, 827–833 (April 1970).*

Key words: Flow stress; impurity softening; lattice solution; lower yield stress; nitrogen; polycrystals; solution hardening; upper yield point; zone-refined iron.

Up to 0.18 at. pct N was introduced into lattice solution in hydrogen-purfied, zone-refined iron polycrystals. Tensile tests were conducted at 128, 173, 223, and 300 K on quenched samples at constant strain rate, 7×10^{-4} sec^{-1}. The following dynamic effects due to increasing nitrogen in lattice solution were found: i) the temperature dependence of the flow stress at strains beyond the end of the Luder's plateau decreased, ii) serrated flow occurred at 300 K, but not at lower temperatures, iii) elongation to maximum load decreased at 300 K, but increased at 173 K, and iv) the magnitude of the yield drop at 173 K decreased substantially. These dynamic effects are interpreted in terms of a change in the relative mobility of nitrogen atoms and dislocations between 128 and 300 K.

Corliss, E. L. R., **Hearing aids,** *Nat. Bur. Stand. (U.S.) Monogr. 117, 26 pages (Oct. 1970) 35 cents, SD Catalog No. C13.44:117.*

Key words: Audition; communications; hearing; hearing aids; selection of hearing aids; speech communication.

This publication contains information, useful to the hard of hearing, on several topics relating to hearing and hearing aids. It is assumed that the individual has already consulted a physician on the diagnosis of his hearing loss, for this is the necessary first step in correcting any faulty hearing condition. The publication may also be of interest to teachers and others wishing to explore this field.
This publication represents an extensive revision of NBS Circular 534, Hearing Aids. It includes new material based upon research conducted at the National Bureau of Standards during the intervening years.

Davis, M. M., **Bronsted acid-base behavior in "inert" organic solvents,** *Chapter 1 in The Chemistry of Nonaqueous Solvents,* **III,** *1–135 (Academic Press Inc., New York, N. Y., 1970).*

Key words: Acid-base behavior; acidity and basicity scales; aprotic organic solvents; hydrogen bonding; titrations.

A unified picture of acid-base behavior in aprotic organic solvents is presented, based on an extensive survey of the literature and experimental results of the author and associates. Evidence given to support this picture includes data pertaining to colligative properties of acids, bases, and salts and also conductance, dielectric constants, distribution between immiscible solvents, and spectral absorption in the infrared, visible, and ultraviolet. The acids upon which attention is centered are proton-donor compounds that are measurably ionized in water, such as aliphatic and aromatic carboxylic acids, substituted phenols, and mineral acids. The bases of principal interest are likewise compounds capable of forming ions in water, for example, aliphatic and aromatic amines and derivatives of guanidine or pyridine. The solvents emphasized are hydrocarbons and halohydrocarbons, but data for dipolar aprotic solvents (for example, acetone, acetonitrile, and nitrobenzene) are included. Contrasts in acid-base behavior and in acidity and basicity scales in aprotic and water-like solvents are discussed.
The role of hydrogen bonding in aprotic solvents is discussed at length. Important types of hydrogen-bonded structures include chelate rings; self-associated acids, bases, and salts; hydrogen-bonded ion pairs; and homo- and heteroconjugate cations and anions. Examples are given in which hydrogen bonding of these types affects such properties as the absorption spectrum of a salt, the catalytic effect of an acid, and the accurate location of a titration endpoint.

Dehl, R. E., **Collagen: Mobile water content of frozen fibers,** *Science* **170,** *738–739 (November 13, 1970).*

Key words: Adsorbed water; calorimetry; collagen; frozen collagen; mobile water; NMR.

The NMR spectra of frozen wet collagen fibers indicate the presence of a considerable amount of unfrozen, mobile water. The quantity of mobile water may be estimated from the approximate convergence of the low temperature NMR splitting constants. An independent estimate of the mobile water content by calorimetry agrees well with the NMR estimate.

Dick, C. E., Lucas, A. C., **K-shell fluorescence yields for light elements,** *Phys. Rev. A,* **2,** *No. 3, 580–586 (September 1970).*

Key words: Beryllium; boron; carbon; fluorescence yield; fluorine; K-shell; magnesium; ω_K

The K-shell fluorescence yield, ω_K, has been measured for the low atomic number elements beryllium, boron, carbon, fluorine and magnesium. The primary vacancies in the K-shell were produced by an intense beam of K x-rays generated by electron bombardment of aluminum and carbon targets. The measured values of ω_K agree quite well with values calculated from a theoretical prediction of Wenzel. They exhibit only fair agreement with semi-empirical formulas which include screening and relativistic effects and with a recent calculation by McGuire based on the K-shell Auger transition rate.

Dobbyn, R. C., Williams, M. L., Cuthill, J. R., McAlister, A. J., **Occupied band structure of Cu: Soft-x-ray spectrum and comparison with other deep-band-probe studies,** *Phys. Rev. B.* **2,** *No. 6, 1563–1575 (September 15, 1970).*

Key words: Band structure; Cu; deep probes; emission; occupied bands; soft x-ray.

We report a new measurement of the soft x-ray $M_{2,3}$ emission spectrum of Cu, using improved experimental techniques. Previously unreported fine structure was observed in the spectrum. Although exact correction for satellite and subband overlap and self-absorption effects is not yet possible, careful consideration has been given them, with the result that the M_3 band profile can be resolved from the accompanying structure in a plausible way. Its features can be taken with reasonable confidence to be characteristic of the true M_3 profile. Comparison is made with the complementary L_3 soft x-ray profile, with band theoretical estimates of both experimental x-ray profiles, and with the results of ultraviolet photoemission, x-ray photoemission and ion neutralization measurements. These comparisons favor a single particle description of the occupied bands of Cu.

Douglas, T. B., **New approach for evaluating lattice-configurational thermodynamic properties,** *J. Chem. Phys.* **51,** *No. 7, 2831–2839 (October 1, 1969).*

Key words: Configurational thermodynamic properties; excluded volume; extrapolations; lattice models; non-combinatorial method; statistical equilibrium.

As a generalization of earlier work of the author [J. Chem. Phys. **40,** 2248 (1964); **45,** 1080 (1966)] a completely noncombinatorial method is derived which gives for any state the exact thermodynamic properties of a system of particles on a lattice infinite in one dimension. The method appears to be essentially equivalent to, but somewhat simpler in development and application than, the matrix method used for the same problems recently. Interaction of unit configurations is explicitly considered only at lattice boundaries, leading directly to a set of independent algebraic equations giving the complete solution for a special state. Two simple examples are given to which alternative combinatorial procedures can be readily applied without approximations, yielding identical explicit results. The general method first given is modified for the imposition of artificial density constraints, and as an illustration it is shown how this variation improves markedly, over the range of disordered densities, the convergence to an infitine plane of the hard-core square-lattice fluid with nearest-neighbor exclusion.

Durst, R. A., **Pick an ion, any ion,** *Ind. Res. pp 36–39 (November 1970).* *Evenson, K. M., Wells, J. S., Radford, H. E.,* **Infrared resonance of OH with the H_2O laser: A galactic maser pump?** *Phys. Rev. Letters* **25,** *No. 4, 199–202 (July 27, 1970).*

Key words: Electrode monitoring; industrial monitoring; ion-selective electrodes; pollutant monitoring.

A brief discussion is given of the types of ion-selective electrodes and the basic principles of their operation. The advantages of these sensors for industrial and environmental pollution monitoring are given, such as, the continuous direct-reading nature of the measurement, fast response time, and portability. Examples of typical industrial and environmental monitoring applications are included, for example, sulfide ion in pulp processing, nitrogen oxides and fluoride in air pollution, and nitrate in soil slurries. Care is necessary in applying these sensors to complex systems where interferences could be a problem and ingenuity is required in modifying the analysis parameters to obtain reliable results. The specificity and sensitivity of these sensors to several serious pollutants will probably result in their future use in pollution-monitoring systems.

Egelstaff, P. A., **Cooperative rotation of spherical molecules,** *J. Chem. Phys.* **53,** *No. 7, 2590–2598 (October 1970).*

Key words: Diffusion; light scattering; neutron scattering; plastic crystal; rotational; spherical molecules.

The rotational diffusion of molecules in the liquid and solid states can be studied by radiation scattering experiments. Both neutron and light scattering data are interpreted, conventionally, on the basis of rotation of single molecules, although in dense systems co-operative rotation is a possibility. It is pointed out that a comparision of incoherent neutron data and depolarised light data allows the co-operative nature of molecular rotational diffusion to be verified. The method is applied to the plastic crystal phase of cyclohexane, and it is shown that individual molecules rotate about 10 times as rapidly as the relaxation rate of the mean orientation of a group of molecules.

Florin, R. E., Wall, L. A., **Small and large radicals in thin-film polymer depolymerization,** *Macromolecules* **3,** *No. 5, 560–566 (September–October 1970).*

Key words: Diffusion effects free radicals; polymer decomposition; polymer depolymerization; polymer irradiation; polymer pyrolysis.

Rates of polymer decomposition are enhanced or retarded as a result of the escape of small free radical or other species through the surface of thin films. Solutions for the rate equations are given as a function of thickness for a mechanism involving the competitive diffusion of small and large radicals. The enhancement of the rates of depolymerization of polytetrafluoroethylene observed with thin films is explained by the model. Comparison of the experimental results with theory indicates that the irradiation of polytetrafluoroethylene produces comparable amounts of both large and small radicals. The mechanisms discussed are undoubtedly operative in many other situations involving the radiolysis or pyrolysis of polymers, for example the radiation induced crosslinking of polymers.

Franklin, A. D., Marzullo, S., **Orientation kinetics of $Gd^{3+}-F^-$ interstitial pairs in CaF_2,** *J. Phys. C. Solid State Phys. Letters to Editor* **3,** *L171–L174 (September 1970).*

Key words: Calcium fluoride; defect dipoles; dielectric relaxation; ESR line broadening; gadolinium; orientational relaxation.

The ESR spectrum from substitutional Gd^{3+} ions with adjacent trapped F^- interstitials broadens significantly above about 100 °C. The temperature-dependent part of the relaxation time associated with this broadening is compatible with the relaxation time derived by dielectric relaxation measurements on identically-treated crystals. These results are interpreted in terms of the orientational diffusion of the trapped F^- interstitial ion around the immobile Gd^{3+} ion on a cation site. The relaxation time is given by $\tau = \tau_0 \exp(Q/kT)$, with $\tau_0 = 8.2 \times 10^{-14}$ s and $Q = 0.38$ eV.

Freeman, D. H., Goldstein, S., Schmuckler, G., **Homogeneous sulfonation of styrene-divinylbenzene copolymers with oleum in organic solvents,** *Istael J. Chem.* **7,** *No. 6, 741–749 (1969).*

Key words: Cation exchangers; ion exchangers; oleum; sulfonation.

In order to obtain homogeneously sulfonated cation exchangers, the copolymers were sulfonated by oleum in a mixture of methylene-chloride and nitro-methane. The influences of the chemical interaction and of the diffusion process on the kinetic behavior of these systems were investigated, and it was shown that raising the temperature of the sulfonation mixture markedly increases the chemical reaction rate, while the effect on the diffusion is small. A curve-fitting technique was used for the interpretation of the degree-of-sulfonation-vs.-time curves. These investigations served as guidelines for the subsequent preparation of homogeneous highly sulfonated copolymers.

French, B. M., Walter, L. S., Heinrich, K. F. J., **Quantitative mineralogy of an Apollo 11 lunar sample** *(Proc. Apollo 11 Lunar Science Conf., Houston, Texas, January 1970), Geochim. Cosmochim.* **34,** *Suppl. 1, 433–444 (February 1970).*

Key words: Apollo 11; electron probe analysis; mineralogy; moon; petrography; rocks.

Petrography and mineral analyses of Sample 10017, collected by the Apollo 11 mission, are reported. They indicate formation by relatively rapid crystallization of a silicate melt. Major components are clinopyroxene, plagioclase and ilmenite. Minor components include troilite, native iron, and apatite. The mineral compositions indicate differentiation during magmatic crystallization, leading to Fe enrichment in the pyroxenes and to alkali enrichment in the feldspars. The mesostasis, the residual liquid produced during crystallization, is strongly enriched in K and Si, but strikingly low in Na; this may be due to volatilization during the later stages of crystallization. The compositional trends, similar to those in other lunar samples, indicate formation by relatively rapid magmatic crystallization, which developed significant chemical fractionation, at low oxygen fugacity and under virtually anhydrous conditions.

Gebbie, H. A., Kuhn, P., Bohlander, R. A., **Scattering by high cirrus: Its effect on submillimeter wave determinations of atmospheric waver vapor, Nature,** *Letter to Editor* **226,** *No. 5242, 71–72 (April 4, 1970).*

Key words: Fourier spectroscopy; high cirrus; submillimeter waves; water vapor.

Submillimeter waves and, by implication in this context, the use of the pure rotation band, offer important advantages for determining the distribution of water vapor with height in the atmosphere. The

reasons are these. 1) We can readily resolve single rotation lines in this region by Fourier Spectroscopy using interferometers. The calibration for intensity of single lines is easily made and a range of lines with different absorption strengths can then be chosen to match the requirements of the inversion procedure used to construct the model radiating atmosphere. 2) The use of long wavelengths allows us to dispense with hot radiation sources and use, for example, the radiation exchange between a room temperature detector and cold sky.

Gills, T. E., Marlow, W. F., Thompson, B. A., **Determination of trace elements in glass by activation analysis using hydrated antimony pentoxide for sodium removal,** *Anal. Chem.* **42,** *1831–1833 (December 1970).*

Key words: Activation analysis; glass; hydrated antimony pentoxide (HAP); radiochemical separations; sodium; trace elements.

A method has been developed for the determination of a number of trace elements at the ppm and ppb levels in high-sodium glass by neutron activation analysis. For glass containing about 10% sodium, neutron irradiation at levels sufficient to allow determination of trace constituents results in production of 10 mCi or more of ^{24}Na. If the ^{24}Na is allowed to decay before analysis, information about elements producing short-lived radioisotopes is lost. In the procedure described the radiosodium is removed by passing the dissolved glass through a column of hydrated antimony pentoxide (HAP). The effluent can be counted directly with a Ge(Li) or NaI(Tl) detector. The method has been applied to the analysis of NBS Standard Reference Material (SRM) glass which was found to contain 1 ppm of Cu and sub-ppm levels of Mn, Au, Ga, Sb, La, Co, and Ir.

Glass, A. J., Guenther, A. H., Editors, **Damage in laser materials,** *Proceedings of a Symposium Sponsored by the American Society for Testing and Materials and by the National Bureau of Standards June 24–25, 1970, NBS, Boulder, Colorado, Nat. Bur. Stand. (U.S.), Spec. Publ. 341, 133 pages (Dec. 1970) $1.25, SD Catalog No. C13.10:341).*

Key words: Ferroelectric materials; glass; laser damage; lasers.

The second ASTM Symposium on Damage in Laser Materials was held at the National Bureau of Standards at Boulder, Colorado on June 24th and 25th, 1970. About 150 attendees heard papers by fourteen speakers, representing the major manufacturers of laser glass, government, industrial and university laboratories. Although the primary emphasis was on Nd:glass as a laser material, damage mechanisms and morphology in ruby, sapphire, and nonlinear optic materials were also considered. It was clear that substantial advances have been made in the last year in the production of damage-resistant laser glass for use in conventional *Q*-switched lasers. New diagnostic techniques have been developed, and in some cases, adopted as quality control procedures by the glass manufacturers. Theoretical understanding of the fundamental damage mechanisms is beginning to emerge, and material properties relevant to these damage mechanisms are beginning to be measured. It was equally clear that a great deal of effort remains to be expended to develop techniques suitable for nondestructive testing of laser materials, and that many properties of laser materials at high energy density are presently poorly understood.

Glaze, D. J., **Improvements in atomic cesium beam frequency standards at the National Bureau of Standards,** *IEEE Trans. Instr. Meas.* **IM-19,** *No. 3, 156–160 (August 1970).*

Key words: Atomic frequency standard; cesium beam; figure of merit; frequency accuracy; frequency multiplier; frequency precision; NBS–III; NBS–5; phase noise; quartz crystal oscillator; ramsey cavity; slave oscillator.

The National Bureau of Standards Frequency Standard, NBS–III, a cesium beam with a 3.66 meter interaction region, has been in operation since 1963. The last published (1966) accuracy capability for NBS–III was 1.1×10^{-12} (1σ). With this performance NBS–III was used in the measurment of the frequency of the hyperfine separation of hydrogen. This was, and is, the most accurate published measurement of any physical quantity. A number of improvements are being made in NBS–III to improve its accuracy capability. In early 1966 the vacuum system was modified to use three commercial 200 liter per second ion pumps. The resulting ultimate pressure was improved by a factor of ten to about 10^{-8} torr (1.3×10^{-6} N/M^2). Several new solid-state, broadband frequency multiplier chains have been constructed with particular attention given to reduction of both power-line related sideband levels and random phase noise sideband levels. Reduction of the random phase noise by more than 20 dB compared to the previous state of the art has been obtained consistently. One of these frequency multiplier chains is presently in use in the 5 to 60 MHz section of the 9.192 . . . GHz excitation system. In addition a solid-state servo system has been employed to control the frequency of the 5 MHz slave oscillator. This servo system and the new frequency multiplier chain have improved both the reliability and long-term stability of NBS–III.
Comparisons were made between NBS–III and one of the commercial cesium standards in the NBS Clock Ensemble. The relative fractional frequency stability of $\sigma(N=2,\ \tau=1$ day, $T=7$ days) $= 1 \times 10^{-13}$ was observed for nine weekly comparisons. Presently at NBS there are no hydrogen masers or thallium beams capable of being used in meaningful measurements against NBS–III. The very long-term frequency stability for this recently improved NBS–III system has not been evaluated fully. Due to the improvements in both electronics systems and evaluative techniques, however, an accuracy of 5×10^{-13} (1σ) for a single evaluative experiment is reported. Substantial NBS effort is being expended toward improvement of the accuracy and figure of merit (presently 10) for NBS–III. New designs and associated components for improved beam optics have been completed. Improved, completely solid-state 5 MHz to 9.2 GHz frequency multipliers have been constructed, and testing is being conducted now. The modified NBS–III beam tube together with new electronic systems will be designated NBS–5. It is expected to be in operation in early 1970 and to exhibit a figure of merit in excess of 500.

Groth, H. G., Wellmann, P., Editors, **Spectrum formation in stars with steady-state extended atmospheres,** *Proceedings of the International Astronomical Union Colloquium No. 2, Commission 36, Munich, Germany, April 16–19, 1969, Nat. Bur. Stand. (U.S.), Spec. Publ. 332, 342 pages (August 1970) $1.75, SD Catalog No. C13.10:332.*

Key words: Extended atmospheres; interpretation of stellar spectra; line formation.

In section 1 practical details concerning the equivalence of observational and theoretical descriptions of stellar spectra are reviewed, particularly the difficulty of identifying the observed reference level (continuum) with the theoretical continuum in the case when many lines are present. In this connection thought must be given to how integrals over frequency should be normalised and evaluated because the effective continuous absorption coefficient does not remain constant over the range from 0 to ∞. The choice of spectroscopic details by which to determine T_{eff}, log g and abundances requires careful consideration.
In section 2 the factors by which an extended atmosphere are recognized are summarized and the question is posed do all stars have extended atmospheres. Another question requiring an answer is whether the concepts microturbulence and macroturbulence are physically real concepts or whether they are merely fitting parameters to make a simple LTE theory account for the observed spectra of supergiants in which rather wide lines occur and many multiplets show rather steep gradients. In section 3 the types of line sensitive to non-LTE conditions are described. These are resonance lines, lines arising from metastable levels, subordinate lines for which the upper level is sufficiently separated from the continuum and other levels that this upper level is chiefly populated by radiative processes from the ground or other low lying levels and lines which go into emission in low density atmospheres as a result of optical-pumping (fluorescent) processes. Such lines should not be used for abundance determinations by means of LTE theory though this is frequently done.
Theoretical considerations are discussed in section 4 where first the problem of the two-level atom is sketched and then the problem is generalised to a many-level atom. The parameter λ which gives the probability that a photon is lost from the line by de-excitation processes other than spontaneous emission is defined and it is pointed out that non-LTE physics has the effect of adding a scattering

term to the expression for the source function. One example is given of the effect of changing the line source function from the Planck function to a form suitable for isotropic coherent scattering. The line becomes deeper and wider for the same number of atoms. Interpretational problems in stellar spectra are discussed in section 5. It is noted that many lines in main-sequence early type spectra show the effects of departures from LTE. These effects are shown to a conspicuous degree by the spectra of shell stars. The example of He I 5876 in 10 Lacertae, O9V, is discussed and the implication for interpreting the He I lines in all B type main-sequence stars are touched upon. Helium-weak and helium-strong spectra probably indicate variations in density of the outer atmosphere rather than true abundance differences. The spectra of supergiants are also considered and it is pointed out that the Ia supergiants of type B may be hydrogen-poor.
Finally in section 6 the problem of choosing simplified physical representations of line forming when non-LTE physics must be used is discussed. Some relevant points concerning the observed spectral lines used for spectral classification are illustrated by means of partial energy-level diagrams.

Guttman, C. M., DiMarzio, E. A., **Separation by flow. II. Application to gel permeation chromatography,** *Marcromolecules* **3,** *No. 5, 681–691 (September–October 1970).*

Key words: Chromatography; gel filtration; gel permeation chromatography; macromolecules; separation by flow.

Models of a Gel Permeation Chromatography column are proposed in which there is flow through each of the beads as well as around them. Diffusion is allowed within and outside of the beads. By making general arguments on particle current flow, the volume elution is computed as a function of solute particle size for a simplified view of the column. The equation for the location of volume elution peaks thus derived show functional dependences on the particle radius and the column geometry very much like equations derived by previous workers for models in which there was no flow in the beads. The method of Herman's is extended to allow for flow within the beads. Two times characterize the system; the time for a particle to diffuse into and out of the bead and the time to flush the particle out of the bead. The width of the volume elution peak (in contradistinction to the work of Herman's) no longer becomes infinite as the diffusion coefficient goes to zero since the residence time within the bead is never larger than the flush time. Explicit formulae are given for the first three moments of the volume elution; it is shown that the elution volume for a monodispersed species is gaussian. In all cases systems with open pores which allow flow show better separation capabilities than those which do not allow flow.

Haar, L., Shenker, S. H., **A phenomenological equation of state,** *Proc. 5th Symp. Thermophysical Properties, Boston, Mass., September 30–October 2, 1970, C. F. Bonilla, Ed., pp. 223–226 (American Society of Mechanical Engineers, New York, N.Y., 1970).*

Key words: Compressibility factors; equation of state; high density; high temperature; pairwise potentials; Redlich Kwong; second virial coefficient; thermodynamics.

A simple phenomenological equation of state for high temperature gases is proposed. It is developed from considerations of the two body pair interactions, and it has no arbitrary parameters. The equation has been applied to two simple gases, nitrogen and argon. The results compare quite well with experimental data up to 10,000 bar and in the range of two to four times the critical temperature. Also included for comparison is the widely used Redlich Kwong equation. The present work compares favorably with the Redlich Kwong at the lowest-temperature; however, as temperature is increased the present work becomes increasingly more accurate, whereas the corresponding states equation tends to degrade with temperature.

Hastie, J. W., Hauge, R. H., Margrave, J. L., **High temperature chemistry: Stabilities and structures of high temperature species,** *Ann. Rev. Phys. Chem.* **21,** *475–498 (1970).*

Key words: High temperature species; stability structure.

Recent experimental and theoretical work on the stabilities and structures of high temperature species has been reviewed. Emphasis was given to data which may be used for the thermodynamic characterization of a high temperature species, such as molecular geometry vibrational and electronic energy levels. The techniques from which stability and structural data have been obtained for high temperature species are also discussed. These include, Knudsen effusion and photoionization mass spectrometry, matrix isolation infrared spectroscopy, electron diffraction, electric dipole deflection, electronic spectroscopy, microwave spectroscopy and semi-empirical and abinitio molecular orbital calculations.

Hayward, E., **Photonuclear reactions,** *Nat. Bur. Stand. (U.S.), Monogr. 118, 46 pages (August 1970) 50 cents, SD Catalog No. C13.44:118.*

Key words: Nuclear hydrodynamics; particle-hole calculations; photon scattering; photonuclear; sum rules.

This paper reviews photonuclear reactions in the approximate energy range 10 to 30 MeV. Various sum rules are discussed and applied to experimental data. Several different theories are described and their predictions compared with experiment, and as often as possible open questions and discrepancies are pointed out.

Hirshfeld, A. T., Hoppes, D. D., **Transition mixing ratios determined from a study of the electron and gamma-ray distributions from oriented ^{192}Ir,** *Phys. Rev. C* **2,** *No. 6, 2341–2349 (December 1970).*

Key words: Beta rays, angular distribution; gamma rays; hyperfine field in iron; ^{192}Ir, magnetic moment; nuclear orientation; transition missing ratios.

The angular distributions measured for 12 gamma rays in ^{192}Os and ^{192}Pt resulting from the decay of cryogenically oriented ^{192}Ir have been used to determine the following E2/M1 mixing ratios: 201 keV, $\delta^2 > 3.7$; 296 keV, $\delta = -(6^{+3}_{-1})$; 308 keV, $\delta = -(7.1 \pm 0.6)$; 417 keV, $\delta = 4^{+7}_{-3}$; 485 keV, $\delta = 5.8 \pm 0.8$; 604 keV, $\delta = 1.5 \pm 0.1$, following the Rose-Brink sign convention. The angular distribution of the 672 keV beta group and the above gamma measurements limit the relative contribution, I_L, of different operator tensor ranks, L, involved in each beta transition. The results for electron capture transitions terminating at levels in osmium are: 694 keV level, $I_1 > 0.9$; 584 keV level $I_0 > 0.6$, $I_2 < 0.1$. For beta transitions feeding platinum states, we determine: 921 keV level, $I_1 > 0.8$; 785 keV level, $I_1 > 0.92$, $I_2 < 0.03$. The ^{192}Ir ground state magnetic moment is positive.

Jacox, M. E., Milligan, D. E., **Matrix-isolation study of the vacuum-ultraviolet photolysis of methyl chloride and methylene chloride. Infrared and ultraviolet spectra of the free radicals CCl, H_2CCl, and CCl_2,** *J. Chem. Phys.* **53,** *7, 2688–2701 (October 1, 1970).*

Key words: CCl; CCl_2; force constants; free radical; HCCl; $HCCl_2$; H_2CCl; infrared spectrum; matrix isolation; photolysis; ultraviolet spectrum.

Infrared and ultraviolet spectroscopic studies have been conducted on the products of the vacuum-ultraviolet photolysis of normal and isotopically substituted methyl chloride and methylene chloride isolated in argon and nitrogen matrices at 14 K. The cage effect has been formed to inhibit halogen detachment processes in these systems. Infrared absorptions attributed to CCl, HCCl, and H_2CCl and the 2800-A ultraviolet absorption of CCl appear in the methyl chloride photolysis studies. Observation of a "negative anharmonicity" for the lowest frequency infrared absorption of H_2CCl can be explained by postulating that the molecule is planar. The C-Cl stretching force constant of H_2CCl is exceptionally high. The implications of $(p-d)$ π bending, which may account for the large C-Cl stretching force constant, are explored. An absorption near 2300 Å behaves appropriately for assignment to a second electronic transition of CCl, providing support for the previous tentative assignment of a group of emission bands to such a transition. Photolysis of methylene chloride in a matrix environment leads principally to the stabilization of CCl_2. A revised estimate of the force constants of CCl_2 is given.

Johnson, D. R., Powell, F. X., **Microwave detection of thioformaldehyde,** *Science* **169,** *679–680 (August 14, 1970).*

Key words: Astronomically important; electrical discharge; interstellar medium; microwave spectroscopy; rotational spectrum; thioformaldehyde.

Thioformaldehyde (H_2CS) has been detected and characterized from its microwave spectrum. Preliminary analysis of rotational transitions for $H_2C^{32}S$ shows this new species to have C_{2v} symmetry with rotational constants of $A = 292729$ MHz, $B = 17698$ MHz, and $C = 16652$ MHz. The possibility of detection of thioformaldehyde in the interstellar medium is discussed and a table of transitions expected to be of importance there is presented.

Krauss, M., **Potential energy surfaces,** *Ann. Rev. Phys. Chem.* **21,** *39–46 (1970).*

Key words: Activation energy; configuration interaction; correlation energy surface; Hartree-Fock; H_3^+; H_3; H_3^-; H_4; LiH_2; LiHF; HNO; HeH_2^+; proton transfer.

Ab initio energy surfaces applicable to chemical kinetics and collisional phenomena are reviewed. The calculations are divided into two categories, Hartree-Fock and beyond. It is noted that Hartree-Fock calculations are routine but that correlation techniques are necessary for reaction collisions. Definitive work exists for H_3^+ and H_4 but the activation energy of H_3 is still inaccurate relative to the scattering calculational requirements. Other qualitative work is described for H or Li interaction with diatomics.

Lafferty, W. J., **Microwave spectrum, dipole moment, and conformation of cyclopentene oxide,** *J. Mol. Spectry.* **36,** *No. 1, 84–93 (October 1, 1970).*

Key words: Cyclopentene oxide; dipole moment; epoxy cyclopentene; microwave spectrum; ring conformation; rotational constants.

The microwave spectrum of cyclopentene oxide has been studied. Rotational constants for the ground state and two excited vibrational states of one ring conformation have been obtained. Ground state constants are $A_0 = 5709.38 \pm 0.02$, $B_0 = 4541.12 \pm 0.02$ and $C_0 = 3248.97 \pm 0.02$ (errors are 2 standard deviations). The dipole moment components of the molecule are $\mu_a = 1.16_3 \pm 0.033$, $\mu_c = 1.63_0 \pm 0.031$, and $\mu = 2.00_2 \pm 0.015$. The rotational constants and dipole moment components obtained experimentally can be satisfactorily explained only if the boat form is the most stable conformation of the ring.

Lamb, V. A., **Evidence for a complex chloromolybdate ion in a molten salt medium from transference experiments,** *J. Electrochem. Soc.* **117,** *No. 10, 1269–1270 (October 1970).*

Key words: Hexachloromolybdate complex ion; molten salt; transference numbers.

Transference experiments have been performed with solutions of potassium hexachloromolybdate in molten eutectic mixtures of potassium chloride and lithium chloride. The results indicate that a complex molybdenum-containing anion exists at 800 °C.

Latanision, R. M., Westwood, A. R. C., **Surface- and environment-sensitive mechanical behavior,** *Chapter in Advances in Corrosion Sciences and Technology,* **1,** *51–145 (Plenum Press, New York, N.Y., 1970).*

Key words: Complex-ion embrittlement; dislocations; liquid metal embrittlement; surface; surface active agent.

The influences of surface structure and environment on the mechanical behavior of crystalline inorganic solids are reviewed and possible mechanisms discussed. In particular, the various roles of such factors as the atomic, electronic, and defect structure of the near-surface regions, the presence of adsorbed surface-active species, alloyed layers, oxide films, gaseous or liquid environments, etc. are considered in connection with the Roscoe, Rebinder, and Joffe effects, liquid-metal embrittlement, complex-ion embrittlement, hydrogen embrittlement, and other phenomena.

Ledbetter, H. M., **On the martensite crystallography of the cubic to orthorhombic transformation in Au-47.5 Cd,** *Scripta Met.* **4,** *No. 11, 931–937 (November 1970).*

Key words: Crystallography; gold-cadmium alloy; martensite; phase transformations; twinning.

Complete calculations of the geometrical features of the cubic to orthorhombic martensitic transformation in the Au-47.5 Cd alloy system have been made for both Type I and Type II transformation twinning. None of the usual crystallographic features are sufficiently sensitive to distinguish between these two possible modes of lattice invariant deformation. Alternatives are offered which are believed to be experimentally simpler than those previously proposed.

Lesclaux, R., Searles, S., Sieck, L. W., Ausloos, P., **Irradiation of cyclohexene with 8.4, 10.0 and 11.6–11.8 eV photons. Dissociation of neutral excited cyclohexene and reactions of $C_6H_{10}^+$,** **J. Chem. Phys. 53,** *No. 8, 3336–43 (October 15, 1970).*

Key words: Cyclohexene; ion-molecule reactions; photoionization; photolysis; unimolecular-/dissociation.

The photolysis of cyclohexene has been investigated at photon energies above (10.0 eV, 11.6–11.8 eV) and below (8.4 eV) its ionization potential (8.9 eV). The ionic processes were studied in a mass spectrometer equipped with a photon source. The parent $C_6H_{10}^+$ ion was seen to undergo the following reactions with cyclohexene:

$$C_6H_{10}^+ + \text{cyclo}-C_6H_{10} \rightarrow \text{cyclo}-C_6H_{12} + C_6H_8^+ \quad k = 0.7$$

$$\times 10^{-10} \text{ cm}^3/\text{molecule-sec} \rightarrow C_{12}H_{20}^+ \quad k = 4.1 \times 10^{-10} \text{ cm}^3/\text{molecule-sec}$$

Analysis of the yields of cyclohexane formed in the first of these reactions in the photolysis at 10.0 eV over the pressure range from 1 to 10 torr indicates that the relative importance of the two reactions is the same in this pressure range as in the ion source of the mass spectrometer at a pressure of 10^{-2} torr. At 11.6–11.8 eV, the parent ion also dissociates, mainly to form $C_5H_7^+$ and CH_3. Evidence is presented which indicates that at these energies, the majority of the $C_6H_{10}^+$ ions retain a cyclic structure. The neutral, electronically excited cyclohexene molecule dissociates mainly as follows:

$$C_6H_{10}^* \rightarrow 1,3-C_4H_6 + C_2H_4, \text{ at 8.4 eV}, \Phi = 0.82$$

$$\rightarrow C_5H_7 + CH_3, \text{ at 8.4 eV}, \Phi = 0.08.$$

The photolysis of 3,3,6,6-d_4-cyclohexene demonstrated that the first of these processes occurs predominantly by the "symmetrical" cleavage of the 3–4 and 5–6 C–C bonds, at all energies.

Levin, E. M., **Liquid immiscibility in oxide systems,** *Chapter in Phase Diagrams Materials Science and Technology,* **3,** *The Use of Phase Diagrams in Ceramics, Glass and Metal Technology, pp. 143–236 (Academic Press, Inc., New York, N.Y., 1970).*

Key words: Glass chromatography; immiscibility and courses of crystallization; immiscibility and practical applications; immiscibility and thermodynamics; immiscibility in oxides; liquid immiscibility; $Ln_2O_3-B_2O_3$ phase diagrams; mechanism of phase separation; metastable liquid immiscibility; microphase separation; phase diagrams of metastable immiscibility; spinodal; structural interpretation of immiscibility; super-duty silica brick.

Stable and metastable liquid immiscibility in oxide systems is discussed from the standpoint of thermodynamics, interpretation, and application. The classic Gibbs free energy of formation-composition diagrams are used to illustrate the difference between a stable and a metastable immiscibility gap and to define the spinodal. Phase equilibrium principles are applied to liquid immiscibility and typical courses of crystallization are described. Structural interpretation is applied to the occurrence and extent of immiscibility including the temperature of the monotectic and the effect of homogenizers. The general incompatibility of compound formation and liquid immiscibility is demonstrated for the rare earth oxide-boric oxide systems. Occurrence and methods of study of micro-phase separation are elucidated. Three mechanisms of microphase separation are

418-535 OL - 71 - 7

discussed briefly: nucleation and growth, spinodal decomposition, and intersecting growth theory. Binary and ternary phase diagrams showing liquid immiscibility are presented. Application to the following commercial products are discussed: super-duty silica brick, Vycor glass, Pyrex glass, glass ceramics, and glass chromatography.

Levin, E. M., Roth, R. S., **The system niobium pentoxide-phosphorus pentoxide,** *J. Solid State Chem.* **2,** *No. 2, 250–261 (1970).*

Key words: Nb_2O_5-P_2O_5; $NbPO_5$; $Nb_2P_4O_{15}$; Nb_9PO_{25}; $Nb_{44}P_2O_{115}$; P_2O_5-Nb_2O_5; phase diagram; ReO_3-type compounds.

A partial phase diagram of the system has been determined experimentally, using the quenching technique and identifying the phases by x-ray powder diffractometry. The major phase, $NbPO_5$, melts above 1650 °C. It transforms at about 1253° C from a low-temperature, tetragonal phase to a high-temperature, monoclinic phase, isostructural with $TaPO_5$. The $9Nb_2O_5 \cdot P_2O_5$ phase shows a limited solid solution range and melts incongruently at 1435 °C. The eutectic between 9:1 and $NbPO_5$ is at 1365 °C and 67 mol % Nb_2O_5. At 96.4 mol % Nb_2O_5 another phase was found, stable over only 80 °C and isostructural with the 9:1 phase. A new monoclinic phase, '22:1' ss was found, with a limited stability field in both temperature and composition. In the subsystem $NbPO_5$ one compound was identified of probable composition $NB_2O_5 \cdot 2P_2O_5$, with pseudocubic symmetry and melting incongruently at about 1025 °C. X-ray powder diffraction data and unit cell dimensions are listed for the phases.

Lias, S. G., Collin, G. J., Rebbert, R. E., Ausloos, P., **Photolysis of ethane at 11.6–11.8 eV,** *J. Chem. Phys.* **52,** *No. 4, 1841–1851 (February 15, 1970).*

Key words: Ethane; free radicals; ions; photolysis; primary processes; vacuum ultraviolet.

The photolysis of ethane, carried out with an argon resonance lamp, has been reinvestigated with the related purposes of (1) measuring quantum yields of all fragments formed in the dissociation of excited ethane, and (2) associating these fragments with the primary processes occurring in the photolysis of ethane. These, and their relative abundances are

$$C_2H_6^* - C_2H_6^*, 5\%$$
$$- CH_4 + CH_2, 16\%$$
$$- C_2H_5 + H, 41\%$$
$$- C_2H_4 + H_2, 23\%$$
$$- CH_3 + CH_3, 15\%.$$

These results are compared with conclusions reached in earlier studies on the photolysis of ethane with xenon and krypton lamps in order to determine the effect of energy on the relative probabilities of the primary processes. It is found that direct bond scission increases in importance with increasing energy, while processes involving rearrangement decrease in importance.
The radical and molecular fragments formed in the dissociation of excited ethane were determined by (a) analyzing the products formed in C_2H_6-C_2D_6-NO (1:1:0.1) mixtures and (b) C_2D_6 in the presence of H_2S, which scavenges free radicals to form isotopically-unique hydrocarbon products, and (c) C_2H_6 in the presence of C_3D_6, which scavenges H-atoms to form propyl radicals which in turn, react with radicals in the system to form characteristic products. Such experiments, as well as quantum yield determinations, were also carried out at the krypton and xenon lines.

Lias, S. G., Rebbert, R. E., Ausloos, P., **Irradiation of xenon-propane and argon-propane mixtures with gamma rays and 21.2 eV photons,** *J. Chem. Phys.* **52,** *No. 2, 773–783 (January 15, 1970).*

Key words: Deactivation; ion-molecule reactions; photoionization; radiolysis; unimolecular ion fragmentation.

Mixtures of xenon or argon with propane (20:1) are irradiated in the presence of radical scavengers by γ-rays and by 21.2 eV photons from a helium resonance lamp. The ion-pair yields of products originating in ionic fragmentation reactions or ion-molecule reactions are derived from isotopic analyses of product molecules formed with C_3D_8-C_3H_8 mixtures or with $CD_3CH_2CD_3$. At a given pressure, only minor differences are seen between the radiolysis and photolysis in the modes of dissociation of parent propane ions formed by charge transfer with a particular rare gas. Higher energy ionic fragmentation processes are seen to be quenched with increasing pressure; in the case of xenon-propane mixtures, it is demonstrated that the parent ion yield increases as primary fragmentation processes are quenched. In the irradiated argon-propane-scavenger mixtures, isotope effects in the ionic fragmentation mechanism are seen which indicate that collisional deactivation of the excited deuterated fragment ions is more efficient that that of the corresponding protonated ions. In the photolytic experiments, it was deduced that the decomposition of neutral excited propane molecules constitutes about 10% of the product forming processes in the xenon mixtures, while in the radiolytic experiments, the maximum contribution of neutral excited molecule decomposition is 5%. Similar deductions for the argon mixtures were not feasible.

Marshak, H., Langsford, A., Tamura, T., Wong, C. Y., **Total neutron cross section of oriented$_{165}$ Ho from 2 to 135 MeV,** *Phys. Rev. C* **2,** *No. 5, 1862–1881 (November 1970).*

Key words: Black-nucleus model; coupled channel calculation; Ho_{165}; nuclear orientation; nuclear Ramsauer effect; nuclear shape; optical-model; total neutron cross section.

The difference in the total neutron cross section due to nuclear orientation, $\Delta\sigma_{def}$, has been measured for ^{165}Ho over the energy range of 2 to 135 MeV. The results show that $\Delta\sigma_{def}$ oscillates as well as changing sign, contrary to our classical concept of the interaction. The data, both σ_t and $\Delta\sigma_{def}$, are successfully fitted by adiabatic-coupled channel calculations using the optical-model. The parameters for the optical-model were determined by fitting σ_t and σ_R data (over approximately the same energy range as in the present work) for the two spherical nuclei Cd and Pb. The only additional quantity being introduced was the quadrupole deformation parameter for ^{165}Ho which is known to be 0.33. The data for $\Delta\sigma_{def}$ can also be explained quite well by a simple semiempirical model which makes use of the black-nucleus model, the nuclear Ramsauer effect and the experimental σ_t data. The temperature dependence of $\Delta\sigma_{def}$ agrees very well with our calculated values for the degree of nuclear orientation, which is consistent with ^{165}Ho being almost a pure quadrupole shaped nucleus.

Meshkov, S., **Commentary on meson spectroscopy,** *Chapter in Experimental Meson Spectroscopy, C. Baltay and A. H. Rosenfeld, Ed., pp. 535–546 (Columbia Univ. Press, New York, N.Y., 1970).*

Key words: A_2; mesons; resonances; spectroscopy; SU(3); $SU(6)_w$.

A description of a method for describing the split A_2 is presented, as well as some comments on the general problem of describing mesons and analyzing their structure.

Milligan, D. E., Jacox, M. E., **Infrared spectrum of the ClHCl- ion isolated in an argon matrix,** *J. Chem. Phys.* **53,** *No. 5, 2034–2040 (September 1, 1970).*

Key words: Bichloride anion; ClHCl free radical; electron attachment; HCl dimer; hydrogen bonding; infrared spectrum; matrix isolation; ultraviolet spectrum; vacuum-ultraviolet photolysis.

Upon vacuum-ultraviolet photolysis at 14 K of samples of HCl isolated in an argon matrix at mole ratios favorable for the presence of an appreciable concentration of dimeric HCl, prominent absorptions appear at 696 and 956 cm^{-1}. The positions, and contours, and relative intensities of these absorptions correspond within experimental error with those previously attributed to the ClHCl free radical isolated in an argon matrix. Studies of a chlorine-37 enriched sample have confirmed the presence of two chlorine atoms in the molecule. A broad, unstructured absorption at 2870 Å may also be contributed by this ClHCl species. When a small concentration of atomic potassium or cesium is co-deposited with the Ar:HCl sample, evidence is obtained for the formation of an alkali metal-containing complex. Photoionization of the alkali metal atoms upon exposure of the resulting sample to the radiation of a medium-

pressure mercury are leads to the appearance of very prominent absorptions at 969 and 956 cm^{-1}. It is proposed that these absorptions may more suitably be assigned to the $ClHCl^-$ ion, trapped in an inert, essentially non-ionic environment. Implications of this reassignment with regard to the nature of the hydrogen bonding of $ClHCl^-$ are discussed, and possible mechanisms for the production of $ClHCl^-$ under the conditions of these experiments are considered.

Moore, C. E., **Ionization potentials and ionization limits derived from the analyses of optical spectra,** *Nat. Stand. Ref. Data Ser., Nat. Bur. Stand. (U.S.),* **34,** *22 pages (Sept. 1970) 75 cents, SD Catalog No. C13.48:34.*

Key words: Atomic spectra, ground terms; ground terms, atomic spectra; ionization limits; ionization potentials.

A current table of ionization potentials expressed in electron volts and a detailed table giving the limits from which they have been derived are presented. For each spectrum the ground term is given, with the limit as the ground state. The energy levels of terms of the lowest configuration determined from ground state zero, are also included for selected spectra. The literature references used for each spectrum are indicated by number and listed in a bibliography with some 200 entries.
The latest recommended conversion factor (cm^{-1} to eV) 0.000123981 corresponding to 1 eV = 8065.73 cm^{-1} has been used throughout.

Moore-Sitterly, C. E., **Fundamental spectroscopic data,** *IAU Commission 14, August 1967 Meeting, Trans. Intern. Astron. Union* **13A,** *229–266 (1967). Moore-Sitterly, C. E., Rare-earth spectra—the 1966 picture, Proc. First International Conf. Spectroscopy, Bombay, India, January 9–18, 1967,* **1,** *1–13 (1967).*

Key words: Cross section; transition probabilities; wavelength standards.

The present report summarizes important activities in the field since the Twelfth General Assembly of the Union held in Hamburg in 1964. The main topics deal with standards of wavelength, transition probabilities, line broadening, atomic collision cross sections, molecular spectra of astrophysical interest, general progress in studies of laboratory spectra and current work on the solar spectrum.

Moore-Sitterly, C. E., **Silicon in the sun,** *Chapter in Vistas in Astronomy (Commemoration of H. N. Russell) A. Beer, Ed.,* **12,** *307–312 (Pergamon Press, Inc., New York, N.Y., 1970).*

Key words: Atomic and ionic in the sun; silicon in the spectra of silicon; silicon spectra in the sun's atmosphere sun.

A brief survey is given of Silicon lines in the spectra of the solar photosphere, chromosphere, and corona. These lines are not only from the spectrum of the neutral atom, but arise, also, from the ionic spectra of every stage of ionization, i.e., Si I through Si XIV. The ionization potentials range from 8 to 2673 eV, and the wavelengths of the solar identifications span the interval from 6 Å to 25129 Å. The wide range of excitation and ionization thus represented makes silicon a suitable element for detailed study of solar models, fluxes, abundances and the like.

Okabe, H., **photodissociation of HNCO in the vacuum ultraviolet; Production of NCO $A^2\Sigma$ and NH($A^3\pi$, $c'^1\pi$)** *J. Chem. Phys.* **53,** *No. 9, 3507–3515 (November 1, 1970).*

Key words: Bond dissociation energy; fluorescence; HNCO; NCO $A^2\Sigma$; NH $A^3\pi$, $c^1\pi$; photodissociation; vacuum ultraviolet.

Strong emission bands originating from NCO $A^2\Sigma$ and NH($A^2\pi$, $c^1\pi$) were found in the photodissociation of HNCO in the vacuum ultraviolet. In addition, weak bands coming from NCO $B^2\pi$ were observed. Threshold energies of incident photons to produce these bands were measured, from which the following bond dissociation energies and heats of formation were obtained: D(H-NCO) = 4.90 ± 0.01 eV, D(HN-CO) = 3.38 ± 0.1 eV, D(N-CO) = 2.14 ± 0.15 eV, ΔH_f(HNCO) = −1.0 ± 0.14 eV, ΔH_f(NCO) = 1.6 ± 0.15 eV. The emission spectrum, NCO $A^2\Sigma \rightarrow X^2\pi$, produced from the photolysis at the Xe and Kr lines shows that NCO $A^2\Sigma$ is highly excited in bending vibration, indicating that the upper state of HNCO from which NCO $A^2\Sigma$ predissociates, has a bent NCO configuration. NH $c^1\pi$ formed is highly rotationally excited. Experimental evidence is presented to show that NH $A^3\pi$ is produced primarily by a secondary process, CO $a^3\pi$ + NH $X^3\Sigma \rightarrow$ CO $X^1\Sigma$ + NH $A^3\pi$. Primary processes in the near ultraviolet photolysis of HNCO are discussed on the basis of bond dissociation energies obtained in the present work.

Parker, H. S., Harding, C. A., **Vapor growth of Al_2O_3 bicrystals,** *J. Am. Ceram. Soc.* **53,** *No. 11, 583–585 (November 11, 1970).*

Key words: Aluminum oxide; bicrystals; crystal growth; vapor crystal growth.

Bicrystals containing symmetrical tilt boundaries with either the [10$\bar{1}$0] or the [11$\bar{2}$0] direction as the rotation axis have been grown at a temperature of 1740 °C by a vapor growth technique utilizing the reaction:

$$2AlCl_3(g) + 3CO_2(g) + 3H_2(g) \rightarrow Al_2O_3(s) + 6HCl(g) + 3CO(g).$$

Specimens as large as 3 × 5 × 20 mm have been produced in a 24 hour growth period. Chemical purity of the specimens is very high, with less than 0.1 ppm total cation impurities as determined by activation analysis.

Parker, R. L., **Crystal growth mechanisms: Energetics, kinetics, and transport,** *Solid State Phys.* **25,** *151–299 (Academic Press, Inc., New York, N.Y., 1970).*

Key words: Crystal; crystal growth; crystallization; growth mechanisms; morphological stability; nucleation; phase changes; transport processes.

A review is given of the mechanisms of crystal growth. Subjects discussed include thermodynamics and statistical mechanics of phase changes; the mathematical physics of crystal growth trnasport processes; nucleation; interface structure and interface kinetics; morphological stability; impurity effects; and fluid flow effects in crystallization. Particularly emphasized are the results of quantitative studies, both theoretical and experimental, on well defined systems. Experimental techniques and apparatus are not covered, nor are solid-solid transformations or the crystallization of polymers.

Pella, P. A., DeVoe, J. R., **The determination of tin in copper-base alloys by Mössbauer spectrometry,** *Anal. Chem.* **42,** *No. 14, 1833–1835 (December 1970).*

Key words: Alloys; analysis; internal standard; Mössbauer spectrometry; stannic oxide.

The Mössbauer spectrometric method was applied to the determination of tin in NBS SRM copper-base alloys. After converting the Sn in the alloy to SnO_2 the absorption intensity of SnO_2 was measured versus β-Sn as an internal standard absorber. Stannic oxide was obtained by the dissolution of the alloys in nitric acid. This produces a precipitate contaminated by the coprecipitation of a number of elements. Through the use of an appropriate standard, it was shown that the Mössbauer technique can measure the SnO_2 concentration without interference. The results for alloys 52c, 184, and 37e were 7.82±.05% (7.85), 6.31±.06% (6.38), and 0.99±.01% (1.00), respectively, where the uncertainties are the relative standard deviation of the mean values and the numbers in parentheses are the NBS certified values.

Perloff, A., **The crystal structure of sodium hexamolybdochromate(III) octahydrate, $Na_3(CrMo_6O_{24}H_6)$, $8H_2O$,** *Inorganic Chem.* **9,** *No. 10, 2228–2239 (1970).*

Key words: Heteropolymolybdate; x-ray crystal structure.

The detailed structure of the heteropoly salt $Na_3(CrMo_6O_{24}H_6) \cdot 8H_2O$ has been determined using three-dimensional x-ray diffraction data. The crystals are triclinic, space group $P\bar{1}$, with cell dimensions $a = 10.9080$, $b = 10.9807$, $c = 6.4679$ Å, $\alpha = 107.594°$, $\beta = 84.438°$ and $\gamma = 112.465°$. There is one formula unit per unit cell. The anion has the same structure as the $(TeMo_6O_{24})^{-6}$ anion with excellent agreement of comparable bond distances. Charge

balance and hydrogen bonding arguments suggest that the anion's hydrogen atoms are bonded to the oxygen atoms which are coordinated to the Cr atom. The anions are linked together through sodium octahedra and hydrogen bonding. No hydrogen atoms could be located directly, but a reasonable hydrogen bonding scheme was inferred from short oxygen-oxygen distances. Final refinement by least-squares analysis with anisotropic temperature factors resulted in an R value of 3.3%.

Prydz, R., Straty, G. C., Timmerhaus, K. D., **Properties of fluorine along the vapor-liquid coexistence boundary,** *J. Chem. Phys.* **53,** *No. 6, 2359–2363 (September 15, 1970).*

Key words: Critical point; fluorine; latent heats of vaporization; saturated liquid densities; saturated vapor densities; vapor pressure.

Saturated liquid and vapor data from the triple point to the critical point are reported. These data were derived from experimental PVT isochores and a vapor pressure equation. The critical point was extracted by fitting an equation to all experimental data within 20 percent of the critical temperature. Separate equations, each constrained to the new critical point, were fitted to the saturated liquid and vapor data. Latent heats of vaporization were calculated from the Clapeyron equation and compared to other published values. A vapor pressure equation based on the IPTS 1968 temperature scale is reported.

Raveche, H. J., Mountain, R. D., **Three body correlations in simple dense fluids,** *J. Chem. Phys.* **53,** *No. 8, 3101–3107 (October 15, 1970).*

Key words: Neutron diffraction; percus-Yevick equation; simple liquids; superposition approximation; three body correlation function; x-ray diffraction; radial distribution function.

Correlations between triples of molecules in simple fluids at thermodynamic equilibrium are studied through their contribution to the isothermal density derivative of the pair probability density. Explicit computations are performed to indicate the role of the triplet function in accounting for the structure of the density derivative of the radial distribution function. The results imply that contributions from triplet correlations are in general quite appreciable. Various consequences of the results are discussed and the procedure is examined in general as a method for studying correlations between triples of molecules in simple fluids.

Risley, A. S., Allan, D. W., Peters, H. E., Johnson, E. H., Vessot, R. F. C., Levine, M., Gray, J. E., Shoaf, J. H., Machlan, H. E., and Glaze, D. J., **Stability characteristics of some atomic frequency standards (Summary),** *Proc. Conf. Precision Electromagnetic Measurements, National Bureau of Standards, Boulder, Colo., June 2–5, 1970, CPEM Digest, pp. 74–75 (1970).*

Key words: Allan variance; cesium beam; frequency stability; hydrogen maser; NBS frequency standard; time scale.

Over a period of three and one-half months a frequency stability comparison was made between seven commercial cesium beams and a NASA (Goddard Space Flight Center) hydrogen maser. Two of the prime purposes in bringing the NASA maser to Boulder were: (1) to determine the general effect upon the NBS Time Scale of including the H maser as a part and (2) to determine the stability of the H maser for sampling times τ longer than 10^3 seconds.
Two of the major results of the time scale and NASA maser comparison were, first, $\sigma_y(N=2,\ T=\tau,\ \tau=1$ day) of the time scale—*including the maser*—was less than 1×10^{-13}, where $y=\delta\nu/\nu$. Second, the inclusion of the maser in the time scale improved the precision about 30 percent.
Another hydrogen maser (from the Smithsonian Astrophysical Observatory) and a new four-foot long cesium beam (NBS–X4) were used along with the NASA maser to measure stabilities $\sigma_y(N=2,\ T=\tau,\ \tau)(\tau\approx1$ day). The stabilities for both masers and for NBS–X4 were better than one part in 10^{13}.

Robertson, B., **Quantum statistical mechanical derivation of generalized hydrodynamic equations,** *J. Math. Phys.* **11,** *No. 8, 2482–2488 (August 1970).*

Key words: Conservation equations; equation of motion; hydrodynamic equations; quantum fluids; quantum mechanical density distribution; quantum statistical mechanics.

Exact differential conservation equations are derived from the mass, momentum, and energy density operators for a one-component simple fluid of Bose or Fermi particles with arbitrary pairwise interactions. These equations are used in a statistical mechanical derivation of exact equations of motion for the expectations of these operators. The equations of motion are coupled to the exact equations relating the local temperature, chemical potential, and fluid velocity to these expectations. The coupled equations are closed in the sense that the expectations and their thermodynamic conjugates listed above are the only unknowns, although some of the dependence in the equations on the conjugates is expressed only implicitly. The equations of motion are memory-retaining nonlocal generalizations of the classical hydrodynamic equations and apply to a normal fluid arbitrarily far from equalibrium. The formalism is not carried as far as has the corresponding classical formalism.

Roth, R. S., Waring, J. L., Parker, H. S., **Effect of oxide additions on the polymorphism of tantalum pentoxide. IV. The system Ta_2O_5-Ta_2WO_8,** *J. Solid State Chem.* **2,** *445–461 (1970).*

Key words: Melting points; phase equilibria; system tantalum oxide-tantalum tungstate.

The low temperature form of pure Ta_2O_5 has been found to exist in two slightly different modifications. The lowest temperature form has a b axis multiplicity of 14 whereas the highest temperatures form (about 1350 °C) has a multiplicity of 11. At intermediate temperatures an "infinite" number of at least partially ordered sequences of these two modifications exist in equilibrium.
The addition of WO_3 to Ta_2O_5 causes the "stabilization" of an "infinite" number of phases similar in structure to the low temperature form of Ta_2O_5. From just less than 10 mol % WO_3 to the last compound in the series at $26\frac{2}{3}$ mol % WO_3 these phases are in equilibrium with liquid and the high temperature structure type of pure Ta_2O_5 is eliminated from the phase diagram. One compound, $14Ta_2O_5{\cdot}2WO_3$ with a multiplicity of 8, was found to melt congruently at about 1815 °C and the last phase, $11Ta_2O_5{\cdot}4WO_3$ with a multiplicity of 13, melts incongruently at about 1605 °C.

Rush, J. J., Schroeder, L. W., Melveger, A. J., **Infrared and Raman spectra of sodium bifluoride: Isotope dilution studies,** *Chem. Phys. Letters* **6,** *No. 5, 533–536 (September 1, 1970).*

Key words: Bending vibration; hydrogen bond; infrared; isotope dilution; lattice mode; raman; sodium; bifluoride; stretching vibration.

IR and Raman spectra for sodium bifluoride containing 2%, 11%, and ~80% $DF_{\bar{2}}$ are presented. Changes in the $DF_{\bar{2}}$ ν_2 and ν_3 IR bands with deuteration are related to coupling between like oscillators or states. Raman assignments are made for the $HF_{\bar{2}}$ ν_1 and lattice liberational (E_g) modes.

Schneider, S. J., **Cooperative determination of the melting point of alumina,** *J. Pure Appl. Chem.* **21,** *No. 1, 117–122 (1970).*

Key words: Al_2O_3; alumina; IUPAC; melting point of Al_2O_3; melting point standards.

A task force on secondary temperature standards, sponsored by the Commission on High Temperatures and Refractories, International Union of Pure and Applied Chemistry, has undertaken a program to investigate various inorganic non-metallic substances for use as high temperature reference materials. As part of this program a cooperative determination of the melting point of Al_2O_3 (alumina) was conducted by the task force. In all, nine scientific groups, representing seven countries contributed experimental data. All work was performed utilizing a common supply of Al_2O_3 of nominal 99.9% purity. Experimental techniques varied depending upon the individual investigator. The value for the alumina point, as recommended by the task force is 2054 °C ±6 (IPTS 1968).

Sengers, J. M. H. L., **Scaling predictions for thermodynamic anomalies near the gas-liquid critical point,** *Ind. Eng. Chem. Fundamentals*, **9**, *No. 3, 470–480 (November 9, 1970).*

Key words: Argon; carbon dioxide; classical equation; critical exponents; critical point; coexistence curve; lattice gas; power laws; rectilinear diameter; steam; thermodynamic anomalies; vapor pressure.

Most classical (or van der Waals type) equations of state of fluids show characteristic critical thermodynamic anomalies and symmetries that are common to them all. These characteristics are deduced from the Taylor expansion, in density and temperature, of these equations at the critical point. It is shown that the anomalies found experimentally are of a different nature, more similar to those predicted by the Ising model for the lattice gas. Consequences for data correlations in the critical region are discussed and examples of such correlations are presented.

Simmons, J. H., Macedo, P. B., **Viscous relaxation above the liquid-liquid phase transition of some oxide mixtures,** *J. Chem. Phys.* **53**, *No. 7, 2914–2922 (October 1, 1970).*

Key words: Immiscibility; oxide glasses; relaxation times; supercritical fluctuations; ultrasonic spectroscopy; viscous relaxation.

The viscosity anomaly observed above the critical points of a series of sodium-borosilicate melts is investigated by ultrasonic shear relaxation spectroscopy. The measurements were conducted at frequencies between 3 and 25 MHz and temperatures between 800 °C and 1300 °C. The samples tested have different critical temperatures as a result of small doping additions to the critical composition of the immiscibility surface in the phase diagram of the sodium-borosilicate system. This permitted measurements over a wide range of reduced temperatures. Analysis of the data yields the three structural relaxation parameters which are: the instantaneous shear modulus, the most probable relaxation time, and the width of the distribution of relaxation times. These parameters are related to the viscosity. It is found that while the instantaneous modulus and the most probable relaxation time appear unaffected by the presence of supercritical composition fluctuations, the width of the spectrum of relaxation times broadens drastically as the critical temperature is approached from above. Similar and parallel curves are formed from the widths of the distributions of relaxation times of all four samples when the temperature is properly normalized by the critical temperature. The general behavior of these curves exhibits the three reduced temperature regions predicted in a previously published topological model. The supercritical broadening of the width of the distribution of relaxation times accounts for the observed viscosity anomaly.

Spencer, L. V., Stanley, W., **On neutron penetration in duet systems with large cross sections,** *Proc. Special Sessions on Gamma-Ray Production and Transport and on Civil Defense Shielding, American Nuclear Society, pp. 199–221 (August 1969).*

Key words: Albedo; Civil Defense; ducts; nuclear weapons data; neutron penetration; structure shielding.

Neutron albedo data for non-hydrogenous wall materials is insensitive to variations of the total cross section with energy and, to some extent, to details of cross section angular distributions. As a result, it makes sense to explore models in which the differential albedo is factored into energy dependent and direction dependent parts. This approximation results in a factoring of the transport equation for large enclosures into two parts, a one-velocity type of problem and a general problem of determining spectra for different orders of reflection. We extend this approach further to identify suitable parameters in terms of which data for elementary types of enclosure can be applied to configurations. These parameters are given, the procedure for combining duct sections is sketched, and calculations for a three-legged duct are compared with Monte Carlo data for such a duct.

Swanson, H. E., McMurdie, H. F., Morris, M. C., Evans, E. H., **Standard x-ray diffraction powder patterns,** *Nat. Bur. Stand. (U.S.), Monogr. 25—Section 8, 171 pages (Sept. 1970) $1.50, SD Catalog No. C13.44:25/sec. 8.*

Key words: Crystal structure; integrated intensities; lattice constants; peak intensities; powder patterns; reference intensities; standard; x-ray diffraction.

Standard x-ray diffraction patterns are presented for 81 substances. Fifty-three of these patterns represent experimental data and 28 are calculated. The experimental x-ray powder diffraction patterns were obtained with x-ray diffractometer, using samples of high purity. All d-values were assigned Miller indices determined by comparison with computed interplanar spacings consistent with space group extinctions. The densities and lattice constants were calculated, and the refractive indices were measured whenever possible. The calculated x-ray power diffraction patterns were computed from published crystal structure data. Both peak height and integrated intensities were reported for the calculated patterns.

Tsai, D. H., Bullough, R., Perrin, R. C., **Molecular dynamical studies of the motion of point defects in a crystalline lattice,** *Proc. Phys. Soc. (London) C: Solid St. Phys.* **3**, *2022–2036 (1970).*

Key words: Atomic diffusion; defect motion; interstitial motion; jump frequency; lattice model; migration energy; migration entropy; molecular dynamics; random-walk theory; vacancy motion.

Molecular dynamical calculations have been employed to study the motion of interstitial and vacancy defects in a bcc lattice with an interaction potential which simulated that of α-iron. Our purpose was to investigate the effects of lattice thermal oscillations on the motion and the interactions of these defects, and to study the random-walk problem of defect motion on an atomic scale. The dynamical results showed that the temperature dependence of the defect jump frequency was in general agreement with the atomic theory of diffusion. From this temperature dependence, the energy and the entropy of defect migration were obtained. For interstitial motion, the migration energy from the dynamical model (0.23 eV) was the same as that from static calculations. For vacancy motion, the migration energy from the dynamical model (0.42 eV) was lower than that from static calculations. Possible reasons for this difference are discussed.

Wasik, S. P., Tsang, W., **Determination of trace amounts of contaminants in water by isotope dilution gas chromatography,** *Anal. Chem.* **42**, *No. 13, 1649–1651 (November 1970).*

Key words: Chromatics; gas chromatography; isotope dilution; olefins; and water analysis.

An isotope dilution technique using gas liquid chromatography is proposed for the quantitative analysis of trace organic pollutants in water supplies. The method was demonstrated using benzene with predeuterated benzene as the isotope with both substances in the p.p. B. concentration range. Columns with aqueous silver nitrate as the stationary phase were used to determine the ratio of the concentration of benzene to predeuterated benzene.

Wasik, S. P., Tsang, W., **Gas-liquid chromatography separations of hydrocarbons using columns with aqueous solutions of complexing metal ions as stationary phases,** *Anal. Chem.* **42**, *No. 13, 1648–1649 (November 1970).*

Key words: Aliphatics; aromatics; complexing effects; gas chromatography; group separation; mercuric nitrate; olefins; silver nitrate; surface effect.

Interesting hydrocarbon selectivity was obtained in gas-liquid chromatography using aqueous solutions of Ag^{+} and Hg^{++} ions as the stationary phases. This was achieved by taking advantage of the complexing properties of these ions and the large surface effect of the solution. Columns may be designed to be specific for certain hydrocarbon groups using this technique.

Waxman, M., Hastings, J. R., Chen, W. T., **Nonlinear statistical analysis of Burnett PVT data,** *Proc. 5th Symp. Thermophysical Properties, Boston, Massachusetts, September 30–October 2, 1970, C. F. Bonilla, Ed., pp. 248–261 (Americal Society of Mechanical Engineers, New York, N.Y., 1970).*

Key words: Burnett; gas; statistical; model dependency; nonlinear; PVT.

The Burnett method, which requires only temperature and isothermal pressure measurements made before and after stepwise expansions between two volumes, is being used extensively for determining gas compressibilities and density or pressure virial coefficients. The measurements are simple, but the data reduction involves rather formidable nonlinear statistical analysis of relationships containing the compressibility factor, defined as a density or a pressure virial expansion, and optional constants. In this paper we compare the results of analyzing different Burnett relationships with independent parameters and no restrictions on the data, using two nonlinear statistical methods, due to Gauss and to Deming, and argon data at 25 °C for pressures up to 250 atm. We discuss the computational difficulties and present background information on the experimental and analytical methods.

Weir, C. E., Block, S., Piermarini, G. J., **Compressibility of inorganic azides,** *J. Chem. Phys.* **53,** *No. 1, 4265–4269 (December 1970).*

Key words: Anisotropic compressibility; azides; compressibility; high pressure; single crystal; x-ray diffraction.

The compressibility of α lead azide, β lead azide, barium azide, potassium azide, sodium azide and thallium azide have been measured by single crystal x-ray diffraction techniques using the diamond anvil cell. Both the anisotropic and volume compressibilities are reported. The pressures were determined by measurements at the known freezing points of *n*-hexane and ethanol. A phase transition occurs in thallium azide at a pressure between the freezing points of chloroform (5390 bars) and *n*-decane (2990 bars). Pressure-temperature observations in the diamond cell of lead azide were carried out to 300 °C and approximately 30 kbar. No phase transitions were observed. Radiation damage to azide crystals under high pressures is reduced significantly.

Weisman, H. M., Sherwood, G. B., **Annotated accession list of data compilations of the office of standard reference data,** *Nat. Bur. Stand. (U.S.), Tech. Note. 554, 196 pages (Sept. 1970) $1.50, SD Catalog No. C13.46:554.*

Key words: Accession list; atomic and molecular properties; chemical kinetics; colloid and surface properties; fundamental particles properties; general collections; mechanical properties; nuclear properties; solid state properties; thermodynamic and transport properties.

The National Bureau of Standards, Office of Standard Reference Data has attempted to acquire all significant reference data compilations on a worldwide basis. This publication lists the collection of documents so acquired, together with their abstracts. The documents are organized in the following categories: General Collections, Nuclear Properties (including Fundamental Particles Properties), Atomic and Molecular Properties, Solid State Properties, Chemical Kinetics, Colloid and Surface Properties, Mechanical Properties, and Thermodynamic and Transport Properties. Sources of availability for the listed publications are also provided.

Wexler, A., **Measurement of humidity in the free atmosphere near surface of the earth** *(Proc. American Meteorological Society Symp. on Meteorological Observations and Instrumentations, Washington, D.C., February 10–14, 1969) Meteorological Monographs 11, No. 33, 262–282 (October 1970).*

Key words: Dew point; hygrometry; meteorology; moisture measurement in gases; psychrometry.

This paper is a survey of the state-of-the-art in hygrometry as applied to humidity measurement in gases near atmospheric pressure. Although not indicated specifically, many of the methods discussed are applicable to humidity measurements in gases at pressures higher or lower than atmospheric. Hygrometric methods, techniques and instruments are divided arbitrarily into the following six classes: (1) methods dependent upon the total removal of water vapor from a moist gas, (2) methods dependent upon the addition of water vapor to produce a saturated gas, (3) methods dependent upon the reversible sorption of water vapor by a sensor, (4) methods dependent upon the measurement of a physical property of a gas, (5) condensation methods, that is, methods dependent upon the liquid-vapor or the solid-vapor equilibrium state of the water substance, and (6) methods dependent upon chemical reactions and procedures. The methods of each class are further subdivided by principles of operation and are examined to assess such characteristics as range, accuracy, sensitivity, speed of response, effect of environmental conditions, and limitations in behavior and utility.

Wiederhorn, S. M., Bolz, L. H., **Stress corrosion and static fatigue of glass,** *J. Am. Ceram. Soc.* **53,** *No. 10, 543–548 (October 1970).*

Key words: Crack propagation; fracture; glass; static fatigue; stress corrosion.

Stress corrosion cracking of six glasses was studied using fracture mechanics techniques. Crack velocities in water were measured as a function of applied stress intensity factor and temperature. Apparent activation energies for crack motion were obtained. Data were consistent with the universal fatigue curve for static fatigue of glass and it was found that the universal fatigue curves depended on glass composition. Of the glass compositions tested, silica glass exhibited most resistance to static fatigue followed by aluminosilicate and borosilicate glass. Sodium was found to be detrimental to stress corrosion resistance. The crack velocity data could be explained by the Charles and Hillig theory of stress corrosion and is probable that stress corrosion of glass is normally caused and controlled by a chemical reaction between the glass and water.

Wiederhorn, S. M., Townsend, P. R., **Crack healing in glass,** *J. Am. Ceram. Soc.* **53,** *No. 9, 486–489 (September 1970).*

Key words: Crack healing; fracture; glass; strength; surface.

This paper discusses strength recovery in glass containing cracks that were observed to close spontaneously. Measurements of bonding across the surfaces of closed cracks were made on soda-lime glass, using fracture mechanics techniques. Approximately 80 percent strength recovery was observed on cracks formed by mechanical shock, while approximately 20 percent strength recovery was observed on cracks that closed after being held open to the atmosphere for several minutes. The high strength recovery during closure of cracks formed by mechanical shock is attributed to the very active nature of the surface formed during fracture. Reaction with air or dry nitrogen is believed to reduce the activity of the fracture surfaces because of oxygen and water adsorption.

Other NBS Publications

J. Res. Nat. Bur. Stand. (U.S.), 75C (Eng. & Instr.), No. 1 (January–March 1971), SD Catalog No. C13.22/sec.C:75/1

Rotary-vane attenuator with an optical readout. W. E. Little, W. Larson, and B. J. Kinder.

Design and operational characteristics of a high-speed (millisecond) system for measurement of properties at high temperature. A. Cezairliyan.

New method of determining residual thiosulfate in processed photographic film. C. I. Pope.

Scanning densitometer for continuous recording of spectral transmission density at low spatial contrast. W. L. McLaughlin, M. Rosenstein, E. Hussmann, and J. J. Lantz, Jr.

Rotating optical attenuator for the generation of subsecond duration sawtooth shape radiance pulses. A. Cezairliyan.

Sound speed measurements in solids; absolute accuracy of an improved transient pulse method. T. M. Proctor, Jr.

Seismic response of infrasonic microphones. A. J. Bedard, Jr.

Publications of the National Bureau of Standards.

Achenbach, P. R., Building research at the National Bureau of Standards, Nat. Bur. Stand. (U.S.), Bldg. Sci. Ser. 0, 59 pages (Oct. 1970) 60 cents, SD Catalog No. C13.29/2:0.

Acquista, N., Abramowitz, S., Structure of the alkali hydroxides. V. The infrared spectra of matrix-isolated RbOH, RbOD, NaOH, and NaOD, J. Chem. Phys. **51,** No. 7, 2911–2914 (October 1, 1969).

Ahearn, A. J., Homogeneity of ion sensitive emulsions and precision of ion beam measurements in spark source mass spectrometry, (Summary), Proc. 16th Annual Conf. on Mass Spectrometry and Allied Topics, May 12–17, 1968, Pittsburgh, Pa., sponsored by ASTM Committee E14, pp. 273–276 (1968).

Andrews, J. R., Improved bias supply for tunnel-diode picosecond pulse generators, IEEE Trans. Instr. Meas. **IM–19,** No. 3, 171–175 (Aug. 1970).

Armstrong, R. W., Waters, H. P., Testing programs and research on restraint systems, Proc. Intern. Engineering Congress, Detroit, Michigan, January 13–17, 1969, Report No. 690247, pp. 1–48 (Society of Automotive Engineers, New York, N.Y., 1969); Abstract in SAE Trans. **78,** 102 (1969).

Armstrong, R. W., Waters, H. P., Stapp, J. P., Human muscular restraint during sled deceleration, Proc. 1968 Stapp Car Crash Conf., October 22–23, 1968, Detroit, Michigan, Report No. 680793, pp. 440–462 (Society of Automotive Engineers, New York, N.Y., 1969); Abstract in SAE Trans. **77,** 179 (1969).

Arthur, M. G., Impulse spectral intensity calibration at the National Bureau of Standards, Proc. Electromagnetic Compatibility Symp., Ft. Monmouth, N.J., June 19–20, 1969, pp. 133–138 (U.S. Army Electronics Command Hdq., Ft. Monmouth, N.J., 1969).

Ausloss, P., Lias, S. G., Carbonium ions in radiation chemistry. Reactions of *t*-butyl ions with hydrocarbons, J. Am. Chem. Soc. **92,** 5037–5045 (1970).

Bagg, T. C., Factors dictating characteristics of systems utilizing microforms, J. Micrographs **3,** No. 3, 143–146 (1970); ABFM Format **1,** No. 2, 1–2 (May 1970).

Baird, R. C., Recent theoretical and experimental results of the determination of antenna pattern and gain from near-field measurements (Summary), Proc. Conf. Precision Electromagnetic Measurements, National Bureau of Standards, Boulder, Colo., June 2–5, 1970, CPEM Digest, p. 60 (1970).

Baird, R. C., Newell, A. C., Wacker, P. F., Kerns, D. M., Recent experimental results in near-field antenna measurements, Electronics Letters **6,** No. 11, 349–351 (May 28, 1969).

Barnes, J. A., Frequency measurement errors of passive resonators caused by frequency-modulated exciting signals, IEEE Trans. Instr. Meas. **IM–19,** No. 3, 147–152 (August 1970).

Barnes, J. A., Chi, A. R., Cutler, L. S., Healey, D. J., Leeson, D. B., McGunigal, T. E., Mullen, J. A., Smith, W. L., Sydnor, R., Vessot, R. F. C., Winkler, G. M. R., Characterization of frequency stability, Nat. Bur. Stand. (U.S.), Tech. Note 394, 50 pages (Oct. 1970) 60 cents, SD Catalog No. C13.46:394.

Bates, R. D., Jr., Flynn, G. W., Ronn, A. M., Laser-induced vibrational fluorescence in nitrous oxide, J. Chem. Phys. **49,** No. 3, 1432–1433 (1968).

Bates, R. G., Staples, B. R., Robinson, R. A., Ionic hydration and single ion activities in unassociated chlorides at high ionic strengths, Anal. Chem. **42,** No. 8, 867–871 (July 1970).

Bennett, H. S., Two-electron F' centers in the alkaline-earth oxides and in the alkali halides, Phys. Rev. B, **1,** No. 4, 1702–1715 (February 15, 1970).

Berger, M. J., Beta-ray dosimetry calculations with the use of point kernels (Proc. Symp. Medical Radionuclides: Radiation Dose and Effects, Oak Ridge Association Universities, Oak Ridge, Tennessee), Atomic Energy Commission Report CONF–691212, pp. 63–86 (June 1970).

Bergstrom, J. C., Bertozzi, W., Kowalski, S., Maruyama, X. K., Lightbody, Jr., J. W., Fivozinsky, S. P., Penner, S., Electroexcitation of the low-lying of 0^{16}, Phys. Rev. Letters 24, No. 4, 152–155 (January 26, 1970).

Birky, M. M., Simultaneous recording of near-field and far-field patterns of lasers, Appl. Opt. **8,** No. 11, 2249–2253 (November 1969).

Blaine, R. L., A statistical study of the effects of trace elements on the properties of portland cement, Proc. 5th Intern. Symp. on the Chemistry of Cements, Tokyo, Japan, October 7–11, 1968, **3,** Part 3, 86–91 (December 31, 1969).

Blandford, J. M., Gurel, L. M., Fibers and fabrics, Nat. Bur. Stand. (U.S.), Consumer Info. Series 1, 31 pages (Nov. 1970) 65 cents, SD Catalog No. C13.53:1.

Blaugher, R. D., Hein, R. E., Cox, J. E., Waterstrat, R. M., Atomic ordering and superconductivity in A–15 compounds, J. Low Temp. Phys. **1,** No. 6, 539–561 (December 1969).

Boyne, H. S., Hall, J. L., Barger, R. L., Bender, P. L., Ward, J., Levine, J., Faller, J., Absolute strain measurements with a 30-meter vacuum interferometer, (Proc. Conf. Laser Applications in the Geosciences, Huntington Beach, Calif., June 1969), Chapter in Laser Applications in the Geosciences, J. Gauger and F. F. Hall, Jr., Ed., pp. 215–225 (Western Periodicals, North Hollywood, Calif., 1970).

Brady, R. F., Jr., Cyclic acetals of ketoses. Part III. Re-investigation of the synthesis of the isomeric Di-*O*-isopropylidene-β-D-fructopyranoses, Carbohydrate Res. **15,** No. 1, 35–40 (1970).

Brenner, Tires. Their selection and care, Nat. Bur. Stand. (U.S.), Consumer Info. Series **2,** 32 pages (Nov. 1970) 65 cents, SD Catalog No. C13.53:2.

Bullis, W. M., Baroody, A. J., Jr., Methods of measurement for semiconductor materials, process control, and devices, Quarterly Report–January 1 to March 31, 1970, Nat. Bur. Stand. (U.S.), Tech. Note 555, 63 pages (Sept. 1970) 65 cents, SD Catalog No. C13.46:555.

Bullis, W. M., Scace, R. I., Measurement standards for integrated circuit processing, Proc. IEEE **57,** No. 9, 1639–1646 (September 1969).

Casella, R. C., Possible failure of the Pomeranchuk theorem–shrinkage of the forward elastic peak, Phys. Rev. Letters **24,** No. 25, 1463–1466 (June 22, 1970).

Champion, E. C., Marinenko, G., Taylor, J. K., Schmidt, W. E., Determination of submicrogram amounts of chromium by coulometric titrimetry, Anal. Chem. **42,** 11, 1210–1213 (September 1970).

Chandler, R. F., Christian, R. A., Comparative evaluation of dummy performance under $-G_x$ impact, Proc. 13th Stapp Car Crash Conf., Boston, Mass., December 2–4, 1969, Report No. 690798, pp. 61–75 (Society of Automotive Engineers, New York, N.Y., 1970); Abstract in SAE Trans. **78,** 171–172 (1969).

Clark, A. F., Childs, G. E., Wallace, G. H., Electrical resistivity of some engineering alloys at low temperatures, Cryogenics **10,** No. 4, 295–305 (August 1970).

Coriell, S. R., Jackson, J. L., Probability distribution of the radius of gyration for two statistical segments, J. Chem. Phys. **53,** No. 8, 3389 (October 15, 1970).

Cornog, D. Y., Cornog, J. R., Human factors engineering in the sorting and handling of mail, Proc. NATO Advanced Study Institute on "Human Factors/Ergonomics," Mondello, Sicily, September 29, 1969, pp. 1–34 (January 21, 1970).

Costrell, L., Development and current status of the standard nuclear instrument module (NIM) system, Nat. Bur. Stand. (U.S.), Tech. Note 556, 15 pages (Oct. 1970) 30 cents, SD Catalog No. C13.46:556.

Coxon, B., The conformations of 1,2:4,6-Di-*O*-benzylidene-α-D-glucopyranose derivatives, Carbohydrates Res. 14. 9–15 (October 1970).

Crissman J. M., Passaglia, E., Eby, R. K., Colson, J. P., Crystal data on n-eicosane ($C_{20}H_{42}$), J. Appl Cryst. **3,** 193–195 (1970).

Cruz, J. E., Jellison, J. C., A digital technique for generating variable frequency multiphase waveforms, Rev. Sci. Instr. **41,** No. 7, 1098–1099 (July 1970).

Currie, L. A., Radioactivity monitors and accuracy in photonuclear experiments, (Summary), Trans. Am. Nucl. Soc. **13,** No. 1, 59 (1970).

Davis, D. D., Transmission of time/frequency signals in the vertical interval, Proc. 108th Technical Conference and Equipment Exhibit, New York, N.Y., October 4–9, 1970, Article No. 43, p. 3 (Society of Motion Picture and Television Engineers, New York, N.Y., 1970).

Davis, D. D., Jespersen, J. L., Kamas, G., The use of television signals for time and frequency dissemination, Proc. IEEE **58,** No. 6, 931–933 (June 1970).

Dickens, B., Brown, W. E., The crystal structure of calcium carbonate hexahydrate at $\sim -120°$, Inorg. Chem. **9,** No. 3, 480–486 (March 1970).

Diller, D. E., Hanley, H. J. M., Roder, H. M., The density and temperature dependence of the viscosity and thermal conductivity of dense simple fluids, Cryogenics **10,** No. 4, 286–294 (August 1970).

Engen, G. F., A new method of charaterizing amplifier noise performance (Summary), Proc. Conf. Precision Electromagnetic Measurements, National Bureau of Standards, Boulder, Colo., June 2–5, 1970, CPEM Digest, pp. 20–21 (1970).

Farrar, T. C., Pulsed and Fourier transform NMR spectroscopy, Anal. Chem. **42**, No. 4, 109A–112A (April 1970).

Frederick, N. V., Scott. W. W., Jr., A simple technique for metalizing boron nitride, Rev. Sci. Instr. **40**, No. 9, 1240 (September 1969).

Freeman, D. H. Zielinski, W. L., Jr., Rittner, W. F., Recognition of crosslinking in the infrared spectra of poly(styrene-divinylbenzene), Proc. Ion Exchange in the Process Industries Conf., Imperial College of Science and Technology, London, England, pp. 27–30 (1970).

Gibson, B. F., O'Connell, J. S., Angular distribution of the reaction $^1H(d^3, He)$ Physics Letters **32B**, No. 5, 331–332 (August 3, 1970).

Goldman, A. J., Analysis of a capacity concept for runway and final-approach path airspace, Proc. Ion National Meeting on Air Traffic Control in the 1970's, Institute of Navigation, St. Louis, Mo., April 14–16, 1970, pp. 119–131 (1970).

Greenberg, L., Newman, M., Some results on solvable groups, Arch. Math. **21**, No. 4, 349–352 (1970).

Greenfeld, S. H., Warner, E. R. Reinhart, H. W., Bibliographies on fabric flammability. Part 5. Testing and test methods, Nat. Bur. Stand. (U.S.), Tech. Note 498–2, 39 pages (Sept. 1970) 45 cents, SD Catalog No. C13.46:498–2.

Grosch, H. R. J., A view of computers from the Bureau of Standards, Input **6**, No. 2, 3–7 (1970).

Halford, D., Frequency stability of quality quartz crystal oscillators: Performance and some critical applications, Proc. Intern Colloq. Chronometrie, Paris, France, September 16–20, 1969, Series A, pp. A–11–1–A–11–3 (September 1969).

Hardy, S. C., Coriell, S. R., Morphological stability of ice cylinders in aqueous solution, J. Crystal Growth **7**, No. 2, 147–154 (September–October 1970).

Hayward, E., Schwartz, R. B., Murray, K. M., Comments on isospin of the B^{11} giant resonance, Phys. Rev. **2**, No. 2, 761–762 (August 1970).

Hellwig, H., The hydrogen storage beam tube, a proposal for a new frequency standard, Metrologia **6**, No. 2, 56–60, (April 1970).

Hellwig, H., Allan, D. W., Glaze, D. J., Vessot, R. F. C., Levine, M., Zitzewitz, P. W., Peters, H. E., Measurement of the unperturbed hydrogen hyperfine transition frequency (Summary), Proc. Conf. Precision Electromagnetic Measurements, National Bureau of Standards, Boulder, Colo., June 2–5, 1970, CPEM Digest, pp. 72–73 (1970).

Henderson, M., Berry, P. L., Progress of federal library automation, Drexel Library Quart. **6**, Nos. 3 & 4, 249–263 (July–October 1970).

Hiza, M. J., Duncan, A. G., A correlation for the prediction of interaction energy parameters for mixtures of small molecules, AIChE J. **16**, No. 5, 733–738 (September 1970).

Hoer, C., Agy, D., A broadhurst resistive coupler, Proc. Conf. Precision Electromagnetic Measurements (Summary), National Bureau of Standards, Boulder, Colo., June 2–5, 1970, CPEM Digest, pp. 18–19 (1970).

Homan, D. N., Zapf, T. L., Two-stage guarded inductive voltage division for use at 100 kHz, Proc. 1969 Instrument Society of America Conf., Houston, Texas, October 27–30, 1969, pp. 69–614 (1969).

Hudson, R. P., Conference Reports—Ultra-low temperatures 1970, Cryogenics **10**, No. 5, 445 (October 1970).

Hunt, C. M., Woolf, A. R., Comparison of some different methods for measuring particle size using microscopically calibrated glass beads, Powder Technol. **3**, 9–23 (1969).

Jennings, D. A., West, E. D., A laser power meter for large beams, Rev. Sci. Instr. **41**, No. 1, 565–567 (April 1970).

Johannesen, R. B., Ferretti, J. A., Harris, R. K., UEAITR: A new computer program for analysis of NMR spectra analysis of the proton spectrum of triisopropylphosphine, J. Magnetic Resonance **3**, No. 1, 84–93 (July 1970).

Joiner, B. L., Laubscher, N. F., Brown, E. S., Levy, B., An author and permuted title index to selected statistical journals, Nat. Bur. Stand. (U.S.), Spec. Publ. 321, 510 pages (Sept. 1970) $5.75, SD Catalog No. C13.10:321.

Jordan, R. H., Stark, M. C., Bunn, C. O., Donaldson, J. L., Obright, W. J., Millie, H. R., Gilsinn, J., Goldman, A. J., Horn, W. A., Systems analysis of inland consolidation centers for marine cargo, Nat. Bur. Stand. (U.S.), Tech. Note 530, 162 pages (Nov. 1970) $1.25, SD Catalog No. C13.46:530.

Kearsley, E. A., Intrinsic errors for pressure measurements in a slot along a flow, (Proc. Fifth Intern. Congress on Rheology, Kyoto, Japan, October 1968), Trans. Soc. Rheology 14:3, 419–424 (1970).

Kerns, D. M., Correction of near-field antenna measurements made with an arbitrary but known measuring antenna, Electronics Letters **6**, No. 11, 346–347 (May 28, 1970).

Kerns, D. M., New method of gain measurement using two identical antennas, Electronics Letters **6**, No. 11, 348–349 (May 28, 1970).

Kidnay, A. J., Hiza, M. J., Physical adsorption in cryogenic engineering, Cryogenics **10**, No. 4, 271–277 (August 1970).

Krauss, M., Mies, F. H., Molecular-orbital calculation of the shape resonance in N_2^-, Phys. Rev. A. **1**, No. 6, 1592–1598 (June 1970).

LaFleur, P. D., Becker, D. A., Editors, Activation analysis section: Summary of activities, July 1969 to June 1970, Nat. Bur. Stand. (U.S.), Tech. Note 548, 164 pages (Dec. 1970) $1.25, SD Catalog No. C13.46:548).

Lance, H. W., Report on metrology sessions at the 24th annual ISA conference, Appl. Opt. **9**, No. 6, 1497–1498 (June 1970).

Lide, D. R., Jr., Editor, Critical evaluation of data in the physical sciences—A status report on the National Standard Reference Data System—June 1970, Nat. Bur. Stand. (U.S.), Tech. Note 553, 77 pages (Sept. 1970) 70 cents, SD Catalog No. C13.46:553.

Maki, A. G., Hexter, R. M., Resonance interactions with ν_5 of CH_3I; A method of determining A_0, J. Chem. Phys. **53**, No. 1, 453–454 (July 1, 1970).

Mandel, J., Paule, R. C., Interlaboratory evaluation of a material with unequal numbers of replicates, Anal. Chem 42, No. 11, 1194–1197 (September 1970).

Marsden, C. P., Tabulation of published data on electron devices of the U.S.S.R. Through March 1970, Nat. Bur. Stand. (U.S.), Tech. Note 526, 122 pages (Oct. 1970) $1.25, SD Catalog No. C13.46:526. Supersedes NBS Technical Note 441.

Marshall, R. D., Thom, H. C. S., Editors, Proceedings of technical meeting concerning wind loads on buildings and structures held at the National Bureau of Standards, Gaithersburg, Maryland, January 27–28, 1969, Nat. Bur. Stand. (U.S.), Bldg. Sci. Ser. 30, 172 pages (Nov. 1970) $1.75, SD Catalog No. C13.29/2:30.

Martin, W. C., Kaufman, V., $4p^2$ configuration in Neutral Zinc (Zn I), J. Opt. Soc. Am. **60**, No. 8, 1096–1099 (August 1970).

Mather, W. G., III, Kit, B. V., Bloch, G. A., Herman, M. F., Man, his job, and the environment: A review and annotated bibliography of selected recent research on human performance, Nat. Bur. Stand. (U.S.), Spec. Publ. 319, 107 pages (Oct. 1970) $1.00, SD Catalog No. C13.10:319.

Mazur, J., Non-self-intersecting random walks in lattices with nearest-neighbor interactions, Chapter in Stochastic Processes in Chemical Physics, pp. 261–280 (John Wiley & Sons, Inc., New York, N.Y., 1969).

McSparron, D. A., Mohan, K., Raybold, R. C., Saunders, R. D., Zalewski, E. F., Spectroradiometry and conventional photometry an interlaboratory comparison, Nat. Bur. Stand. (U.S.), Tech. Note 559, 197 pages (Nov. 1970) $1.50, SD Catalog No. C13.46:559.

Meadow, C. T., Meadow, H. R., Organization, maintenance and search of machine files, Chapter 7 in Annual Review of Information Science and Technology, C. A. Cuadra, Ed., pp. 169–191 (Encyclopedia Britannica, Chicago, Ill., 1970).

Meijer, P. H. E., The importance of dipole-dipole interactions in ultralow temperature physics (Proc. 1970 Ultralow Temperature Symp. sponsored by Office of Naval Research and Naval Research Laboratory, April 23–24, 1970), R. A. Hein, D. U. Gubser, E. H. Takken, Ed., NRL Report 7133, pp. 123–128 (April 1970).

Meinke, W. W., Analytical chemistry—a fading discipline? No! Anal. Chem. **42**, 26A–38A (June 1970).

Melmed, A. J., Carroll, J. J., Some initial observations of TiNi in the field-ion microscope, Appl. Phys. Letters **17**, No. 6, 247–249 (September 15, 1970).

Menis, O., Shultz, J. I., Editors, Analytical coordination chemistry section: Summary of Activities July 1969–June 1970, Nat. Bur. Stand. (U.S.), Tech. Note 544, 151 pages (Sept. 1970) $1.25, SD Catalog No. C13.46:544.

Meshkov, S., Comments on baryon spectroscopy, Proc. Hyperon Resonances Conf., Duke University, Durham, N.C., pp. 471–500 (April 24–25, 1970).

Meshkov, S., How good are symmetry predictions? Proc. Intern. Conf. on Symmetries and Quark Models, Wayne State University, Detroit, Michigan, June 18–20, 1969, Edited by Ramesh Chand, pp. 199–212 (November 1970).

Moore, C. E., Annual Report, July 1, 1968–June 30, 1969, The National Bureau of Standards, Washington, D.C., Bull. Am. Astron. Soc. **2**, No. 1, 99–100 (1970).

Moore, G. A., Is quantitative metallography quantitative? Am. Soc. Testing Mater. Spec. Publ. 480, pp. 3–48 (1970).
Nargolwalla, S. S., Niewodniczanski, J., Suddueth, J. E., Experimental sensitivities for 3-MeV neutron activation analysis, J. Radioanal. Chem. **5,** 403–423 (1970).
Nargolwalla, S. S., Suddueth, J. E., Rook, H. L., Determination of pulse pileup and nuclear interferences in 14-MeV neutron activation analysis for trace oxygen (Summary), Trans. Am. Nucl. Soc. **13,** No. 1, 78–79 (1970).
Neill, A. H., Jr., High-energy light detector for use with pulsed ruby and glass lasers, Appl. Opt. **9,** No. 10, 2392–2393 (October 1970).
Newton, C. J., Ruff, A. W., Jr., X-ray study of annealing in plastically deformed Ag-Sn alloys, Met. Trans. **1,** No. 10, 2833–2838 (October 1970).
Oberholtzer, B. L., Publications of the National Bureau of Standards 1968-1969, Nat. Bur. Stand. (U.S.), Spec. Publ. 305, Suppl. 1, 497 pages (December 1970) $4.50, SD Catalog No. C13.10:305 Suppl.
O'Connell, J. S., Electron scattering sum rule for ^{2}H, ^{3}H, ^{3}He and ^{4}He, Physics Letters **32B,** No. 5, 323–325 (August 3, 1970).
Otoshi, T. Y., Stelzried, C. T., Yates, B. C., Beatty, R. W., Comparisons of waveguide losses calibrated by the DC potentiometer, AC ratio transformer, and reflectometer techniques, IEEE Trans. Microwave Theory Tech. **MTT-18,** No. 7, 406–409 (July 1970).
Peavy, S. T., Varner, R. N., Bremer, S. G., A systems programmer's guide for implementing OMNITAB II, Nat. Bur. Stand. (U.S.), Tech. Note 550, 43 pages (Nov. 1970) 50 cents, SD Catalog No. C13.46:550.
Perel, J., Deslattes, R. D., Extended fine-structure in x-ray absorption spectra of certain perovskites, Phys. Rev. B. **2,** No. 5, 1317–1323 (September 1, 1970).
Plante, E. R., Paule, R. C., Explanation of the H° vs S° correlation, J. Chem. Phys. **53,** No. 9, 3770–3771 (November 1, 1970).
Plitt, K. F., Adhesives for everyday use, Nat. Bur. Stand. (U.S.), Consumer Info. Series 3, 17 pages (Nov. 1970) 40 cents, SD Catalog No. C13.53:3.
Powell, C. J., Comparison of optical data for sodium and potassium with interband-transition absorption theory, Optics Commun. **2,** No. 2, 87–89 (July 1970).
Powell, C. J., Validity of inelastic-electron-scattering data in determining the metallic or insulating properties of adsorbed atomic layers, Phys. Rev. **B-1,** No. 10, 4191–4192 (May 1970).
Radebaugh, R., Siegwarth, J. D., Theory of He^3–He^4 dilution refrigerators (Proc. 1970 Ultralow Temperature Symp., Washington, D.C., April 23–24, 1970; NRL Report 7133) pp. 63–81 (1970).
Radlinski, R. W., Price, J. I., The brake pedal force capability of adult females, Nat. Bur. Stand. (U.S.), Tech. Note 557, 25 pages (Oct. 1970) 35 cents, SD Catalog No. C13.46:557.
Rasmussen, A. L., Laser energy and power measurement with a double reflecting plate calorimeter, Rev. Sci. Instr. **41,** No. 10, 1479–1484 (October 1970).
Reader, J., Sugar, J., Ionization energies of Ce I and Gd I, J. Opt. Soc. Am. Letter to Editor **60,** No. 10, 1421–1422 (October 1970).
Santone, L. C., Berlin, G., Location of fire stations, Proc. WORC Symp. Systems Analysis for Social Problems, National Bureau of Standards, Gaithersburg, Maryland, May 26–28, 1969, pp. 79–91 (December 3, 1970).
Saylor, C. P., Broken Virtue, Capital Chem. **20,** No. 6, 137–140 (September 1970).
Schooley, J. F., Soulen, R. J., Koonce, C. S., Surface potential barrier in $SrTiO_3$, Solid State Commun. **7,** 1077–1079 (1969).
Selby, M. C., The Bolovac and its applications (Summary), Proc. Conf. Precision Electromagnetic Measurements, National Bureau of Standards, Boulder, Colo., June 2–5, 1970, CPEM Digest, pp. 14–15 (1970).
Shields, W. R., Editor, Analytical mass spectrometry section: Summary of activities July 1969 to June 1970, Nat. Bur. Stand. (U.S.), Tech. Note 546, 120 pages (Nov. 1970) $1.25, SD Catalog No. C13.46:546.
Sieck, L. W., Searles, S. K., High pressure photoionization mass spectrometry. Reactions of alkane and cycloalkane molecular ions with water vapor at thermal kinetic energies, J. Chem. Phys. **53,** No. 1, 2601–2604 (October 1, 1970).
Sieck, L. W., Searles, S. K., Rebbert, R. E., Ausloos, P., Reactivity of the cyclohexane Ion, J. Phys. Chem. **74,** No. 21, 3829–3831 (October 15, 1970).
Simmons, J. H., Napolitano, A., Macedo, P. B., Supercritical viscosity anomaly in oxide mixtures, J. Chem. Phys. **53,** No. 3, 1165–1170 (August 1, 1970).
Sitterly, C. M., The present state of Atomic Spectra, J. Opt. Pura Aplicada **11,** No. 3, 103–113 (1969).
Sleater, G. A., Freeman, D. H., Rapid desorption of chromium (III) from cation exchanger with hydrogen peroxide solutions, Anal. Chem. **42,** No. 13, 1666–1668 (November 1970).
Staveley, L. A. K., Hard-sphere model applied to the solubility of gases in low-boiling liquids, J. Chem. Phys. **53,** No. 8, 3136–3138 (October 15, 1970).
Stein, P. G., Image-analyzing microscopes, Anal. Chem. **42,** No. 13, 103A–107A (November 1970).
Stevens, M. E., Introduction to the Special Issue on Optical Character Recognition (OCR), Pattern Recog. **2,** No. 3, 147–150 (September 1970).
Stevens, M. E., Selected R & D requirements in the computer and information sciences, Proc. Fall Joint Computer Cong., Houston, Texas, November 17–19, 1970, pp. 159–168 (AFIPS Press, Montvale, N.J., 1970).
Stevenson, D. R., Technical Standards Coordinator, Rigid poly (vinyl chloride) (PVC) profile extrusions, Nat. Bur. Stand. (U.S.), Voluntary Prod. Stand. 26–70, 7 pages (Oct. 1970) 10 cents, SD Catalog No. C13.20/2:26–70.
Straty, G. C., Prydz, R., Fluorine compatible apparatus for accurate PVT measurements, Rev. Sci. Instr. **41,** No. 8, 1223–1227 (August 1970).
Thomas, A. M., Further study of vacuum vane gauge criteria: Effects of port-vane geometry, J. Vacuum Sci. Technol. **7,** No. 4, 501–503 (July–August 1970).
Weidman, M. P., Campbell, E., A method for designing multi-screw waveguide tuners, Nat. Bur. Stand. (U.S.), Tech. Note 393, 20 pages (Oct. 1970) 30 cents, SD Catalog No. C13.46:393.
White, H., Editor, Vocabulary for Information Processing, Nat. Bur. Stand. (U.S.), Fed. Info. Process. Stand. Publ. (FIPS Pub.) 11, 4 pages (1970) 15 cents, SD Catalog No. C13.52:11.
Yakowitz, H., Some uses of color in metallography, Am. Soc. Testing Mater., Spec. Publ. 480, pp. 49–66 (1970).
Yokel, F. Y., Somes, N. F., Proposed revision of ACI 318–63 Building Code Requirements for Reinforced Concrete, J. Am. Concrete Inst. **67,** No. 9, 723–725 (September 1970).
Young, J. P., Lamb, V. A., Reid, G. I., Berkeley, J. F., Ng, W., Electroplated coatings on maraging steel for retarding catalytic decomposition of hydrazine rocket fuel, Plating **57,** No. 9, 921–926 (September 1970).
Younglove, B. A., Straty, G. C., A capacitor for accurate wide range dielectric constant measurements on compressed fluids, Rev. Sci. Instr. **41,** No. 7, 1087–1089 (July 1970).
Zimmerman, J. E., Low cost sensors with millikelvin temperatures and other virtues (Summary), Proc. Conf. Precision Electromagnetic Measurements, National Bureau of Standards, Boulder, Colorado, June 2–5, 1970, CPEM Digest, p. 1 (1970).

**Publications for which a price is indicated are available by purchase from the Superintendent of Documents, U.S. Government Printing Office, Washington, D.C. 20402 (foreign postage, one-fourth additional). The NBS non-periodical series are also available from the National Technical Information Service (NTIS), Springfield, Va. 22151, which was formerly the Clearinghouse. Reprints from outside journals and the NBS Journal of Research may often be obtained directly from the authors.*

U.S. GOVERNMENT PRINTING OFFICE : 1971 OL—418–535

UNIVERSITY MICROFILMS INC
ATTN SERIALS SECTION
300 NORTH ZEEB RD
ANN ARBOR MICH 48106

U.S. DEPARTM
WASHINGT

OFFICIAL BUSINESS

PENALTY FOR PRIVATE USE, $300

U.S. DEPARTMENT OF COMMERCE
POSTAGE AND FEES PAID

U.S.MAIL

JOURNAL OF RESEARCH of the National Bureau of Standards
A. Physics and Chemistry

Vol. 75A, No. 3 May–June 1971

Contents

Page

The solid phase photolysis and radiolysis of ethylene at 20 to 77 K. R. Gorden, Jr., and P. Ausloos. 141

Kinetic mass spectrometric investigation of the ion-molecule reactions occurring in C_4 and C_5 alkanes following photoionization at 106.7 and 104.8 nm. L. Wayne Sieck, S. K. Searles, and P. Ausloos. 147

An alumina standard reference material for resonance frequency and dynamic elastic moduli measurement. I. For use at 25 °C. R. W. Dickson and J. B. Wachtman, Jr. 155

Optical and mechanical properties of some neodymium-doped laser glasses. R. M. Waxler, G. W. Cleek, I. H. Malitson, M. J. Dodge, and T. A. Hahn. 163

Effect of environment on viscous flow in inorganic oxide glasses. Joseph H. Simmons and Pedro B. Macedo. 175

Phase relations in the SrO-IrO_2-Ir system in air. C. L. McDaniel and S. J. Schneider. 185

The crystal structure of $BaCa(CO_3)_2$ (barytocalcite). B. Dickens and J. S. Bowen. 197

Ionization of hydrofluoric acid at 25 °C. P. R. Patel, E. C. Moreno, and J. M. Patel. 205

Vapor pressure equation for water in the range 0 to 100 °C. Arnold Wexler and Lewis Greenspan. 213

Publications of the National Bureau of Standards. 231

Library of Congress Catalog Card Number: 62–37059

For sale by the Superintendent of Documents, U.S. Government Printing Office, Washington, D.C. 20402. (Order by SD Catalog No. C 13.22/sec.A:75/3). Single copy price varies. This issue $1.50. Subscription price: $9.50 a year; $2.25 additional for foreign mailing.
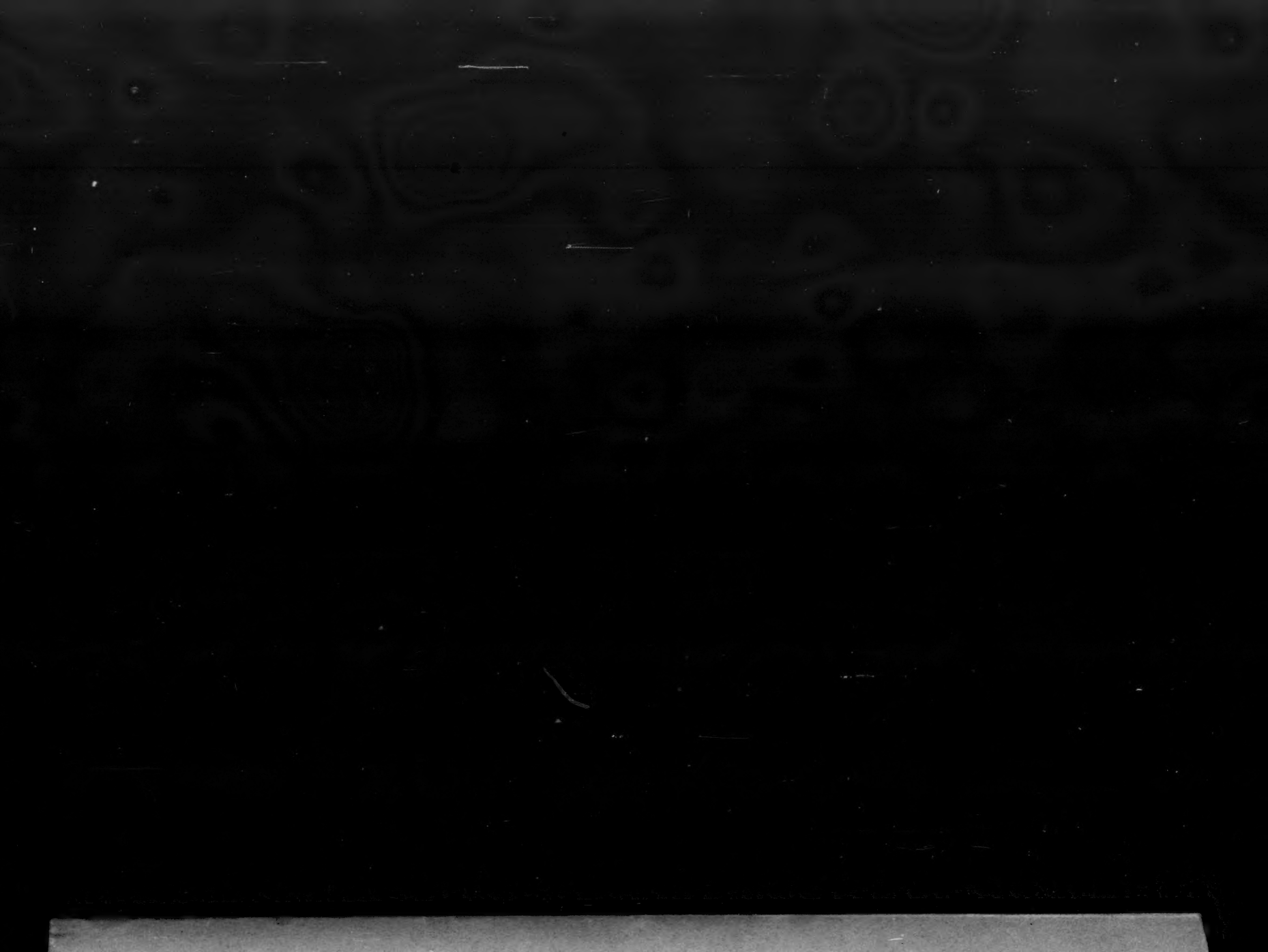
UNITED STATES GOVERNMENT PRINTING OFFICE, WASHINGTON : 1971